STUDY OF ELLIPTIC FLOW IN Au+Au AND Cu+Cu COLLISIONS AT RHIC ENERGIES

A THESIS

submitted to the

FACULTY OF SCIENCE

PANJAB UNIVERSITY, CHANDIGARH

for the degree of

DOCTOR OF PHILOSOPHY

2011

NAVNEET KUMAR

DEPARTMENT OF PHYSICS
CENTRE OF ADVANCED STUDY IN PHYSICS
PANJAB UNIVERSITY, CHANDIGARH
INDIA

Dedicated to

my respected parents

for their hard-work and efforts

which made me able to achieve this goal,

my loving wife 'Anita'

for her continuous push, love, help and care,

my sweet son 'Anhad'

whose birth brought this occasion for me

and my dear friends to support me throughout the way of this journey.

Acknowledgments

I am feeling glad in having this opportunity to thank all those related to my research work in some way or other. My thesis work would have not been possible without the support and encouragement from teachers, colleagues and friends. Hope I'll not miss most of the names in acknowledging them.

Firstly, I express my heartily gratitude to Prof. M. M. Aggarwal, my supervisor at Panjab University, Chandigarh, India for his continuous guidance, encouragement, healthy discussions and support throughout the thesis work. I am very thankful to him for being given the opportunity of working in an International Collaboration and getting a lot of National and International research exposure. I also extend my sincere gratefulness to Prof. A. K. Bhati, Panjab University, Chandigarh, India, for being available to me at my dark times. Its was a invaluable experience to work with both of them.

The next most important person whom I would like to express my deepest regards is Dr. Paul Richard Sorensen, Brookhaven National Laboratory, U.S.A., who is person after Prof. M. M. Aggarwal with whom I spent most of the time for my research work. I thank him for his friendly behavior, long discussions for the research purpose and for always standing behind me. I am very grateful to him for giving me financial support from his own fellowship for visiting the Brookhaven National Laboratory, U.S.A. and helping me in all matters during my stay.

Its my great pleasure to be associated with the Department of Physics, Panjab University, Chandigarh. My sincere thanks is to Prof. C. S. Aulakh, Chairperson, Department of Physics and Ex-Chairpersons Prof. M. M. Gupta, Prof. Nirmal Singh for providing me the various facilities and opportunities for my research work. I would also like to thanks my teachers Prof. Vishwamittar, Prof. Manjit Kaur and Dr. Devinder Mehta for their help and support.

I would like to express my sincere thanks to Dr. Y. P. Viyogi, group leader PMD project for his continuous efforts to lead the group and to give me the exposure of the International physics discussions.

I am also grateful to PMD group at Variable Energy Cyclotron Center (VECC), Kolkata, I am heartily thankful to Dr. Subhsasis Chattopadhyay, for providing me the opportunity to work with Dr. Paul Sorensen and for his help and support in my research work. I am also thankful to Dr. Bedangadas Mohanty, for his encouragement, healthy discussions and time spent with him in VECC. I am also sincerely thankful to Dr. Tapan Nayak, Dr. Anand Kumar Dubey, Dr. Zubeyer Ahmed, Dr. P. Ghosh, Mr. S. Ramnarayan, Mr. V. Singhal, Mr. M. Duttamazumdar, Mr. J. Saini and Mr. G. S. N.

Murthy for being ever ready to help me.

I would like to thank Dr. Art Poskanzer and Dr. Sergei Voloshin, Lawrence Berkley Laboratory, Berkley, U.S.A. for their useful suggestions and discussion on my analysis topic.

I am thankful to our group at Brookhaven National Laboratory. My special thanks is to STAR group head Dr. Timothy Hallman and Dr. Jamie Dunlop for financial assistance to my trips to Brookhaven National Laboratory, U.S.A. .

I take this opportunity to thank my seniors in the department Mr. Ajay Thakur, Dr. Gurinder Singh, Dr. Ashok Kumar, Dr. Jatinder Kaur, Dr. Kuljeet Singh, Dr. Sanjeev Kumar, Dr. Rajesh Thakur, Mr. Birija Prasad Mohanty, Dr. Hardev Singh, Dr. Sham Kumar, Dr Rajiv Sharma, Dr. Jeewan Sharma, Dr. Monika Sharma for their moral support and timely help.

It is a pleasure for me to thank my scholar friends Mr. Sunil Bansal, Mr. Indeprpal Singh, Mr. Sunil Sharma, Mr. Virenderjit Singh, Mr. Surinder Kumar, Mr. Gurjeet Singh, Mr. Anil Partap, Mr. Raj Kumar, Mr. Lokesh Kumar, Mr. Ishwar Dutt, Mr. Sumit Garg, Mr. Vishal Bhardwaj for making my stay lively in the department. I would also thank my others friends in university for being with me in ups and downs during my stay in university. My special thanks is to Mr. Sunil Bansal and Mr. Inderpal Singh for being available always.

My research work would not have been possible without the technical support from the department. I am very thankful to Mr. Satish Sharma, our Laboratory Technician and other members of purchase section of our department, Mr. Dinesh Kumar Gupta, Mr. Ajit Singh, Mr. Roop Lal, Mr. Sanjeev Pathania, Mr. Udham Singh and Mr. Daljit Singh, Mr. Raj Kumar Dogra, for their support at every stage. I am also thankful to Mr. Pushpinder Kumar, Mr. Sanjeev Kumar and Mr. Prem Pathania and other non-teaching staff of our department for help.

I am very thankful to research scholar within our group at Chandigarh, Ms. Bhanu Sharma, Ms. Deepika Rathee, Ms. Isha Chawla for reading my thesis and being ready to help me always. I am thankful to Mrs. Natasha Sharma for her co-operative attitude during my stay in Department.

I am sincerely thankful to my friends, Mr. Lakhwinder Singh, Mrs. Geetanjli, Mrs. Shruti, Dr. Sunil Dogra, Dr. Neeraj Gupta, Ms. Anita Mahajan, Ms. Anju Angurana, Ms. Seema Rani, Dr. Satish Sharma, Mr. Sidharath Prasad, Mr. Mriganka, Mr. Partim Bhaduri, Mr. Vineet Kumar, Mr. Uma Shankar, Mr. Prabhat Pujari, Mr. Chitrasen, Mr. Gaurav Jindal, Mr. Narinder Chugh, Mr. Virender Rana, Mr. Kamal Kishor, Mr. Amit Kumar, Mr. Parveen Kumar, Mr. Rohit Soni and Mr. Vivek Arora for nice time spent with them.

I would like to thanks my colleagues in college, Mr. Harbans Jasuja, Dr. Madhvi, Ms. Anita Arora, Mrs. Pooja Arora, Ms. Mamta, Ms. Lakhwinder Kaur, Mr. Deepak Mittal,

Mr. Gulshan Raheja, Mr. Sunil Arora, Dr. Jagdish Kumar, Mr. Bali Bhahadur, Mr. Rupinder Singh and Mr. Sukhwinder Singh for their encouragement to achieve the this opportunity.

I would also acknowledge the Department of Science and Technology, India and Department of Atomic Energy, Govt. of India for funding our research project and Council of Scientific and Industrial Research (CSIR), India, giving me financial support to attend the International Conference in High Energy Physics (ICHEP08), in U.S.A.

I admire my great friend Mr. Manoj Goyal for being with me throughout my carrier. I am deeply thankful to him for giving me support and encouragement throughout the journey.

In the last, I would like to express gratitude to my parents, grandparents and my sisters families for their blessings which brought me to finish my research work. I am extremely thankful to my loving wife for her unconditional love and help in completing my thesis. I am heartily thankful to my parents and grandparents for their encouragement and patience. I am also thankful to my sisters families and sister-in-law family for their moral support.

"Thank you God for all the blessings and abundance in my life!"

Date :

Chandigarh Navneet Kumar

Abstract

The Relativistic Heavy Ion Collider (RHIC) at Brookhaven National Laboratory (BNL), Upton, U.S.A. has been designed to artificially create the extreme conditions for Quark Gluon Plasma (QGP). In heavy ion collisions different probes for searching the QGP has been studied by correlating the various information from the produced particles.

The study of charged particles produced in Au+Au and Cu+Cu collisions at $\sqrt{s_{NN}}$=200 and 62.4 GeV and photons produced in Au+Au collisions at $\sqrt{s_{NN}}$=200 and 62.4 GeV, collected by Solenoidal Tracker at RHIC (STAR), BNL, U.S.A. has been presented. The detailed information about the charged particles is collected from the Time Projection Chamber (TPC) and of photons from the Photon Multiplicity Detector (PMD).

The photons are produced at all stages of the collisions and don't interact with the created matter, therefore, gives direct indications about the nature of matter created in heavy ion collisions. We present the study of energy dependence of photons elliptic flow using two different methods in Au+Au collisions at 200 and 62.4 GeV. The photons are collected in the region $-3.7 < \eta < -2.3$ using the Photon Multiplicity Detector in the STAR experiment.

We present STAR measurements of elliptic flow (v_2) from two- and four-particle cumulants ($v_2\{2\}$ and $v_2\{4\}$) for Au+Au and Cu+Cu collisions at center of mass energies $\sqrt{s_{NN}}$ = 200 and 62.4 GeV. The difference between $v_2\{2\}^2$ and $v_2\{4\}^2$ is related to v_2 fluctuations (σ_{v_2}) and non-flow (δ_2). Since it is not possible to disentangle v_2 fluctuations and non-flow in this study, we present an upper-limit on v_2 fluctuations $(\frac{\sigma_{v_2}}{v_2})_{max}$ under the assumption of zero contribution from non-flow. Following the assumption that eccentricity fluctuations σ_ε dominates v_2 fluctuations *i.e.* $\frac{\sigma_{v_2}}{v_2} \approx \frac{\sigma_\varepsilon}{\varepsilon}$, we derive the non-flow (δ_2) required by data if different models correctly describe the eccentricity flucutations. These tests based on the difference between $v_2\{2\}^2$ and $v_2\{4\}^2$ may be used to constrain or eliminate eccentricity models of heavy ion collisions. We also present the comparison of eccentricity scaled v_2 using the eccentricity from different models. Elliptic flow results have been compared with three different eccentricity models viz., Monte Carlo Glauber for Nucleon as Participants (MCG-N), Monte-Carlo Glauber Model for Constituent Quarks as Participants (MCG-Q) and Color Glass Condensate based Monte-Carlo Model (fKLN-CGC). The saturation of eccentricity scaled v_2 for the fKLN-CGC model is consistent with nearly perfect hydrodynamics behaviour for the heavy ion collisions at RHIC.

List of Collaborative Publications

1. **Measurement of the bottom contribution to non-photonic electron production in $p+p$ collisions at $\sqrt{s}$=200 GeV,**
   M. M. Aggarwal *et. al.* [STAR Collaboration],
   Phys. Rev. Lett. **105**, 203201 (2010).

2. **Balance Functions from Au+Au, d+Au and $p+p$ Collisions at $\sqrt{s_{NN}}$ = 200 GeV,**
   M. M. Aggarwal *et. al.* [STAR Collaboration],
   Phys. Rev. C **82**, 024905 (2010).

3. **Higher Moments of Net-proton Multiplicity Distributions at RHIC,**
   M. M. Aggarwal *et. al.* [STAR Collaboration],
   Phys. Rev. Lett. **105**, 022302 (2010).

4. **Azimuthal di-hadron correlations in d+Au and Au+Au collisions at $\sqrt{s_{NN}}$ =** 200 **GeV from STAR,**
   M.M. Aggarwal *et. al.* [STAR Collaboration],
   Phys. Rev. C **82**, 024912 (2010).

5. **Pion femtoscopy in p+p collisions at $\sqrt{s}$=200 GeV,**
   M. M. Aggarwal *et. al.* [STAR Collaboration],
   arXiv:1004.0925 [nucl-ex] .

6. **Longitudinal scaling property of the charge balance function in Au + Au collisions at 200 GeV,**
   B. I. Abelev *et. al.* [STAR Collaboration],
   Phys. Lett. B **690**, 239-244 (2010).

7. **Charged and strange hadron elliptic flow in Cu+Cu collisions at $\sqrt{s_{NN}}$ = 62.4 and 200 GeV,**
   B. I. Abelev *et. al.* [STAR Collaboration],
   Phys. Rev. C **81**, 044902 (2010).

8. **Υ cross section in $p+p$ collisions at $\sqrt{(}s) = 200$ GeV,**
   B. I. Abelev *et. al.* [STAR Collaboration],
   Phys. Rev. D **82**, 012004 (2010).

9. **Three-particle coincidence of the long range pseudorapidity correlation in high energy nucleus-nucleus collisions,**
   B. I. Abelev *et. al.* [STAR Collaboration],
   Phys. Rev. Lett. **105** 022301, (2010).

10. **Inclusive π^0, eta, and direct photon production at high transverse momentum in p+p and d+Au collisions at $\sqrt{s_{NN}}$ = 200 GeV,**
    B. I. Abelev *et. al.* [STAR Collaboration],
    Phys. Rev. C **81**, 064904 (2010).

11. **Studying Parton Energy Loss in Heavy-Ion Collisions via Direct-Photon and Charged-Particle Azimuthal Correlations,**
    B. I. Abelev *et. al.* [STAR Collaboration],
    arXiv:0912.1871 [nucl-ex].

12. **Observation of pi+ pi- pi+ pi- Photoproduction in Ultra-Peripheral Heavy Ion Collisions at STAR,**
    B. I. Abelev *et. al.* [STAR Collaboration],
    Phys. Rev. C **81**, 044901 (2010).

13. **Spectra of identified high-p_T $\pi^{\pm}$ and $p(\bar{p})$ in Cu+Cu collisions at $\sqrt{s_{NN}} = 200$ GeV,**
    B. I. Abelev *et. al.* [STAR Collaboration],
    Phys. Rev. C **81**, 054907 (2010).

14. **Longitudinal double-spin asymmetry and cross section for inclusive neutral pion production at midrapidity in polarized proton collisions at $\sqrt{s}$ = 200 GeV,**
    B. I. Abelev *et. al.* [STAR Collaboration],
    Phys. Rev. D **80**, 111108 (2009).

15. **Longitudinal Spin Transfer to Lambda and anti-Lambda Hyperons in Polarized Proton-Proton Collisions at $\sqrt{s_{NN}}$= 200 GeV,**
    B. I. Abelev *et. al.* [STAR Collaboration],
    Phys. Rev. D **80**, 111102 (2009).

16. **Identified particle production, azimuthal anisotropy, and interferometry measurements in Au+Au collisions at $\sqrt{s_{NN}}$ = 9.2 GeV,**
    B. I. Abelev *et. al.* [STAR Collaboration],
    Phys. Rev. C **81**, 024911 (2010).

17. **Azimuthal Charged-Particle Correlations and Possible Local Strong Parity Violation,**

B. I. Abelev *et. al.* [STAR Collaboration],
Phys. Rev. Lett. **103**, 251601 (2009).

18. **Observation of charge-dependent azimuthal correlations and possible local strong parity violation in heavy ion collisions,**
B. I. Abelev *et. al.* [STAR Collaboration],
Phys. Rev. C **81**, 054908 (2010).

19. **Yields and elliptic flow of d(anti-d) and He-3(anti-He-3) in Au + Au collisions at $\sqrt{s_{NN}}$= 200 GeV,**
B. I. Abelev *et. al.* [STAR Collaboration],
arXiv:0909.0566 [nucl-ex].

20. **Long range rapidity correlations and jet production in high energy nuclear collisions,**
B. I. Abelev *et. al.* [STAR Collaboration],
Phys. Rev. C **80**, 064912 (2009).

21. **Neutral Pion Production in Au+Au Collisions at $\sqrt{s_{NN}}$ = 200 GeV,**
B. I. Abelev *et. al.* [STAR Collaboration],
Phys. Rev. C **80**, 044905 (2009).

22. **Center of mass energy and system-size dependence of photon production at forward rapidity at RHIC,**
B. I. Abelev *et. al.* [STAR Collaboration],
Nucl. Phys. A **832**, 134-147 (2010).

23. **Growth of Long Range Forward-Backward Multiplicity Correlations with Centrality in Au+Au Collisions at $\sqrt{s_{NN}}$ = 200 GeV,**
B. I. Abelev *et. al.* [STAR Collaboration],
Phys. Rev. Lett. **103**, 172301 (2009).

24. **System size dependence of associated yields in hadron-triggered jets,**
B. I. Abelev *et. al.* [STAR Collaboration],
Phys. Lett. B **683**, 123-128 (2010).

25. **J/psi production at high transverse momentum in p+p and Cu+Cu collisions at $\sqrt{s_{NN}}$ = 200GeV,**
B. I. Abelev *et. al.* [STAR Collaboration],
Phys. Rev. C **80**, 041902 (2009).

26. **Pion Interferometry in Au+Au and Cu+Cu Collisions at RHIC,**
B. I. Abelev *et. al.* [STAR Collaboration],
Phys. Rev. C **80**, 024905 (2009).

27. **K/pi Fluctuations at Relativistic Energies,**
B. I. Abelev *et. al.* [STAR Collaboration],
Phys. Rev. Lett **103**, 092301 (2009).

28. **Measurement of D* Mesons in Jets from p+p Collisions at $\sqrt{s} = 200$ GeV,**
B. I. Abelev *et. al.* [STAR Collaboration],
Phys. Rev. D **79**, 0112006 (2009).

29. **Observation of Two-source Interference in the Photoproduction Reaction $Au + Au - - - > Au + Au\rho_0$,**
B. I. Abelev *et. al.* [STAR Collaboration],
Phys. Rev. Lett **102**, 112301 (2009).

30. **Energy and system size dependence of phi meson production in Cu+Cu and Au+Au collisions,**
B. I. Abelev *et. al.* [STAR Collaboration],
Phys. Lett. B **673**, 183-191 (2009).

31. **Elliptic flow and the high p_T ridge in Au + Au collisions,**
N. K. Pruthi (For the STAR Collaboration),
Eur. Phys. J. C **62**, 165-167 (2009).

32. **Measurements of phi meson production in relativistic heavy-ion collisions at RHIC,**
B. I. Abelev *et. al.* [STAR Collaboration],
Phys. Rev. C **79**, 064903 (2009).

33. **Systematic Measurements of Identified Particle Spectra in pp, d+Au and Au+Au Collisions from STAR,**
B. I. Abelev *et. al.* [STAR Collaboration],
Phys. Rev. C **79**, 034909 (2009).

34. **Beam-Energy and System-Size Dependence of Dynamical Net Charge Fluctuations,**
B. I. Abelev *et. al.* [STAR Collaboration],
Phys. Rev. C **79**, 024906 (2009).

35. **System-size independence of directed flow at the Relativistic Heavy-Ion Collider,**
B. I. Abelev *et. al.* [STAR Collaboration],
Phys. Rev. Lett **101**, 252301 (2008).

36. **Charge Independent(CI) and Charge Dependent(CD) correlations as a function of Centrality formed from Delta phi imum Delta eta Charged Pair Correlations in Minimum Bias Au+Au Collisions at $\sqrt{s_{NN}}$ = 200 GeV,**
B. I. Abelev *et. al.* [STAR Collaboration],
arXiv:0806.0513 [nucl-ex]. Submitted to PRC.

37. **Indications of Conical Emission of Charged Hadrons at RHIC,**
B. I. Abelev *et. al.* [STAR Collaboration],
Phys. Rev. Lett **102**, 052302 (2009).

38. **Charmed hadron production at low transverse momentum in Au+Au collisions at RHIC,**
B. I. Abelev *et. al.* [STAR Collaboration],
arXiv:0805.0364 [nucl-ex] .

39. **Centrality dependence of charged hadron and strange hadron elliptic flow from $\sqrt{s_{NN}}$ = 200 GeV Au + Au collisions,**
B. I. Abelev *et. al.* [STAR Collaboration],
Phys. Rev. C **77**, 054901 (2008).

40. **Forward Neutral Pion Transverse Single Spin Asymmetries in p+p Collisions at $\sqrt{s_{NN}}$ = 200 GeV,**
B. I. Abelev *et. al.* [STAR Collaboration],
Phys. Rev. Lett **101**, 222201 (2008).

41. **Spin alignment measurements of the K*0(892) and phi (1020) vector mesons in heavy ion collisions at $\sqrt{s_{NN}}$ = 200 GeV,**
B. I. Abelev *et. al.* [STAR Collaboration],
Phys. Rev. C **77**, 061902 (2008).

42. **Hadronic resonance production in d+Au collisions at $\sqrt{s_{NN}}$= 200 GeV at RHIC,**
B. I. Abelev *et. al.* [STAR Collaboration],
Phys. Rev. C **78**, 044906 (2008).

43. **ρ^0 photoproduction in ultraperipheral relativistic heavy ion collisions at $\sqrt{s_{NN}}$= 200 GeV,**
B. I. Abelev *et. al.* [STAR Collaboration],
Phys. Rev. C **77**, 034910 (2008).

44. **Longitudinal double-spin asymmetry for inclusive jet production in p+p collisions at $\sqrt{s_{NN}}$= 200 GeV,**

B.I. Abelev *et. al.* [STAR Collaboration],
Phys. Rev. Lett **100**, 232003 (2008).

45. **Forward Lambda production and nuclear stopping power in d + Au collisions at $\sqrt{s_{NN}}$= 200 GeV,**
B. I. Abelev *et. al.* [STAR Collaboration],
Phys. Rev. C **76**, 064904 (2007).

46. **Enhanced strange baryon production in Au + Au collisions compared to p + p at $\sqrt{s_{NN}}$= 200 GeV,**
B. I. Abelev *et. al.* [STAR Collaboration],
Phys. Rev. C **77**, 044908 (2008).

47. **Global polarization measurement in Au+Au collisions,**
B. I. Abelev *et. al.* [STAR Collaboration],
Phys. Rev. C **76**, 024915 (2007).

48. **Elliptic flow in ridge-like and jet like events in heavy ion collisions at RHIC energies,**
N. K. Pruthi (For the STAR Collaboration)
Proceeding DAE-BRNS HEP symposium, Vol 18, 262-265 (2008).

49. **Elliptic flow in ridge-like and jet like events in heavy ion collisions at RHIC energies,**
N. K. Pruthi (For the STAR Collaboration)
Proceeding DAE-BRNS NP symposium, Vol 53, 629-630 (2008).

50. **Transverse momentum spectra of charged particles in proton-proton collisions at $\sqrt{s} = 900$ GeV with ALICE at the LHC,**
K. Aamodt *et. al.* [ALICE Collaboration],
Phys. Lett. B **693**, 53-68 (2010).

51. **Midrapidity antiproton-to-proton ratio in pp collisions at $\sqrt{s} = 0.9$ and 7 TeV measured by the ALICE experiment,**
K. Aamodt *et. al.* [ALICE Collaboration],
Phys. Rev. Lett. **105**, 072002 (2010).

52. **Charged-particle multiplicity measurement in proton-proton collisions at sqrt(s) = 7 TeV with ALICE at LHC,**
K. Aamodt *et. al.* [ALICE Collaboration],
Eur. Phys. J. C **68**, 345-354 (2010).

53. **Charged-particle multiplicity measurement in proton-proton collisions at sqrt(s) = 0.9 and 2.36 TeV with ALICE at LHC,**
K. Aamodt *et. al.* [ALICE Collaboration],
Eur. Phys. J. C **68**, 89-108 (2010).

54. **Alignment of the ALICE Inner Tracking System with cosmic-ray tracks,**
K. Aamodt *et. al.* [ALICE Collaboration],
JINST 5:P03003 (2010).

55. **First proton-proton collisions at the LHC as observed with the ALICE detector: Measurement of the charged particle pseudorapidity density at $\sqrt{s_{NN}}$ = 900 GeV,**
K. Aamodt *et. al.* [ALICE Collaboration],
Eur. Phys. J. C **65**, 111-125 (2010).

Contents

List of Figures

List of Tables

Chapter 1

Relativistic Heavy Ion Collisions

1.1 Introduction

The main goal of Relativistic Heavy Ion Collisions [1–4] is to study the properties of strongly interacting matter and QCD phase transitions. Relativistic heavy ion collisions are the only mean to compress and heat up matter in the laboratory to search for the formation of quark-gluon plasma supposed to be existed in first few microseconds after the big bang and possibly exists in core of neutron stars as predicted by quantum chromodynamics. The heavy ion collisions are well studied to produce conditions similar to those prevalent in the early universe. The probes to study Quark-Gluon Plasma in heavy ion collisions have been discussed.

1.2 Quark Gluon Plasma (QGP)

The Relativistic Heavy Ion Collisions are used to study the nature of the strongly interacting matter by creating extreme conditions of very high temperature and energy-density. The QCD in such extreme conditions predicts a phase transition to a new state of matter called quark gluon plasma (QGP) [5, 6]. The transition to the deconfined phase is associated with a rapid increase in energy-density with temperature and a more gradual increase in pressure [7, 8]. The energy-density and pressure give information about the equation of state and hence, about the basic degrees of freedom. Figure 1.1 shows energy-density

as a function of temperature [9], where T_c represents the critical temperature. These calculations are performed for non-zero temperature and non-zero chemical potential. The ϵ/T^4 is proportional to number of degrees of freedom. At critical temperature $T_c \approx 170$ MeV, ϵ/T^4 increases rapidly which indicates increase in degrees of freedom, showing the quarks and gluons becomes the relevant degrees of freedom. The arrows indicate the Stefan-Boltzmann limit:

$$\epsilon = g\frac{\pi^2}{30}T^4, \tag{1.1}$$

where g is the number of degrees of freedom. For hadron gas, the number of degrees of freedom are given by the three pion states (π^+, π^-, π^0), *i.e.,* g=3, Eq. 1.2 becomes:

$$\epsilon = 3\frac{\pi^2}{30}T^4, \tag{1.2}$$

In the QGP phase, the number of degrees of freedom are determined by quarks and gluons, which becomes very large as compared to hadron gas phase and energy-density is given as :

$$\epsilon_{QGP} = \left(16 + \frac{21}{2}n_{flavour}\right)\frac{\pi^2}{30}T^4, \tag{1.3}$$

The critical temperature depends on the number of flavors and the mass of quark. The blue line in the Fig. 1.1 shows the expectations for three light quark flavors, the red shows the two light quark calculations and the green curve shows the calculations for two light quarks (u,d) and a heavy quark (s).

The highest temperature that has been attained in collisions of Gold nuclei accelerated by Relativistic Heavy Ion Collider at Brookhaven National Lab (BNL) is expected to be above the lattice QCD predicted value of critical temperature/energy-density. The experimental observations of properties of matter in the extreme conditions of temperature and pressure significantly extend our understanding of one of the most fundamental interactions and the equation of state of nuclear matter.

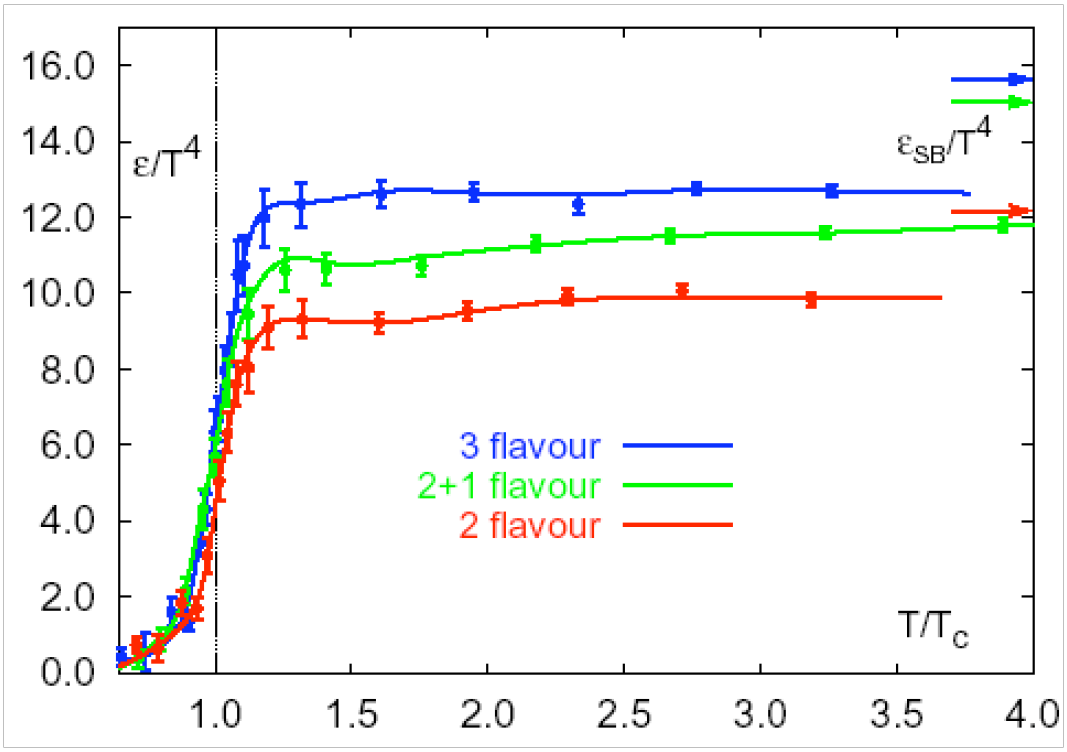

Figure 1.1: Lattice calculations of Energy density as a function of temperature [9].

The phase diagram for the nuclear matter in terms of net baryon density (μ_B) and temperature is shown in Fig. 1.2. The Lattice QCD predicts boundary in the phase diagram separating the matter dominated by hadronic degrees of freedom from the matter dominated by quark-gluon degrees of freedom. The boundary between the two is called 'QCD phase boundary'. The point in the phase diagram where first order phase transition ends is called 'critical point'. The region close to $\mu_B \sim 0$ shown with dotted line represents the rapid crossover with no real transition. The only region known in this matter is hadronic matter, everything else are lattice predictions. The space-time evolution of heavy ion collisions with longitudinal coordinate z and the time coordinate t is also shown in Fig. 1.3. Let us consider the head-on collision of two Lorentz contracted nuclei along the beam axis taken as z-axis. Soon after the collision of nuclei at (z, t)=(0,0) the nucleons inside the overlap region start interacting to produce matter with densities much higher than normal nuclear matter density. If the amount of energy-density deposited in small interaction region in heavy ion collisions becomes large enough and temperature of system reaches the critical temperature, then phase transition is supposed to occur and region

containing deconfined quarks and gluons formed *i.e.* QGP. The expansion of system is then governed by QGP equation of state. During the hadronization system is likely to evolve through the mixed phase of quarks, gluons and hadrons. The complete hadronization of quarks and gluons results in hadron gas which continue expansion upto *chemical freeze-out* temperature/time at which their relative abundance doesn't change. The cooling of system so that even hadrons don't interact elastically, gives rise to *kinetic freeze-out*.

The relativistic heavy ion experiments have been performed with Alternating Gradient Synchrotron (AGS) at Brookhaven National Laboratory, U.S.A., Super Proton Synchrotron (SPS) at CERN, Geneva and Relativistic Heavy Ion Collider (RHIC) at Brookhaven National Laboratory, U.S.A. at center of mass energies $\sqrt{s}_{NN}$ = 4.75, 17.2, 200 GeV respectively. The Large Hadron Collider (LHC) at CERN, Geneva has recently taken first data for Pb+Pb collisions at center of mass energy $\sqrt{s}_{NN}$ = 2.76 TeV.

Since particles after the kinetic freeze-out are detected by the detectors, therefore, most of information about the early stage of the collisions washed out by final state interactions. However, there are number of signatures [10–14] which provides the information about the QGP and early stages of the collisions.

RHIC collisions have provided us an opportunity to study QCD at finite temperature and very high energy density. However, in an actual heavy ion collision which evolves as dynamical system, the sufficient conditions for matter to exist as QGP may only be achieved partially.

1.3 QGP Probes

In relativistic heavy ion collisions, under the conditions of high density and temperature, deconfined state of quarks and gluons called QGP is expected to form. The hadrons made from deconfined phase are supposed to give information about the QGP phase. Photons and dileptons don't interact with the created matter and give direct indication about the nature of matter but they are difficult to study due to small cross sections. The hadronic observables are most commonly studied particles to probe the matter created in heavy

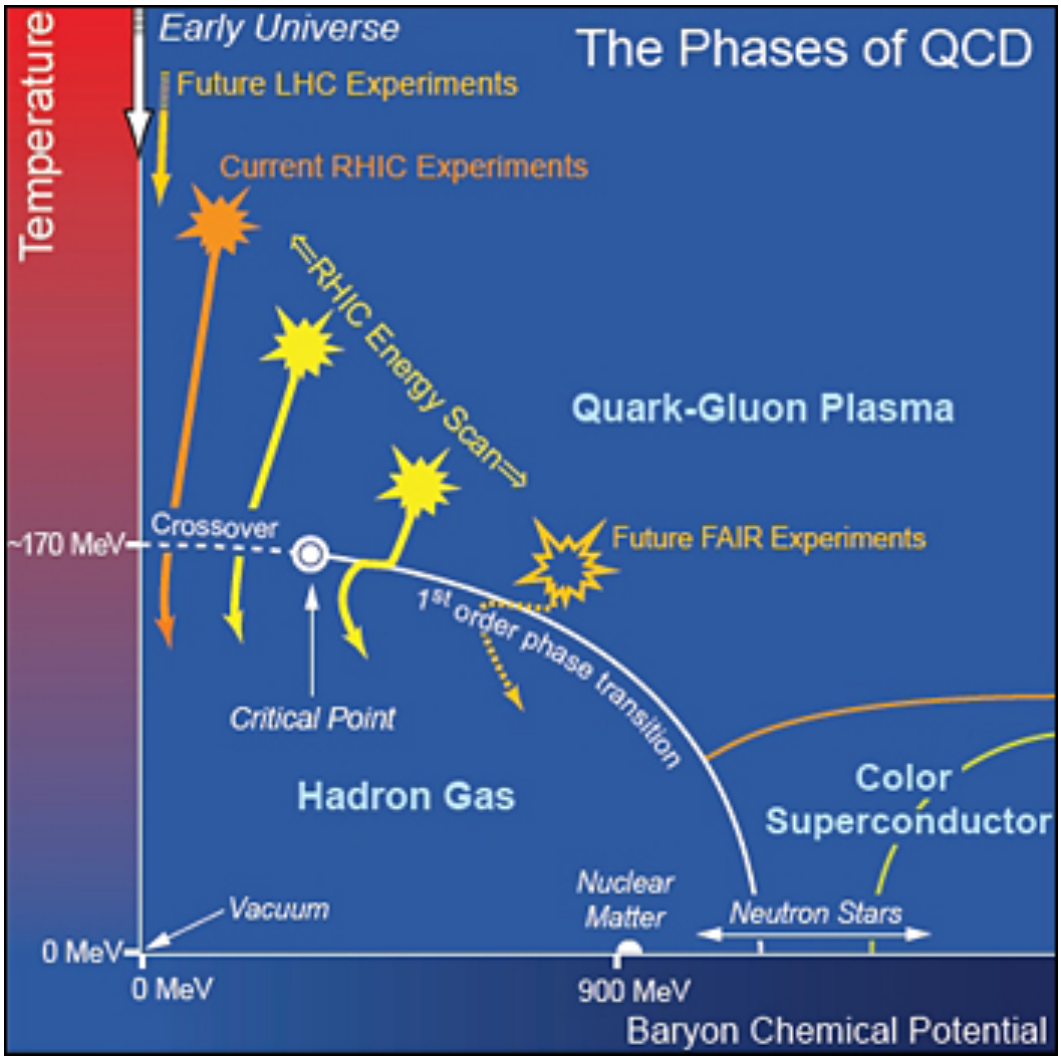

Figure 1.2: A schematic phase diagram of strongly interacting matter.

ion collisions. In the following section, some of the basic probes of QGP are discussed.

1.3.1 Direct Photons

The direct photons and dileptons provide information about the early stages of the collisions as they are not affected much by the later stages of the collisions. In QGP the direct

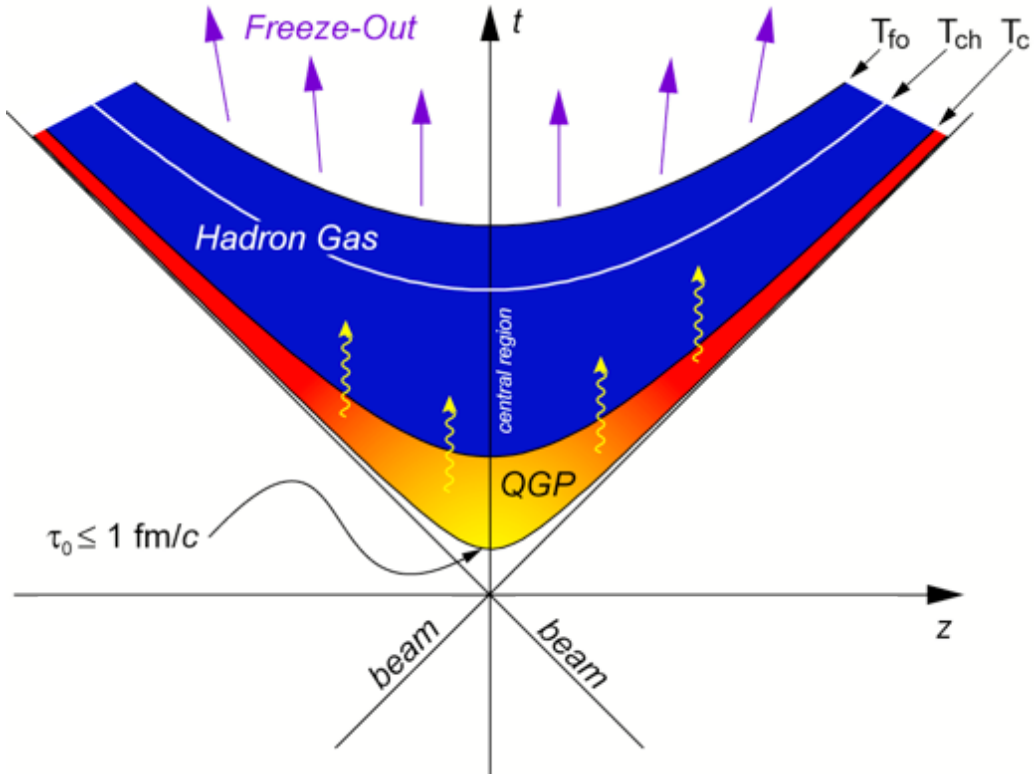

Figure 1.3: Space-time evolution of the heavy ion collisions.

photons are mostly created by the process,

$$q + \bar{q} \rightarrow \gamma + g \tag{1.4}$$

This process is called annihilation process and represented by the Feynman diagrams in Fig. 1.4 and the other process,

$$q + \bar{q} \rightarrow \gamma + \gamma \tag{1.5}$$

is also allowed process but the probability for its occurrence is smaller by a factor of the order of α_e/α_s or about 0.02. Where α_e is electromagnetic fine structure constant and α_s is related to strong interactions coupling constant g as:

$$\alpha_e = \frac{e^2}{4\pi}, \qquad \alpha_s = \frac{g^2}{4\pi} \tag{1.6}$$

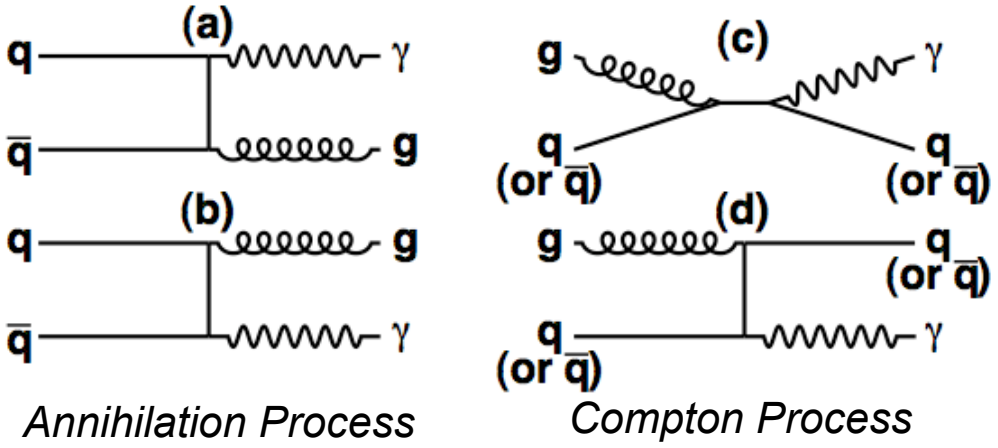

Figure 1.4: The Feynman diagrams for the processes which leads to the production of photons in the Quark Gluon Plasma. The Processes (a) and (b) represents annihilation process, (c) and (d) represents Compton process.

Because $\alpha_e << \alpha_s$, only the annihilation process is considered for direct photon production from QGP phase.

The gluon can interact with the a quark or anti-quark to produce a photon by the reactions,

$$g + q \rightarrow \gamma + q \tag{1.7}$$

$$g + \bar{q} \rightarrow \gamma + \bar{q} \tag{1.8}$$

These reactions are analogous to Compton scattering of the photons, hence called Compton processes. The produced photons interact with particles in the collision region only through electromagnetic interactions. Therefore, the mean free path of photon is expected to be too large and photon may not suffer any collision after it is produced. Also the production and momentum distribution of photons depend upon the momentum distribution of quarks, anti-quarks and gluons in the plasma. The rapidity distributions of direct photons reflect the initial rapidity distribution of produced mesons or directly the QGP [15]. Hydrodynamical calculations show that the temperature of the photons spectrum is reduced in the events of first order phase-transition to QGP [16–18]. The p_T distribution of direct photons can be used for this study. Figure 1.5 shows the photon

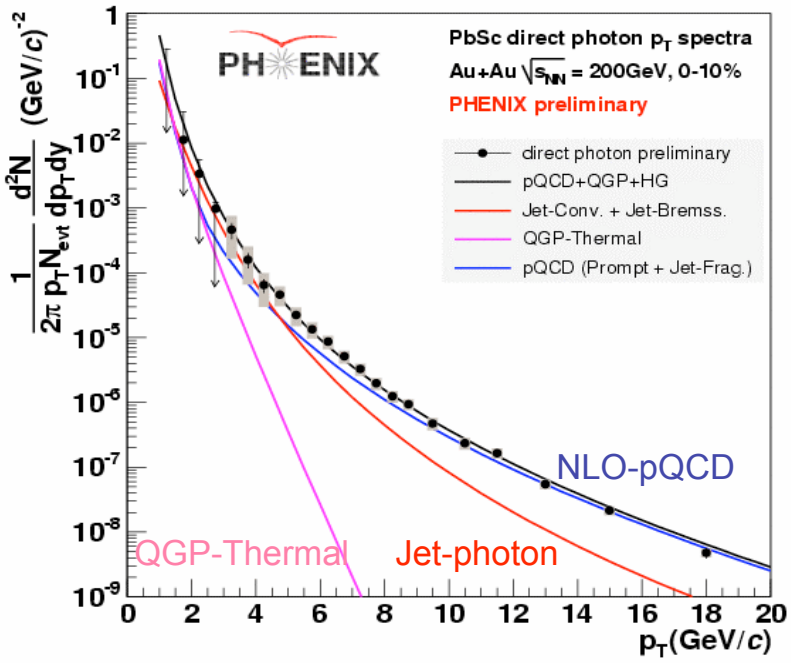

Figure 1.5: Direct photons spectrum for Au+Au 200 GeV by PHENIX experiment at RHIC.

spectrum for most central Au+Au collisions at 200 GeV obtained in PHENIX experiment at RHIC. The blue solid lines represent the photon yield from pQCD and black solid line represent the total photons yields from pQCD+QGP+HG. The spectrum obtained in PHENIX shows consistency with NLO-pQCD (Next-to-Leading Order-Perturbative QCD) predictions.

Figure 1.6 shows the direct photon measurements from WA98 experiment at SPS at $\sqrt{s_{NN}}$ =17.3 GeV [19]. The invariant direct photon multiplicity for central Pb+Pb collisions has been shown. The model calculations [20] with the assumption that chemically and thermally equilibrated quark-gluon plasma is formed at $\tau_0 = 1/3T_0$ are also displayed. The QGP is assumed to expand, cool, enter into a mixed phase and attain freeze out from a hadronic phase. QM represents the radiations from QGP and mixed phase. HM represents the radiations from hadronic matter in the mixed and hadronic phase. T_0 and τ_0 are the initial temperature and initial time of the system.

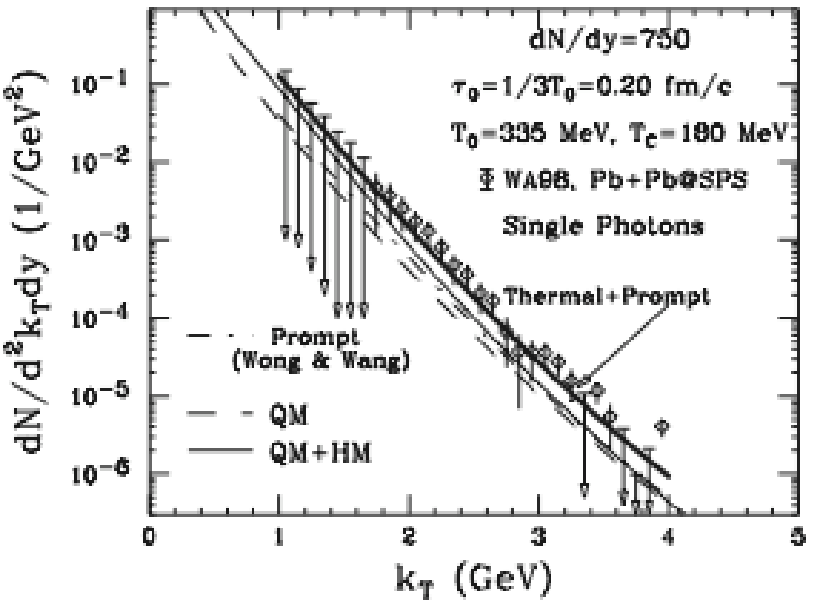

Figure 1.6: The invariant direct photon multiplicity for central Pb+Pb collisions at 17.3 GeV obtained in WA 98 experiment.

1.3.2 Strangeness Enhancement

Strangeness Enhancement is one of the signatures of the QGP [21]. The strangeness content in the hadronic matter and in a quark-gluon plasma is different [22–28]. The s and $\bar{s}$ quarks are enhanced in quark gluon plasma [24]. As, in a QGP scenario, quarks and gluons are produced in abundance. The two main production channels for $s\bar{s}$ are,

$$q + \bar{q} \rightarrow s + \bar{s} \tag{1.9}$$

$$g + \bar{g} \rightarrow s + \bar{s} \tag{1.10}$$

If $s\bar{s}$ production is considered from $q\bar{q}$ interactions, it would take about 8 times the lifespan of a QGP fireball to attain chemical equilibrium in strangeness. So, it was proposed that many quark-antiquark pairs are created dominantly by gluon-gluon fusion. In the QGP region, the energy available is so large that the temperature attained is of the same order as mass of strange quark. In such a case the coupling of gluons to the strange quarks would be similar to that with light quarks and as a result, strange quarks/antiquarks would be produced more frequently as compared to nucleon-nucleon collisions. The strangeness

enhancement in a baryon rich matter can also be a result of Pauli exclusion principle. Since initially the u and d quarks are in the abundance as compared to s quarks, the $u\bar{u}$ and $d\bar{d}$ pair production is prohibited by Pauli exclusion principle, which is not the case for $s\bar{s}$. Furthermore, the u and d quarks annihilate respectively with the $\bar{u}$ and $\bar{d}$ antiquarks, while $s\bar{s}$ annihilation occurs less frequently until the saturation of s and $\bar{s}$ abundances.

The strangeness enhancement is observed in terms of strangeness enhancement factor. It is defined as the yield per participating nucleon of a given type of strange particle in heavy ion collision relative to strange particle yield in a some reference system (*e.g.* $p+p$ collision at RHIC).

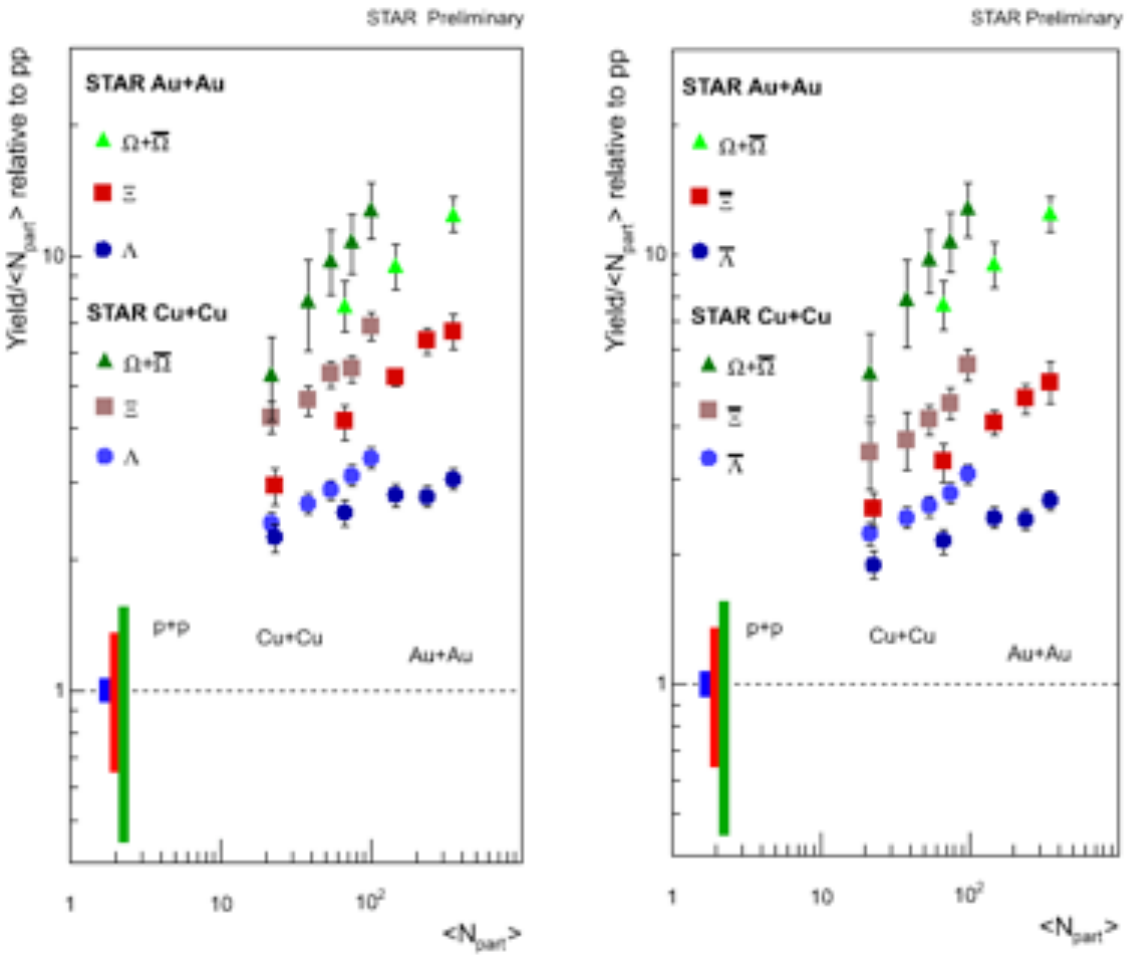

Figure 1.7: Mid-rapidity $E(i)$ as a function of $\langle N_{part}\rangle$ for $\Lambda, \bar{\Lambda}$ ($|y| < 1.0$), $\Xi^-, \Xi^+, \Omega^-, \Omega^-$ ($|y| < 0.75$) and inclusive $p(|y| < 0.5)$. Boxes at unity shows uncertainties combined in the $p+p$ data [30].

.

The strangeness enhancement has been studied at AGS, SPS and RHIC. The strangeness enhancement has been observed in Au+Au and Cu+Cu collisions at RHIC [29]. The enhancement yield $E(i)$ is defined as:

$$E(i) = \frac{Yield^{AA}(i)\langle N_{part}^{NN}\rangle}{Yield^{NN}(i)\langle N_{part}^{AA}\rangle} \tag{1.11}$$

Figure 1.7 shows the strangeness enhancement yield *vs.* $< N_{part} >$ observed in Au+Au and Cu+Cu collisions at mid-rapidity for different particles. No enhancement has been observed in $p + p$ collisions. Strangeness enhancement is seen in Au+Au and Cu+Cu collisions, especially in the more central collisions, when compared to the $\langle N_{part}\rangle$ scaled $p + p$ data from the same energy. In the Au+Au and Cu+Cu collisions, strangeness enhancement is found to increase with centrality and strangeness content.

1.3.3 High p_t Suppression

The energetic partons are also produced in relativistic heavy ion collisions due to the hard scattering. The interactions of these high energy partons with the medium can also provide probes for produced medium. The hard partons (jets) interact with the medium and thus suffer energy losses. The amount of energy loss reflects the gluon density of the medium. It was proposed that energy loss of the partons in QGP is much higher than that in normal hadronic matter. This phenomenon leads to the jet quenching [31–33], which is defined as the suppression of high p_T hadrons in the nucleus-nucleus collisions relative to that in a p+p collision scaled by number of elementary nucleon-nucleon collisions. The observable commonly used for this comparison, the nuclear modification factor defined as:

$$R_{AB}(p_T) = \frac{d^2N^{AB}/dp_Td\eta}{T_{AB}d^2\sigma^{pp}/dp_Td\eta}, \tag{1.12}$$

where $d^2N^{AB}/dp_Td\eta$ is the differential yield in A + B collisions, $d^2\sigma^{pp}/dp_Td\eta$ is the measured differential cross section for $p + p$ inelastic collisions. The term $T_{AB} = \langle N_{bin}\rangle/\sigma^{pp}_{inelastic}$, where $\langle N_{bin}\rangle$ is mean number of binary nucleon-nucleon collisions, is introduced to account for the nuclear geometry. R_{AB} is unity if A + B collision is superposition

of $p + p$ collisions.

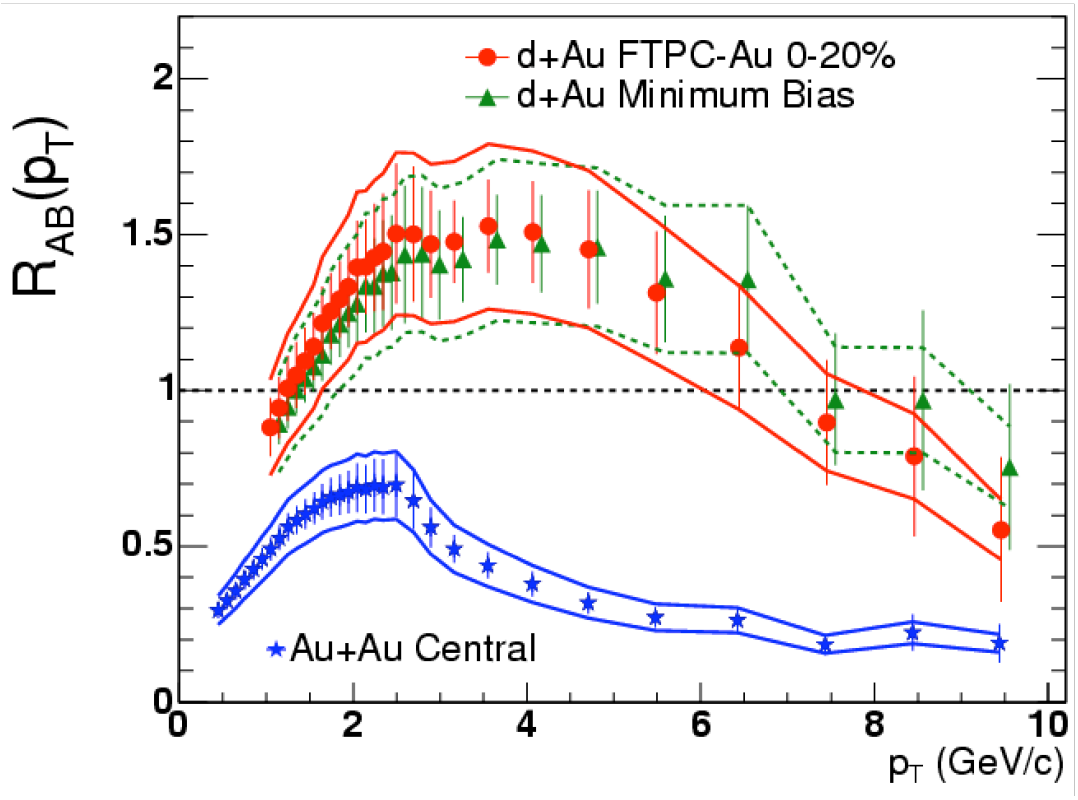

Figure 1.8: R_{AB} for d+Au and Au+Au collisions.

Figure 1.8 shows the R_{AB} for minimum bias central d+Au and Au+Au collisions. It is observed that $R_{AB} > 1$ for $2 < p_T < 7GeV/c$ for d+Au collisions. The R_{AB} shows the prominent suppression in hadron production at high p_T in Au+Au central collisions. Figure 1.9 shows the latest results for R_{AA} in the ALICE experiment at Large Hadron Collider and their comparison with results from STAR and PHENIX experiments at RHIC. At LHC, the suppression is more than that of RHIC energy.

Also, high p_T suppression in central $Au + Au$ collisions can be calculated by comparing hadrons spectra in central and peripheral $Au + Au$ collisions. The term R_{CP} (Fig. 1.10) used for this is defined as

$$R_{CP} = \frac{\langle N_{bin}^{peripheral} \rangle d^2N^{central}/dp_T d\eta}{\langle N_{bin}^{central} \rangle d^2N^{peripheral}/dp_T d\eta} \tag{1.13}$$

where $d^2N^{central}/dp_T d\eta$ and $d^2N^{peripheral}/dp_T d\eta$ are differential yields in central and peripheral collisions. $N_{bin}^{central}$ and $N_{bin}^{peripheral}$ are number of binary collisions. Figure 1.10

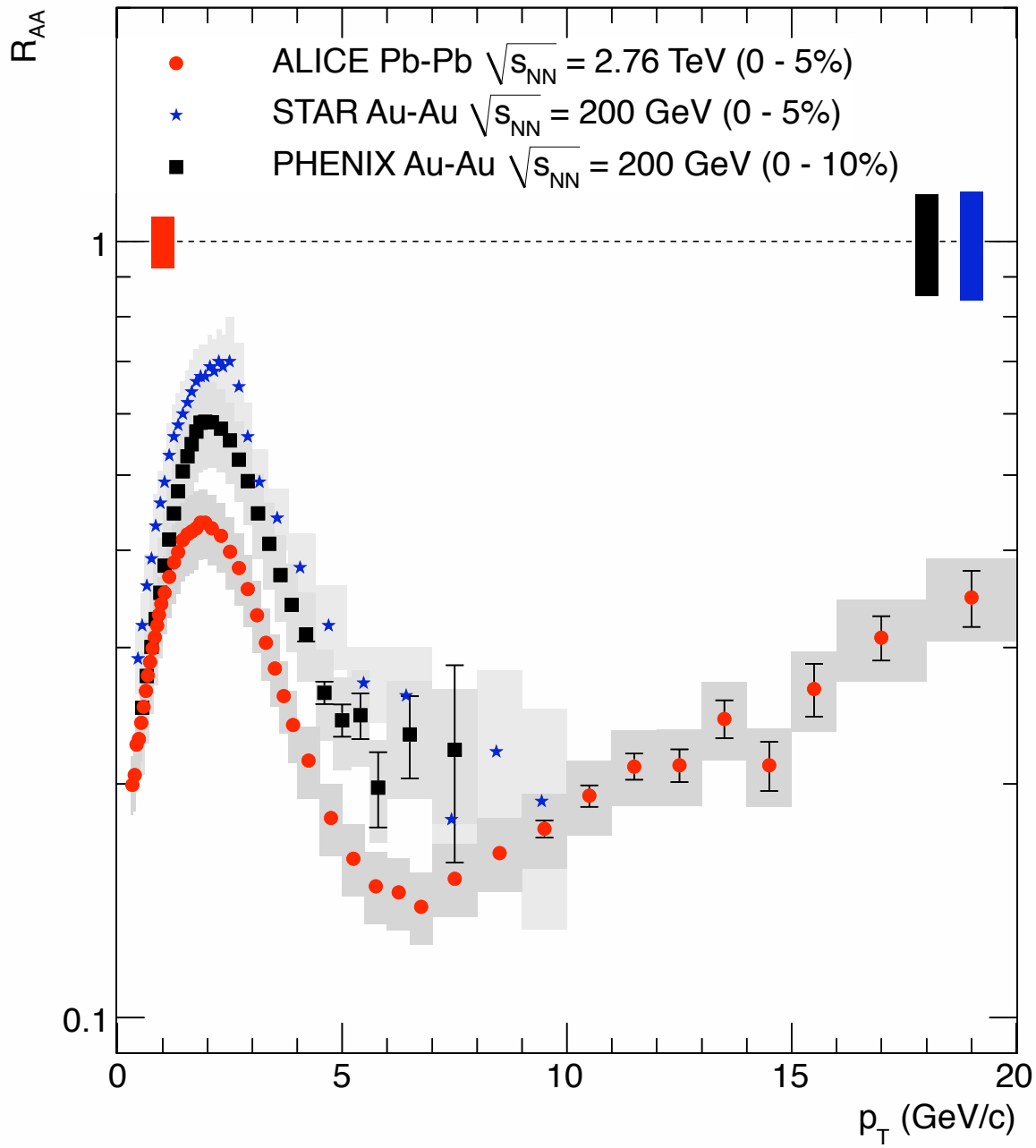

Figure 1.9: Recent calculations of R_{AA} in ALICE experiment at Large Hadron Collider and comparison with RHIC results.

shows the high p_T suppression observed in the PHENIX experiment.

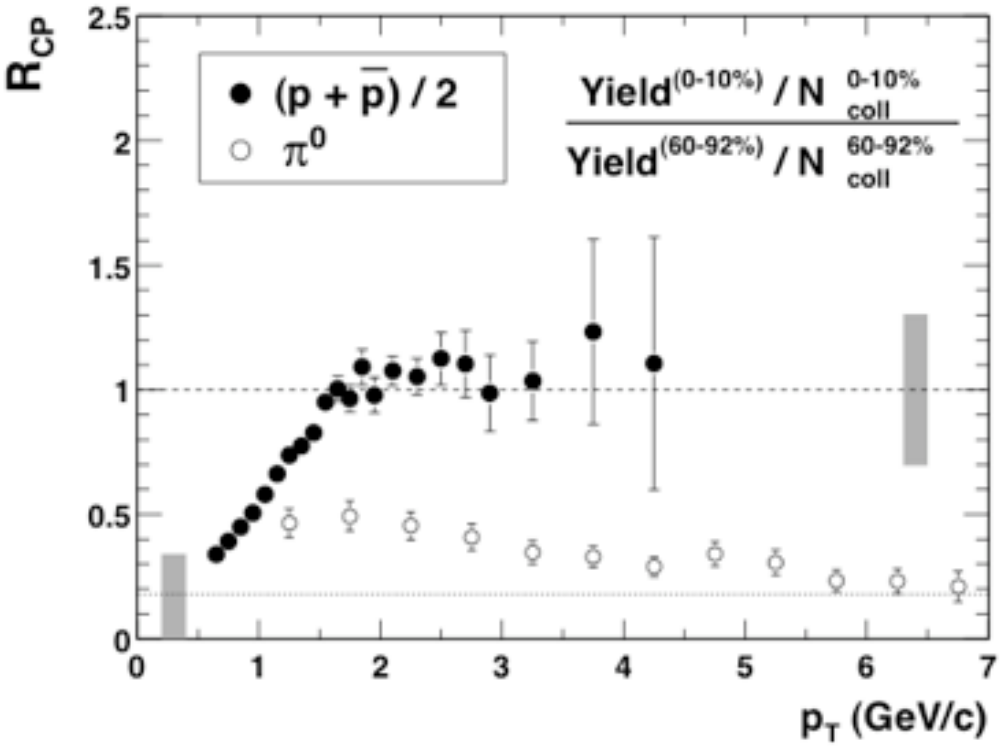

Figure 1.10: R_{CP} observed in PHENIX experiment.

,

1.3.4 Jet Quenching

Dihadron azimuthal correlations can also be used to study the effect of jet quenching. The azimuthal correlations of high p_T particles from jets show narrow near side correlation and broader away side correlation. This is known as jet quenching, wherein away side jet is suppressed due to energy loss while traveling through the medium. Figure 1.11 shows azimuthal correlations of high p_T particles in p+p, d+Au and Au+Au collisions. The $N_{trigger}$ is the number of particles which lie in the p_T range, $4 < p_T^{trig} < 6$ GeV/c, referred as trigger particles. The associated particles in the same event lie in the range $2 < p_T < p_T^{trig}$. The near side and away side peaks are visible in p+p and central d+Au collisions but in central Au+Au collisions, only near side peak is visible while the away side peak disappeared. The away side peak suppression occurs only in case of central Au+Au collisions because of interactions of particles with the larger medium.

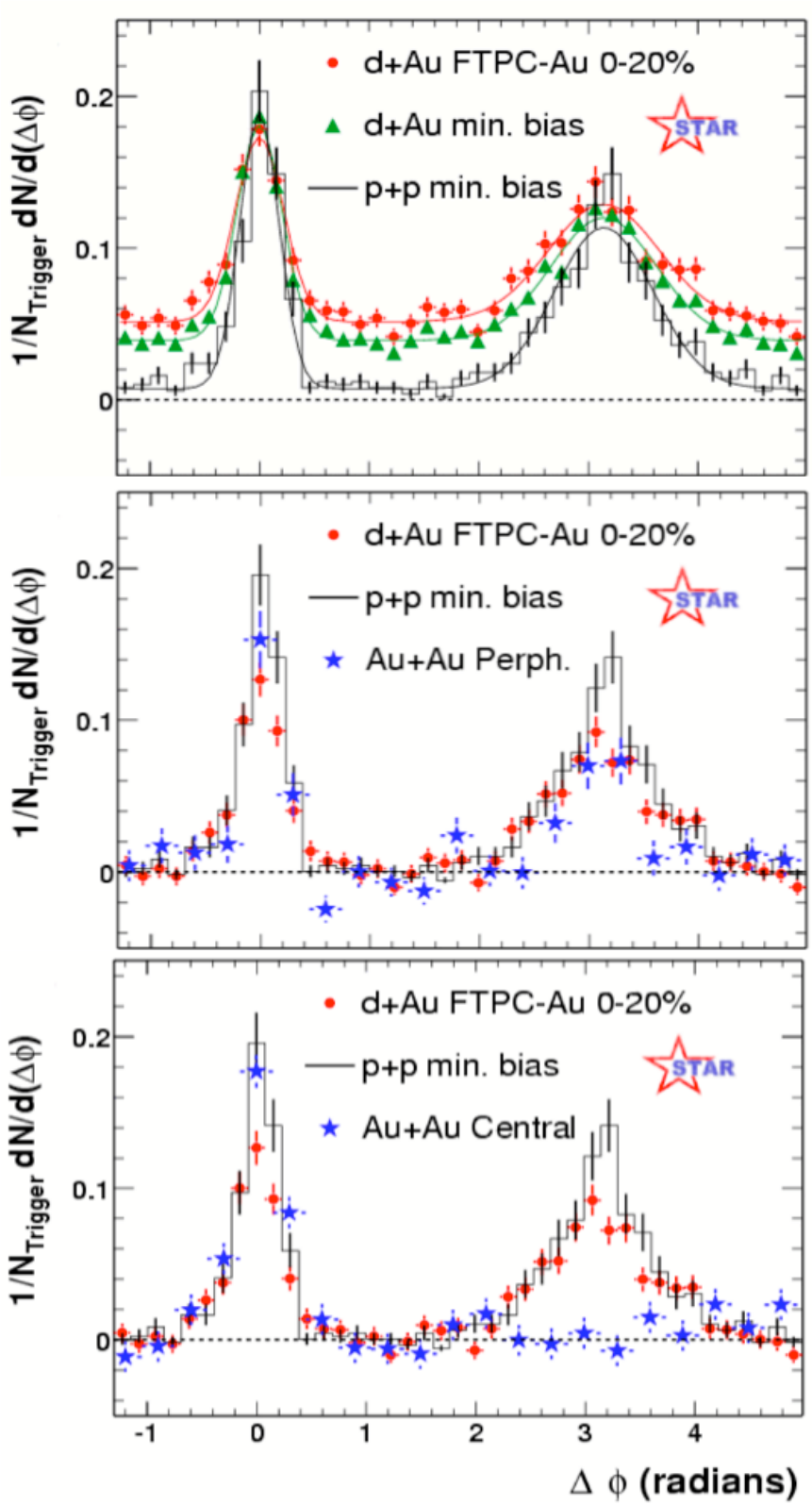

Figure 1.11: Dihadron azimuthal correlations for p+p, d+Au and Au+Au collisions.

1.3.5 J/ψ Suppression

J/ψ is a bound state of a charm quark c and an anti-charm quark $\bar{c}$. The QCD predicts that the production of J/ψ is suppressed when there is phase transition from confined to deconfined phase of quarks and gluons. Therefore, J/ψ suppression [34] is also a clear signal of QGP. In the nuclear collisions, J/ψ are produced at very early stage of the collision by the hard and prethermal interactions. If the collisions produce the deconfined matter *i.e.* QGP then c and $\bar{c}$ produced in the early stages cannot bind to form hadrons while passing through the deconfined phase and just fly apart from each other. Also during the hadronization, the production of c and $\bar{c}$ is strongly suppressed due to its heavy mass. Therefore, it is unlikely that $c(\bar{c})$ produced during the early stages find another $\bar{c}(c)$ produced during the hadronization to form J/ψ. Therefore, the production of J/ψ is suppressed in case of QGP production.

Deconfinement can be understood as a consequence of color charge screening in the dense matter. The color charge of quark in QGP is screened due to the presence of quarks, anti-quarks and gluons in the plasma. This screening is called "Debye screening". The Debye screening weakens the forces between c and $\bar{c}$, thus support the dissociation of J/ψ at high temperature which results in suppressed production of J/ψ. Consider a non-relativistic treatment of $c\bar{c}$ spectra with potential of the form

$$V(r) = -\frac{\alpha}{r} + \sigma r \tag{1.14}$$

which is sum of attractive coulomb potential and a confining linear potential. In the presence of deconfined medium, there is no confining potential and coulomb potential get screened,

$$V(r) = -\frac{\alpha^{'}}{r} e^{-r/r_D} \tag{1.15}$$

If the Bohr radius of the $c\bar{c}$ is larger than the screening length r_D, then J/ψ state will dissociate into its constituents *i.e.,* bound state of $c\bar{c}$ will not exist. Thus, deconfinement takes place when the r_D falls below the size of common hadrons. However the bound

state of heavy quarks has much smaller binding radii and hence, can survive beyond the deconfinement point.

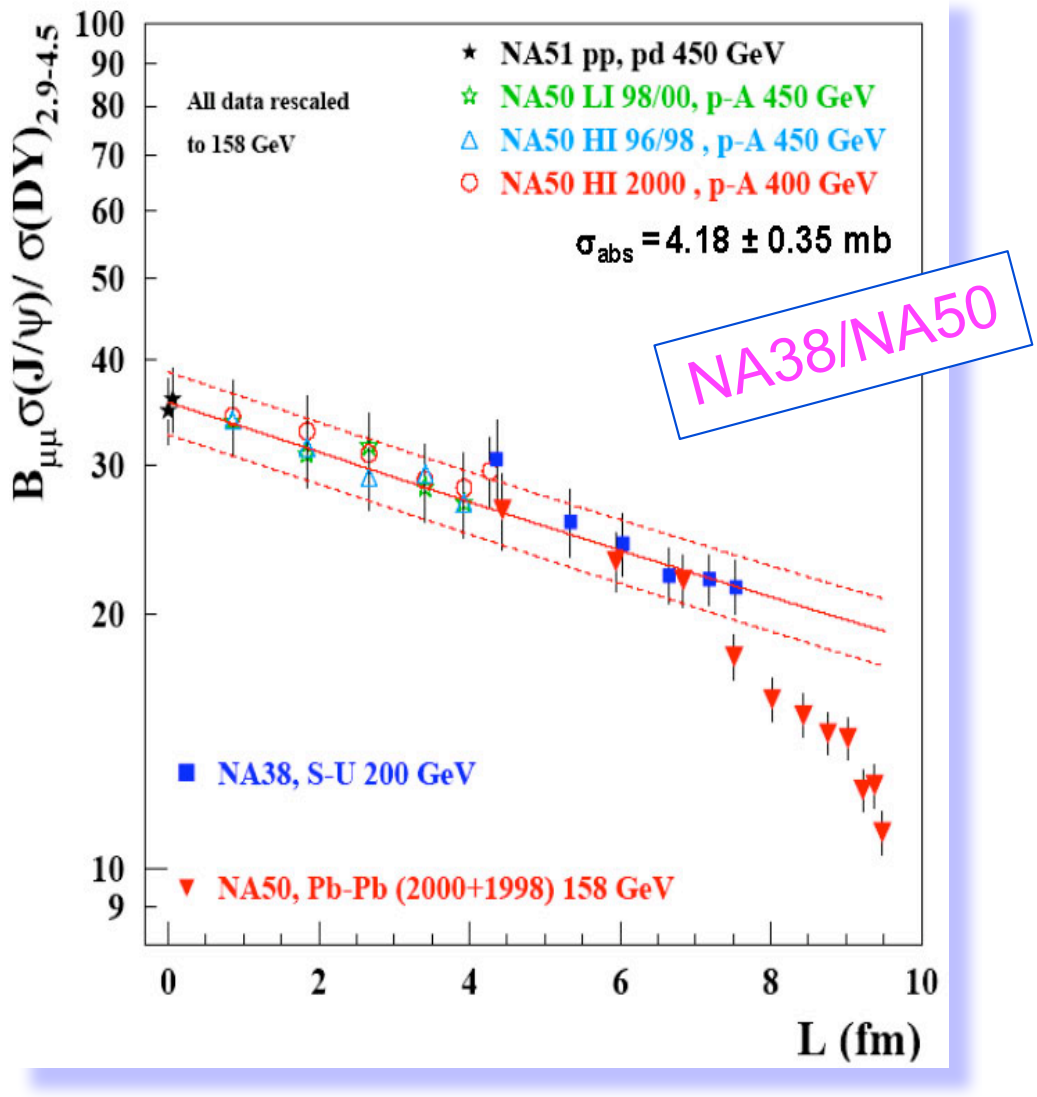

Figure 1.12: $B_{\mu\mu}\sigma(J/\psi)/\sigma(DY)$ as a function of L, a varialbe related to normal nuclear absorption calculated using Glauber Model. Anomalous suppression (red triangles) found by NA collaboration in Pb+Pb collision at 158 GeV.

Anomalous J/ψ suppression observed by NA 50 collaboration in Pb+Pb collisions at SPS shown in Fig. 1.12, has given the evidence for QGP formation [35, 36]. Here, solid lines show the normal absorption of J/ψ in nuclear matter and red triangles below the line represent the anomalous suppression.

1.3.6 Hanbury-Brown-Twiss (HBT) Interferometry

The HBT interferometry is used to study the final state of the fireball evolution known as *freeze-out* in heavy ion collisions. It is based on Hanbury-Brown-Twiss effect [37] that enables the estimate of source size through the two body correlations of the emitted particles. The effect was first used by Henbury-Brown and Twiss to study the angular diameter of star. The HBT measurement of particles detected in final state of collisions gives the information of longitudinal and transverse radii as well as lifetime of the source at thermal freeze-out [37–41]

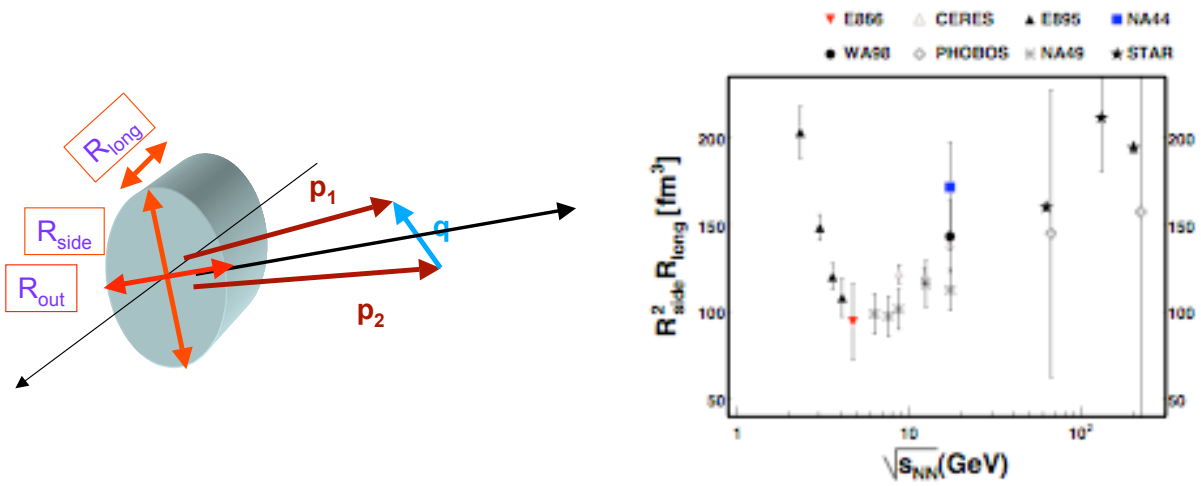

Figure 1.13: (Left) Schmatic representation of femtoscopic radii, (Right) Energy dependance of freeze out volume [46].

The space time evolution is related to the order of phase transitions in the collision. Therefore, knowledge of space-time information from HBT is important probe for QGP study. The two-particle correlation function for HBT measurements is:

$$C(\vec{q},\vec{K}) = \frac{A(\vec{q},\vec{K})}{B(\vec{q},\vec{K})}, \tag{1.16}$$

where $A(\vec{q},\vec{K})$ is distribution of particle pairs from the same event with relative momentum $\vec{q} = \vec{p_1} - \vec{p_1}$ and average momentum $\vec{K} = (\vec{p_1} + \vec{p_1})/2$ and $A(\vec{q},\vec{K})$ is corresponding distribution for the pairs of particles from different events [42]. The relative momentum $\vec{q}$ is decomposed according to Bertsch-Pratt convention [43–45] into the variables q_{long} along beam direction, q_{out} parallel to transverse momentum of the pair $\vec{K}$ and q_{side} perpendicular

to both q_{long} and q_{out} and correlation function is decomposed as:

$$C(q_{out}, q_{side}, q_{long}) = (1 - \lambda) + \lambda K_{coul}(q_{inv})(1 + e^{-q_{out}^2 R_{out}^2 - q_{side}^2 R_{side}^2 - q_{long}^2 R_{long}^2}), \quad (1.17)$$

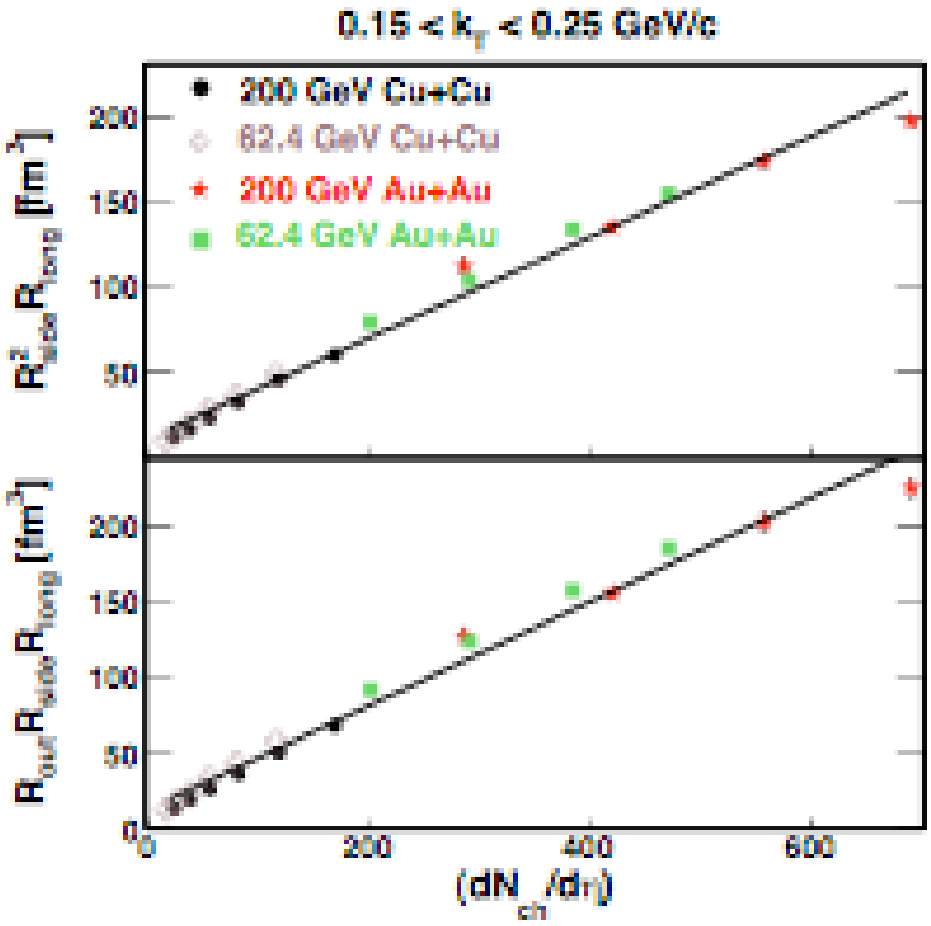

Figure 1.14: The pion freeze-out volume (colored lines) as a function of charged particles multiplicity for Au+Au and Cu+Cu collisions [46] at 200 and 62.4 GeV.

where λ is fraction of correlated pairs. K_{coul} is squared nonsymmetrized Coulomb wave function integrated over a Gaussian source corresponding to longitudinal co-moving system with Gaussian radii R_{out}, R_{side} and R_{long}, called femtoscopic radii are shown in Fig. 1.13 (Left). The estimate of pion freeze out volume is given by the equations:

$$v_f = R_{side}^2 R_{long} \quad (1.18)$$

$$v_f = R_{out} R_{long} R_{side} \quad (1.19)$$

Figure. 1.14 represent linear dependence of freeze-out volume on the multiplicity of charged particles which is consistent with the assumption of a universal pion mean-free-path length at freeze-out [47]. Also Fig. 1.13 (Right) shows the energy dependence of the freeze-out volume from the different experiments. The results show that in the AGS, the measured volume decreases and in the SPS and RHIC energy regimes volume increases monotonically.

1.3.7 Net-Charge Fluctuations

The net-charge fluctuations are also used as a signature of quark-gluon-plasma. The measurement of net charge in the system created in heavy ion collisions gives the indication of the formation of quarks and gluons [48] because in QGP phase the unit of charge is 1/3 while in hadronic phase it is 1. However, the measurement of net charge is independent of these units but fluctuations in net charge measurement depends on squares of charges and to the phase from which it originates. Since there are inherent event-by-event fluctuations in observable like volume fluctuations so usually ratios of the parameters are used to study fluctuations to minimize the effect of volume fluctuations. For the net charge fluctuations the ratio of positive to negative charge particles ($R = N_+/N_-$) is used. The observable D, which is measure of charge fluctuations per unit entropy used to study these fluctuations is defined as [49]:

$$D = \langle N_{ch} \rangle \langle \delta R^2 \rangle = 4 \frac{\langle \delta Q^2 \rangle}{\langle N_{ch} \rangle} \tag{1.20}$$

The value of D is compared for hadronic and QGP phase. For the pion gas value of D is

$$D_{\pi-gas} \approx 4, \tag{1.21}$$

and for free quarks, gluons system

$$D_{QGP} \simeq 3/4, \tag{1.22}$$

However charge fluctuations have been evaluated in lattice QCD along with entropy density [50] and D is found to be

$$D_{Lattice-QCD} \simeq 1 - 1.5, \tag{1.23}$$

Large difference of D in QGP and hadronic phase can be measured experimentally.

1.3.8 Anisotropic Flow

The measurement of momentum space anisotropy of the emitted particles in heavy ion collisions is sensitive to the early time as spatial anisotropy in the early times of collisions converted into momentum space anisotropy (Fig. 1.15) of the final state particles. Therefore, momentum space anisotropy measurements of emitted particles give the information about the early stages of the systems evolution [51].

The azimuthal distribution of the particles is represented by the fourier expansion [52],

$$E\frac{d^3N}{d^3p} = \frac{1}{2\pi}\frac{dN}{p_T dp_T dy}(1 + 2v_1 cos(\varphi - \Psi_{RP}) + 2v_2 cos[2(\varphi - \Psi_{RP})] + ...), \tag{1.24}$$

where φ is the angle of emitted particle w.r.t. reaction plane (the plane defined by the beam axis and vector connecting the centre of the two colliding nuclei *i.e* impact parameter direction) and Ψ_{RP} is azimuthal angle of reaction plane. The second harmonic coefficient v_2 called elliptic flow is most commonly studied parameter for the anisotropy measurements and is defined as:

$$v_2 = \langle cos[2(\varphi_i - \Psi_{RP})]\rangle, \tag{1.25}$$

Where angle bracket implies average over all events. Figure 1.16 shows the first measurement of elliptic flow at RHIC. The large values of elliptic flow indicate the hydrodynamical behaviour in which v_2 is proportional to spatial eccentricity. The rectangles show the expected v_2 from hydrodynamics. For $n_{ch}/n_{max} \geq 0.5$, data shows agreement with ideal hydrodynamics. Figure 1.17 shows the first measurements of elliptic flow at Large

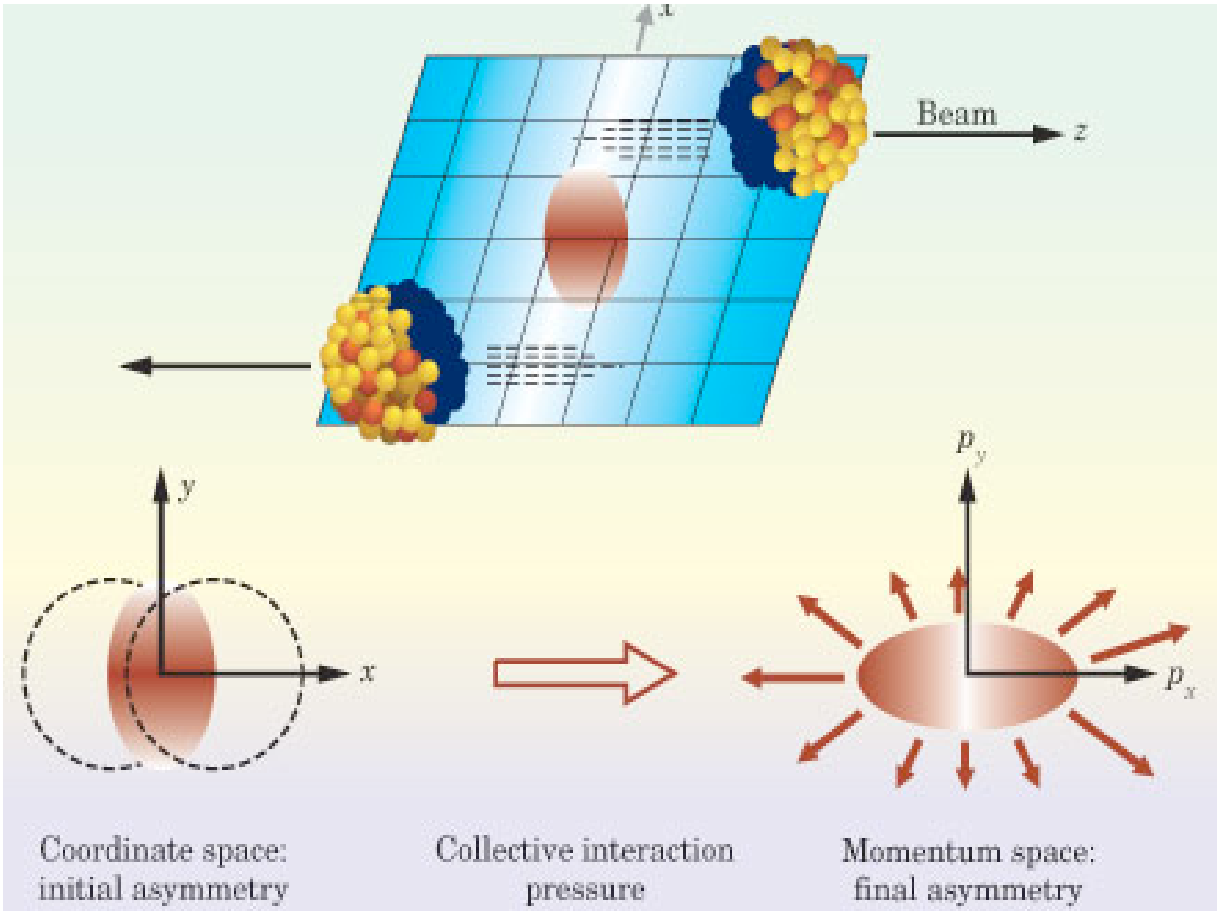

Figure 1.15: Schematic representation of Initial spatial space anisotropy converted into momentum space anisotropy due to interactions of particles inside the medium.

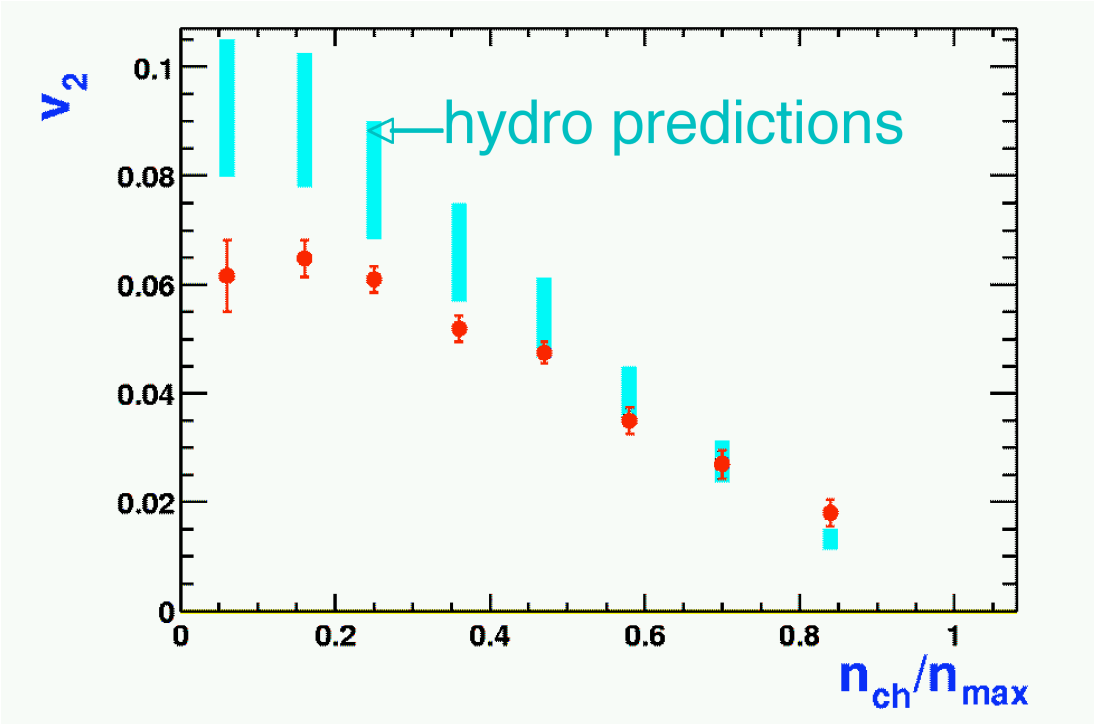

Figure 1.16: Elliptic flow (solid points) as a function of centrality [53] defined as n_{ch}/n_{max}. The open rectangles shows the values expected for v_2 in the hydrodynamical limit, scaled from ε, the initial space eccentricities of overlap region. The lower edges correspond to ε multiplied by 0.19 and the upper edges to ε multiplied by 0.25.

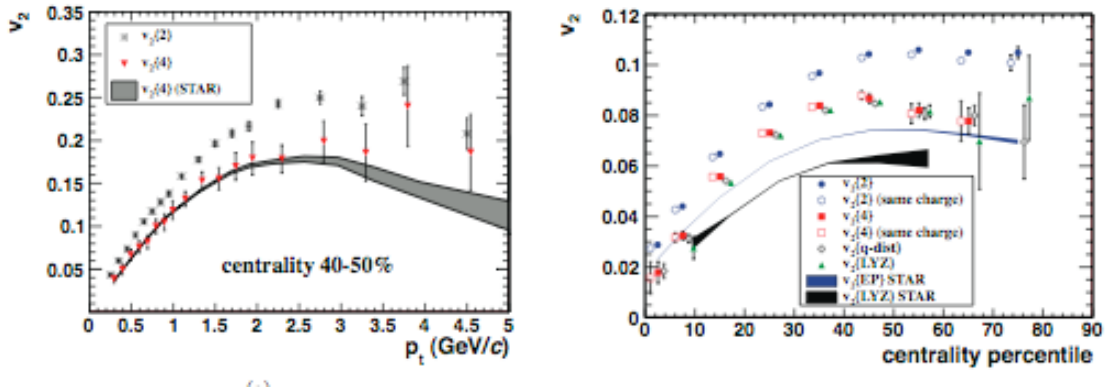

Figure 1.17: First measurements of elliptic flow from ALICE experiment in Pb+Pb collisions at $\sqrt{s_{NN}}$ =2.76 TeV from various methods and comparison with STAR.

Hadron Collider in Pb+Pb collisions at $\sqrt{s_{NN}}$ =2.76 TeV from the ALICE experiment and comparison with Au+Au 200 GeV results from STAR. The elliptic flow follows same trend as STAR but values are much higher for the same centrality. Also, for the same centrality $v_2\{2\}$ shows higher values in ALICE for the same p_T.

Figure 1.18 shows the comparison of differential elliptic flow coefficient $v_2(p_T)$ for

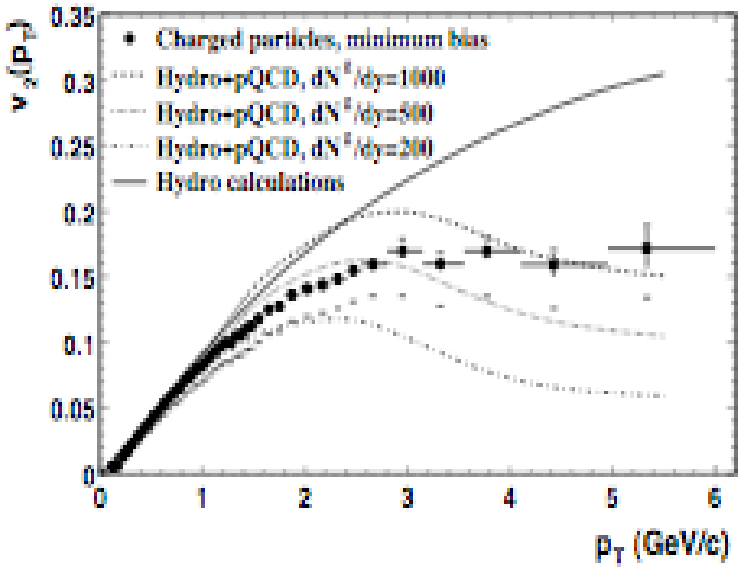

Figure 1.18: Comparison of $v_2(p_T)$ [54] for minimum-bias events(circles) with hydro+pQCD calculations [55] assuming the initial gluon density dN^q/dy=1000(dashed lines), 500(dotted lines) and 200 (dashed-dotted lines). Also pure hydrodynamical calculations are shown (solid lines).

.

charged particles with hydrodynamical calculations. The model gives good description of data for $p_T < 2\ GeV/c$ but for higher p_T role of the hard scattering becomes prominent.

The Reaction plane angle (Ψ_{RP}) cannot be measured experimentally in high energy collisions, so elliptic flow is measured from the azimuthal distribution of the emitted particles. Since elliptic flow is basically the correlations related to event plane, there may be some correlations which add up to elliptic flow but not related to reaction plane. These correlations mislead the calculation of v_2.

Figure 1.19 shows the quark number scaling of v_2. The v_2, p_T and $KE_T(= m_T - m)$ are scaled by number of constituent quarks n_q where n_q=3 for baryons and n_q=2 for mesons. The scaling for p_T/n_q is not very good for the whole range but KE_T/n_q shows excellent scaling throughout the range. This is the indication of inherent quark degrees of freedom in the created matter. Elliptic flow (v_2) measurements [57] indicate that the matter created in collisions at Relativistic Heavy Ion Collider (RHIC) behave as a prefect liquid with a

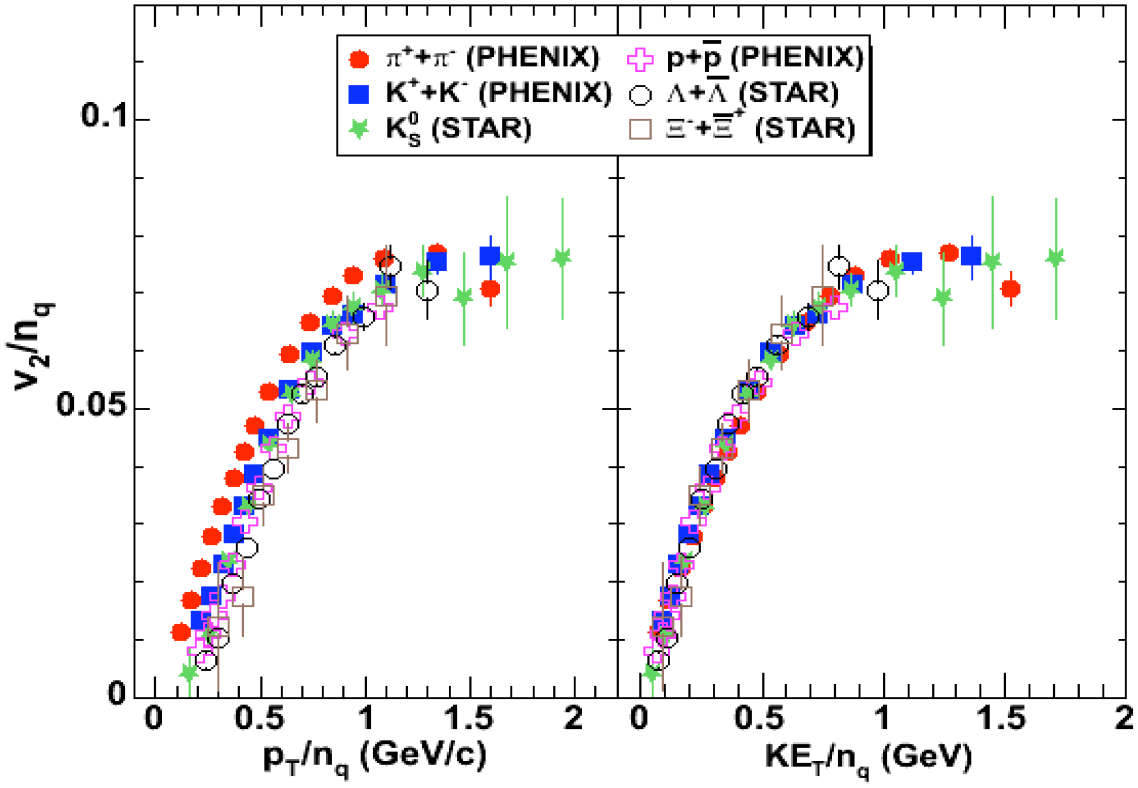

Figure 1.19: v_2/n_q vs. p_T/n_q and v_2/n_q vs. KE_T/n_q for identified particles obtained from minimum bias events for Au+Au 200 GeV collisions by STAR and PHENIX experiments [56].

viscosity near a conjectured lower bound $\eta/s \geq 1/4\pi$ [58]. This conclusion is primarily based on hydrodynamic model predictions [57, 59]. Uncertainty about the conditions at the beginning of the hydrodynamic expansion, however, leads to large uncertainties in the model expectations [60, 61]. Since v_2 reflects the initial spatial eccentricity of the overlap region when two nuclei collide, fluctuations of v_2 should depend strongly on fluctuations in the initial eccentricity. Measurements of the system-size and energy dependence of v_2 and v_2 fluctuations are therefore useful for understanding the initial conditions of the expansion phase of heavy-ion collisions.

1.4 Thesis Organization

The work presented in this thesis is based on data collected by STAR detector at RHIC for Au+Au and Cu+Cu collisions at centre of mass energies, $\sqrt{s_{NN}}$=200 and 62.4 GeV.

An attempt has been made to study elliptic flow (v_2), non-flow and v_2 fluctuations. Theoretical models for the eccentricity calculations have been compared with the data to study the effect of fluctuations on measurement of elliptic flow. The second chapter gives the overview of STAR experiment and basic details of the sub-detectors used in STAR detector. In the third chapter, the methods to study elliptic flow have been discussed. The fourth chapter deals with the details about the working of Photon Multiplicity Detector (PMD) and study of photon's elliptic flow. In the fifth chapter, eccentricity models used in analysis have been discussed. The last chapter includes the results for charged hadrons elliptic flow, comparison of eccentricity fluctuations from models with the maximum limit of the v_2 fluctuations in STAR data, calculation of non-flow using models and discussion of the results.

Bibliography

[1] J. Adams *et. al.* [STAR Collaboration], Nucl. Phys. **A** 757, 102-183 (2005).

[2] I. Arsene *et. al.* [BRAHMS Collaboration], Nucl. Phys. **A** 757, 1-27 (2005).

[3] K. Adcox *et. al.* [PHENIX Collaboration], Nucl. Phys. **A** 757, 184-283 (2005).

[4] B. B. Back *et. al.* [PHOBOS Collaboration], Nucl. Phys. **A** 757, 28-101 (2005).

[5] J. C. Collins and M. J. Perry, Superdene matter: Neutrino or asymptotically free quarks?, Phys. Rev. Lett. **34**. 1353 (1975).

[6] A. Chodos *et al.*, Phys. Rev. D **9**, 3471 (1974).

[7] T. Blum *et al.*, beta function and equation os state for QCD with two flavors of quarks. Phys. Rev. D **51**, 5153 (1995).

[8] F. Karsh, Lattice QCD at finite temperature and density. hep-lat/9909006, hep-lat/0106019.

[9] F. Karsch and E. Laermann, Quark-Gluon Plasma 3, Editors: R. C. Hwa and X. N. Wang, World Scientic, Singapore (2003).

[10] J. W. Harris and B. Müller, Ann. Rev. Nucl. Part. Sci. **46**, 71 (1996).

[11] K. Kajantie and L. MCLerran, Ann. Rev. Nucl. Part. Sci. **37**, 293 (1987) and references therein.

[12] V. Bernard, Quark-Gluon Plasma Signatures, (Edition Frontières, Paris, 1990) and references therein.

[13] C. P. Singh, Phys. Rev. Rep. **236**, 147 (1993) and references therein.

[14] B. Müller, Rep. Prog. Phys. **58**, 611 (1995) and references therein.

[15] A Dumitru, U. Katscher, J.A. Maruhn, H. Stocker. W. Greiner and D. H. Rischke, Z. Phys. A **353**, 187 (1995).

[16] J. Alam, D. K. Srivastava, B. Sinha and D. N. Basu, Phys. Rev. D **48** , 1117 (1993).

[17] A. Dumitru, U. Katscher, J. A. Maruhn, H. Stocker, W. Greiner and D. H. Rischke, Phys. Rev. C **51**, 2166 (1995).

[18] J. J. Neumann, D. Seibert and G. Fai, Phys. Rev. C **51**, 1460 (1995).

[19] M. M. Aggarwal *et al.* [WA 98 Collaboration], Phys. Rev. Lett. **85**, 3595 (2000).

[20] D. K. Srivastava and B. Sinha, Phys. Rev. C **64**, 034902 (2001).

[21] P. Koch, B. Muller and J. Rafelski, Phys. Rep. **142**, 321 (1986).

[22] J. Rafelski, Nucl. Phys. A **544**, 279c (1992).

[23] H. C. Eggers and J. Rafelski, Int. J. Mod. Phys. A **46**, 1067 (1986).

[24] P. Koch, B. Müller and J. Rafelski, Phys. Rep. **142**, 167 (1986).

[25] T. Matsui, B. Svetitsky and L. D. . MCLerran, Phys. Rev. D **34**, 2047 (1986).

[26] J. Rafelski, Phys. Rept. **88**, 331 (1982).

[27] M. Gazdzicki and M. I. Gorenstein, Acta Phys. Pol. B **30** 2705 (1999).

[28] Mark I. Gorenstein, arXiv:hep-ph/0011304v2 (2008).

[29] B. I. Abelev *et al.*, Phys. Rev. C **77**, 044908 (2008).

[30] E. Andersen *et al.* [WA97 Collaboration], Phys. Lett. B **449**, 401 (1999). F. Antinori *et al.* [WA97/NA57 Collaboration], Nucl. Phys. A **698**, 118c (2002).

[31] M. Gyulassy, Nucl. Phys. B **571**, 197 (2000).

[32] M. Gyulassy, Nucl. Phys. A **661**, 637 (1999).

[33] C. Alder *et al.*, Phys. Rev. Lett. **89**, 202301 (2002).

[34] T. Matsui and H. Satz, Phys. Lett. B **178**, 416 (1986).

[35] M. Gonin *et al.*, Nucl. Phys. A **610**, 404c (1996).

[36] M. C. Abreu *et al.*, Nucl. Phys. A **661**, 93 (1999).

[37] S. Pratt, Phys. Rev. D **33**, 1314 (1986); Y. Hama and S. S. Padula, Phys. Rev. D **37**, 3237 (1988).

[38] S. E. Koonin, Phys. Lett. B **70**, 43 (1977).

[39] F. B. Yano and S. E. Koonin, Phys. Lett. B **78**, 556 (1978).

[40] S. Pratt, Phys. Rev. Lett. **53**, 1219 (1984).

[41] U. Heinz and K. S. Lee, Phys. Lett. B **259**, 162 (1992).

[42] U. Heinz and B. V. Jacak, Ann. Rev. Nucl. Sci. **49**, 529-579 (1999).

[43] G. Bertsch, M. Gongand and M. Tohyama, Phys. Rev. C **37**, 1896 (1988).

[44] S. Chapman, P. Scotto and U. W. Heinz, Phys. Rev. Lett. **74**, 4400 (1995).

[45] M. I. Podgoretsky, Sov. J. Nucl. Phys. **37**, 272 (1983).

[46] B. I. Abelev *et al.*, Phys. Rev. C **80**, 024905 (2009).

[47] D. Adamova *et al.* [CERES Collaboration], Phys. Rev. Lett. **90**, 022301 (2003).

[48] H. Appelshauser *et al.* [NA49 collaboration], Phys. Lett. B **459**, 679-686 (1999); S. V. Afanasev *et al.* [NA49 collaboration], hep-ex/0009053.

[49] S. Jeon and V. Koch, Phys. Rev. Lett. **85**, 2076 (2009).

[50] S. Gottlieb *et al.*, Phys. Rev. D **55**, 6852 (1997).

[51] J. Y. Ollitraut, Phys. Rev. D **46**, 229, (1992).

[52] S. Voloshin and Y. Zhang, Z. Phys. C **70**, 665 (1996).

[53] K. H. Ackermann *et al.* [STAR Collaboration], Phys. Rev. Lett **86**, 402-407 (2001).

[54] B. I. Abelev *et al.* [STAR Collaboration], Phys. Rev. Lett **90**, 032301 (2003).

[55] M. Gyulassy, I. Vitev and X. N. Wang, Phys. Rev. Lett **86**, 2537, (2003).

[56] A.. Adare *et al.* [PHENIX Collaboration], Phys. Rev. Lett **98**, 162301 (2007).

[57] K. H. Ackermann *et al.* [STAR Collaboration], Phys. Rev. Lett. **86**, 402 (2001); C. Adler *et al.* [STAR Collaboration], Phys. Rev. Lett. **87**, 182301 (2001); C. Adler *et al.* [STAR Collaboration], Phys. Rev. Lett. **89**, 132301 (2002); J. Adams *et al.* [STAR Collaboration], Phys. Rev. Lett. **92**, 052302 (2004); J. Adams *et al.* [STAR Collaboration], Phys. Rev. C **72**, 014904 (2005); J. Adams *et al.* [STAR Collaboration], Phys. Rev. Lett. **95**, 122301 (2005); K. Adcox *et al.* [PHENIX Collaboration], Nucl. Phys. A **757**, 184 (2005); J. Adams *et al.* [STAR Collaboration], Nucl. Phys. A **757**, 102 (2005); B. Alver *et al.* [PHOBOS Collaboration], Phys. Rev. Lett. **98**, 242302 (2007); B.B. Back *et al.* [PHOBOS Collaboration], Phys. Rev. C **72**, 051901(R) (2005); B.B. Back *et al.* [PHOBOS Collaboration], Phys. Rev. Lett. , 122303 (2005).

[58] P. Kovtun, D. T. Son and A. O. Starinets, Phys. Rev. Lett. **94**, 111601 (2005).

[59] P. Huovinen, P. F. Kolb, U. W. Heinz, P. V. Ruuskanen and S. A. Voloshin, Phys. Lett. B **503**, 58 (2001); D. Teaney, Phys. Rev. C **68**, 034913 (2003); K. Dusling and D. Teaney, Phys. Rev. C **77**, 034905 (2008) [arXiv:0710.5932 [nucl-th]].

[60] T. Hirano, U. W. Heinz, D. Kharzeev, R. Lacey and Y. Nara, Phys. Lett. B **636**, 299 (2006); T. Lappi and R. Venugopalan, Phys. Rev. C **74**, 054905 (2006).

[61] H. J. Drescher, A. Dumitru, A. Hayashigaki and Y. Nara, Phys. Rev. C **74**, 044905 (2006) [arXiv:nucl-th/0605012]; H. J. Drescher and Y. Nara, Phys. Rev. C **76**, 041903 (2007) [arXiv:0707.0249 [nucl-th]].

Chapter 2

The STAR Experiment

2.1 Relativistic Heavy Ion Collider (RHIC)

The Relativistic heavy ion collider (RHIC) at Brookhaven National Laboratory (BNL), USA, had been setup to accelerate Au ions upto 100GeV/nucleon energy. It is also capable to accelerate and collide other ions combination *e.g. p+p, d+Au, Cu+Cu* (upto energies 250 GeV for protons and 100 GeV/nucleon for heavy ions). RHIC consists of two concentric rings of super-conducting magnets that focus and guide the beam, a radio frequency system that capture, accelerate and store beams. Rings diameter is approximately 1.22 km. RHIC was designed for Au+Au luminosity (L) of about $2 \times 10^{26} cm^{-2} sec^{-1}$ at the highest energy but the luminosity has been increased much higher. The luminosity for the lighter ions is much higher. For p+p collisions, L $\sim 10^{31} cm^{-1} sec^{-1}$. Beam is not continuous instead it is made up of 57 separate "bunches" , each containing billions of ions.

Figure 2.1 shows accelerator complex including the accelerators used to bring the gold ions up to injection energy. The Tandem Van de Graaff uses static electricity to accelerate atoms removing some of their electrons. It accelerate gold ions in the charge state Q= -1e to 15 MeV. The ions then pass through a stripping foil where the electrons are knocked off so that their most probable charge state become Q= +12e. With charge changed from negative to positive, ions gain another 1MeV/u of energy as they accelerate through

second Van De Graaff. On exiting the Tandem, ions pass through a second stripping foil bringing their most probable charge state to Q= +32e. They are injected into Booster synchrotron and are accelerated to 95 MeV/u. A stripper in the transfer line between the booster and the Alternating Gradient Synchrotron (AGS) increases their charge state to Q=+77e. In AGS, ions are accelerated to 10.8 GeV/u. After that, ions pass through final stripper foil where the remaining K-shell electrons are removed (Q= +79e). Finally, they are injected into RHIC where they are accelerated to top energy and can be stored upto 10 hours. The RHIC parameters are listed in Table 2.1.

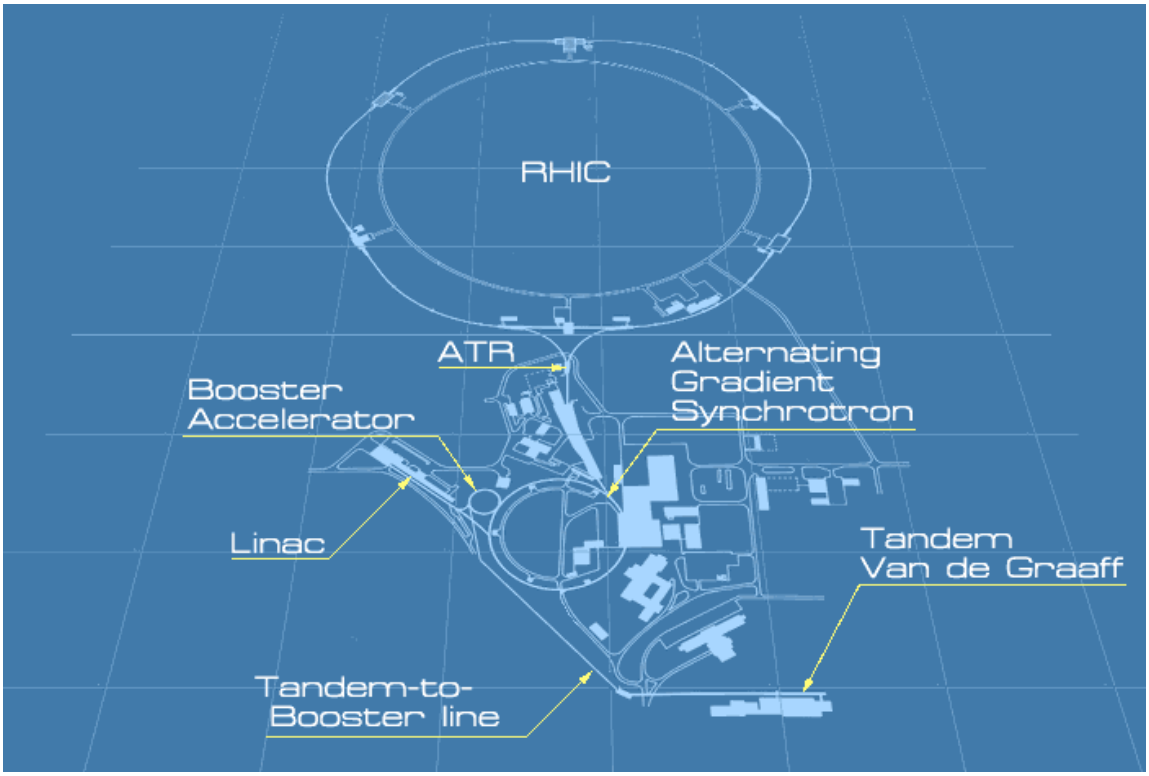

Figure 2.1: Layout of RHIC complex.

Performance specification	**Heavy ions**	***p-p***
Beam energy	30-100 GeV/c	30-100 GeV/c
Luminosity	$2 \times 10^{26} cm^{-2} sec{-}1$	$1.4 \times 10^{31} cm^{-2} sec{-}1$
Number of bunches/ring	60-120	60-120
Number of ions/bunch	10^{29}	10^{11}
Luminosity life time	$\sim 10h$	$> 10h$

Table 2.1: RHIC parameters.

2.1.1 The Detectors at RHIC

The RHIC has four detectors, viz., PHENIX, BRAHMS, PHOBOS, STAR. All the four detectors are dedicated to different physics studies of matter under extreme conditions of temperature and pressure. Figure 2.2 shows the positions of all detectors in the RHIC ring. The PHENIX is located at 8^o clock position. The BRAHMS is located at 2^o clock position. The PHOBOS is located at 10^o clock position and the STAR is located at 6^o clock position. Presently, only two of the four detectors are running. BRAHMS and PHOBOS has accomplished their goals and have stopped taking data, but STAR and PHENIX are still taking data to achieve their goals.

The PHENIX [1] detector shown in Fig. 2.3, is the largest of the four detectors at RHIC. It is designed especially to measure the direct probes of the Quark Gluon Plasma such as electrons, muons and photons. The sub-detectors in the PHENIX detector are grouped into two central arms and two forward muon arms. The central arms consist of tracking subsystems for charged particles. A Time Expansion Chamber (TEC), a TOF and RICH detectors provide particle identification. A lead-scintillator (PbSc) calorimeter and lead-glass(PbGI) calorimeter measure the photons and electrons. Two muon spectrometers cover pseudorapidity range $1.1 < |\eta| < 2.4$ with full azimuthal coverage.

The BRAHMS [2], Broad Range Hadron Magnetic Spectrometer shown in Fig. 2.4, is one of the two smaller detectors at RHIC. It is designed to measure charged hadrons over a wide range of rapidity $0 < |y| < 4$ and transverse momentum $0.2 < p_T < 3.0$ GeV/c to study reaction mechanism of relativistic heavy ion collisions at RHIC. It consists of two

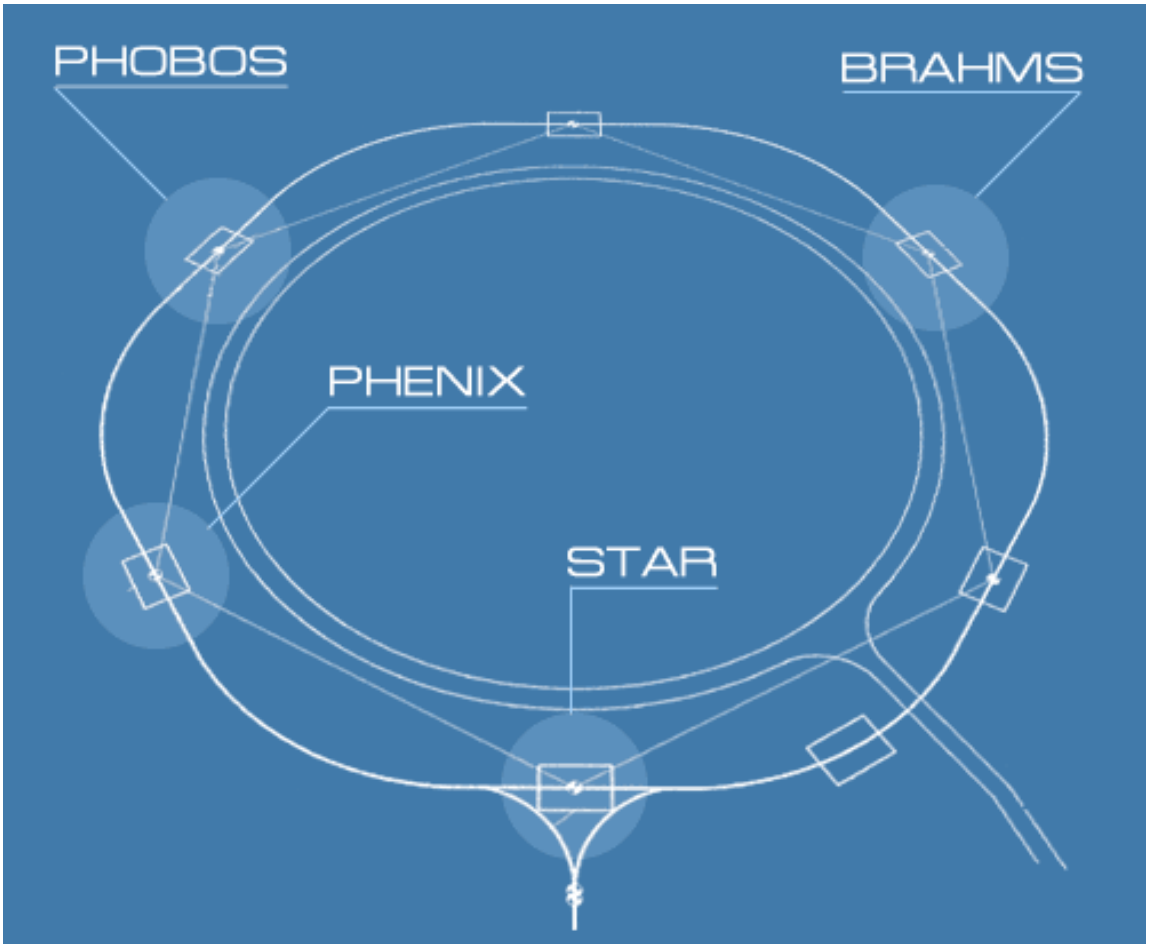

Figure 2.2: Global view of detectors at RHIC complex.

small solid-angle spectrometers as well as some global detectors (Multiplicity, BBCs and ZDCs). Tracking detectors (T1-T5, TPM1,and TPM2), time of flight arms and Cherenkov detectors (C1 and RICH) enable momentum determination and particle identification.

The PHOBOS [3] detector shown in Fig. 2.5, is designed to detect charged particles over full solid angle using multiplicity detector and measure identified charge particles near mid-rapidity in two spectrometer arms. Charged particles are detected over the pseudo-rapidity coverage $|\eta| < 5.4$ using an Octagon Multiplicity detector and six Ring Multiplicity detectors. Two small acceptance spectrometers at mid-rapidity and time-of-flight wall allow for particle identification. Additional detectors include a Vertex detector,

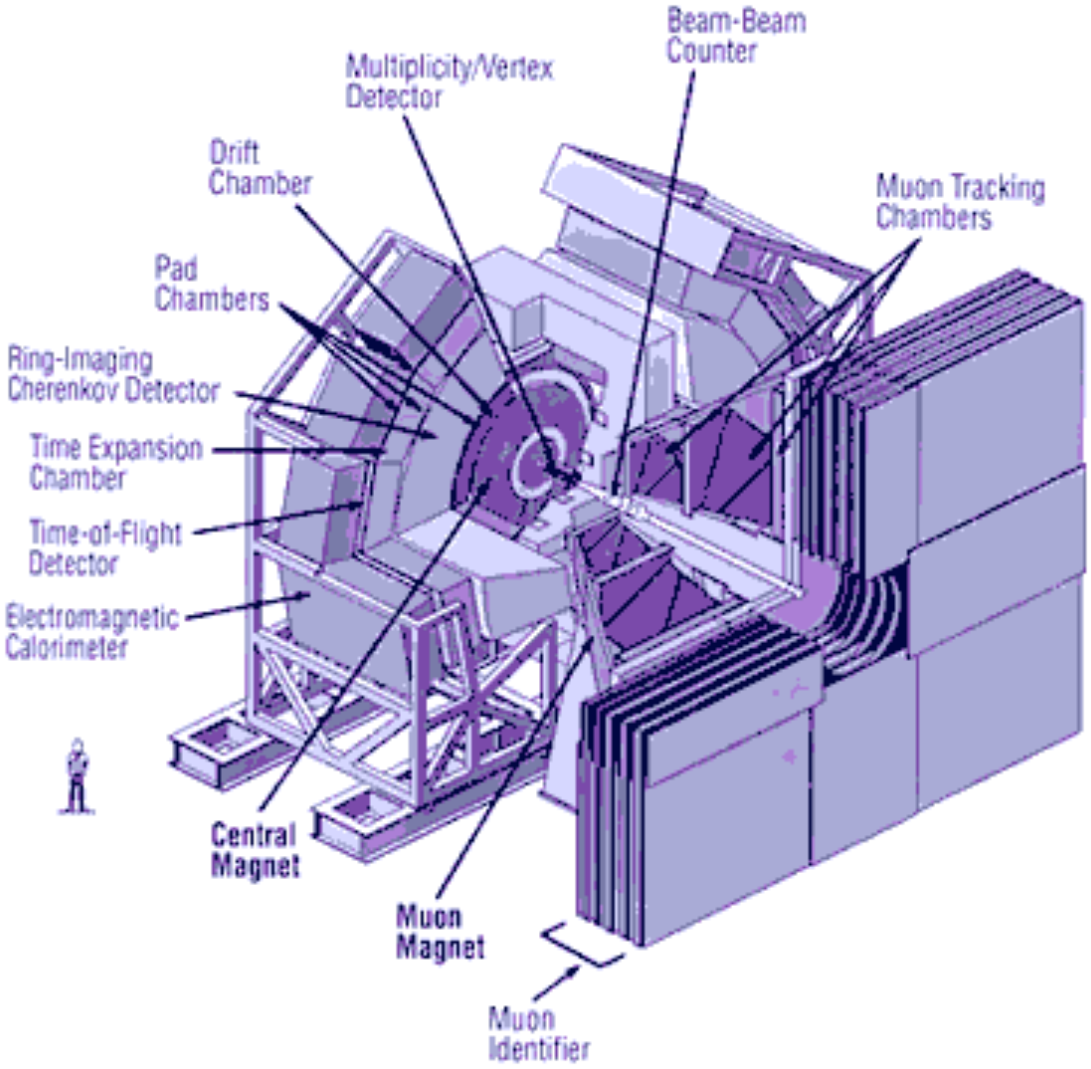

Figure 2.3: The PHENIX Detector.

sets of scintillator paddles and a Cherenkov detector array for vertex determination, event triggering and centrality selection.

The STAR [4] detector shown in Fig. 2.6, is designed primarily for the measurement of hadrons production over a large solid angle. It is a large acceptance detector which covers the full azimuthal ($0 \leq \phi \leq 2\pi$) for $|\eta| < 1.8$ and $2.5 < |\eta| < 4.0$. It consists of second biggest working Time Projection Chamber for particle tracking. The STAR also has a number of sub-detectors, discussed in detail in the following sections.

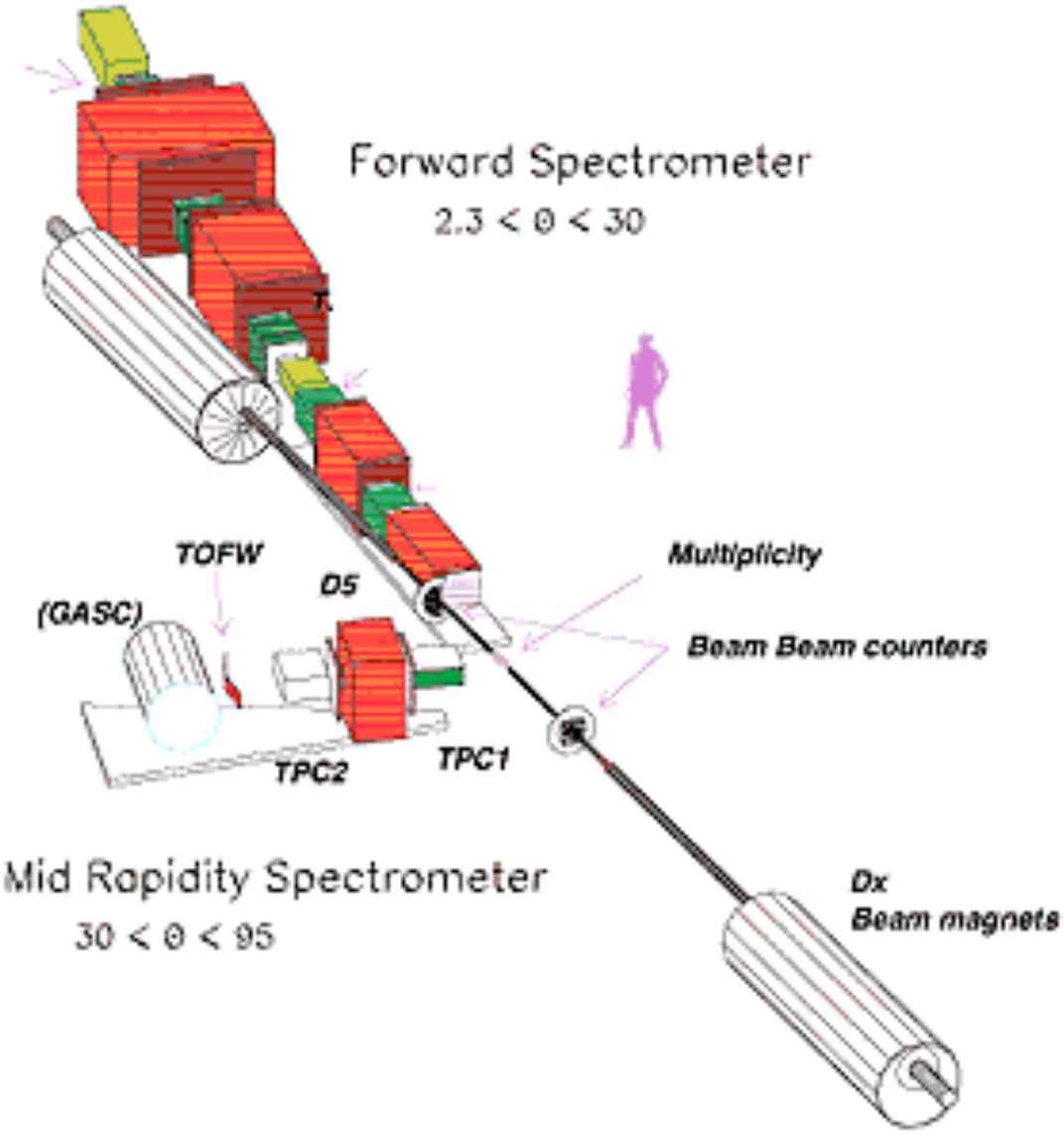

Figure 2.4: The BRAHMS Detector.

2.2 The STAR Detector

The Solenoidal Tracker at RHIC (STAR) is designed primarily to measure hadrons production over a large solid angle, featuring detector systems for high precision tracking, momentum analysis and particle identification at mid-rapidity [4]. The large acceptance of STAR makes it particularly well suited for event-by-event characterization of the heavy ion collisions and for the detection of hadron jets. The layout of STAR experiment [4]

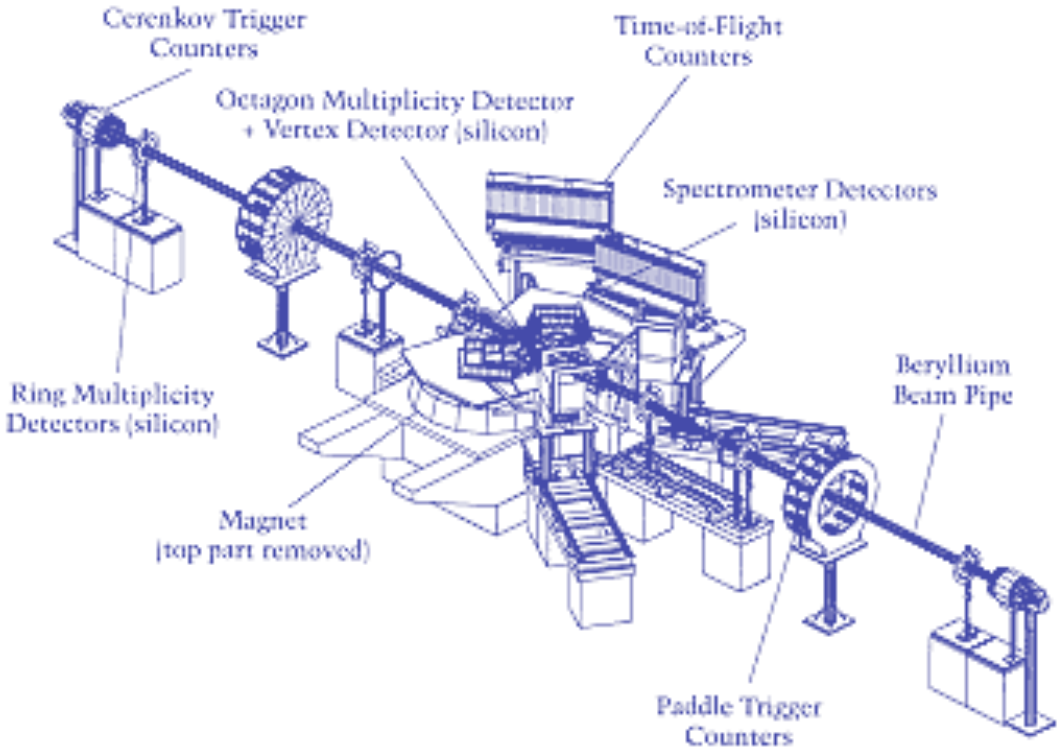

Figure 2.5: The PHOBOS Detector.

is shown in Fig 2.6. A cutaway side view of STAR detector is displayed in Fig. 2.7. A solenoidal magnet [5] with a uniform magnetic field ∼0.5 T has been used for charged particle momentum analysis. Charged particles tracking close to interaction region is accomplished by a Silicon Vertex Detector (SVT) [6,7] consisting of 216 silicon drift detectors (equivalent to total 13 millions pixels) arranged in three cylindrical layers at distance of approximately 7, 11 and 15 cm from the beam axis. The silicon detectors cover a pseudo-rapidity range $|\eta| \leq 1$ with complete azimuthal symmetry ($\Delta\phi = 2\pi$). Silicon tracking close to the interaction allows precision localization of the primary interaction vertex and identification of the secondary vertices from weak decay of particles, viz., Λ, Ξ and Ωs. A large volume Time Projection Chamber (TPC) [8,9] for charged particles tracking and

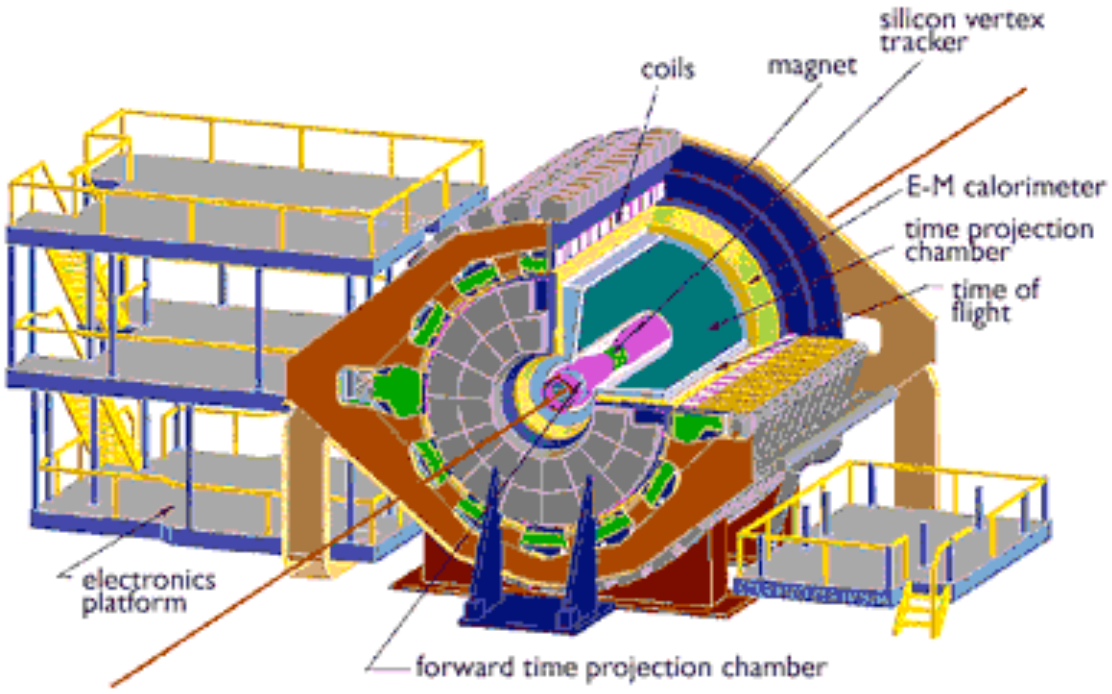

Figure 2.6: The STAR Detector.

particle identification is located at the radial distance of 50 to 200 cm from the beam axis. The TPC is 4m long and it covers a presodo-rapidity range $|\eta| \leq 1.8$ for tracking with complete azimuthal symmetry ($\Delta\phi = 2\pi$) providing the equivalent of 70 millions voxels via 136, 608 channels and front end electronics (FEE) [10,11]. Both SVT and TPC contribute to particle identification using ionization energy loss, with energy loss resolution (dE/dx) of 7%(σ). The momentum resolution of the SVT and TPC reaches a value of $\delta p/p = 0.02$ for majority of tracks in the TPC. The $\delta p/p$ resolution improves as the number of hit points along the track increases and as the particle momentum decreases as expected. For tracking in forward region, a radial drift TPC (FTPC) [12, 13] is installed covering $2.5 < |\eta| < 4$ with complete azimuthal coverage and symmetry. Recently, Time of flight (TOF) detector has also been installed in the STAR which has extended the capabilities of the particle identification of STAR. A Barrel Electromagnetic Calorimeter (BEMC) and Endcap Electromagnetic Calorimeter (EEMC) are designed to measure the trans-

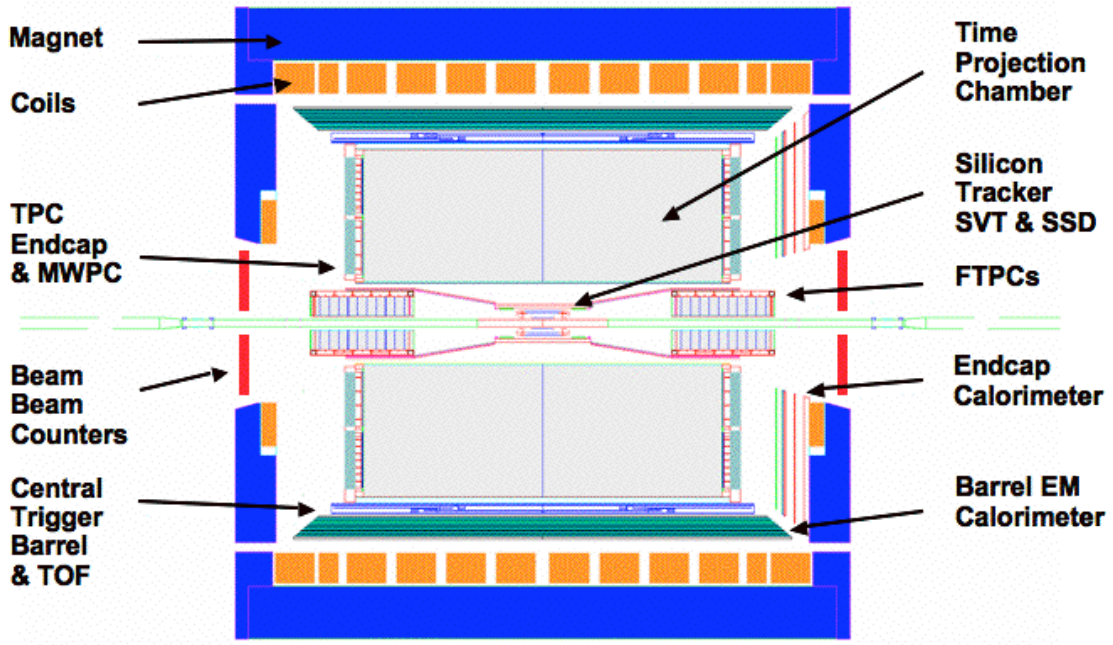

Figure 2.7: Side view of STAR Detector.

verse energy and high transverse momentum photons, electrons and electromagnetically decaying hadrons. The BEMC and EEMC have pseudorapidity coverage of $-1 < \eta < 1$ and $-1 < \eta < 2$ respectively, with full azimuthal coverage.

STAR also consists of some fast detectors, Central Trigger Barrel (CTB), Zero-Degree Calorimeter (ZDC) and Beam-Beam Counter (BBC) which are used to provide input to trigger system.

The CTB consists of 240 scintillator slates arranged around the outer radius of TPC. It covers $|\eta| < 1$ with full azimuthal coverage. It triggers on the central collisions and measure the charged particle multiplicity in the mid-rapidity region.

The ZDCs are located on the beam axis at ± 18 m away from the TPC center and cover polar angle $\theta < 2.5$ mrad. They measure neutrons at the beam rapidity originating

from the break up of the colliding nuclei, while charged fragments get swept away by the beam steering magnets that bend the incoming nuclei towards the interaction point. The number of neutrons detected in the ZDCs can be obtained by amount of energy deposited in the collisions. ZDCs are used for triggering as well as monitoring the beam luminosity.

The BBC subsystem consists of two disk shaped scintillating detectors situated at a distance of ± 3.5 m from the interaction point, covering the pseudo-rapidity $3.3 < |\eta| < 5.0$. Each BBC disk is composed of scintillating tiles that are arranged in hexagonal closest packing. The BBCs are sensitive to the high-energy hadrons that are focused in the high rapidity region. The z position of the main interaction vertex can also be selected with the timing signal difference of the two BBCs.

2.2.1 Time Projection Chamber (TPC)

The TPC is primary tracking detector [14, 15] in STAR. The TPC records the tracks of particles, measures their momenta over range of 100 MeV/c to 30 GeV/c and identify the particles over a momentum range 100 MeV/c to greater than 1 GeV/c by measuring their ionization energy loss (dE/dx). It covers ± 1.8 units of pseudorapidity with full azimuthal coverage ($0 \leq \pi \leq 2\pi$).

The STAR TPC is shown schematically in Fig. 2.8. It sits in a large solenoidal magnet that operates at 0.5 T [16]. The TPC is 4.2 m long and 4 m in diameter. The main components in the TPC are Central Membrane (CM), field cage cylinders and readout end caps. The electric field uniformity is critical since track reconstruction precision is of the order of millimeter and electron drift paths are up to 2.1 meters. The Central membrane is a disk from which the Inner field cage passes and is operated at 28 kV.

The field cage cylinders serve the purpose of gas containment and provide uniform electric field. These provide a series of equipotential rings that divide the space between the central membrane and the anode planes into 182 equally spaced segments. One ring at the center is common to both ends. The central membrane is attached to this ring. The TPC is filled with P10 gas (10% methane, 90% argon) regulated at 2 mbar above atmospheric pressure. Its primary attribute is a fast drift velocity which peaks at a low

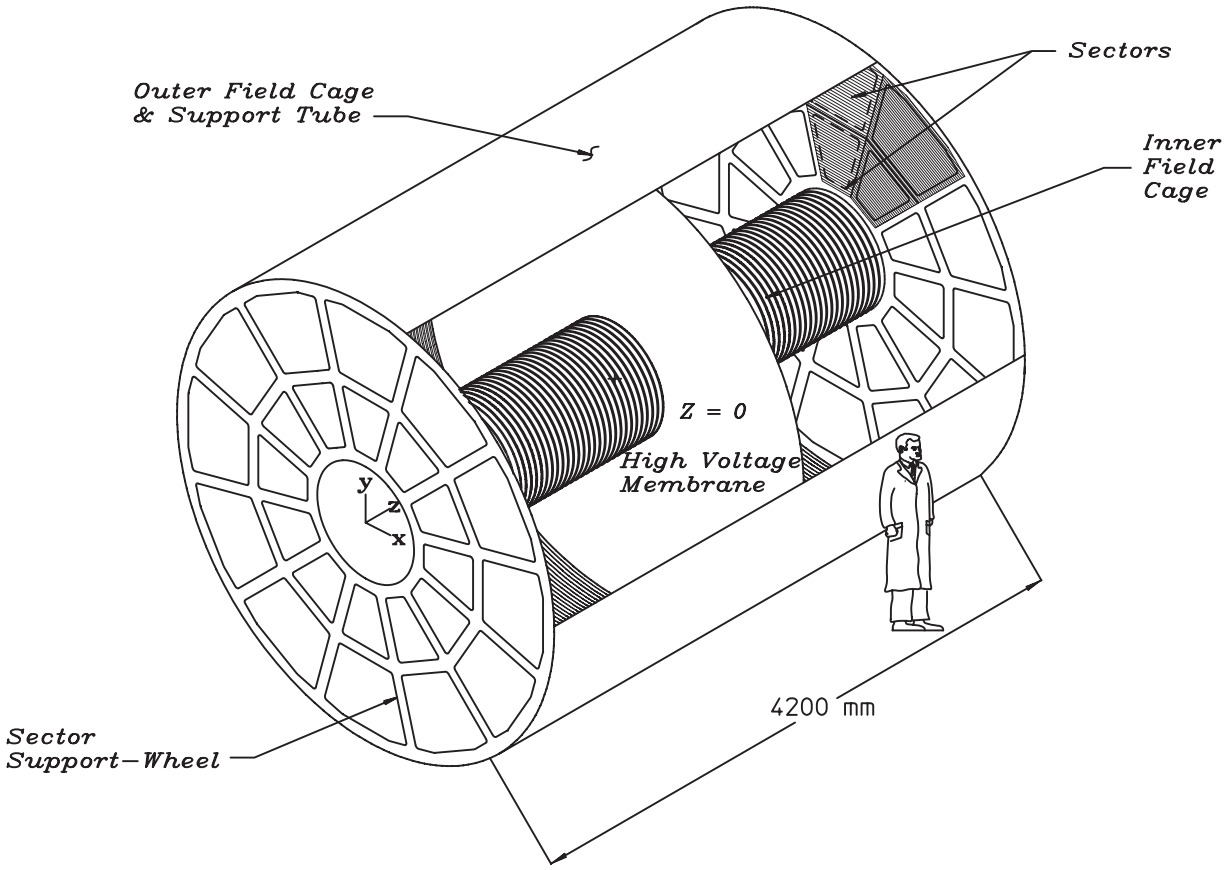

Figure 2.8: Schematic view of STAR TPC.

electric field. Operating on the peak of the velocity curve makes the drift velocity stable and insensitive to small variations in temperature and pressure. Low voltage greatly simplifies the field cage design.

The endcap readouts are at ground and are organized into 12 sectors in each side of TPC. The geometry of one sector is shown in Fig. 2.9. Each sector is further divided into an inner and outer sector. The number of pads in the inner sector are 1,750 having dimensions 2.85 mm $\times$ 11.5 mm. These pad rows are numbered from 1-13. The spacing between the anode wire and pad plane is 2 mm and the anode is operated at 1170 V . The isolation gap between the pads is 0.5 mm for both the inner and outer sectors. The number of pads in the outer sector are 3,742 with the pad dimension 6.20 mm $\times$ 19.5 mm. The pad rows in outer sector are numbered from 14-45. The anode wire to pad plane

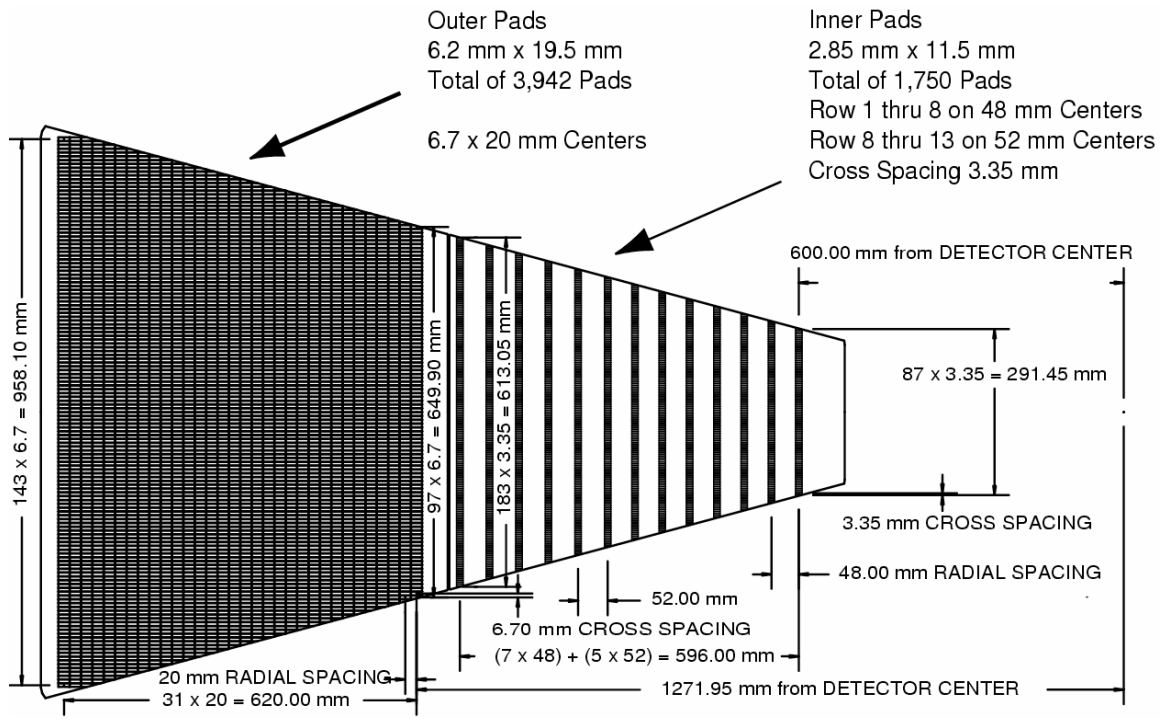

Figure 2.9: The anode pad plane with one full sector shown. The inner sub-sector is on the right and it has small pads arranged in widely spaced rows. The outer sub-sector is on the left and it is densely packed with larger pads.

spacing is 4 mm in outer sector and the anode is operated at 1390 V. The smaller size of the pads in the inner sector is to improve two-track resolution. Combining the inner and outer sector, TPC has 5,690 pads per sector which corresponds to 1,36,560 channels for 24 sectors.

The readouts are Multi-Wire Proportional Chambers (MWPC). The chambers consist of four components; a pad plane and three wire planes (Fig. 2.10). The amplification/readout layer is composed of the anode wire plane of small wires with the pad plane on one side and ground wire plane on the other. The high voltage of the anode wires provides necessary electric field for the avalanche multiplication of the electrons from the track ionization. The ground wires terminates the field in the avalanche region as well as calibrate the pad electronics. The third wire plane is gating grid, which separates the drift region from the amplification region. The gating grid control the entry of electrons from the drift volume into the MWPC. The readout pads image the avalanche charges. The signal on the pads is then amplified, integrated and digitized by the front-end electronics. The location of the readout pads gives the information about the x and y coordinates.

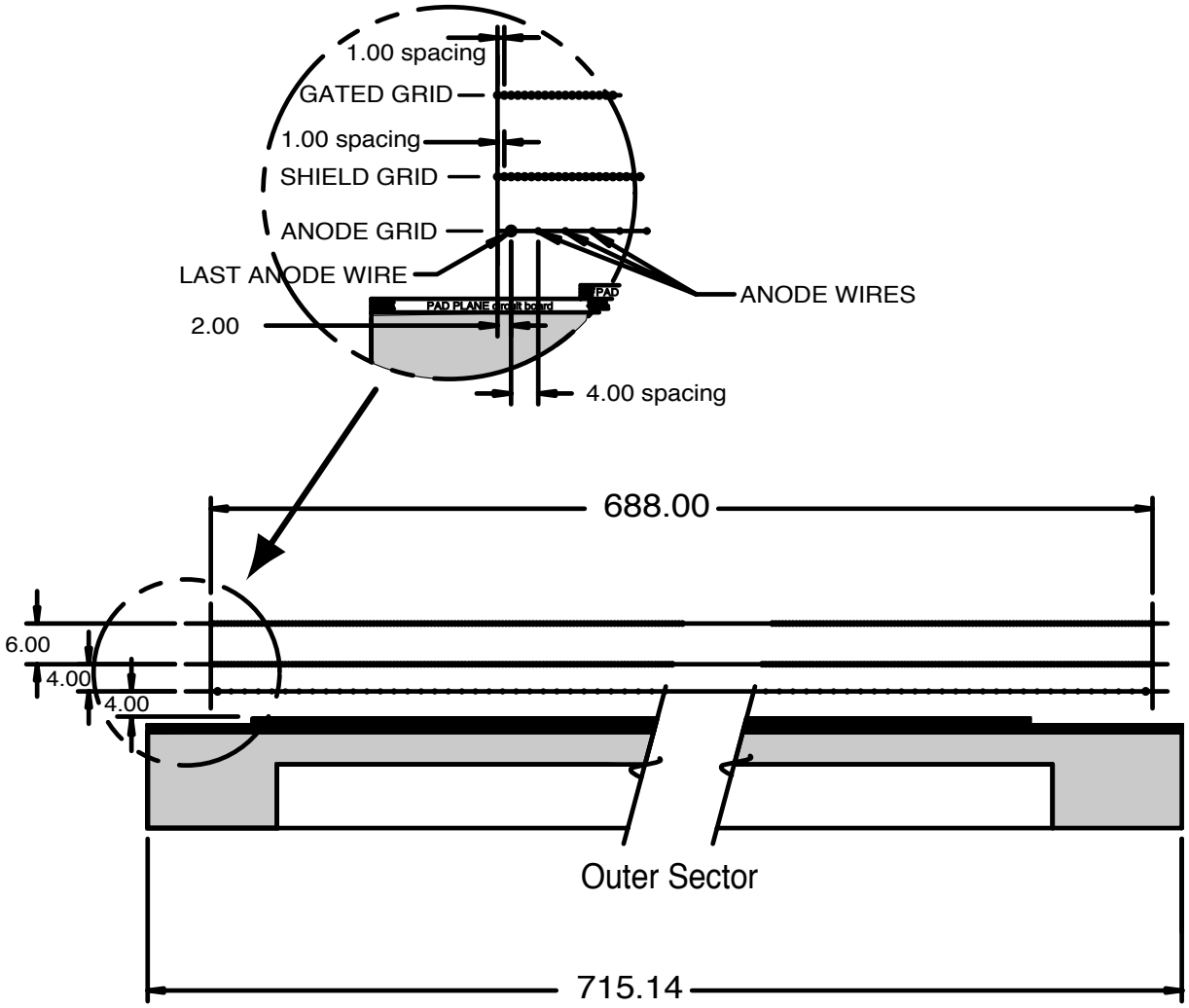

Figure 2.10: A cutaway view of an outer sub-sector pad plane. The cut is taken along a radial line from the center of the TPC to the outer field cage so the center of the detector is towards the right hand side of the figure. The figures shows the spacing of the anode wires relative to the pad plane, the ground shield grid, and the gated grid. The bubble diagram shows additional detail about the wire spacing. The inner sub-sector pad plane has the same layout except the spacing around the anode plane is 2 mm instead of the 4 mm shown here. All dimensions are in millimeters.

The position of the ionizing particle along the z-direction is reconstructed by measuring drift time and drift velocity.

2.2.2 Trigger Detectors

The trigger detectors in STAR consist of a Central Trigger Barrel (CTB) and two Zero Degree Calorimeters (ZDCs) at ± 18 m from the detector center, close to zero degree relative to the beam axis. The CTB in an array of scintillator slates arranged in a barrel at

the outer diameter of the TPC. Each of the two Zero Degree Calorimeters (ZDCs) subtend an angle of ≈ 2.5 mrad at the interaction point. These calorimeters are designed to measure energies of neutrons emitted from the nuclear fragments of the spectator matter. In contrast to fixed target experiments, where one can measure energies of all spectator nucleons in forward direction, at RHIC protons and charged fragments get deflected away from the ZDCs by the dipole magnets in the beamline meant to steer the hadron beams toward the collisions point. Thus, the ZDC signal is mainly produced by neutrons. Nevertheless, they still provide possibly the best determination of the collision centrality at RHIC and are used for the triggering some other observables based on multiplicity.

2.2.3 Forward Time Projection Chambers (FTPC)

The Forward Time Projection Chambers (FTPC) increase the acceptance of STAR experiment [17] . They cover pseudo rapidity range $2.5 < |\eta| < 4.0$ on the both sides of STAR with full azimuthal coverage and measure momenta to an accuracy of 12 %. The increased acceptance improves the event characterization in STAR and allow the study of asymmetric systems like $p + A$ collisions. FTPC is placed inside the STAR magnet. The schematic diagram of the FTPC is shown in Fig. 2.11. It is a cylindrical structure of 75 cm in diameter and 20 cm long with a radial drift field and readout chambers located in 5 rings on the outer cylindrical surface. Each ring has two padrows and is subdivided azimuthally into 6 readout chambers. The radial field is used to improve the two track separation in the region close to the beam pipe where particle density is highest. The field cage is formed by the inner HV-electrode, a thin matelized plastic tube and the outer cylinder wall at ground potential. The front end electronics (FEE) amplifies, shapes and digitizes the signal that are mounted on the back of the readout chambers. The ionization electrons are drifted to the anode sense wires and induced signals on the adjacent cathodes and readout by 9600 pads (each 1.6 $\times 20$ mm^2). The drifting medium is mixture of Ar/CO_2 (50%|50%), which in non-flammable and shows little ageing effect in comparison to hydrocarbons. Because of the curved readout chambers, the anode wires can't be orthogonal to the axial direction of the pads. Even the wires can't be parallel to the

pads and cylindrical axis because of focusing effects that lead to periodic shifts in the position measurements. However, if two or more wires cross the pad under a small angle this effect vanishes. So, FTPC use three wires crossing each pad at an angle of 17.4 mrad. FTPC also contains a laser calibration system which provides straight ionized tracks of the known position to infer corrections for spatial distortions caused by mechanical or drift field imperfections and helps to calibrate the drift velocity in the non-uniform radial drift field. The reconstruction of the track is done by calculating the track points from the charge distribution at readout electronics and points are grouped to form track. Using the magnetic field map, upto 10 position measurements per track are used to fit the momentum [18].

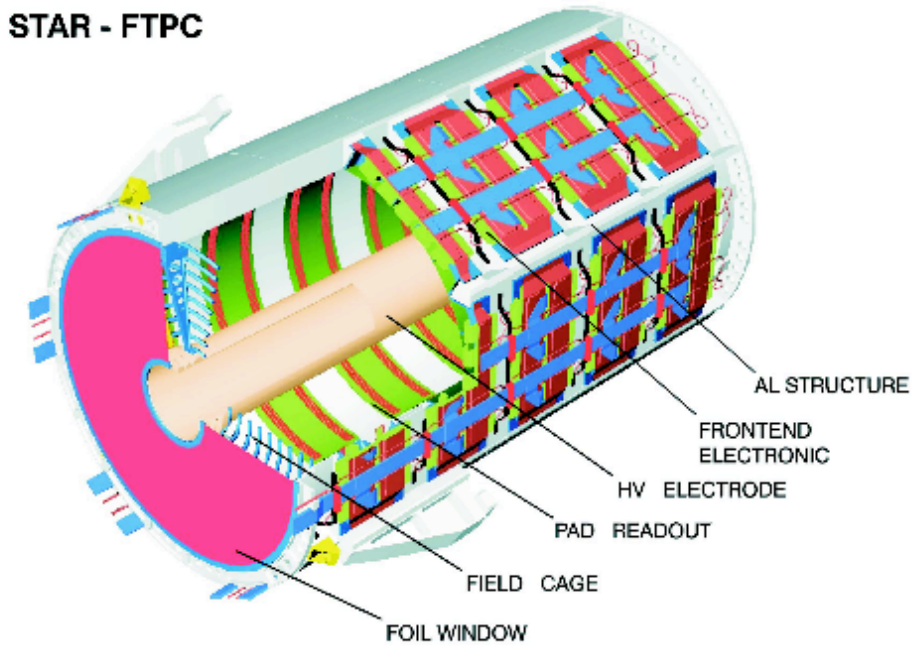

Figure 2.11: Schematic layout of an FTPC in the STAR experiment.

2.2.4 Silicon Vertex Tracker (SVT)

The Silicon Vertex Tracker is a three barrel microvertex detector based upon silicon drift detector technology. SVT enhances the physics capabilities of the main STAR component, the STAR Time Projection Chamber (TPC). In addition to improving primary vertexing, two track resolution and the energy loss measurements for particle identification, it also enables reconstruction of very short lived particles (primarily strange and multi-strange baryons and D-mesons). The SVT covers the pseudorapidity range of $|\eta| < 1$ with full azimuthal coverage.

The SVT consists of 216 Silicon Drift Detectors (SDD) containing over 13 million pixel multiplexed onto just 1300 readout channels. The SDDs are arranged in three cylindrical layers at distance of about 7, 11 and 15 cm from the beam axis. For inner tracking, a fourth layer has been installed after 2001 RHIC run. There are 40 anodes for each drift direction. The pixel readout of the SDD makes it a good choice for the high multiplicity environment in heavy ion reaction at RHIC. Since there are three layers of SDDs, a minimum of the three space points are required to determine the track parameters when the track is in a uniform magnetic field. Pions having lower transverse momenta ($\approx$ 50 MeV/c) can be detected in the SVT. The TPC has a lower momentum cut off which is about 150 MeV/c. Therefore, 50 MeV/c, the lower limit of SVT gives a significant enhancement to the STAR's capabilities.

There are 24 SVT readout electronic (RDO) boxes mounted on each side of STAR [19]. The RDO system is split into three functional blocks: (i) a monitoring power trigger and slow control interface block (PTB), (ii) an analog-to-digital converter and data storage block (AMB), (iii) a fiber optic transfer block (FOB). Each RDO box has 54 analog inputs. Data acquisition is performed at 3/8 of the RHIC strobe frequency (25 MHz).

2.2.5 Silicon Strip Detector (SSD)

The STAR Silicon Strip Detector (SSD) [20] constitutes fourth layer of the inner tracking system installed between the Silicon Vertex Tracker (SVT) and the Time Projection

Chamber (TPC). SSD enhances the tracking capabilities of STAR by accurately measuring two dimensional hit position and energy loss of charged particles. SSD is placed at a distance of 230 mm from the beam axis covering pseudo-rapidity range of $|\eta| < 1.2$ which leads to a total silicon surface close to 1 m^2 [21].

SSD is designed on the basis of two clamshells, each containing 10 carbon-fiber ladders. Each ladder is 1060 mm long, featuring a triangular cross-section of 40 mm base, supports 16 wafers using double-sided silicon strip technology. The ladders are made of high modulus carbon-fiber and set of ladders are assembled on C-shaped rib to allow installation on common SVT/SSD support structure. Each wafer has dimensions 75 mm $\times$ 42 mm $\times$ 300 μm. The total number of readout channels is 4,91,520 which are divided into four sectors, two clamshells shared in two sides (the p-side and the n-side) of the SSD. The strips on the P and N sides are inclined by 35 mrad with respect to each other and symmetrically with respect to wafer edge. Each of the 320 detection modules is composed of a silicon wafer, two hybrid circuits supporting the front-end electronics and a mechanical structure. The Control Board which receives the signals from the modules is connected to the hybrid with a kapton cable. The analog signals are transferred from the Control Board to the ADC Board, both located at the end of the ladder. The ADC board reads sequentially the data of a full ladder at 10 MHz and digitizes to 10 bits. The interface between the detector and the STAR system is done through four Readout Boards located on TPC wheels. After getting trigger, the readout board freeze the data in the front end electronics. It then reads all the Front-End Channels and sends the data to DAQ receiver board. When the slow control needs to access the Front-End boards, it reconfigures the readout board such that no trigger is accepted.

2.2.6 Barrel Electromagnetic Calorimeter (BEMC)

The Barrel Electromagnetic Calorimeter is installed to trigger rare high p_T processes (jets, leading hadrons, direct photons, heavy quarks) and provides large acceptance for photons, electrons, π^0 and η mesons in the system spanning polarized $p + p$ through $Au + Au$ collisions.

The BEMC is located inside the aluminum coil of the STAR solenoid and covers $|\eta| < 1.0$ and 2π in azimuth, matching the acceptance for full TPC tracking. The front face of the calorimeter is at a radius of $\approx$220 cm and is parallel to the beam axis. It includes a total of 120 calorimeter modules, each subtending 6^o in $\Delta\phi$ (~ 0.1 radian) and 1.0 unit in $\Delta\eta$. Sixty modules are in ϕ and two in η. Each module is 26 cm wide and 293 cm long with an active depth of 23.5 cm plus about 6.6 cm in structural plates. The modules are segmented into 40 towers, 2 in ϕ and 20 in η, with each tower subtending 0.5^o in $\Delta\phi$ and 0.05 in $\Delta\eta$. The full Barrel Calorimeter is thus physically segmented into a total of 4800 towers, each of which is projective, pointing back to the center of the interaction diamond. The Calorimeter is a sampling calorimeter, and the core of each module consists of a lead-scintillator stack and shower maximum detectors situated approximately 5 radiation lengths from the front of the stack. There are 20 layers of 5 mm thick lead, 19 layers of 5 mm thick scintillator and 2 layers of 6 mm thick scintillator. The thicker scintillator layers are used in the preshower portion of the detector. The SMD is used to provide fine spatial resolution in a calorimeter having segmentation (towers) signicantly larger than an electromagnetic shower size. The total area covered by the BEMC, outside the STAR TPC is over 60 m^2. The calorimeter has a total depth of about 20 radiation length at $\eta = 0$

The BEMC electronics includes trigger, readout of phototubes and SMD, high voltage system for phototubes, low voltage power, slow control functions, calibration controls and interfaces to the STAR trigger, DAQ and slow controls. The bulk of the front end electronics including signal processing, digitization, buffering, formation of trigger primitives and the first level of readout is located in custom EMC crates outside the magnet iron.

2.2.7 Endcap Electromagnetic Calorimeter (EEMC)

The STAR Endcap Electromagnetic Calorimeter provides full azimuthal coverage for high-p_T photons, electrons and electromagnetically decaying mesons over the pseudo-rapidity range $1 < \eta \leq 2$. It adds capability to detect photons and electromagnetically decaying mesons (π^0, η) to identify electrons and positrons and to trigger on high-energy particles

of these types. The EEMC includes a shower maximum detector optimized to discriminate between π^0 or η mesons over the 10-40 GeV energy region as well as preshower and postshower layers intended for electron and hadron discrimination. It also enhances triggering capabilities of the STAR for jets. EEMC is useful in the study of polarized $p+p$ collisions [22–24].

The EEMC is made of Pb/plastic scintillator. The actual pseudorapidiy coverage is $1.086 \leq \eta \leq 2.00$, leaving a small gap between the endcap and barrel calorimeter. The full annulus is divided into two halves. A standard layer of the calorimeter consists of Pb/stainless steel laminate followed by a 4 mm thick (Kuraray SCSN-81) plastic scintillator. Each radiator sheet comprises 4.57 mm thick calcium-loaded Pb sheets laminated on each face with 0.5 mm stainless steel, for a total of ≈ 0.85 radiation lengths. The four especially configured layers provide preshower, postshower and SMD functions. The total mass of the radiator sheets and active elements, for the two EEMC halves combined is $\approx$ 25000 kg. The whole assembly represents 21.4 radiation length at normal incidence and provides a shower energy sampling fraction of 6.6%, resulting in sufficient energy resolution and depth to measure electromagnetic shower energy at the levels needed for the required physics goals. The tower segmentation is produced using megatile construction. Megatiles span either 6^o or 12^o in azimuthal angle (ϕ), with machined isolation grooves separating each into 12 or 24 trapezoidal tiles respectively. One 30^o sector of a calorimeter layer contains two 12^o Megatiles, aligned flush against the tie-rods on each side, and a 6^o keystone megatile. At the edge of each megatile, optical connectors couple the WLS fibers from the 12 tiles within a given 6^o sector to 0.9-mm diameter clear fibers, which then run to the rear of the STAR poletip.

SMD is placed about five radiation length deep within the EEMC to provide fine granularity which is crucial to distinguish the transverse shower profiles characteristic of single photons *vs.* the close lying photon pairs from π^0 and η^0 decay. The SMD is made of extruded polystyrene-based scintillator strips of triangular cross section, organized orthogonally. The triangular cross section results in a sharing of the energy deposition among adjacent strips that enhances the position resolution and the stability of the measured

shower prole shape.

The EEMC trigger electronics and tower readout are similar to those used for BEMC. Pulse height information from the EEMC towers is digitized in 12-bit flash ADCs for every RHIC beam crossing and stored in digital pipelines for subsequent processing. The STAR level 0 trigger can compare individual tower ADC values and multi-tower sums to various thresholds and search for simply correlated information from other detector subsystems or individual towers will provide adequate energy resolution and dynamic range to include both single MIPs (*e.g.*, charged hadrons that do not shower) and electrons up to 150 GeV [25].

2.2.8 Time of Flight (TOF)

The Time of Flight detector significantly enhances the possibility for the particle identification in STAR. Combining with other detectors, it allows STAR to extract maximum amount of information available from soft physics on event-by-event basis.

The Time of Flight detector consists of a highly-segmented cylindrical detector immediately surrounding the TPC, arranged in 120 trays. Each individual tray is 2.4 m long, 21.3 m wide and 8.5 cm deep ($z \times \phi \times r$). The design of TOF is based on Multi-Gap Resistive Plate Chamber (MRPC) [26]. The Multi-Gap Resistive Plate Chamber is a detector capable of giving hundred picosecond time resolution and high detection efficiency ($> 95\%$) for minimum ionizing particles.

2.2.9 Photon Multiplicity Detector (PMD)

The Photon Multiplicity Detector (PMD) has been installed to measure the photon multiplicity in the forward rapidity region of the STAR experiment. It is at a distance of 5.42 m from the vertex on the east side of the STAR. The PMD covers a pseudorapidity range of $-3.8 \leq \eta \leq -2.3$ with full azimuthal coverage [27]. It measures the multiplicity and spatial distribution of the photons on an event-by-event basis.

Photon Multiplicity Detector has two detector planes: (i) Pre-shower plane (ii) Charged Particle Veto (CPV). Each plane consists of a large array of hexagonal cells (41,472 in

each plane) in which each cell behaves as an independent proportional counter. A mixture of Ar and CO_2 in ratio of 70 : 30 is used as sensitive medium. A honeycomb of 24×24 cells form a unit module. The set of unit modules is enclosed in a gas tight chamber called a supermodule. The number of unit modules in supermodules varies from 4 to 9. Each of the two plane consists of 12 such supermodules. A 15 mm thick lead plate is used as converter, which is sandwiched between preshower and CPV planes. The metallic walls of the honeycomb act as common cathode, kept at high negative potential and from each cell gold plated tungsten wire is passed that acts as anode and is kept at ground potential and connected to readout electronics. Detailed description of the PMD is given in Chapter 4.

Bibliography

[1] K. Adeoxs *et al.*, Nucl. Instrum. & Meth. A **499**, 469 (1974).

[2] M. Adamczyk *et al.*, Nucl. Instrum. & Meth. A **499**, 437 (1974).

[3] B. B. Back *et al.*, Nucl. Instrum. & Meth. A **499**, 603 (1974).

[4] K. H. Ackermann *et al.*, Nucl. Instrum. & Meth. A **499**, 624 (1974).

[5] F. Bergama *et al.*, Nucl. Instrum. & Meth. A **499**, 629 (1974).

[6] D. Lynn *et al.*, Nucl. Instrum. & Meth. A **447**, 264 (2000).

[7] R. Bellwied *et al.*, Nucl. Instrum. & Meth. A **499**, 636 (2003).

[8] H. Wiemann *et al.*, IEEE. Trans. Nucl. Sci. **NS-44**, 671 (1997).

[9] M. Anderson *et al.*, Nucl. Instrum. & Meth. A **499**, 655 (2003).

[10] S. Klein *et al.*, IEEE. Trans. Nucl. Sci. **NS-43**, 1768 (1996).

[11] M. Anderson*et al.*, Nucl. Instrum. & Meth. A **499**, 675 (2003).

[12] A. Schuttauf *et al.*, Nucl. Phys. A **661**, 677c (2003).

[13] K. H. Ackermann *et al.*, Nucl. Instrum. & Meth. A **499**, 709 (2003).

[14] H. Wieman *et al.*, IEEE Trans. Nuc. Sci. **44**, 671 (1997).

[15] J. Thomas *et al.*, Nucl. Instum & Meth. A **478**, 166 (2002).

[16] F. Bergsma *et al.*, Nucl. Instum & Meth. A **478**, 629 (2003).

[17] F. Bieser *et al.*, The Forward Time Projection for the STAR Detector, MPI PhE/98-3 (1998).

[18] M. Anderson *et al.*, Nucl. Instrum. & Meth. A **499**, 659-678 (2003).

[19] R. Bellwied *et al.*, Nucl. Instrum. & Meth. A **499**, 640-651 (2003).

[20] STAR SSD Collaboration, Proposal for a silicon strip detector for STAR, STAR note SN-0400.

[21] L. Arnord *et al.*, Nucl. Instrum. & Meth. A **499**, 652-658 (2003).

[22] G. Bunce, N. Saito, J. Soffer and W. Vogelsang, Annu. Rev. Nucl. Part. Sci. **50**, 525 (2000).

[23] L. .C. Bland, arxiv:hep-ex/0002061.

[24] L. .C. Bland *et al.*, STAR Note 401, (1999).

[25] C. E. Allgower *et.al.*, Nucl. Instrum. & Meth. A **499**, 740-750 (2003).

[26] M. C. S. Williams *et al.*, Nucl. Instrum. & Meth. A **374** (1996).

[27] M. M. Aggarwal *et al.*, Nucl. Instrum. & Meth. A **499**, 751-761 (2003).

Chapter 3

Elliptic Flow Methods

3.1 Introduction

In relativistic heavy ion collisions, initial anisotropy in the coordinate space is converted into momentum space anisotropy through the interactions of the constituents (Fig. 3.1). Therefore, momentum space anisotropy of the final state particles provide information about the early stages of the system evolution [1]. The anisotropy in the momentum space is correlated with the reaction plane/event plane [2–5]. The measurement of this event plane correlation is called elliptic flow. Relativistic heavy ion collisions are studied to deduce whether the quarks and gluons become deconfined during the high energy-density phase of collisions *i.e.,* in the stage of high energy density. The observable used to measure this anisotropy is known as 'anisotropic flow'. The anisotropic flow is also a measure of re-scattering *i.e.,* it is sensitive to the number of interactions and parton-parton scattering cross sections in the overlap region of colliding nuclei which leads to thermalization. Therefore, anisotropic flow is measure of the degree of thermalization at the early time of the collisions. It is also a signature of the pressure at early times and provide the information on the Equation of State (EoS) of the matter created in relativistic heavy ion collisions.

The anisotropic flow is characterized by the harmonic coefficients of a Fourier decomposition of the azimuthal distribution of the emitted particles [6–8].

$$\frac{dN}{d\phi} = \frac{a_0}{2} + \sum_{n=1}^{\infty} a_n cos(n\phi) + \sum_{n=1}^{\infty} b_n sin(n\phi) \tag{3.1}$$

where

$$a_n = \frac{1}{\pi} \int_{-\pi}^{\pi} \frac{dN}{d\phi} cos(n\phi) d\phi \tag{3.2}$$

and $b_n = 0$ due to reflection symmetry with respect to reaction plane. ϕ is azimuthal angle of emitted particle w.r.t the reaction plane (Ψ_{RP}).

$$a_n = a_0 \langle cos(n\phi) \rangle \equiv a_0 v_n \tag{3.3}$$

Therefore, Eq. (3.1) becomes

$$\frac{dN}{d\phi} = \frac{a_0}{2} \Big[1 + 2 \sum_{n=1}^{\infty} v_n cos(n\phi) \Big] \tag{3.4}$$

The anisotropic flow is defined as $v_n = \langle cos((n\phi) \rangle$, where the average is taken over all the particles in an event and over all events with nearly equal multiplicities. Since

$$\langle sin((n\phi) \rangle = 0 \tag{3.5}$$

the anisotropic flow can also be written as

$$v_n = \langle e^{\iota n\phi} \rangle \tag{3.6}$$

The anisotropic flow corresponding to the first and second harmonics play important role in anisotropy studies and are named directed flow and elliptic flow, respectively. The name 'directed flow' also called sidewise flow is due to the fact that such flow looks like a sideward bounce of fragments away from each other in the reaction plane and 'elliptic flow' is due to the fact that azimuthal distributions with non-zero second harmonic represents an ellipse. Figure 3.2 shows the geometrical representation of positive and negative elliptic

flow and directed flow.

Directed flow mostly affects the particles in forward and backward rapidities. At low energies (<100 AMeV), the attractive nuclear mean field dominates which results in a negative directed flow and in-plane elliptic flow but at higher energies individual nucleon-nucleon collisions dominate the attractive nuclear mean field and produce positive pressure, which deflects the projectile and target fragment away from each other in the center of mass frame resulting in positive directed flow. Also, the participant nucleons compressed in the overlap region cannot escape reaction plane due to the presence of spectators producing out-of-plane elliptic flow.

The anisotropy refers to the correlations of the emitted particles with the reaction plane. The reaction plane cannot be measured in experiments and anisotropic flow is usually studied from azimuthal correlations between the particles. But some of the azimuthal correlations are not related to the reaction plane, *e.g.* correlations between the particles from resonance decays, momentum conservation, quantum statistical effects, Bose-Einstein Condensation *etc.* are termed as non-flow. These non-flow cannot be distinguished from anisotropic flow and thus contribute to flow. So precise measurement of anisotropic flow requires the measurement of non-flow contribution too.

The elliptic flow from the Relativistic Heavy Ion Collider (RHIC) is found close to the ideal hydrodynamical predictions [9–16] but systematic studies show that this agreement can be achieved only for particular combination of the dynamical modelling *i.e.*, taking initial conditions from the Glauber model, perfect fluid quark gluon plasma (QGP) core and dissipative hadronic corona [17]. If we use initial conditions from the Color Glass Condensate (CGC) model rather than Glauber model, then results are not consistent because of the larger initial state anisotropy of CGC model than the Glauber model [18–20]. The disagreement of data from ideal hydrodynamics taking initial conditions from CGC and partial agreement using initial conditions from the Glauber models may be due to the absence of initial state fluctuations [21–28] which would add to some measurements of elliptic flow. Therefore, measurement of v_2 fluctuations is also an important parameter to compare with theoretical models. For the precise measurements of anisotropic flow, a

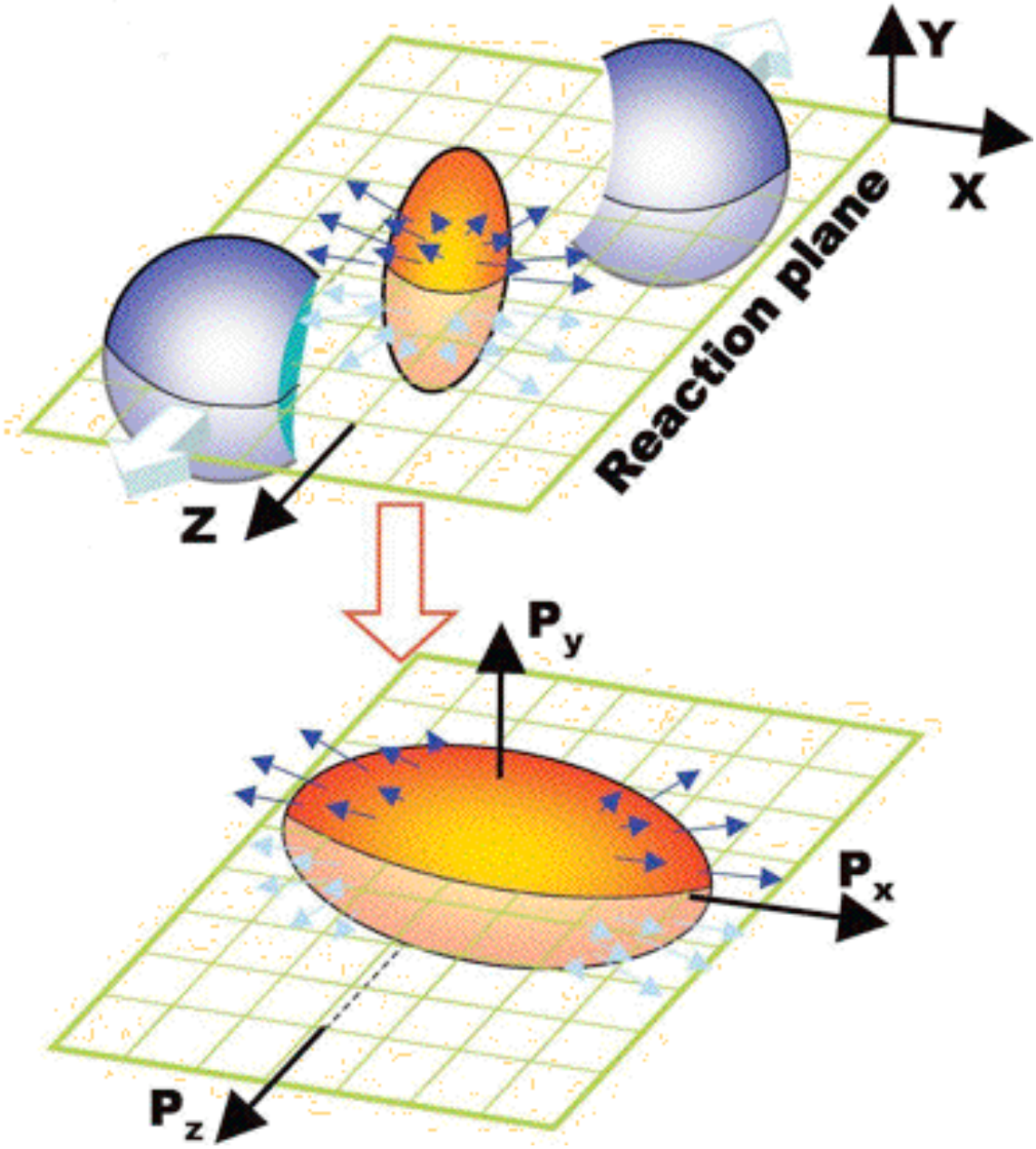

Figure 3.1: Spatial space anisotropy converts into momentum space anisotropy.

number of methods have been developed. These methods basically belong to two categories of azimuthal correlations viz., 'two-particle correlation methods' and 'multi-particle correlation methods'. The multi-particle correlation methods are believed to give better measurement of elliptic flow by suppressing the non-flow correlations.

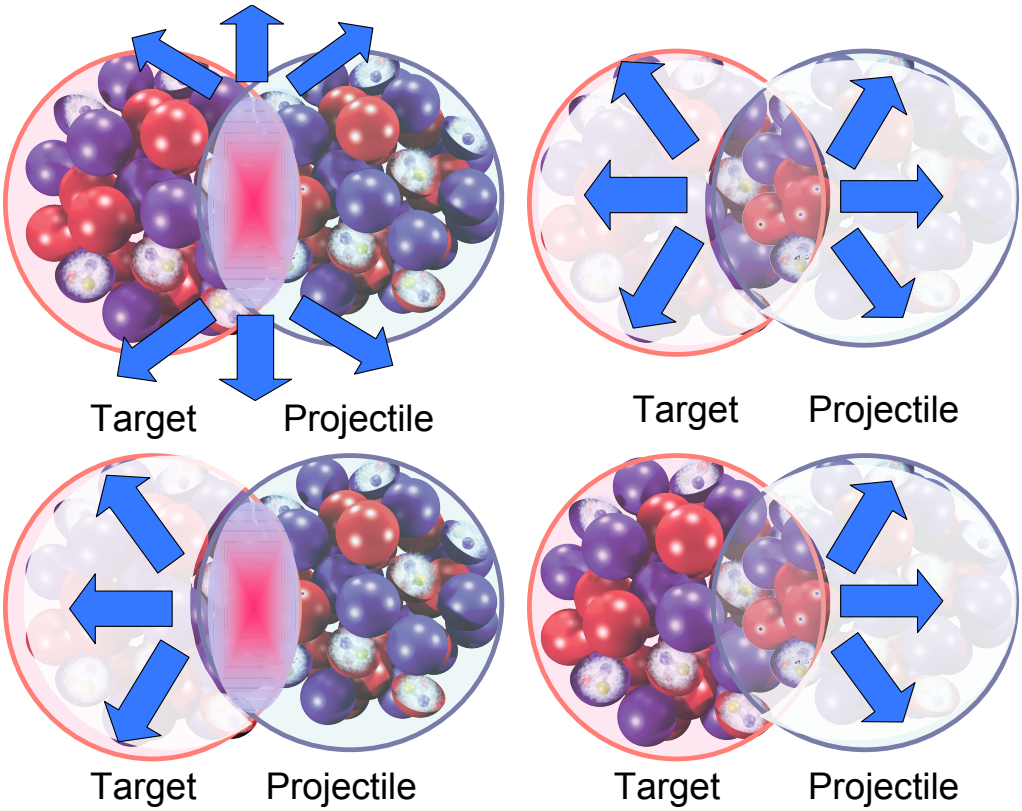

Figure 3.2: Anisotropies in the transverse plane (Top Panel) Out of plane (negative) elliptic flow (left) and in-plane (positive) elliptic flow (right). (Bottom Panel) Directed flow on target side (negative) (left) and projectile side (positive) (right).

In this thesis, the Q-Cumulant method, generating function method and q-distribution method have been applied to data for the elliptic flow studies and Glauber models and Color Glass Condensate model are used to estimate v_2 fluctuations. After estimating the fluctuations, we can also infer the non-flow contributions to the elliptic flow. Also, comparison is made between the models and data for obtaining information about the initial state fluctuations. The different methods of measuring elliptic flow are discussed below.

3.2 Elliptic Flow Methods

3.2.1 Two-Particle Correlation Methods

(i) Event Plane Method

In the event plane method, flow is calculated by estimating the reaction plane angle Ψ_{RP} [29]. The flow measurements are made w.r.t. the event plane and are corrected for the resolution of event plane relative to reaction plane. The event plane can be determined independently for each harmonic of the anisotropic flow. For n^{th} harmonic, components of flow vector (Q_n) and event plane angle (Ψ_n) are defined as:

$$Q_n cos(n\Psi_n) = X_n = \sum_i w_i cos(n\phi_i) \tag{3.7}$$

$$Q_n sin(n\Psi_n) = Y_n = \sum_i w_i sin(n\phi_i) \tag{3.8}$$

$$\Psi_n = tan^{-1}\left(\frac{\sum_i w_i sin(n\phi_i)}{\sum_i w_i cos(n\phi_i)}\right)/n, \tag{3.9}$$

where ϕ_i is the azimuthal angle of the i^{th} particle in an event and w_i are the weights used to optimize the event plane resolution. The transverse momentum of the particles can be used as weights. This method is sensitive to the non-flow correlations and needs acceptance corrections for the non-uniform azimuthal coverage. There are number of methods available to flatten the azimuthal distribution of event plane [30, 31] among which commonly used methods for flattening are phi weighting, re-centering and shifting.

The phi weighting can be done by weighting the Q-vector of each track with inverse of the azimuthal distribution of the particle average over many events,

$$w_i = \frac{1}{\langle N(\phi_i)\rangle} \tag{3.10}$$

For re-centering one needs to subtract Q-vector average over number of events from the Q-vector of each track in an event and shifting can be done by fitting the non-flat azimuthal distribution of Q-vector angles with Fourier expansion and calculating the shift necessary to force a flat distribution. The observed elliptic flow is the second harmonic of

the azimuthal distribution of the particles with respect to measured event plane;

$$v_2^{obs} = \langle cos(2(\phi - \Psi_n)\rangle, \tag{3.11}$$

but in the fourier expansion $dN/d\phi \propto 1 + \sum_n 2v_n \cos n\,(\phi - \Psi_{RP})$, Ψ_{RP} is the real reaction plane angle. The event plane resolution is used to find the accuracy of event plane angle in approximating the real reaction plane angle and real v_2 corrected for event plane resolution is given by,

$$v_2 = \frac{v_2^{obs}}{\langle cos(2(\Psi_n - \Psi_{RP}))\rangle} \tag{3.12}$$

The event plane resolution can be obtained by dividing the event into two sub-events and calculating the resolution for sub-event. The full event plane resolution can be estimated from the correlations $\langle cos[n(\Psi_n^a - \Psi_n^b)]\rangle$ [30] of the event planes of independent sub-events Ψ^a, Ψ^b. Normally each event is divided into two statically equivalent sub-events. Sub-event plane resolution is defined as:

$$\langle cos[n(\Psi_n^a - \Psi_{RP})]\rangle = \sqrt{\langle cos[n(\Psi_n^a - \Psi_n^b)]\rangle} \tag{3.13}$$

and the full event plane resolution can be obtained by using the event plane resolution of the sub-events taking into account that the multiplicity of the full event is twice the multiplicity of the sub-event,

$$\langle cos[n(\Psi_n - \Psi_{RP})]\rangle \leq \sqrt{2}\langle cos[n(\Psi_n^a - \Psi_{RP})]\rangle \tag{3.14}$$

(ii) Scalar Product Method

Like the event-plane method, each event is divided into two sub-events and correlation between the two sub-events is defined as:

$$\langle Q_n^a . Q_n^b\rangle = \langle v_n^2 M^a M^b\rangle \tag{3.15}$$

where M^a and M^b are the multiplicities of the sub-event a and b, respectively. Q_n^a and Q_n^b are calculated using:

$$Q_n cos(n\Psi_n) = \sum_i cos(n\phi_i) \tag{3.16}$$

$$Q_n sin(n\Psi_n) = \sum_i sin(n\phi_i) \tag{3.17}$$

Scalar product method [32] is a variation of event plane method which weights event with the magnitude of the flow vector Q. The flow relative to the true reaction plane can be calculated using

$$v_n = \frac{\langle Q_n u^*_{n,i} \rangle}{2\sqrt{\langle Q_n^a Q_n^{b\,*} \rangle}}, \tag{3.18}$$

where $u_{n,i} = cos(n\phi_i) + \iota sin(n\phi_i)$ is unit vector of i^{th} particle. The vectors Q_n^a and Q_n^b are calculated from sub-events a and b, respectively.

Both the methods mentioned above are based on two-particle azimuthal correlations . But as mentioned earlier there are two-particle correlations which are not related to the event plane. Therefore it is important to estimate those correlations by using alternate approach. The best way to minimize those correlations is to use multi-particle correlation methods to study elliptic flow.

3.2.2 Multi-Particle Correlation Methods

(i) q-distribution Method

This method is based on the fitting of the distribution of the magnitude of reduced flow vector q ($= Q/\sqrt{M}$). The x and y components of the reduced flow vector for the n^{th} harmonic are defined as:

$$q_{n,x} = \frac{1}{\sqrt{M}} \sum_i cos(n\phi_i) \tag{3.19}$$

$$q_{n,y} = \frac{1}{\sqrt{M}} \sum_i sin(n\phi_i), \tag{3.20}$$

where ϕ is azimuthal angle to each track. The Central Limit Theorem (CLT) ensures that q_n distribution will be a Gaussian shifted by $\sqrt{M}v_n$ in the x direction [30, 33, 34] , if enough tracks are used:

$$\frac{d^2N}{q_n dq_n d(\Delta\phi)} = \frac{1}{2\pi\sigma_x\sigma_y} e^{\left[-\frac{(q_n cos(n\Delta\phi)-\sqrt{M}v_n)^2}{2\sigma_x^2} - \frac{q_n^2 sin^2(n\Delta\phi)}{2\sigma_y^2}\right]}. \tag{3.21}$$

$$\begin{aligned} \sigma_{n,x}^2 &= \frac{1}{2}(1 + v_{2n} - 2v_n^2 + (M-1)(\delta_n + 2\sigma_{v_n}^2), \\ \sigma_{n,y}^2 &= \frac{1}{2}(1 - v_{2n} + (M-1)(\delta_n + 2\sigma_{v_n}^2))., \end{aligned} \tag{3.22}$$

where M is the number of tracks used in the calculation of q_n and $\Delta\phi$ is the angle between a given q_n and the true reaction plane. Gaussian fluctuations of v, σ_{vn} are directly put into σ_x and σ_y by modeling a *2D Gaussian* along the reaction plane axis and perpendicular to it [35]. The parameter δ_n accounts for the broadening of the distribution that arises from non-flow correlations and, in simulations, is given by

$$\delta_n = \langle \cos n(\phi_1 - \phi_2) \rangle_{non-flow}. \tag{3.23}$$

In practice, since the exact direction of the reaction plane is not known, $|q_n|$ is measured. To describe the $|q_n|$ distribution, the Eq. 3.21 integrated over $\Delta\phi$ [30, 33, 34] gives:

$$\begin{aligned} \frac{dN}{q_n dq_n} = \frac{1}{\sqrt{\pi}\sigma_x\sigma_y} e^{-\frac{1}{2}\left(\frac{q_n^2+Mv_n^2}{\sigma_x^2}\right)} \times \\ \sum_{k=0,2,4,\ldots}^{\infty} \left(1 - \frac{\sigma_x^2}{\sigma_y^2}\right)^k \left(\frac{q_n}{v_n\sqrt{M}}\right)^k \frac{1}{k!}\Gamma\left(\frac{2k+1}{2}\right) I_k\left(\frac{q_n v_n\sqrt{M}}{\sigma_x^2}\right), \end{aligned} \tag{3.24}$$

where Γ is the gamma function and I_k are modified Bessel's functions. Here we consider $n = 2$ (*i.e.* the second harmonic) which corresponds to elliptic flow. The $k = 0$ term produces a Bessel-Gaussian function and $k = 2$ term is only a small correction so that

the first two terms in the series are sufficient. The quantity σ_y^2 only contributes to $k \geq 2$ terms so that σ_x^2 dominates the observed width of the distribution.

In case v_2 fluctuates from event to event along the *participant* axis, we neglect the σ_{vn} terms in Eqs. (3.22) and convolute with a fluctuation function:

$$\frac{dN}{q_2 dq_2}(\langle v_2 \rangle, \sigma_{v_2}) = \int dv_2 f(v_2 - \langle v_2 \rangle, \sigma_{v_2}) \frac{dN}{q_2 dq_2}, \tag{3.25}$$

where $f(v_2 - \langle v_2 \rangle)$ is the probability for a particular event to have a given flow value v_2. The approximation of zero v_2 fluctuations corresponds to $f = \delta(v_2 - \langle v_2 \rangle)$ where δ is the Dirac delta function. In this case, $\langle v_2 \rangle$ should approximate $v_2\{4\}$, the v_2 calculated from the four-particle correlations. In the analysis presented in this thesis, we assumed a *1D Gaussian* shape along the participant axis for the v_2 distribution: $f = \frac{1}{\sqrt{2\pi(\sigma_{v2})^2}} \exp(-\frac{(v_2 - \langle v_2 \rangle)^2}{2(\sigma_{v2})^2})$, and extract the standard deviation (σ_{v_2}) of the distribution by fitting data.

Since the v_4 and $2v_2^2$ terms in Eq. (3.22) are small and so cancelled, $\sigma_{n,x}$ and $\sigma_{n,y}$ are approximately equal, and neglecting '-1', Eq. (3.22) reduces to a single equation for σ_q

$$\sigma_q^2 \simeq \frac{1}{2}(1 + M\delta_n + 2M\sigma_{vn}^2). \tag{3.26}$$

Equation (3.26) shows that the width of the q distribution is broadened not only by v_n fluctuations, but also by non-flow. One can think of non-flow correlations as effectively reducing the number of independent particles, decreasing the multiplicity and making the statistical fluctuations greater. It seems that in most analysis methods δ_n and σ_{v_n} appear in the same combination for the second harmonic: $\delta_2 + 2\sigma_{v_2}^2$, thus making it difficult to disentangle the two effects with precision. Non-statistical dynamic contribution to the width of the q-distribution is defined as:

$$\sigma_{tot}^2 \equiv \delta_2 + 2\sigma_{v_2}^2 \tag{3.27}$$

then Eq. (3.26) becomes

$$\sigma_q^2 = \frac{1}{2}(1 + M\sigma_{tot}^2) \tag{3.28}$$

This is the width in x and y directions that would be used for the q-distribution.

3.2.3 Cumulants

(i) Generating Function Method

This method is based on the cumulants expansion of multi-particle azimuthal correlations [32]. The principle of this method is that when cumulants of higher order are used to study anisotropic flow, the relative contribution from the non-flow decreases and hence systematic uncertainties decrease.

The measured two-particle azimuthal correlations can be written as

$$\left\langle e^{in(\phi_1-\phi_2)}\right\rangle = \left\langle e^{in\phi_1}\right\rangle\left\langle e^{-in\phi_2}\right\rangle + \left\langle\left\langle e^{in(\phi_1-\phi_2)}\right\rangle\right\rangle, \tag{3.29}$$

where $\left\langle\left\langle e^{in(\phi_1-\phi_2)}\right\rangle\right\rangle$ by definition is the second order cumulant. For perfect detector, the first term in the Eq. 3.29 vanishes and cumulant reduce to measured two-particle correlations. There are several physical contributions to $\left\langle\left\langle e^{in(\phi_1-\phi_2)}\right\rangle\right\rangle$ which separate into flow and non-flow. Therefore, for the perfect detector Eq. (3.29) becomes

$$\left\langle e^{in(\phi_1-\phi_2)}\right\rangle = v_n^2 + \delta_n \tag{3.30}$$

for n^{th} harmonic δ_n denotes the non-flow contribution to n^{th} harmonic. Similarly four-particle correlations can be decomposed as:

$$\left\langle e^{in(\phi_1+\phi_2-\phi_3-\phi_4)}\right\rangle = \left\langle e^{in(\phi_1-\phi_3)}\right\rangle\left\langle e^{in(\phi_2-\phi_4)}\right\rangle + \left\langle e^{in(\phi_1-\phi_4)}\right\rangle\left\langle e^{in(\phi_2-\phi_3)}\right\rangle + \left\langle\left\langle e^{in(\phi_1+\phi_2-\phi_3-\phi_4)}\right\rangle\right\rangle \tag{3.31}$$

If the particles are correlated pairwise, the two possible combinations which lead to non-vanishing value for L.H.S of Eq. (3.31), these pairs can be either (1,3) and (2,4) or (1,4) and (2,3). This yields first two terms of Eq. (3.31). The last term is fourth order cumulants by definition, which is independent of the two-particle non-flow correlations. There may be contribution from the four-particle non-flow correlations but their contribution scales with the multiplicity like $1/M^3$. [34]. Eq. (3.31) can be written as

$$\left\langle e^{in(\phi_1+\phi_2-\phi_3-\phi_4)}\right\rangle = 2\left\langle e^{in(\phi_1-\phi_3)}\right\rangle^2 + \left\langle\left\langle e^{in(\phi_1+\phi_2-\phi_3-\phi_4)}\right\rangle\right\rangle \tag{3.32}$$

The flow contribution to the cumulant can be obtained by subtracting two-particle correlations from 4-particle correlations *i.e.,* rearranging the above equation,

$$\left\langle\left\langle e^{in(\phi_1+\phi_2-\phi_3-\phi_4)}\right\rangle\right\rangle = 2\left\langle e^{in(\phi_1-\phi_3)}\right\rangle^2 - \left\langle e^{in(\phi_1+\phi_2-\phi_3-\phi_4)}\right\rangle = -v_n^4 \tag{3.33}$$

In previous analysis, cumulant were calculated by using generating function [32]

$$G_n(z) = \prod_{j=1}^{M}\Big[1+\frac{w_j}{M}\Big(z^* e^{in\phi_j} + z e^{-in\phi_j}\Big)\Big] = \prod_{j=1}^{M}\Big[1+\frac{w_j}{M}\ (2xcos(n\phi_j)+2ysin(n\phi_j))\Big] \tag{3.34}$$

where ϕ_j are the azimuthal angle of the outgoing particles w.r.t. a fixed direction in the laboratory frame. The product runs over all the particles (i.e. multiplicity of the event M) in the single event and $z = x + iy$ is arbitrary complex number. The weight w_j is a function of particle type, transverse momentum and the rapidity. Number of particles M are chosen to be same for all events *i.e.* fixed multiplicity for each centrality. Cumulant for the n^{th} order can be calculated by averaging the generating function over all the events, *i.e.*,

$$C_n(z) \equiv M\Big[\langle G_n(z)\rangle^{1/M} - 1\Big] \tag{3.35}$$

The cumulant of $2k$-particle correlations $c_n\{2k\}$ are coefficients of $z^k z^{*k}/((k!)^2$ in the power series expansion of $C_n(z)$. The first three cumulants are calculated by truncating the series expansion upto $|z|^6$ and computing the $C_n(z)$ at following interpolations points:

$$z_{p,q} = x_{p.q} + \iota y_{p,q}, \qquad x_{p,q} \equiv r_0\sqrt{p}\ cos\Big(\frac{2q\pi}{q_{max}}\Big), \qquad y_{p,q} \equiv r_0\sqrt{p}\ sin\Big(\frac{2q\pi}{q_{max}}\Big), \tag{3.36}$$

for $p = 1, 2, 3$ and $q = 0.....q_{max} - 1$, where $q_{max} \geq 8$. The parameter r_0 is chosen so as to compromise between the errors due to higher order terms in the power series expansion and the numerical errors. Under the assumption that numerical errors are proportional to the total number of elementary operations performed (of the order of MN_{evts}). The $r_0 \sim (\epsilon N_{evts}^{3/2} M)^{1/8}\sqrt{M/\langle w^2\rangle}$, where ϵ is the accuracy of elementary operations.

$C_n(z_{p,q})$ are averaged over the phase space of z to give

$$C_p \equiv \frac{1}{q_{max}} \sum_{q=0}^{q_{max}-1} C_n(z_{p,q}) \qquad\qquad p = 1, 2, 3 \tag{3.37}$$

The cumulant for 2-, 4- and 6-particle correlations are given by

$$C_n\{2\} = \frac{1}{r_0^2}\Big(3C_1 - \frac{3}{2}C_2 + \frac{1}{3}C_3\Big), \tag{3.38}$$

$$C_n\{4\} = \frac{2}{r_0^4}\Big(-5C_1 + 4C_2 - C_3\Big), \tag{3.39}$$

$$C_n\{6\} = \frac{6}{r_0^6}\Big(3C_1 - 3C_2 + C_3\Big), \tag{3.40}$$

For the detector with full azimuthal coverage each cumulant $c_n\{2k\}$ gives the estimate of the corresponding integrated flow V_n, which is denoted by $V_n\{2k\}$:

$$V_n\{2\}^2 = c_n\{2\}, \qquad V_n\{4\}^4 = -c_n\{4\}, \qquad V_n\{6\}^6 = -c_n\{6\}/4. \tag{3.41}$$

The statistical uncertainty on $c_n\{2k\}$ is of the order $(\langle w^2\rangle^k/\sqrt{M^{2k}N_{evts}})$. The relative error on $V_n\{2k\}$ is of the order

$$\frac{\delta V_n\{2k\}}{V_n\{2k\}} \sim \frac{1}{\chi_n^{2k}\sqrt{N_{evts}}}. \tag{3.42}$$

where $\chi_n \equiv V_n\sqrt{M/\langle w^2\rangle}$.

The order of magnitude is correct as long as χ_n is not larger than unity which is the case for most of experiments at relativistic energies.

(ii) Q-Cumulant Method

This method [36] of calculating the cumulants has several advantages over the generating function method. Primarily it is much faster since it does not involve multiple passes over data or nested loops over tracks and is more transparent. Cumulants are calculated directly from Q-vector without using generating function. We don't need to tune interpolating parameters like r_0 in cumulants method and even this is not biased by multiplicity fluctuations. The flow is calculated the same way as in the conventional

cumulant method from cumulants using the relations,

$$v_n\{2, QC\}^2 = \langle 2 \rangle \tag{3.43}$$

$$v_n\{4, QC\}^4 = 2.\langle 2 \rangle^2 - \langle 4 \rangle, \tag{3.44}$$

Cumulants for two- and four-particle correlation are denoted by $c_n\{2, QC\}$, $c_n\{4, QC\}$ and defined as:

$$c_n\{2, QC\} = \langle 2 \rangle \tag{3.45}$$

$$c_n\{4, QC\} = \langle 4 \rangle - 2.\langle 2 \rangle^2 \tag{3.46}$$

The cumulants are calculated from Q-vector. Q-vector evaluated for harmonic n^{th} is a complex quantity denoted by Q_n and defined as :

$$Q_n \equiv \sum_{i=1}^{M} e^{\iota n \phi_i}, \tag{3.47}$$

and calculated as

$$Q_{n,x} = \sum_{i=1}^{M} cos(n\phi_i), \qquad Q_{n,x} = \sum_{i=1}^{M} sin(n\phi_i), \tag{3.48}$$

The summation runs over all the particles in an event with multiplicity M and ϕ_i is azimuthal angle of the i^{th} particle.

The two-particle cumulants $c_n\{2, QC\}$ are obtained by decomposing $\mid Q_n \mid^2$ to give

$$\langle 2 \rangle = \frac{|Q_n|^2 - M}{M(M-1)} \tag{3.49}$$

and the four-particle correlations are calculated by decomposing the $\mid Q_n \mid^4$ to give

$$\langle 4 \rangle = \frac{|Q_n|^4 + |Q_{2n}|^2 - 2Re.[Q_{2n}Q_n^*Q_n^*] - 4(M-2).|Q_n|^2}{M(M-1)(M-2)(M-3)} + \frac{2}{(M-1)(M-2)} \tag{3.50}$$

These Equations are used to calculate two- and four-particle correlations to calculate the anisotropic flow.

It has also been proposed to use weights for each event within a particular centrality class based on the number of tracks analyzed for that event. The weighted two- and four-particle correlations are then

$$\langle\langle 2\rangle\rangle = \frac{\sum_{i=1}^{N} M_i(M_i-1).\langle 2\rangle}{\sum_{i=1}^{N} M_i(M_i-1)} \tag{3.51}$$

$$\langle\langle 4\rangle\rangle = \frac{\sum_{i=1}^{N} M_i(M_i-1)(M_i-2)(M_i-3).\langle 4\rangle}{\sum_{i=1}^{N} M_i(M_i-1)(M_i-2)(M_i-3)}, \tag{3.52}$$

and the two and four particle cumulants are calculated from equations 3.51 and 3.52 as

$$c_n\{2, QC\} = \langle\langle 2\rangle\rangle \tag{3.53}$$

$$c_n\{4, QC\} = \langle\langle 4\rangle\rangle - 2\langle\langle 2\rangle\rangle^2 \tag{3.54}$$

This weighting was proposed as a method to reduce the dependence of the results on multiplicity. However, the application of multiplicity weights makes the $v_2\{2, QC\}$ and $v_2\{4, QC\}$ results more dependent on the width of the multiplicity bins used to define centrality.

Bibliography

[1] H. Sorge, Phys. Rev. Lett. **78**, 2309 (1997).

[2] W. Reisdorf and H. G. Ritter, Annu. Rev. Nucl. Part. Sci. **47**, 663 (1997).

[3] N. Herrmann, J. P. Wessels and T. Wienold, Annu. Rev. Nucl. Part. Sci. **49**, 581 (1999).

[4] J. Y. Ollitrault, Nucl. Phys. A **638**, 195c (1998).

[5] A. M. Poskanzer, nucl-ex/0110013 (2001).

[6] J. Y. Ollitrault, Phys. Rev. D **46**, 229 (1992).

[7] S. Voloshin and Y. Zhang, Z. Phys. C **70**, 665 (1996).

[8] A. M. Poskanzer and S. A. Voloshin, Phys. Rev. C **58**, 1671 (1998).

[9] C. Adler *et al.* [STAR Collaboration], Phys. Rev. Lett. **87**, 182301 (2001).

[10] J. Adams *et al.* [STAR Collaboration], Phys. Rev. Lett. **92**, 052302 (2001).

[11] K. Adcox *et al.* [PHENIX Collaboration], Phys. Rev. Lett. **89**, 212301 (2002).

[12] S. S. Adler *et al.* [PHENIX Collaboration], Phys. Rev. Lett. **91**, 182301 (2003).

[13] J. Y. Ollitrault, Eur. J. Phys. **29**, 275 (2008).

[14] T. Hirano, N. Van der Kolk and A. Bilandzic, arXiv:nucl-th/0808.2684.

[15] S. A. Voloshin, A. M. Poskanzer and R. Snellings, arXiv:nucl-ex/0809.2949.

[16] U. W. Heinz, arXiv:nucl-th/0901.4355.

[17] T. Hirano and M. Gyulassy, Nucl. Phys. A **769**, 71 (2006).

[18] A. Kuhlman, U. Heinz and Y. V. Kovchegov, Phys. Lett. B **638**, 171 (2006).

[19] A. Adil, H. J. Drescher, A. Dumitru, A. Hayashigaki and Y. Nara, Phys. Rev. C **74**, 044905 (2006).

[20] T. Lappi and R. Venugopalan, Phys. Rev. C **74**, 054905 (2006).

[21] X. l. Zhu, M. Bleicher and H. Stoecker, Phys. Rev. C **72**, 064911 (2005).

[22] R. S. Bhalerao and J. Y. Ollitrault, Phys. Lett. B **641**, 260 (2006).

[23] B. Alver et al. [PHOBOS Collaboration], nucl-ex/0702036; Phys. Rev. C **77**, 014906 (2008).

[24] R. Andrade, F. Grassi, Y. Hama, T. Kodama and O. Socolowski Jr., Phys. Rev. Lett. **97**, 202302 (2006).

[25] H. J. Drescher and Y. Nara, Phys. Rev. C **75**, 034905 (2007); Phys. Rev. C **76**, 041903 (2007).

[26] W. Broniowski, P. Bozek, and M. Rybczynski, Phys. Rev. C **76**, 054905 (2007).

[27] S. A. Voloshin, A. M. Poskanzer, A. Tang, and G. Wang, Phys. Lett. B **659**, 537 (2008).

[28] T. Hirano, U. Heinz, D. Kharzeev, R. Lacey and Y. Nara, Phys. Rev. C **77**, 044909 (2008).

[29] K. H. Ackermann *et al.,* Nucl. Instrum. & Meth. A **499**, 624 (2003).

[30] A. Poskanzer and S. Voloshin, Phys. Rev. C **58**, 1671 (1998).

[31] C. Alt *et al.*, Phys. Rev. **C 68**, 034903 (2003).

[32] N. Borghini, P. M. Dinh, and J. Y. Ollitrault, Phys. Rev. C **64**, 054901 (2001).

[33] J. Y. Ollitrault, arXiv:nucl-ex/9711003; Phys. Rev. C **58**, 1671 (1998).

[34] N. Borghini, P. M. Dinh and J. Y. Ollitrault, Phys. Rev. C **63**, 054906 (2001).

[35] S. A. Voloshin, A. M. Poskanzer, A. Tang and G. Wang, arXiv:nucl-ex/0612021.

[36] A. Bilandzic, R. Snellings, S. Voloshin, [arXiv:nucl-ex/1010.0233.

Chapter 4

Photon Multiplicity Detector and Photons Flow

A Preshower Photon Multiplicity Detector (PMD) [1,2] was installed in the STAR experiment by Indian Collaboration. PMD is capable of studying photon production in nucleus-nucleus collisions in the forward rapidity region (Fig. 4.1) where high particle density precludes the use of calorimeter. The inclusion of PMD has increased the phase space coverage of STAR detector by covering the pseudorapidity region of $-2.3 \geq \eta \geq -3.8$ with full azimuthal acceptance and in the p_T down to $\sim$ 25 MeV/c [3]. This pseudorapidity region for the PMD was selected to minimize the effect of upstream materials while maximizing the overlap with the coverage of FTPC [4]. The coupling of photons production measurements from PMD with charge particle measurements from FTPC has increased the capability of STAR detector to study charge-neutral fluctuations [5]. The detector is mounted on the east side of STAR detector in the Wide Angle hall (WAH) at a distance of 542 cm from the interaction point. The basic parameters of the PMD are listed in the Table 4.1.

The Photon Multiplicity Detector allows measure photons and their spatial distribution on event-by-event basis. Combining this with the information from other detectors PMD is capable of investigating the following topics of physics:

- determination of reaction plane and probes of thermalization via studies of azimuthal

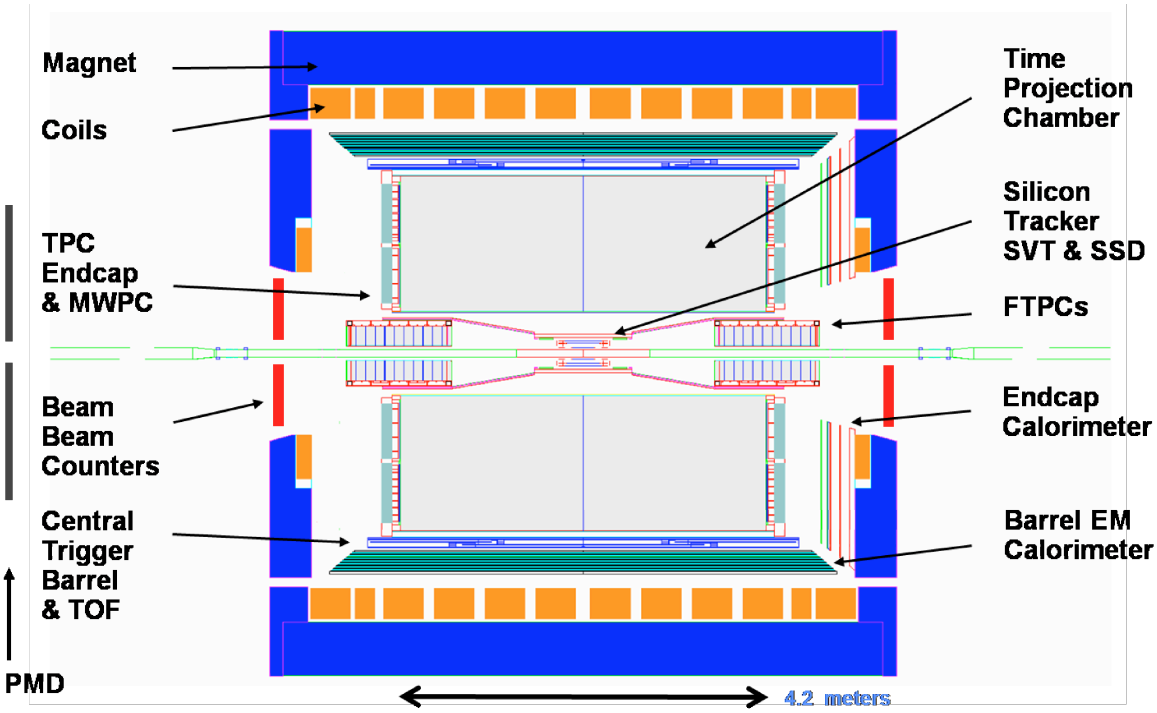

Figure 4.1: Cross-sectional view of the detectors in STAR experiment. The PMD is shown with thick vertical black lines.

anisotropy.

- critical phenomena near the phase boundary leading to fluctuations in the global variables like multiplicity, mean transverse momentum and pseudorapidity distributions.

- signals of chiral-symmetry restoration (*e.g.* disoriented chiral condensate [6–9]) through the measurements of charged particles multiplicity (N_{ch}) and photons in a common part of phase space and study of the observables N_γ and N_{ch}/N_γ with full azimuthal coverage.

4.1 Principle of the PMD

The schematic front view and cross-sectional view of the PMD are shown in Figs. 4.3 and 4.4. It consists of highly segmented detector placed behind the lead converter of thickness 3 radiations length ($3X_0$). The charged particle veto detector in front of the

Table 4.1: Basic parameters of the STAR PMD [1]

Paramter	**Value**
Distance from the vertex	542 cm
η coverage	$-2.3 - -3.8$
ϕ coverage	2π
Number of Cells	82,944
Area of the detector	4.2 cm^2
Cell Size	1 cm^2
Configuration	Veto and pre-shower
Weight of the detector	900 Kg

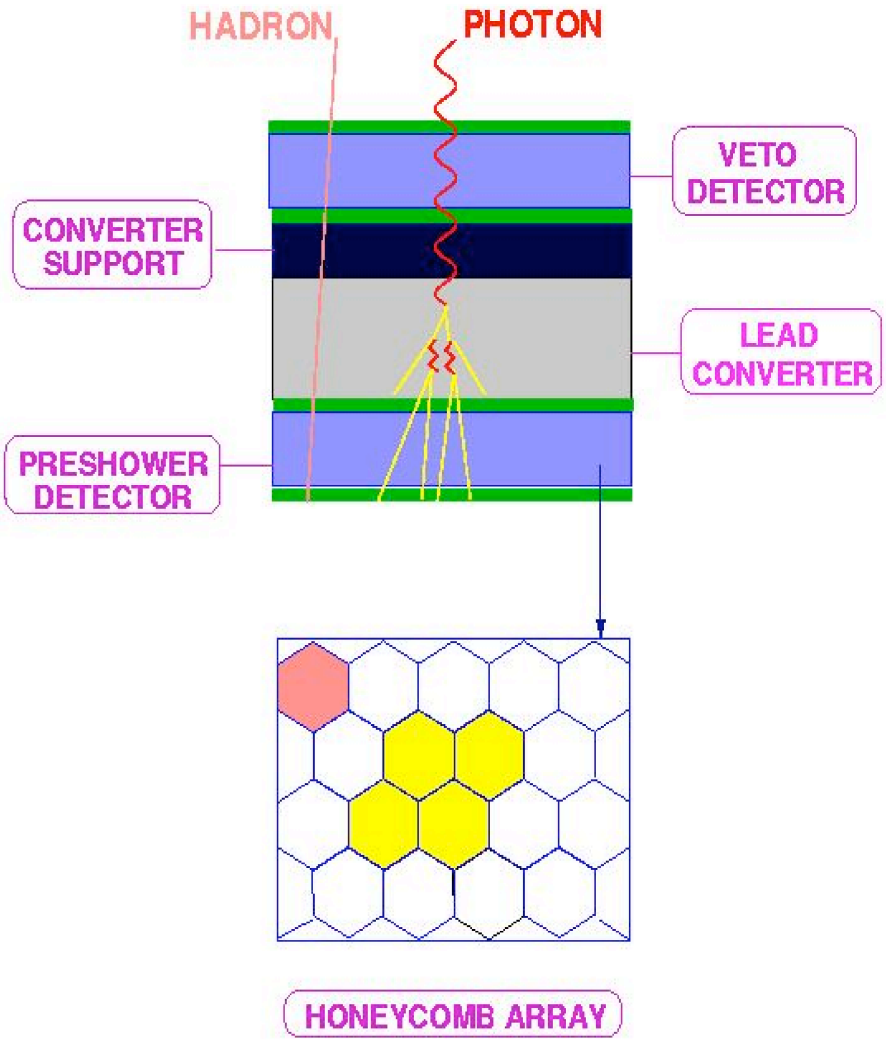

Figure 4.2: Principle of Photon Multiplicity Detector.

converter is used to reject the charged particles. A photon passing through lead converter initiate an electromagnetic shower and produce large signals on several cells of the sensitive volume of the detector. Charged hadrons normally affect only one cell and produce a signal resembling the minimum ionizing particles (MIPs). The principle (Fig. 4.2) behind the STAR-PMD is same as the pre-shower detectors used in WA93 and WA98 experiments at CERN SPS [10, 11]. The thickness of the converter is chosen to be $3X_0$, for the following reasons:

- the high conversion probability of the photons.
- the small transverse shower spread which minimize the shower overlap in high multiplicity environment.

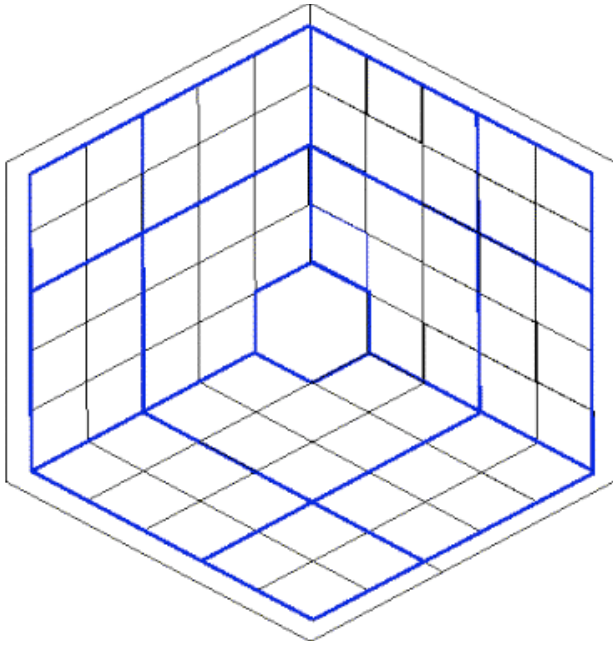

Figure 4.3: Schematic front view of Photon Multiplicity Detector.

The detector consists of a large number of honeycomb chambers known as cells, where each cell act as independent proportional counter. They are filled with the mixture of Ar and CO_2 gas in the ratio 70:30 because of insensitivity of the mixture to the neutrons. The choice of the technology used in detector was based on the following considerations:

- The low energy δ-electrons should be prevented from traveling to nearby cells and causing significant crosstalk among adjacent cells.

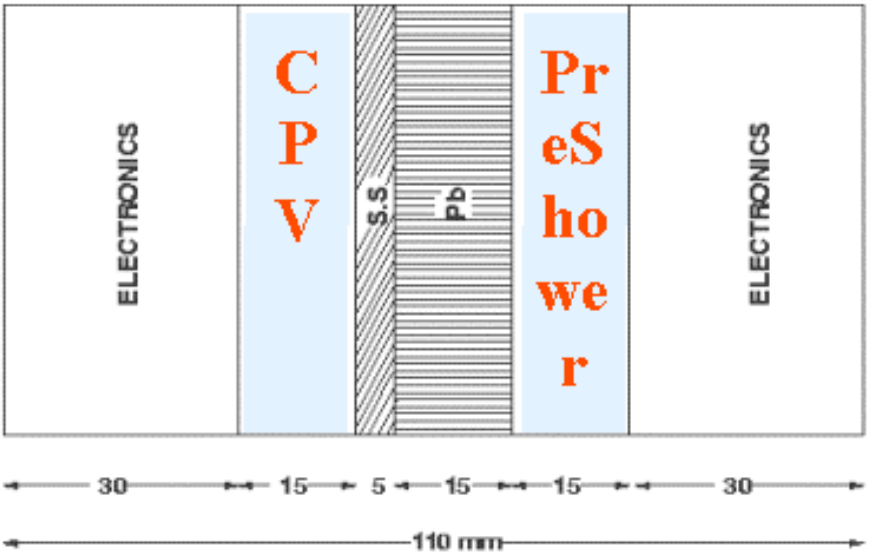

Figure 4.4: Cross-sectional view of Photon Multiplicity Detector.

- The detector material should be insensitive to neutrons. In a hydrogenous material neutrons tend to produce large signals due to recoil protons, which can mimic a photon signal.
- The multihit probability of the a cell must be small.
- The active volume of the detector should be thin and very close to the converter to minimize the transverse spread.
- The detector technology should be amenable to modular design with minimum dead spaces at the boundaries.
- The charged particles should be confined preferably to one cell so that the occupancy doesn't increase significantly.
- The efficiency of the detection of charged particles should be high.

4.2 Mechaniucal Design and Fabrication of the PMD

4.2.1 Mechanical Parts

The mechanical parts of the PMD are :

- Honeycomb Chambers.
- Lead converter plates.
- Support assembly.

4.2.2 Honeycomb Arrays

The honeycomb is fabricated using 0.2 mm thick copper sheets. Individual cells are formed using the die forming technique. The cells are arranged in a matrix of 24 x 24 in a high precision jig and spot-soldered to form the honeycomb. The honeycomb module has stiff 1 mm diameter copper studs which are attached by reflow soldering. These studs are situated at eight different locations, four at the corners of the rhombus and four at the centers of each edge. They are used to bring out the high voltage connections of the cathode onto the printed circuit boards (PCBs). They also act as guides for attaching the PCBs on both sides of the honeycomb array, which ensures proper alignment. Small notches are provided at the corners of each cell so that gas flow from one cell to another smoothly.

The copper honeycombs obtained from the manufacturer are cleaned using soap solution and water in ultrasonic cleaners and then dried in warm air. The honeycomb cathode structure is then dip-coated with high conductivity graphite paint. The basic parameters of a unit cell are listed in the Table 4.2.

Table 4.2: Basic parameters of a unit cell.

Parameter	Values
Shape	Hexagonal
Total No. Of Cells (CPV + Preshower)	82,944
Cell Cross-Section	1.0 cm^2
Cell Depth	0.8 cm

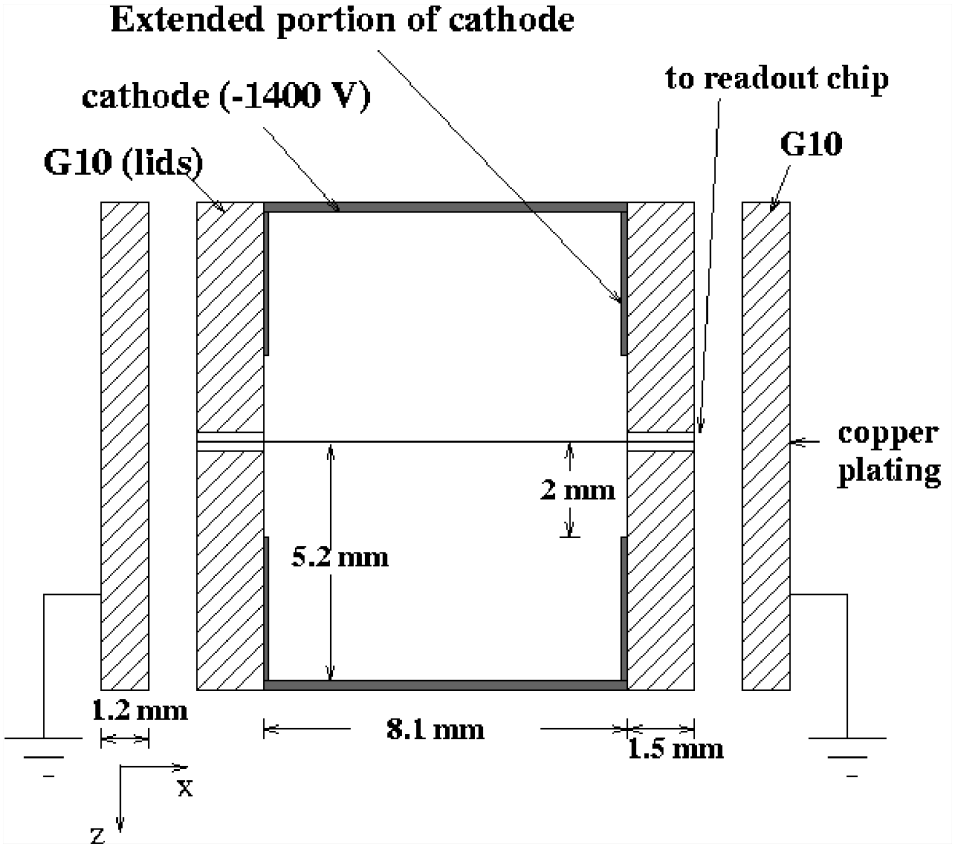

Figure 4.5: Cross-sectional view of an extended unit cell.

4.2.3 Honeycomb Chambers

The honeycomb chambers are fabricated in the form of unit modules made of unit cells. A unit module with extended cathode for the field shaping is shown in Fig. 4.5 . The unit module consists of a rhombus of side $\approx$ 260 mm containing a matrix of 24 x 24 cells. This shape has identical boundaries on all four sides. The wall thickness at the boundaries is half than that of the inner walls. When such arrays are joined together to form a super module, the half-thick boundary walls merge to form a seamless array of hexagonal cells. In order to keep the number of these independent proportional counters small and to reduce the dead area due to the boundaries, nine unit modules arranged in a 3×3 matrix are enclosed within a gas tight enclosure known as supermodule.

4.2.4 Unit Module Assembling

The Components of a unit module are shown in Fig. 4.6. The steps involved in the unit cell assembling are mounting the PCBs and wire insertion. The top PCB containing the electronic boards has solder islands at the centre of each cell with a 0.4 mm gold plated tungsten wire through a hole. Signal tracks from 64 cells are brought out to a 70 pin connector. The PCBs on the bottom side have only soldering islands without signal tracks, which serve as anchor points. The two PCBs are attached on the both sides of the honeycomb, aligned with copper studs. Gold plated tungsten wires are first cleaned and wounded onto a smaller spools. This wire is then stretched through the holes on the PCB, using a simple jig. The basic aim of the jig is to provide tension (30% of the elastic limit to the wire before soldering onto the island on the PCB. Other end of the hole, from where wires emerges, are then closed with a tiny amount of fast-setting epoxy to make them gas tight. This scheme prevents solder flux creeping into the cell and makes soldering easier. At the end of the assembly, all the soldered joints are tested for dry solder using a milli-ohmmeter.

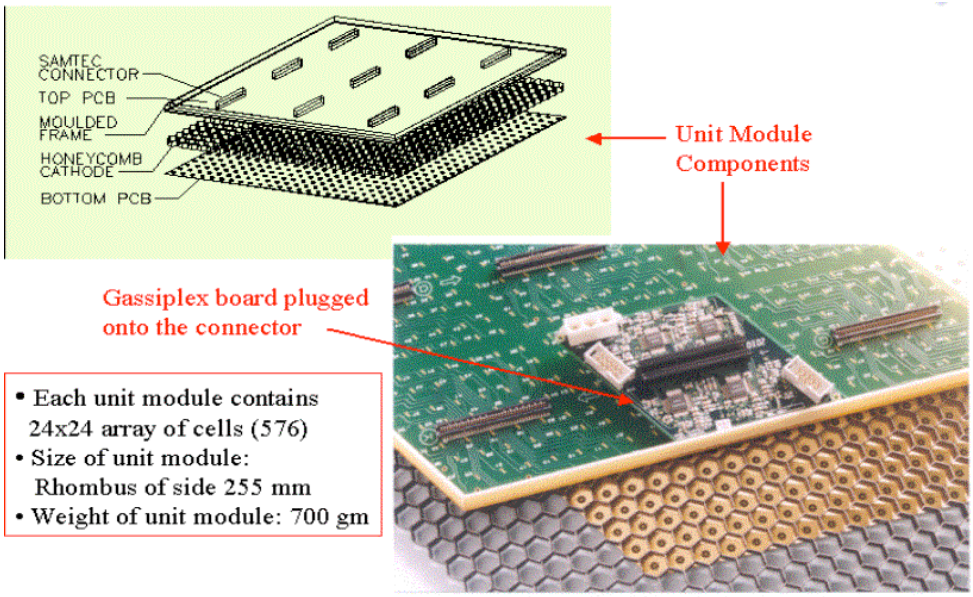

Figure 4.6: Various components of a unit module.

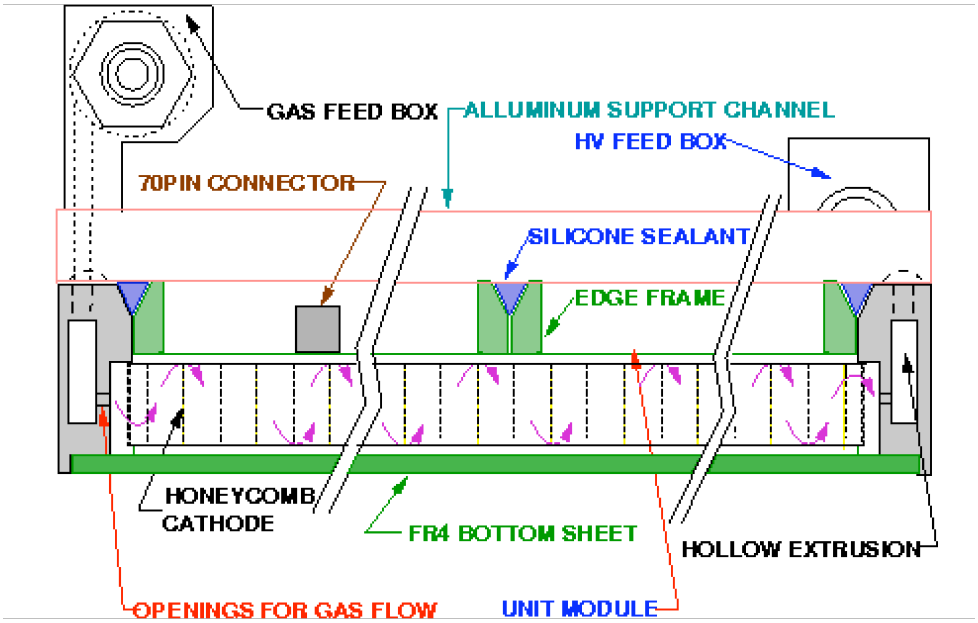

Figure 4.7: Schematic view of a section of a supermodule.

4.2.5 Supermodule Assembly

Supermodule is a gas tight chamber made of 3 mm thick FR4 grade glass epoxy plate as the base plate and a 7 mm thick and 25 mm high aluminium boundary wall. One cell at each corner of the supermodule is retained without anode wire to allow the screw to pass through a glued gas tight stainless steel tube for fixing the supermodule onto the support plate. The following steps are followed for assembling a supermodule:

1. A base frame made of 50 mm $\times$ 25 mm aluminium channels is fixed to the bottom to retain planarity of the bottom sheet during further operation. A Schematic of a section of supermodule showing different components such as gas inlet, high voltage feeder, support channels and sealing for gas tightness is shown in Fig. 4.7.

2. Nine assembled unit modules are placed to fill the inner area of the supermodule enclosure, leaving 1 mm gap on all the sides to accomodate general assembly tolerance and to provide insulation between the honeycomb cathode and the boundary (Fig. 4.8). Teflon spacers are inserted into the gap along the boundary to prevent any movement of unit modules and also to insulate honeycomb cathode from the

walls.

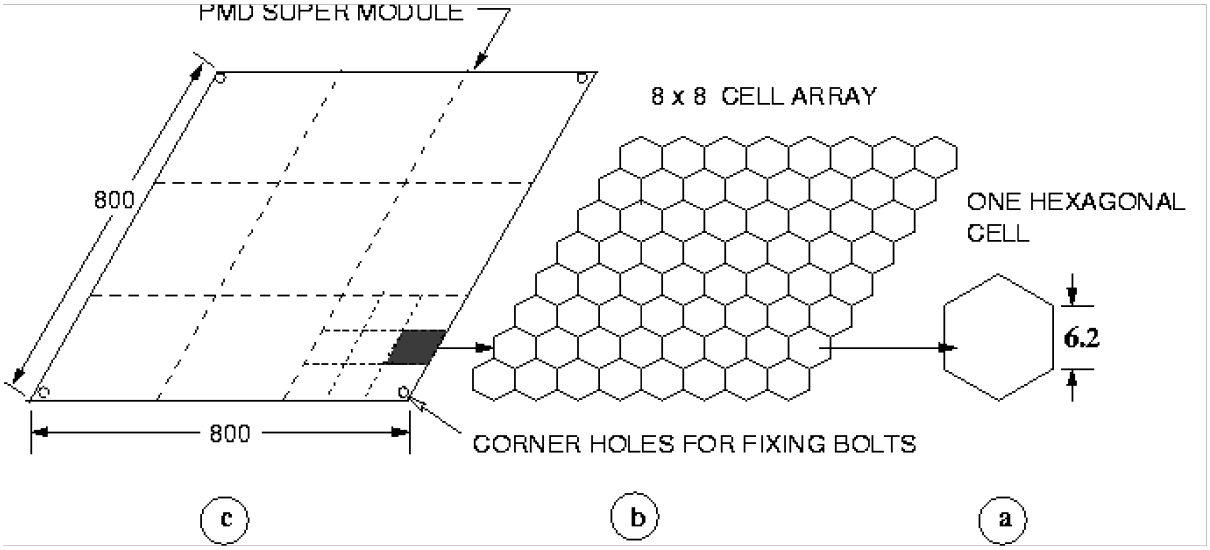

Figure 4.8: Assembly of super module from unit modules.

Five different types of the supermodules used in PMD, are listed in Table 4.3.

Table 4.3: Types of Supermodules

Type of Supermodule	Total Number
SM4 (with 4 UM)	6
SM5 (with 4 UM)	2
SM6 (with 4 UM)	10
SM8 (with 4 UM)	4
SM9 (with 4 UM)	2

The supermodules are further divided into two categories :

1. The Mirror type (M)
2. The Normal type (N)

Total 24 supermodules are used in the preshower and veto detector.

4.2.6 Supermodule Numbering Scheme

The CPV and pre-shower planes consist of 12 supermodules each with 4, 5, 6, 8, 9 unit modules. Therefore, it is important to adopt a numbering scheme to assign every channel

in a supermodule a particular address. The address of each channel is important for the software mapping of the detector. The numbering scheme for CPV and PMD are shown in Fig. 4.9 and 4.10 respectively. Supermodules in the CPV are numbered from 1 to 12 whereas in the PMD plane they are numbered from 13 to 24. Arrows associated with "i" and "j" in figures corresponds to the direction of row and column for every supermodule. One corner of the supermodule is marked to denote the origin of rhombus array. The x-axis increases toward the right and y-axis increases upward.

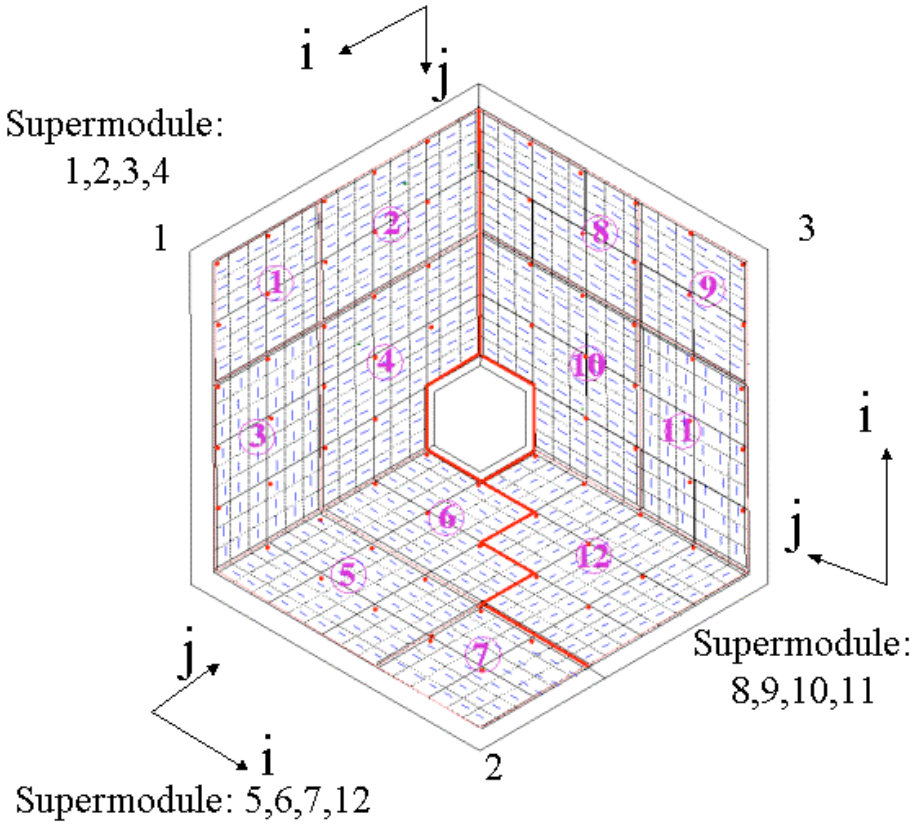

Figure 4.9: CPV plane numbering scheme, row and column scheme for the channels.

4.2.7 Lead Converter Plates

Rhombus shaped lead converter plates are sandwiched between the CPV and the pre-shower plane. The features of the converters are listed in the Table. 4.4

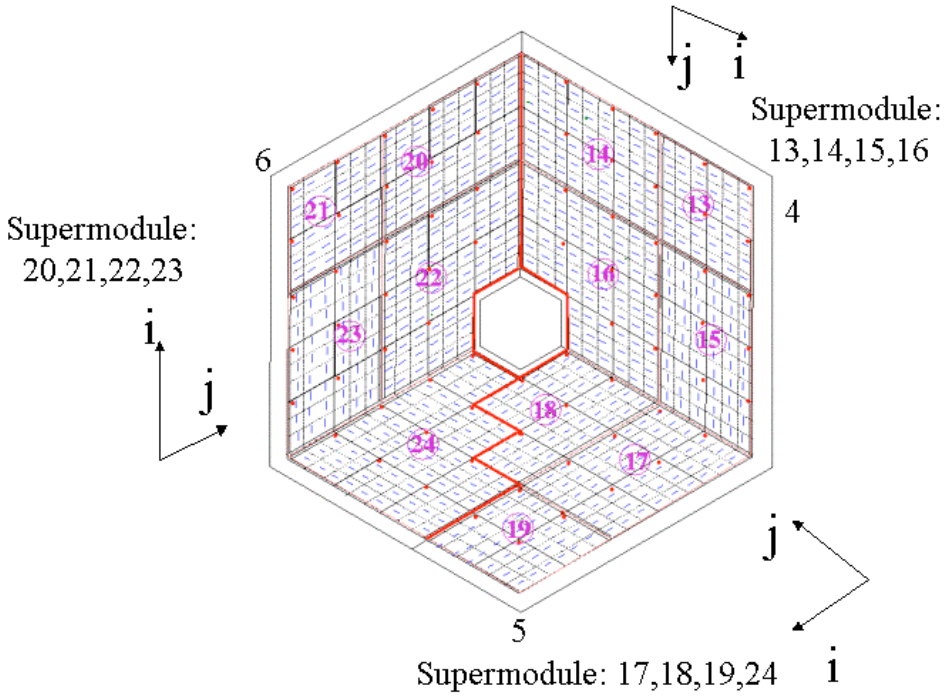

Figure 4.10: PMD plane numbering scheme, row and column scheme for the channels.

Table 4.4: Features of Lead Converters

Components	Features	Safety Aspects
4% Antimony Lead Plates,	Thickness of each plate: 15 mm Size: 254 Rhombus Weight: $\sim$ 10 Kg Each plate mounted on the SS support plate by two M6 socket head cap screws.	Each plate is painted with polyurethane paint after applying suitable primer.

4.2.8 Support Assembly

The drawing of the support assembly has been shown in Fig. 4.11. It has two parts :

1. The support plates .
2. The suspension movement mechanisms.

A 5 mm thick stainless steel plate is used to support the lead converter plates and supermodules in each half of the PMD. It has tapped holes for screws corresponding to holes positions in the lead plates and in the supermodules. The two halves of the detector are supported on the girders and hang freely in a vertical position. The support structure

allow both x- and z- movements of the detector. Each half of the detector can be separated for the access by a smooth independent movement control by limit switches. The service of the two halves are also independent. When fully open, the two halves provide sufficient clearance for the poletip support of the STAR magnet to move in.

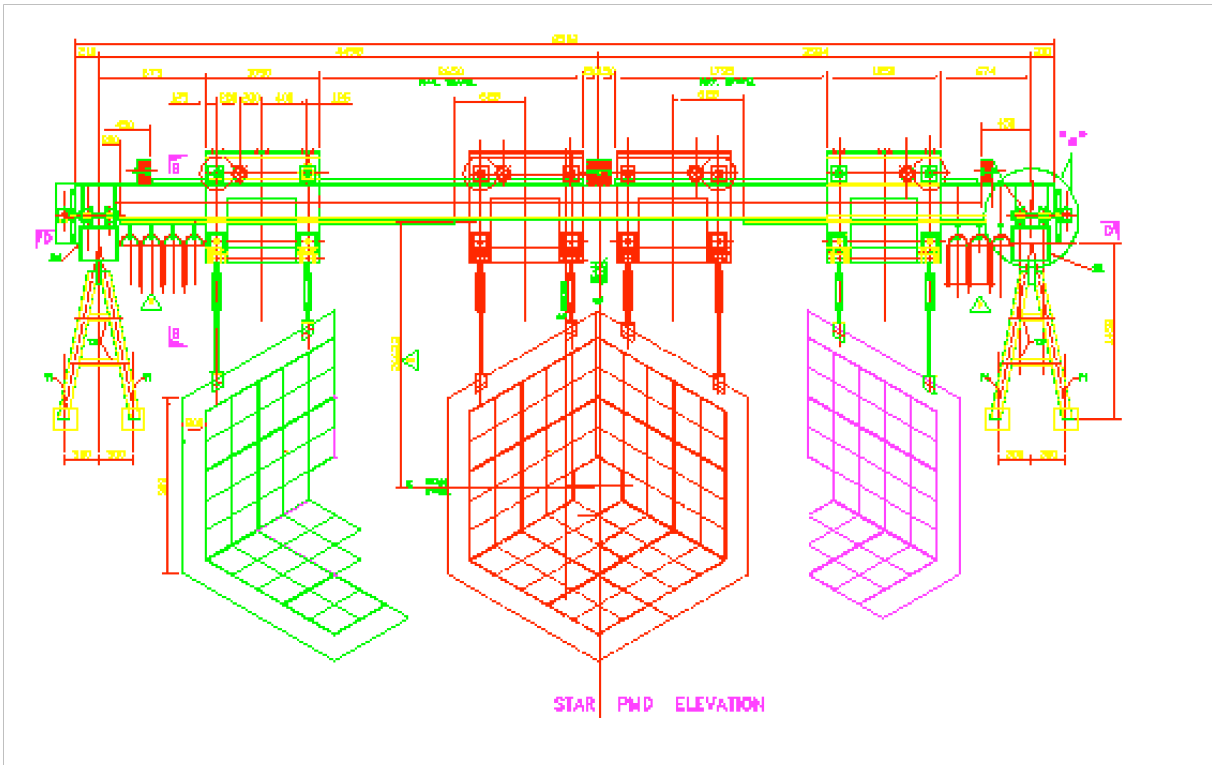

Figure 4.11: Schematic view of the PMD support assembly.

4.3 Gas System

The front and rear view of the gas system are shown in Figs. 4.12 and 4.13. The various aspects of the PMD gas system are given in Table 4.5.

4.4 Front End Electronics

The front-end electronics for processing the PMD signals is based on the use of 16-channel GASSIPLEX chips developed at CERN [12] which provides analog multiplexed signal and readout using the custom built ADC board (C-RAMS), which are obtained for CAEN,

Table 4.5: PMD gas system

Components	Features	Safety Aspects
1. Two Component Gas	Ar (70 %) + CO2 (30%)	Non inflammable,
2. Valves	Manual Control	Operating pressure is only 1 mbar above the atmospheric pressure,
3. Flow meters	Manual Monitoring Ar: 50 liters/hr CO2: 30 liters/hr	Total Flow rate 45 litres/hr.

Figure 4.12: Front view of the PMD gas system.

Italy. C-RAMS can handle a maximum of 2000 multiplexed signals. Considering the symmetry requirement of the detector hardware, the readout of the entire PMD has been divided into 48 chains. Each chain covers three unit modules and has 1728 channels. Each readout in the chain is driven by three components :

1. A Translator board.

2. 27 FEE boards each consisting of four GASSIPLEX chips.

Figure 4.13: Rear view of the PMD gas system.

3. A Buffer Amplifier board.

The Translator board (Fig. 4.14) converts the NIM levels of all control signals into the level required for the operation of GASSIPLEX chips. Operating voltage for these chips is ±2.75 V.

The cells in the unit modules are arranged in clusters of 8×8 cells connected to a 70-pin connector. This cluster of 64 cells is readout by a FEE (Fig. 4.15) having four GASSIPLEX chips. For the geometrical considerations, the FEE boards are also made in rhombus shape. To reduce the voltage drop across the long chain, a bus like design had been used to provide power to the FEE boards.

The buffer amplifier (Fig. 4.16) is used for the transmission of train of analog multiplexed signal to the readout module via a low impedance cable.

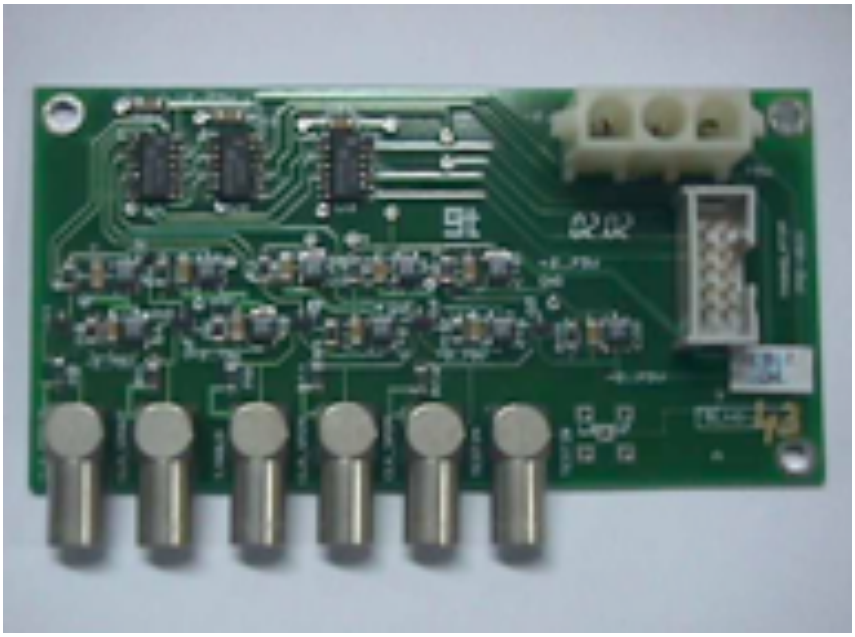

Figure 4.14: The Translator Board.

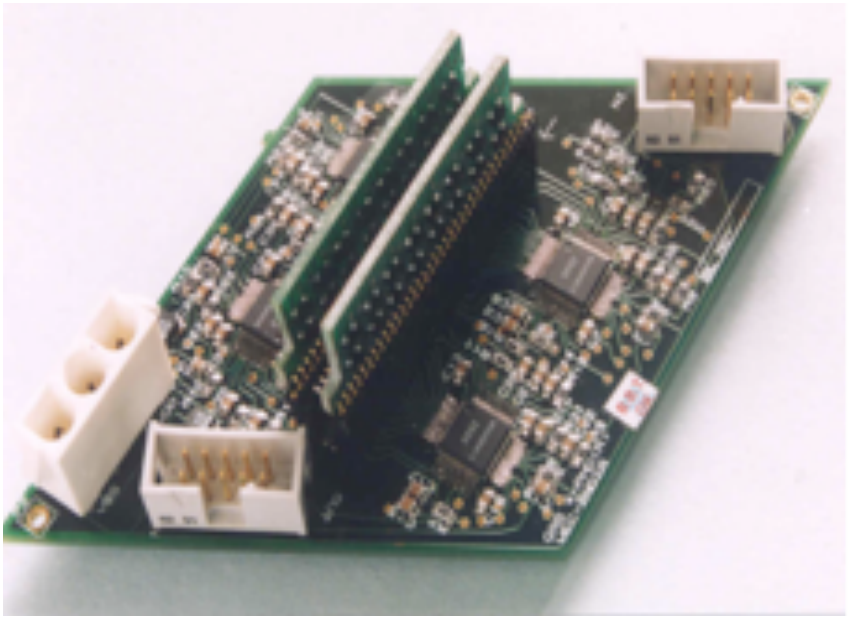

Figure 4.15: A FEE board containing four GASSIPLEX chips.

4.4.1 Noise/Pedestal

The minimum noise level of the electronics is known as pedestal. For proper quality control in the assembly of each FEE board, each GASSIPLEX chip is tested for full functionality of the each channel and also pedestals have been measured. All pedestals must lie in the negative range of values as it is an input polarity for the ADC. All the GASSIPLEX

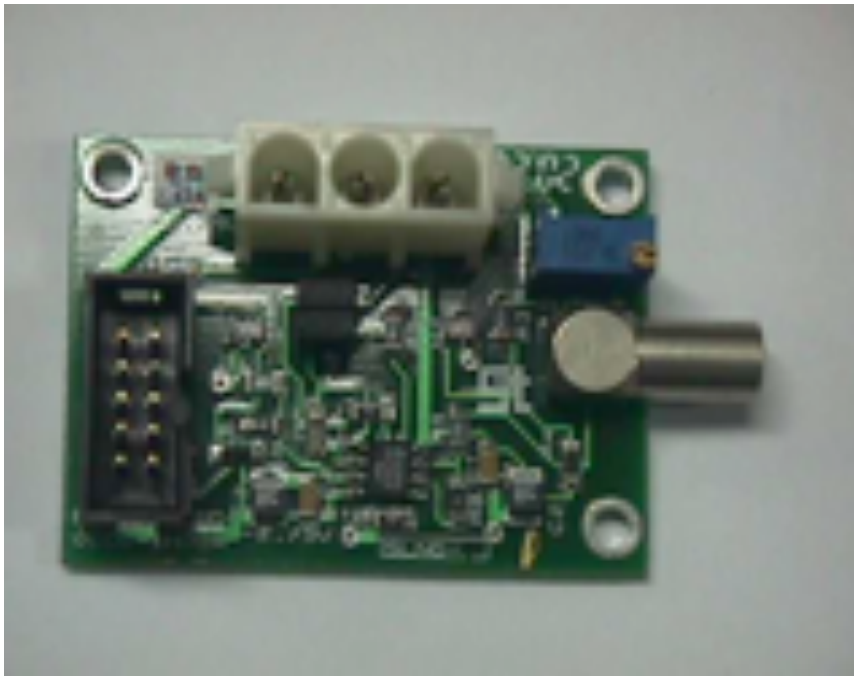

Figure 4.16: The Buffer Board.

chips are grouped into four pedestals classes and only the chips from same group has been mounted on the same FEE board. The FEE boards are then adopted in order to obtain a maximal homogeneity in the pedestal values.

The pedestal values for the each channels have been measured before connecting to the detector. The results for a daisy chain are shown in Fig. 4.17, in which top panel shows the pedestal value mean (Left) and sigma (Right) for each channel in one chain. All the boards have large mean values showing all are working. Right plot on the top shows the sigma values for all the channels in this chain. The distribution of sigma for all the channels is shown in bottom right panel. Similarly, the distribution of the mean pedestal values of all channels is given in bottom left panel.

4.5 PMD Trigger Scheme

Figure 4.18 shows the timing diagram for the trigger scheme in PMD. After the RHIC collision, L0 (Level zero trigger) arrives after 1.1 μs. However, the peaking time of the GASSIPLEX is only about 1 μs. This makes it necessary to use a pre-trigger which is

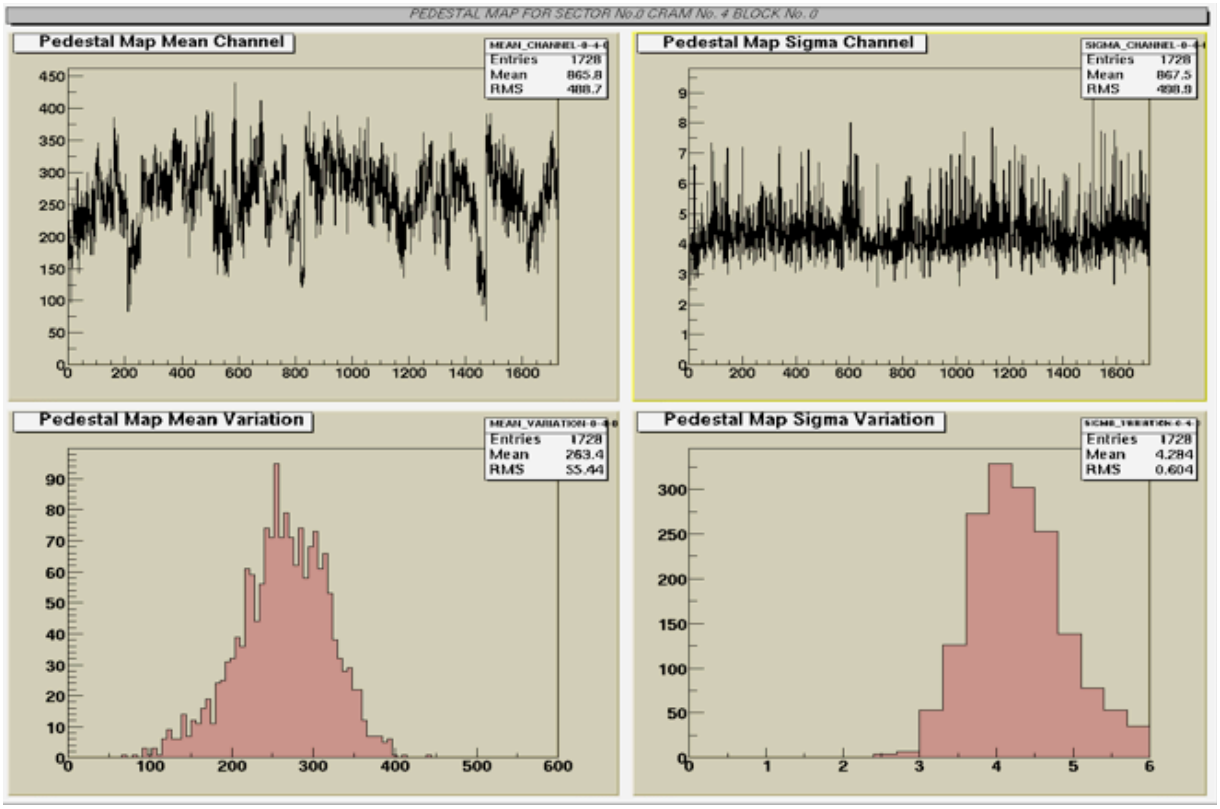

Figure 4.17: (Top Panel) (Left) Pedestal values verses channel numbers. (Right) Sigma values verses channel numbers. (Bottom Panel) (Left) Integrated pedestal (Right) Distribution of RMS values.

generated earlier and sent to GASSIPLEX to strobe the T/H. The STAR trigger scheme provides such a pre-trigger signal [13].

The signals on the T/H stage of the GASSIPLEX are held until the arrival of the validation of L0 to continue with digitization and data transfer. If L0 is not validated within specified time, a clear signal is generated which resets the GASSIPLEX and makes it available for taking the fresh interaction after about 10 μs.

However, when L0 comes within pre-defined time, T/H and busy signals are sent and if pre-trigger exists for this L0, then trigger is sent to sequencer which in turn generates the clock, T/H, clear, busy etc.

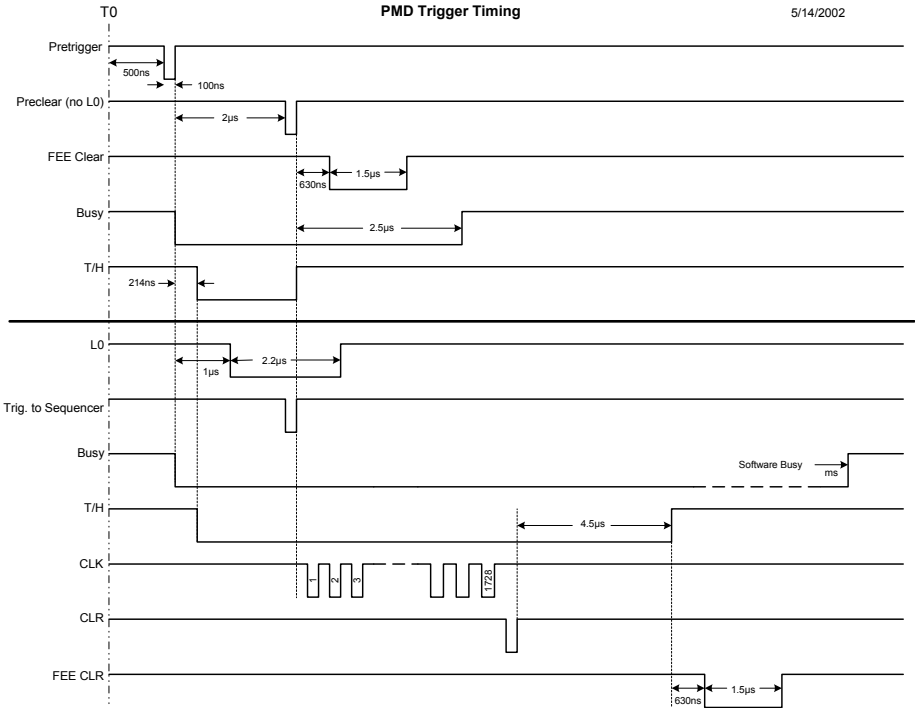

Figure 4.18: Timing diagram for the PMD pre-trigger and L0 validation.

4.6 PMD Data Analysis

The Photon Multiplicity Detector contains two planes, the charged particles veto (CPV) and pre-shower plane having lead converter of three radiation length thickness sandwiched between them. A photon passing through the lead converter in front of the pre-shower plane gives electromagnetic shower. The electrons and positrons coming out of the shower hit a number of cells in the pre-shower.

For analyzing the PMD data, data is cleaned by identifying and removing the hot and noisy channels. Hot channels are those channels, which fires abnormally high in the chain than the average frequency of firing during the run. After removing the hot channels cell-to-cell gain calibration is done to study the uniform response of the cell in η and ϕ. Then clustering has been done for the tracks hitting the cell in pre-shower plane. To distinguish the clusters due to photons and charged hadrons the following properties of photon clusters and charged hadron clusters are kept in mind,

- Charged particles do not produce shower in the lead converter and hit mostly a

single cell in the CPV and pre-shower plane, produce a cluster with single isolated cell in the preshower plane. However, photons produce electromagnetic shower in the lead converters and hit a number of cells in the pre-shower plane.

- The energy deposited by the charged particles is less than energy deposited by the photons in the sensitive volume of the preshower plane.

Also, the hadron is expected to be a MIP and deposit a minimum amount of energy ($\approx$ 2.5 KeV) [14, 15] and give signal only in the pre-shower plane. To get the good sample for the photon clusters it is necessary to study the efficiency and purity of the photon counting. The variation of photon counting efficiency and purity with various cuts decides the criteria for photon-hadron discrimination. Figure 4.19 shows the efficiency and purity of photon sample as a function of MIP E_{dep} cut. One MIP E_{dep} is equivalent to 2.5 KeV obtained from simulations [16]. The efficiency of the photon counting decreases from 70% to 30% with MIP E_{dep} cut and purity is varies from 40% to 50% with MIP E_{dep} cut. To select optimum value for purity and efficiency, it is appropriate to use the threshold values to be close to $3\times E_{dep}^{MIP}$. Similar studies of purity and efficiency as a function of N_{cell} suggest that the second condition for photon-hadron discrimination to be $N_{cell} > 1$ (number of cells).

To estimate the number of photons (N_γ) from the detected photon-like clusters (N_γ-like), we use the photon reconstruction efficiency (ϵ_γ) and purity (f_p) for the photon-like sample and defined as,

$$\epsilon_\gamma = N_{cls}^{\gamma.th}/N_{inc}^{\gamma} \tag{4.1}$$

$$f_p = N_{cls}^{\gamma.th}/N_{\gamma-like}, \tag{4.2}$$

where N_{inc}^{γ} is the number of incident photons from the HIJJING event generator, $N_{cls}^{\gamma.th}$ is the number of photon clusters above the photon-hadron discrimination threshold and $N_{\gamma-like}$ is the total number of clusters above the hadron rejection threshold. The photon multiplicity in the data is obtained as, $N_\gamma = (f_p/\epsilon_\gamma)N_{\gamma-like}$ [14,15,17]. Figure 4.20 shows the ϵ_γ and f_p for minbias Au+Au 200 GeV collisions. The photon reconstruction efficiency

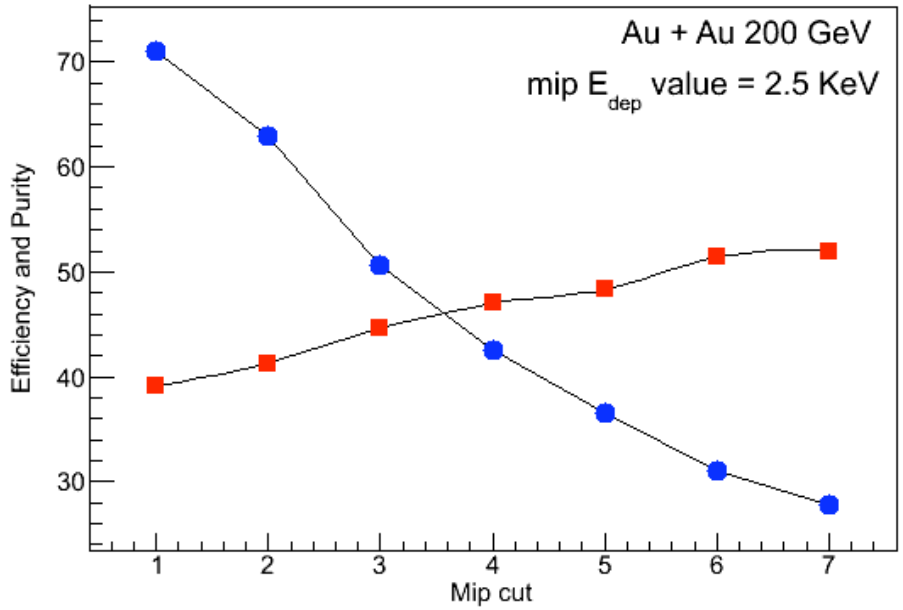

Figure 4.19: Efficiency (solid circles)and purity (solid squares) of photon counting as a function of MIP E_{dep} cut for Au+Au collisions at 200 GeV. One mip value is $\approx$ 2.5 KeV.

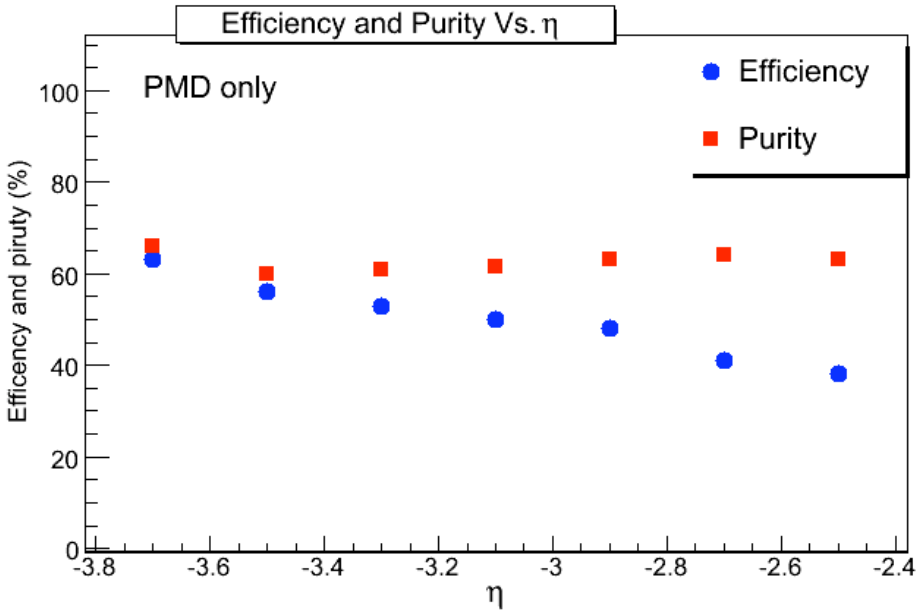

Figure 4.20: Pseudorapidity dependence of photon reconstruction efficiency and purity for Au+Au 200 GeV collisions.

varies from 40% at η=-2.3 to 60% at η=-3.7 for all the collisions centralities obtained in simulations. The purity of the photon sample is nearly constant for Au+Au collisions. More detail of various steps of photon clusters selection, charged particles discrimination and other data checks [16, 18].

4.6.1 Photon's Elliptic Flow

In relativistic heavy ion collision, the colliding nuclear matter emerges as flow pattern due to incompressibility of nuclear matter. Information about the equation of state for the nuclear matter can be extracted from the collective flow of nuclear matter deflected sidewards from the hot and dense region formed by overlap of colliding nuclei. Collective flow can be studied by measuring the momentum distribution of the produced particles. It has been suggested that if flow occurs in the plasma state, then the subsequent hadronization may affect the kinematic quantities of different particle species differently. It is, therefore, desirable to measure the anisotropy of different particle species in the final state. It is advantageous to study the event shape with photons because their transverse distribution and their parent pions are not affected by final state Coulomb effects.

Photons multiplicity measurements using the preshower PMD have already been used to study the collective flow at the SPS energies [19, 20]. The centrality dependence of the flow is sensitive to equation of state and shows different behavior for hadron gas and quark-gluon plasma. PMD has the advantage of studying flow in the forward rapidity region.

4.6.2 Data Selection

The Au+Au 200 and 62.4 GeV data sets [16, 23] are analyzed to study elliptic flow from the photon clusters collected by pre-shower Photon Multiplicity Detector in the STAR experiment. The minimum bias trigger is used for the collection of data, which is defined by the coincidence of two zero-degree calorimeters (ZDCs) [21] located at ± 18 from the centre of the interaction region along the beam line, using charged particles hits from an array of scintillators slates arranged in a barrel called the Central Trigger Barrel and two Beam-Beam Counters (BBCs) [22]. The events with collision vertex position lie within ± 30 cm from the centre of TPC along the beam pipe are selected. This analysis is done using the preshower plane of PMD. The supermodules in the preshower plane are numbered from 13 to 24. Only the run numbers, in which -1400V was applied to preshower plane are used. Some of the supermodules, not working properly in the run

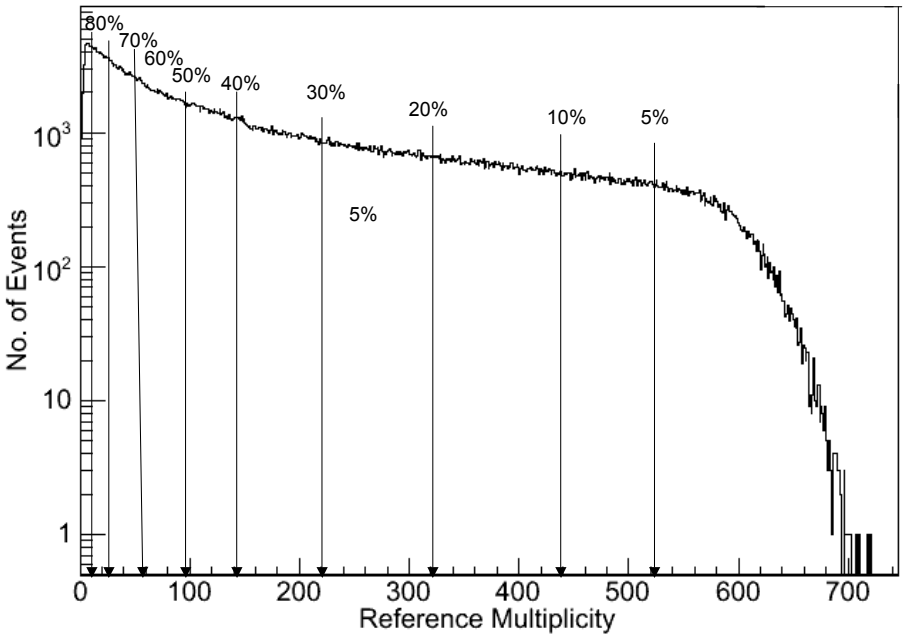

Figure 4.21: Reference multiplicity distribution for the Au+Au 200 GeV collisions used for the centrality selection.

declared 'bad' are not used in the analysis. The centrality of the events is defined by using the standard definition of centrality determination adopted in STAR. It uses uncorrected charged particles multiplicity within the pseudorapidity region $|\eta| < 0.5$ having more than 10 space points and distance of closest approach from the primary vertex 2 cm. The reason to use this region instead of $|\eta| < 1.0$ is to reduce the effect of detector acceptance and efficiency.

Figure 4.21 shows the reference multiplicity measured within $|\eta| < 0.5$. Vertical lines show the multiplicity cuts and corresponding fraction of cross-section. These multiplicity cuts decide the centrality classes used in analysis. Figure 4.22 shows the total number of clusters in PMD for Au+Au 200 GeV Collisions. Multiplicity distribution for various centralities are shown in figure.

4.7 Results and Discussion

The elliptic flow using two-particle correlations ($v_2\{2\}$) has been calculated using two methods :

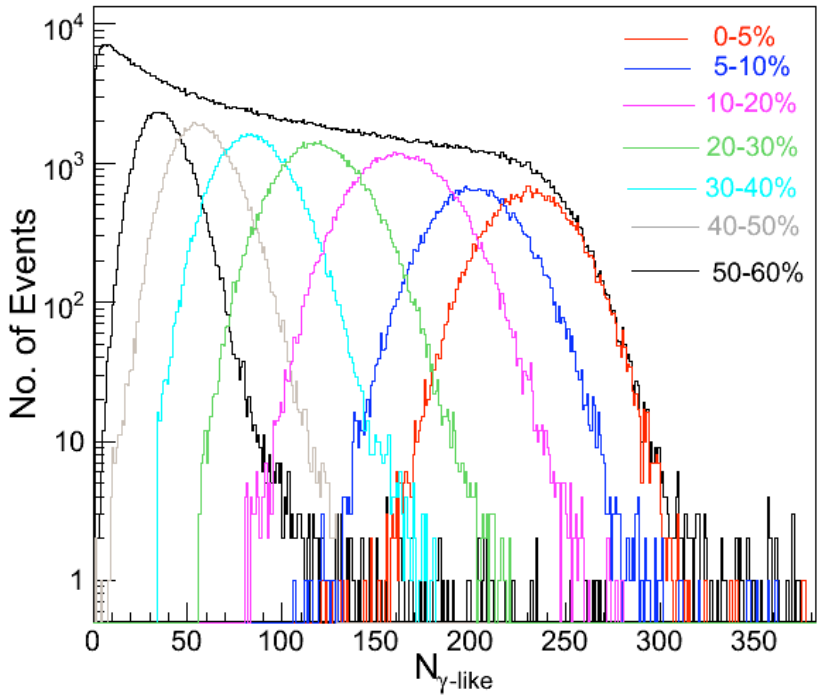

Figure 4.22: Total numbers of clusters in PMD for Au+Au 200 GeV collisions. Multiplicity distribution of different centralities are shown.

(1). Generating function method.

(2). Q-Cumulant method.

4.7.1 Elliptic Flow in Au+Au 62. 4 GeV

The number of good supermodules used for the analysis and the MIP value for each supermodule are listed in Table 4.6 [24].

Table 4.6: Super-Modules and the MIP values.

S.No.	SM Number	MIP value
1	14	46
2	15	87
3	16	67
4	17	86
5	18	40
6	19	165
7	21	102
8	22	79
9	23	98

The cuts used for photon-hadron discrimination are :

1. N_{cell} >1 .
2. ADC >3*MIP

The XY display of hits for the Pre-shower plane for the pseudorapidity region $-2.3 > \eta > -3.8$ is shown in Fig. 4.23. The blank spaces shows the bad supermodules, not used in the analysis. Figure 4.24 shows pseudorapidity and azimuthal distribution of the photons clusters used in the analysis. The number of event used the analysis are ∼321544.

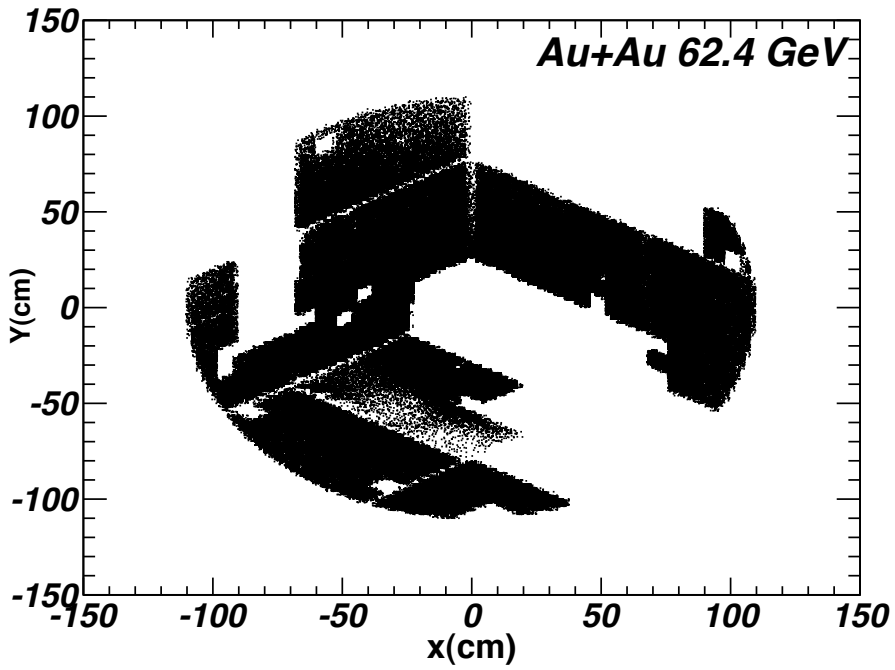

Figure 4.23: XY display of hits on preshower plane for the region $-2.3 > \eta > -3.8$ in Au+Au 62.4 GeV.

Figure 4.25 shows the centrality dependence of $v_2\{2\}$ calculated from Generating function method and Q-Cumulant method. The elliptic flow increases while going from central to peripheral collisions. Both the methods give the same values within errors for $v_2\{2\}$. The azimuthal corrections are applied to the data for the Q-Cumulant method while the Generating function method gives very small values for the acceptance corrections that lies within errors bars.

Also an attempt has been made to get symmetric azimuthal distribution for the photon clusters by putting cut on pseudorapidity to get more consistent values of elliptic flow.

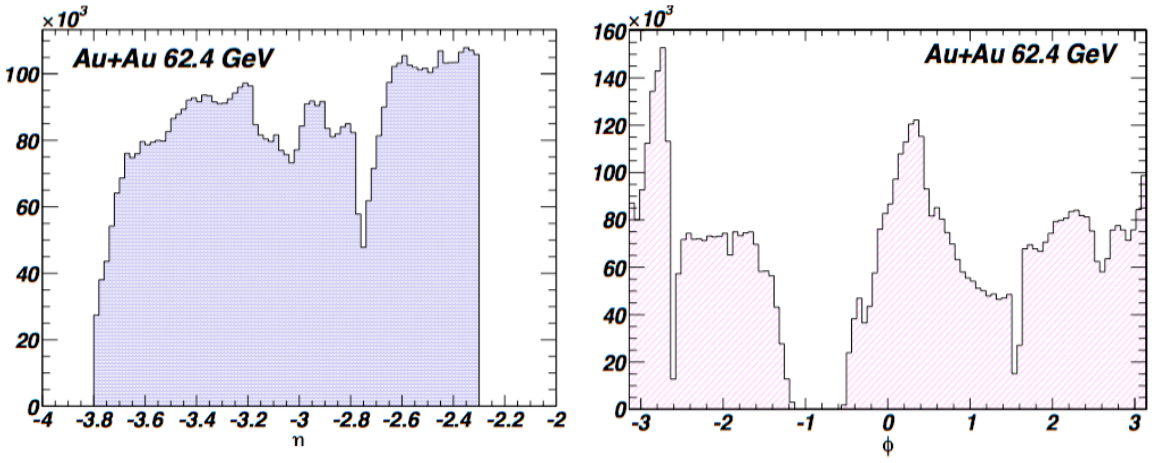

Figure 4.24: (Left) Pseudorapidity distribution and, (Right) Azimuthal distribution of the photons clusters for $-2.3 > \eta > -3.8$ in Au+Au 62.4 GeV.

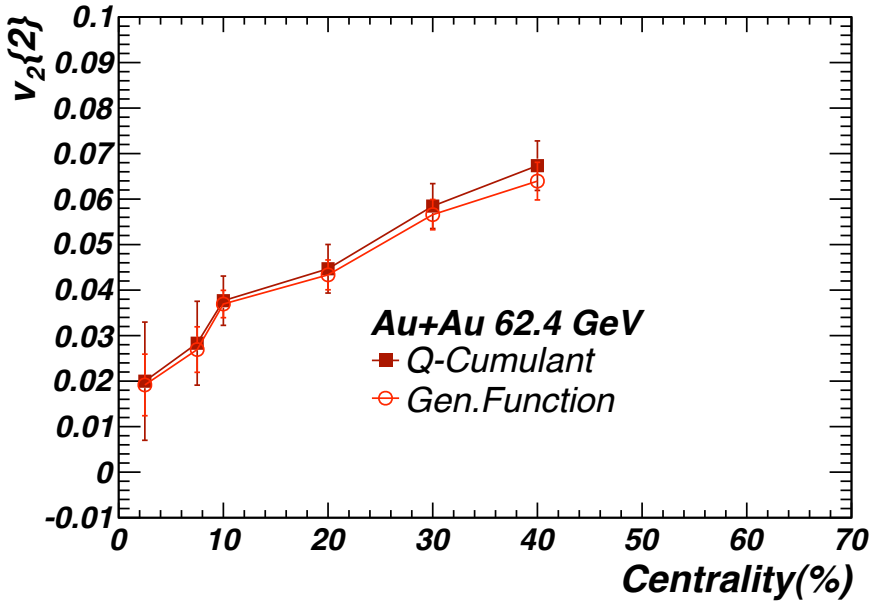

Figure 4.25: Centrality dependence of $v_2\{2\}$ for $-2.3 > \eta > -3.8$.

Figure 4.27 shows the pseudorapidity and azimuthal distributions of the photon clusters for the pseudorapidity region $-2.75 > \eta > -3.8$. Centrality dependence of the elliptic flow calculated in this region is shown in Fig. 4.28. The elliptic flow calculated for the pseudorapidity region $-2.75 > \eta > -3.8$ increases as the centrality decreases. The $v_2\{2\}$ for the peripheral collisions closely shows the same values as calculated for pseudorapidity region, $-2.3 > \eta > -3.8$ shown in Fig. 4.25. The $v_2\{2\}$ has been shown only for centrality

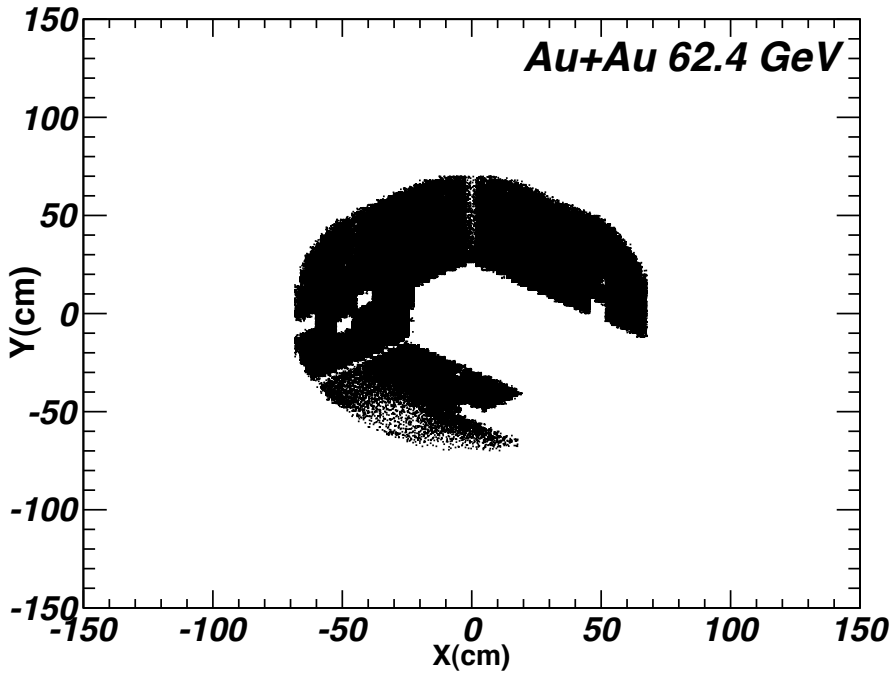

Figure 4.26: XY display of hits on preshower plane for the $-2.75 > \eta > -3.8$.

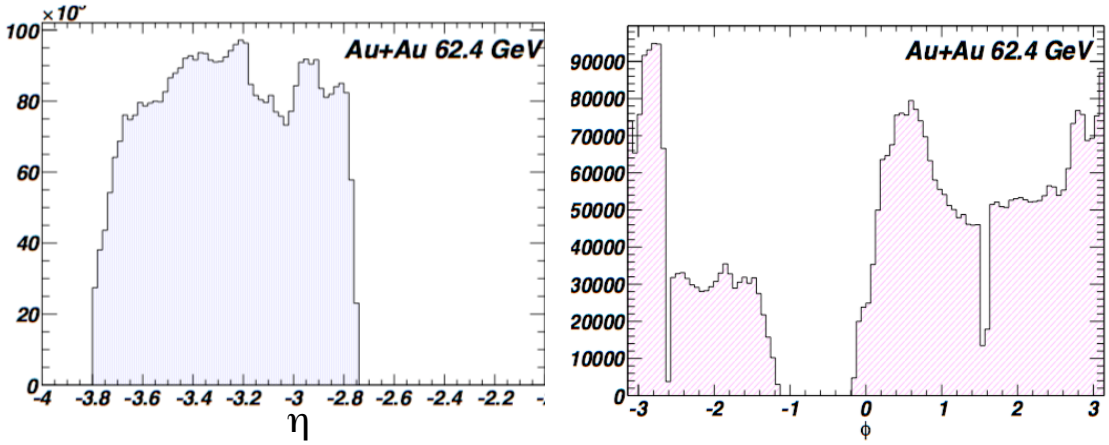

Figure 4.27: (Left) Pseudorapidity distribution and, (Right) Azimuthal distribution of the photons clusters for $-2.75 > \eta > -3.8$.

0-5% to 40-50% , because number of events become less for the most peripheral collisions due to low statistics.

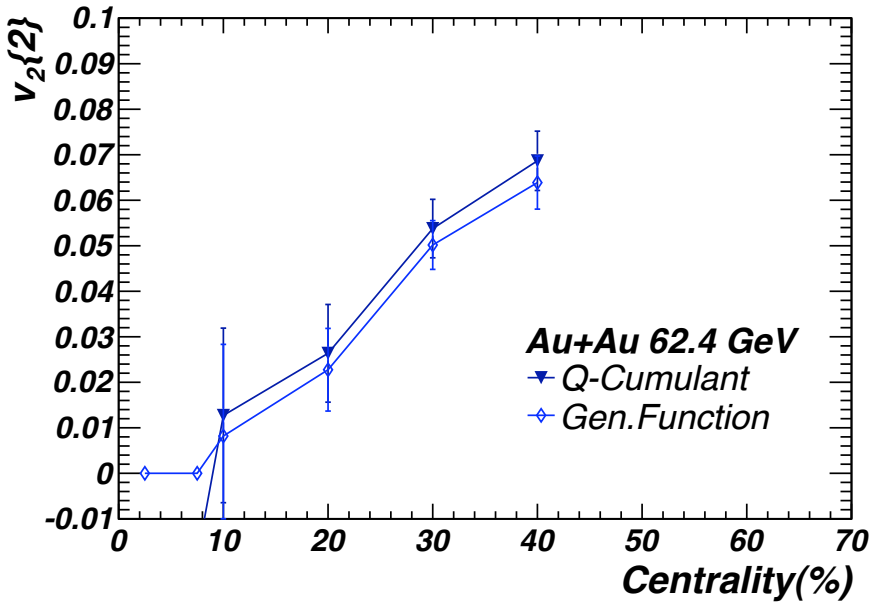

Figure 4.28: Centrality dependence of $v_2\{2\}$ for $-2.75 > \eta > -3.8$.

4.7.2 Elliptic Flow in Au+Au 200 GeV

The number of good supermodules used to analyze Au+Au 200 GeV data and the MIP value for each supermodule are listed in the Table 4.7 [25]. The same cuts are used for the photon-hadron discrimination as used for 62.4 GeV collisions and the number of events used are ∼374825.

Table 4.7: Super-Modules and the MIP values.

S.No.	SM Number	MIP value
1	1	135
2	5	128
3	7	96
4	9	60
5	10	88
6	11	140

The XY display of hits for Preshower plane in the pseudorapidity region $-2.3 < \eta < -3.8$ is shown in Fig. 4.29. The pseudorapidity and azimuthal distribution on the photon clusters is shown in Fig. 4.30. The azimuthal distribution of the photons clusters is not flat due to number of bad supermodules. The Au+Au 200 GeV data gives very high values

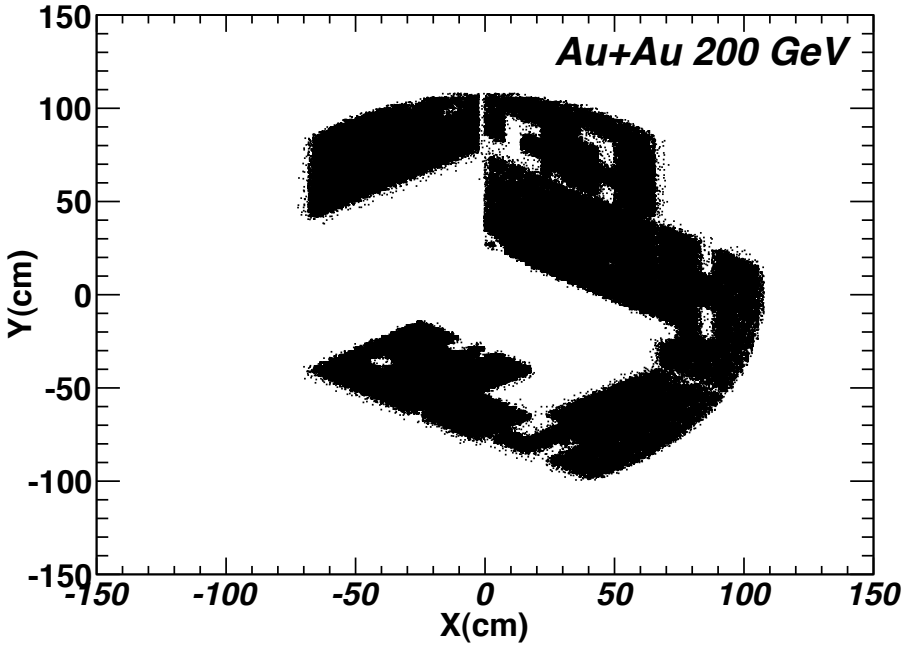

Figure 4.29: XY display of hits in the preshower plane in the pseudorapidity region $-2.3 < \eta < -3.8$.

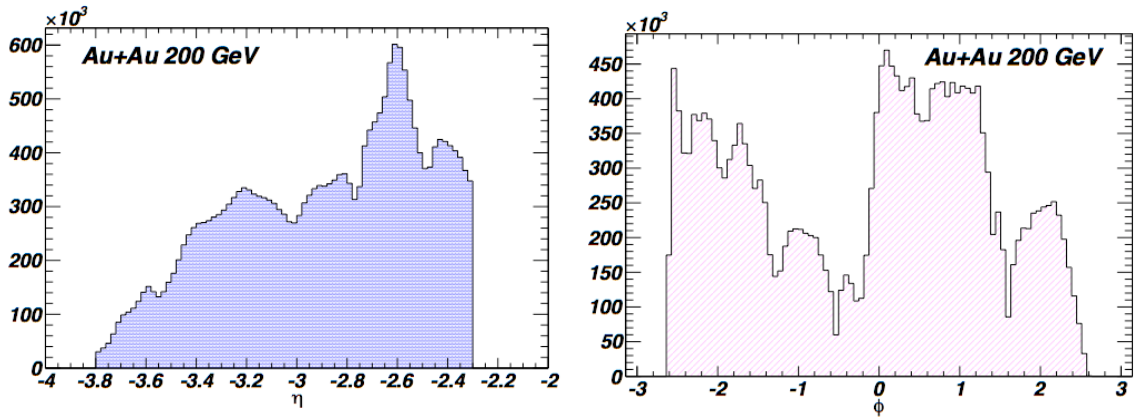

Figure 4.30: (Left) Pseudorapidity distribution and, (Right) Azimuthal distribution of the photons clusters for $-2.3 > \eta > -3.8$ in Au+Au 200 GeV.

for the $v_2\{2\}$ for the complete data set [25]. So run-by-run study of the cumulants has been done to checkout the bad run. Figure 4.31 shows the run number dependence of the two-particle cumulant. The cumulant shows very high value for the a file corresponding to run number 8133041. Therefore, the final $v_2\{2\}$ shown in Fig 4.32 has been calculated leaving the data corresponding to the run number 8133041. The most central collisions

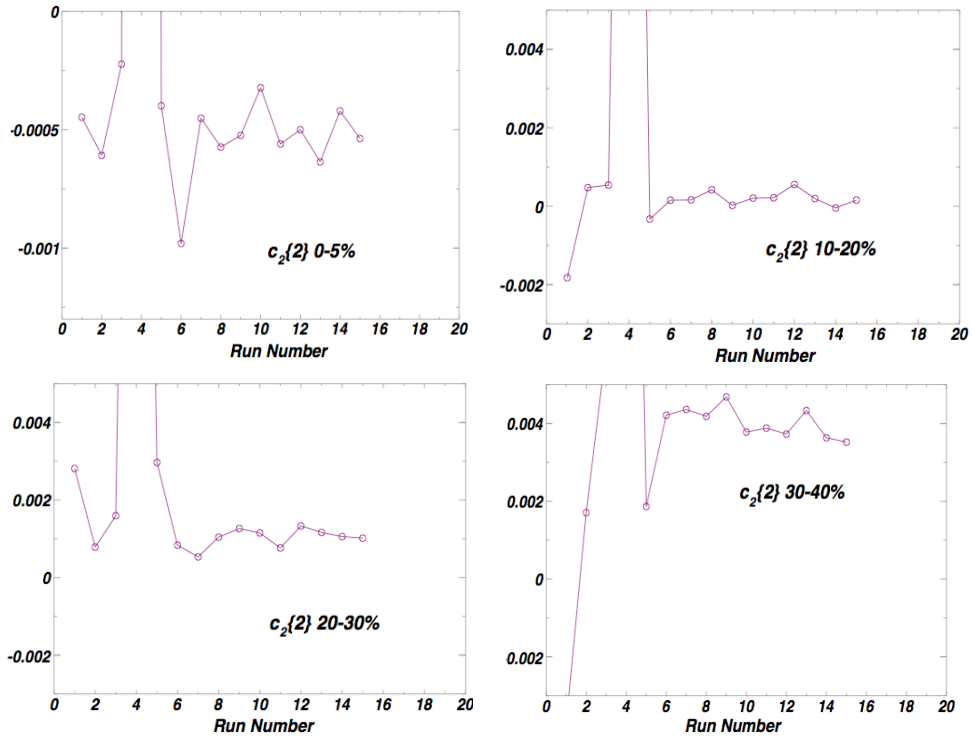

Figure 4.31: Dependence of two-particle cumulants on the run number for different centralities.

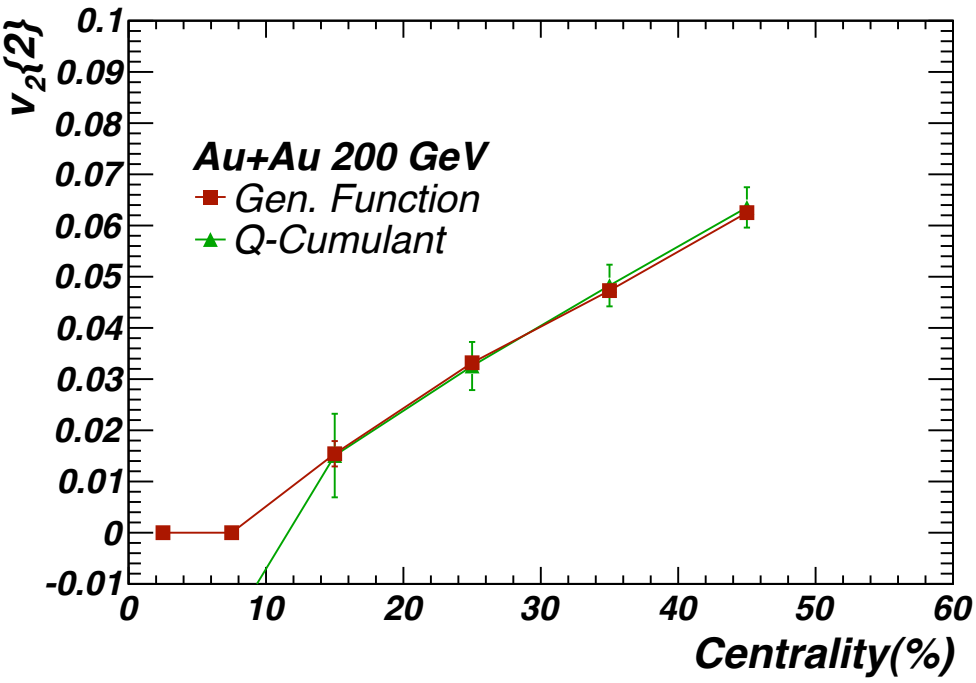

Figure 4.32: Centraiity dependence of $v_2\{2\}$ for Au+Au 200 GeV collisions.

show imaginary/zero values of the $v_2\{2\}$ and increase while going toward mid central collisions. The $v_2\{2\}$ for the most peripheral collisions is not shown due to low statistics.

4.7.3 Energy Dependence of Photons Flow

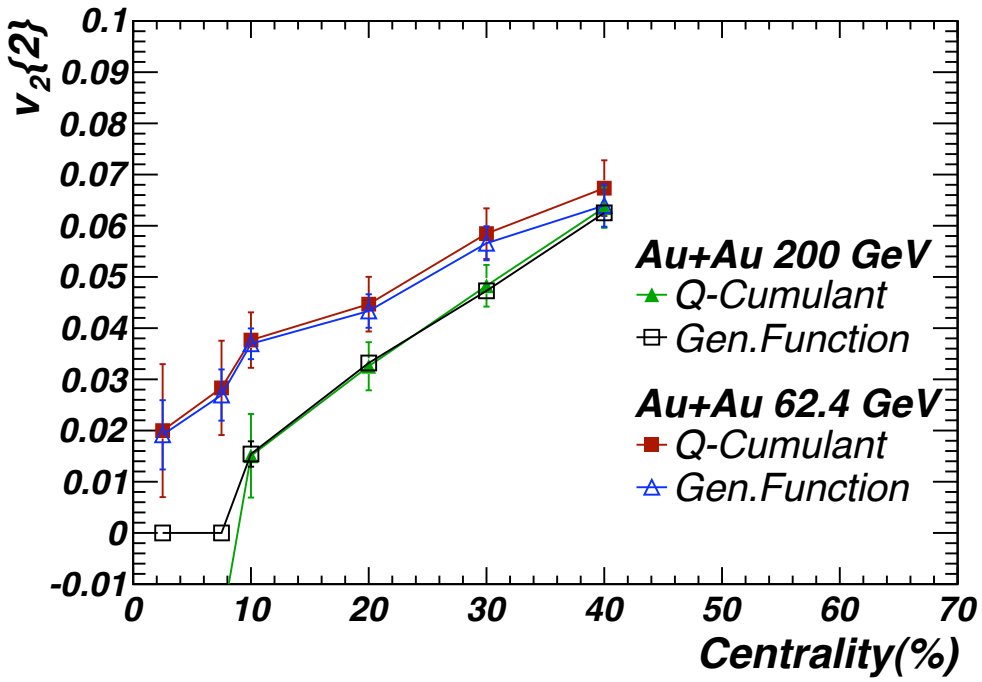

Figure 4.33: Comparison of $v_2\{2\}$ in Au+Au collisions at 200 and 62.4 GeV.

Figure 4.33 shows the comparison of $v_2\{2\}$ in Au+Au collisions at 200 and 62.4 GeV. $v_2\{2\}$ for 62.4 GeV collisions is little higher than collisions at 200 GeV in central collisions but the values are same within errors for the mid-peripheral collisions.

4.8 Summary

The $v_2\{2\}$ has been calculated for the Au+Au 200 and 62.4 GeV collisions using the data [24, 25] for the Photon Multiplicity Detector using Generating function and Q-Cumulant method. The elliptic flow calculated from two-particle correlation ($v_2\{2\}$) shows the increase from central to peripheral collisions for Au+Au collisions at 200 and 62.4 GeV with both the energies showing the nearly same values within errors.

The elliptic flow from the four-particle correlation ($v_2\{4\}$) has not been shown because of low statistics of the data which doesn't allow to calculate the four-particle cumulants. Therefore, large data sets and better azimuthal coverage are required for the detailed study of the elliptic flow. The STAR has collected large data for the Au+Au 200 GeV collisions recently in Run 10. Acceptance is reasonably good for the run to study the elliptic flow.

Bibliography

[1] M. M. Aggarwal *et. al.*, Nucl. Instrum. & Meth. A, **499**, 751 (2003).

[2] Photon Multiplicity Detector for STAR: technical proposal, VECC Internal report, VECC/EQC/00-04, May 2000 (revised: January 2001).

[3] A preshower PMD for STAR experiment, STARNote310, (1997).

[4] STAR FTPC Proposal, MPI-PhE/98-3, (1998).

[5] M. M. Aggarwal *et. al.* [WA98 Collaboration], Phys. Rev. C **64**, 011901 (2001).

[6] B. K. Nandi, T. K. Nayak, B. Mohanty, D. P. Mahapatra and Y. P. Viyogi, Phys. Lett. B **461**, 142 (1999).

[7] B. Mohanty, D. P. Mahapatra and T. K. Nayak, Phys. Rev. C **66**, 044901, (2002).

[8] B. Mohanty, Int. J. Mod. Phys. A **18**, 1067 (2003).

[9] M. M. Aggarwal, G. Sood and Y. P. Viyogi, Phys. Lett B **638**, 39 (2006).

[10] M. M. Aggarwal *et. al.*, Nucl. Instrum. & Meth. A **372** 143 (1996).

[11] M. M. Aggarwal *et. al.*, Nucl. Instrum. & Meth. A **421** 558 (1999).

[12] ALICE HMPID Technical Design Report, CERN/LHCC 99-32, (1999).

[13] STAR RICH Proposal, YRHI-98-22 (1998) ; G. J. Kunde *et. al.*, STAR Note SN0349, (1998).

[14] M. M. Aggarwal *et. al.*, Nucl. Instrum. & Meth. A **499** 751 (2003).

[15] M. M. Aggarwal *et. al.*, Nucl. Instrum. & Meth. A **488** 131 (2002).

[16] Ph.D. Thesis, Lokesh Kumar (1999), http://drupal.star.bnl.gov/STAR/theses .

[17] J.Adams *et al.* [STAR Collaboration], Phys. Rev. Lett. **95** 062301 (2005) ; P. K. Netrakanti, Ph. D. Thesis;, N. Gupta, Ph. D. Thesis and S. M. Dogra, Ph. D. Thesis ; http://drupal.star.bnl.gov/STAR/theses

[18] Ph.D. Thesis, Monika Sharma (1997), http://drupal.star.bnl.gov/STAR/theses .

[19] M. M. Aggarwal *et. al.* [WA 93 Collaboration], Phys. Lett. B **403**, 390 (1997).

[20] G. C. Mishra , P.hD. Thesis, Utkal University, (1999).

[21] C. Alder *et. al.*, Nucl. Instrum. & Meth A **470** 488 (2001).

[22] F. S. Bieser *et. al.*, Nucl. Instrum. & Meth A **499** 766 (2003).

[23] Neeraj Gupta, M. Sharma. S. Dogra, S. Singh, N. K. Pruthi and L. Kumar, "Systematic study of photon production at forward rapidity in STAR". to be published in January issue, 2010 Indian Journal of Physics.

[24] J. Adams *et al.* [STAR Collaboration], Phys. Rev. Lett. **95**, 62301 (2005).

[25] B. I. Abelev *et al.* [STAR Collaboration], Nucl. Phys. A **832**, 134 (2009).

Chapter 5

Eccentricity Models

Elliptic flow has been found to be very important for understanding the initial conditions in the relativistic heavy ion collisions [1–3]. The elliptic flow calculated from different methods shows 20% spread in its values (Fig. 5.1) [4]. The better accuracy for v_2 measurements is required for the comparison with relativistic viscous hydrodynamical model calculations because 30% uncertainty in the elliptic flow values leads to 100% uncertainty in the ratio of shear viscosity to entropy [5]. The non-flow has been found to contribute to the elliptic flow calculated from the different methods [6]. Recently, It has been studied that fluctuations in elliptic flow may affect the measured values of the elliptic flow [7, 8]. It has been also recognized that some measurements are relative to the participant plane and some to the reaction plane. Figure 5.2 shows schematic view of the participant plane and the reaction plane for a nucleon-nucleon collision. The reaction plane is spanned by the impact parameter and the beam direction. The participants are those constituents which take part in primary interactions. The minor axis of the participant zone and the beam direction define the participant plane.

The centrality dependence of elliptic flow (v_2) at SPS [9] doesn't show perfect agreement with hydrodynamical models. However, RHIC data shows agreement to some extent with hydrodynamical models under particular combination of dynamical modeling *i.e.*, initial conditions from Glauber Model, perfect fluid Quark Gluon Plasma core and dissipative hadronic corona [10]. But this doesn't represent the centrality dependence of

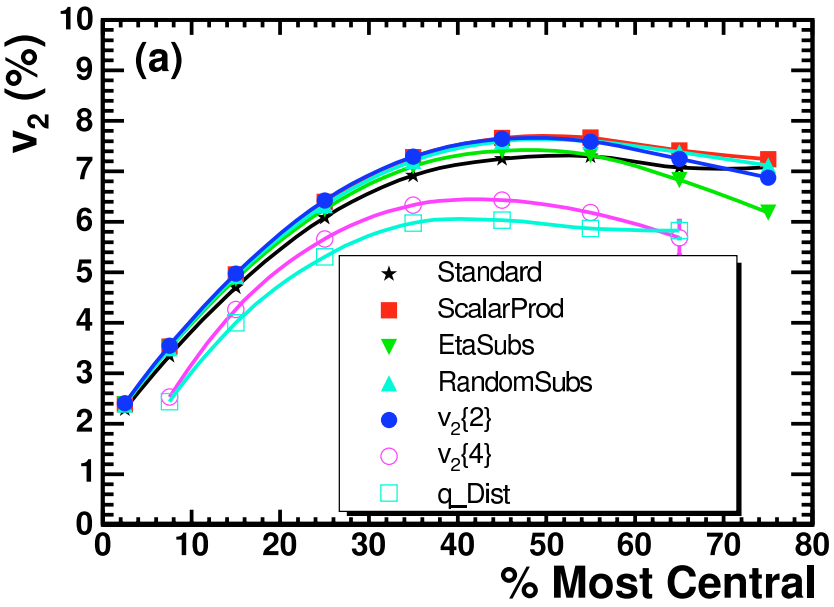

Figure 5.1: Charged hadron v_2 *vs.* centrality from various methods.

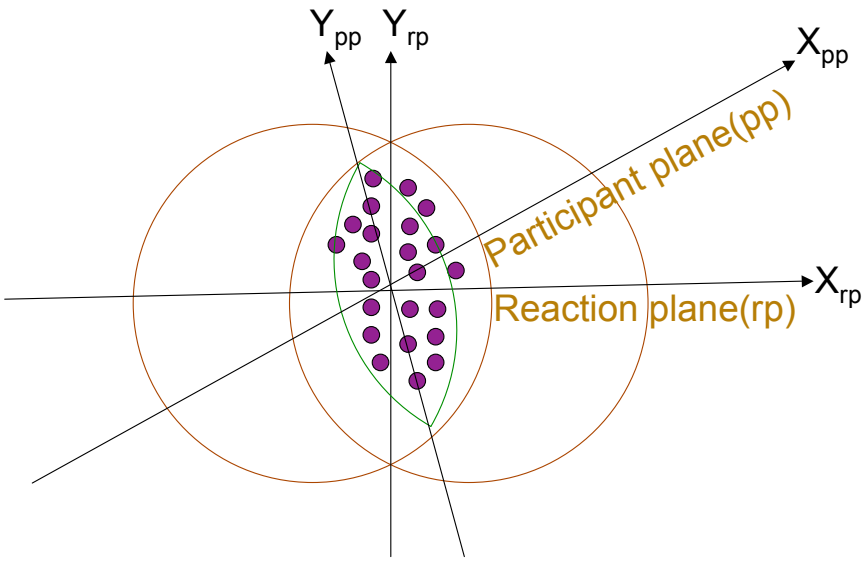

Figure 5.2: Schematic view of a nucleon-nucleon collision in a plane transverse to beam direction. The dots represent participant nucleons. Due to fluctuations, overlap zone shift w.r.t. to reaction plane (rp).

elliptic flow in hydrodynamical model. This could be due to the absence of initial state fluctuations in the hydrodynamical model. The fluctuations in v_2 may be due to the fluc-

tuations in initial spatial anisotropy of the overlap region, which can't be calculated in experiments. The measurement of fluctuations in initial spatial anisotropy can be made by using different models. So, to find the model which better represents the data and initial state fluctuations we use the following models:

1. Monte-Carlo Glauber Model for Nucleons as Participants (MCG-N).
2. Monte-Carlo Glauber Model for Constituent Quarks as Participants (MCG-Q).
3. Color Glass Condensate (CGC) based Monte-Carlo Model (fKLN-CGC).

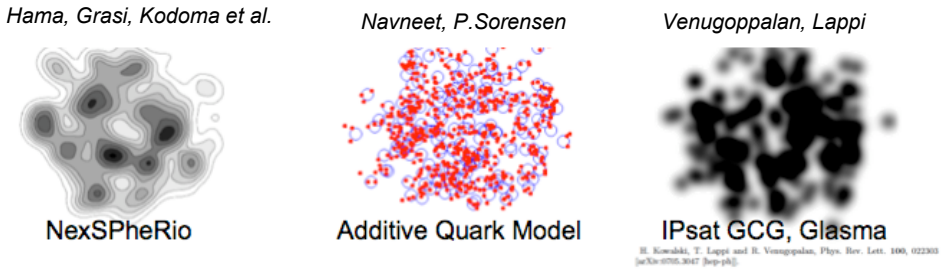

Figure 5.3: Geometrical representations of the eccentricity models.

Geometrical representations of the these eccentricity models are shown in Fig. 5.3. The details of these models are described below:

5.1 Monte-Carlo Glauber Model for Nucleons as Participants (MCG-N)

The Monte-Carlo Glauber Model for Nucleons as Participants is based on the following assumptions [11], which are appropriate for heavy ion collisions:

1. The collisions are characterized in terms of classical impact parameter (b).
2. The nucleons are assumed to move in a straight line along the beam axis.
3. A fix transverse interaction range is used which is determined by nucleon-nucleon total inelastic cross section (σ_{inel}^{NN}) in free space.

Using these assumptions the charged particles multiplicities are obtained using the Wood-Saxon density distribution and negative binomial multiplicity distribution for N+N collisions which are described below:

The most important inputs to these models are nucleon densities measured in low energy electron scattering experiments and the energy dependence of the inelastic nucleon-nucleon cross section. The following Woods-Saxon nucleon density distribution is used:

$$\rho(r) = \rho_0 \left\{ 1 + exp\left[\frac{(r-R)}{a} \right] \right\}^{-1}, \tag{5.1}$$

where r is the radius vector, R is radius of nucleus, a is "skin depth" and ρ_0 is nucleon density at r=0. The measured nucleon-nucleon cross-sections are 42 mb and 35.6 mb for 200 and 62.4 GeV respectively, are used. The input parameters used for Au + Au and Cu + Cu [12, 13] collisions are listed in Table 5.1.

Table 5.1: Input parameters of Woods-Saxon nucleon density distribution.

Parameter/System	Au + Au	Cu + Cu
R	6.38 fm ±0.06	4.218 fm ± 0.014
a	0.535 fm ± 0.027	0.596 fm ± 0.005

In calculations, impact parameter is selected randomly and positions of the nucleons relative to geometrical centers of the colliding nuclei were calculated according to nucleon density $\rho(r)$. The minimum distance between the nucleons inside a nuclei is checked before colliding them so that nucleons may not overlap each other inside the nuclei. Then, two nuclei are collided under the assumptions mentioned earlier. A nucleon-nucleon collision is assumed to take place if their distance d in the transverse plane (orthogonal to beam axis) satisfies the following condition:

$$d \leq \sqrt{\sigma_{inel}^{NN}/\pi}, \tag{5.2}$$

where σ_{inel}^{NN} is the inelastic nucleon-nucleon cross-section at given energy of the collisions.

The negative binomial distribution (NBD) [14, 15] used to estimate the event multiplicity of the each simulated event is:

$$P_{NBD}^{\bar{n},k}(n) = \frac{\Gamma(n+k)}{\Gamma(k)\Gamma(n+1)}\left(\frac{\bar{n}}{\bar{n}+k}\right)^2\left(\frac{k}{\bar{n}+k}\right) \tag{5.3}$$

The multiplicity of an event is generated using:

$$\overline{n} = f(\sqrt{s_{NN}})((1-x_{hard}) + 2x_{hard}N_{bin}/N_{part}), \tag{5.4}$$

where $f(\sqrt{s_{NN}}) = 0.5933ln(\sqrt{s_{NN}}) - 0.4153$ and then sampling a negative binomial distribution with parameter $\overline{n}$, mean number of sources, k=2.1 for each participant and x_{hard} =0.11. This parameterization provides a good description of multiplicity distribution in heavy ion collisions for all the centralities in the energy range $\sqrt{s_{NN}} = 20 - 200\ GeV$. The number of binary collisions (N_{bin}) are obtained by counting the number of nucleon-nucleon collisions and N_{part} is the number of participants nucleons in collision from both the nuclei. The multiplicity distributions obtained for Au+Au and Cu+Cu collisions at 200 and 62.4 GeV using the above procedure are shown in Fig. 5.4.

In the STAR data, centrality of an event is defined using the number of charged particle tracks in the TPC having pseudo-rapidity $|\eta| < 0.5$. Accordingly, centrality bins in models were defined using the multiplicity distributions for $|\eta|$ <0.5 to treat data and models on equal footing. In this way, our calculations of eccentricity fluctuations also contain impact parameter and N_{part} fluctuations which are intrinsic to experimental determination in the given centrality interval.

All parameters $\langle\varepsilon_{std}\rangle$, $\langle\varepsilon_{part}\rangle$, $\langle N_{part}\rangle$ and $\langle b\rangle$ are calculated by averaging over the events in each centrality bin. The quantities ε_{std} and ε_{part} correspond to eccentricity in reaction plane and participant plane respectively, and are calculated as :

$$\varepsilon_{std} = \varepsilon_{RP} = \frac{\sigma_y^2 - \sigma_x^2}{\sigma_y^2 + \sigma_x^2}, \tag{5.5}$$

$$\varepsilon_{part} = \frac{\sqrt{(\sigma_y^2 - \sigma_x^2)^2 + 4\sigma_{xy}^2}}{\sigma_y^2 + \sigma_x^2}, \tag{5.6}$$

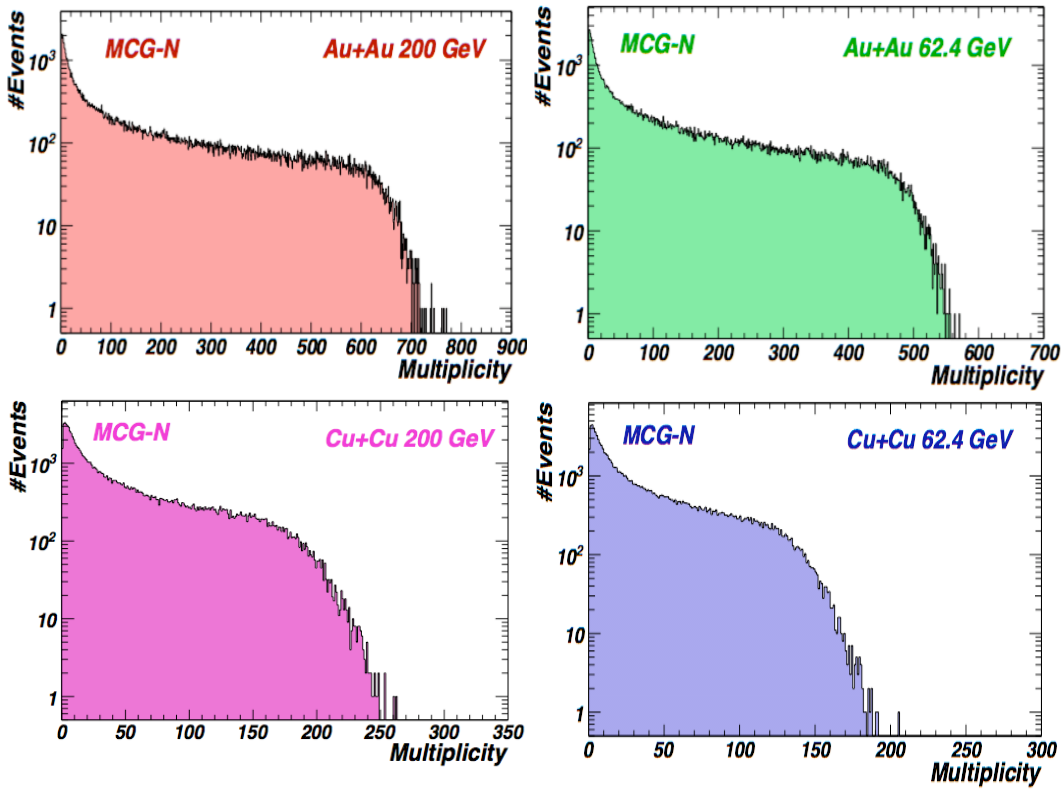

Figure 5.4: Multiplicity distributions from Monte-Carlo Glauber Model for Nucleons as Participants (MCG-N) for (a) Au+Au 200 GeV (b) Au+Au 62.4 GeV (c) Cu+Cu 200 GeV (d) Cu+Cu 62.4 GeV.

where variances are calculated using;

$$\sigma_x^2 = \langle x^2 \rangle - \langle x \rangle^2 \tag{5.7}$$

$$\sigma_y^2 = \langle y^2 \rangle - \langle y \rangle^2 \tag{5.8}$$

$$\sigma_{xy} = \langle xy \rangle - \langle x \rangle \langle y \rangle, \tag{5.9}$$

where (x,y) is the position of participant nucleon in reaction plane and $\langle ....\rangle$ denotes the average over number of collisions in given centrality bin. The parameters $\varepsilon\{2\}$ and $\varepsilon\{4\}$ used to compare eccentricity fluctuations with the maximum limit of v_2 fluctuations in data are calculated using the Eqs.:

$$\varepsilon\{2\}^2 = \langle {\varepsilon_{part}}^2 \rangle \tag{5.10}$$

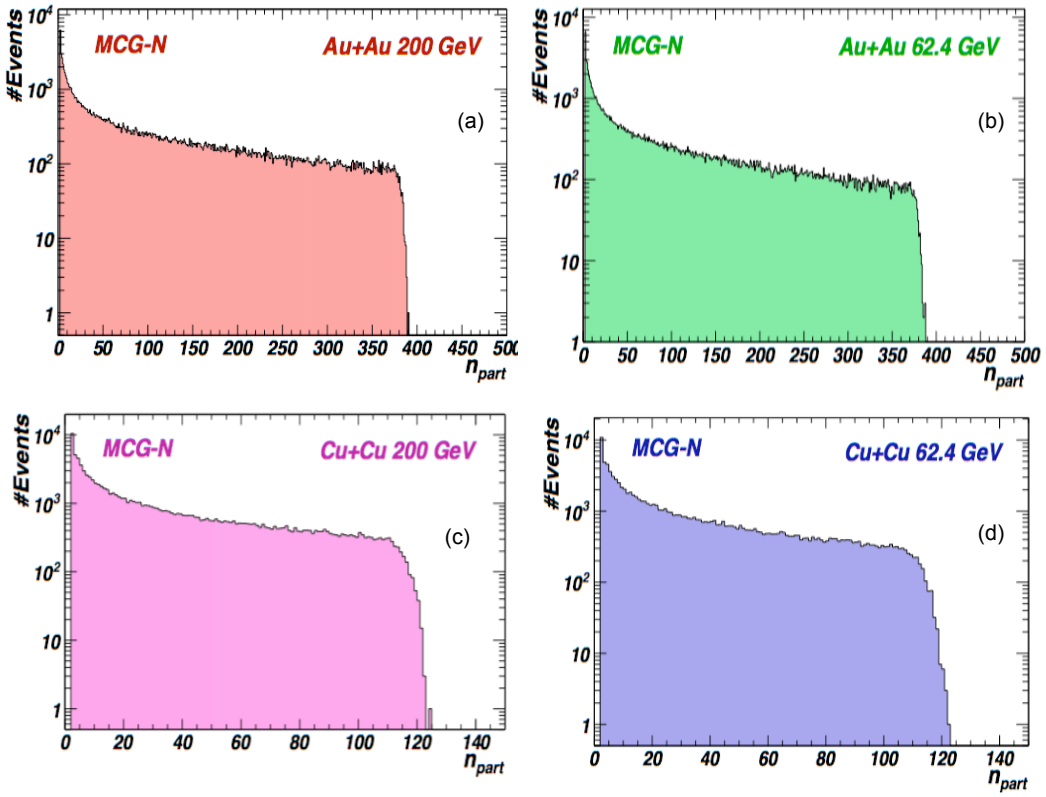

Figure 5.5: Number of participants (n_{part}) distributions from Monte-Carlo Glauber Model for Nucleons as Participants (MCG-N) for (a) Au+Au 200 GeV (b) Au+Au 62.4 GeV (c) Cu+Cu 200 GeV (d) Cu+Cu 62.4 GeV.

$$\varepsilon\{4\}^4 = 2\langle {\varepsilon_{part}}^2\rangle^2 - \langle {\varepsilon_{part}}^4\rangle \tag{5.11}$$

In Monte-Carlo Glauber Model for Nucleons as Participants (MCG-N), the nucleons inside the nucleus are distributed according to Woods-Saxon distribution. The gaussian distribution can also be used in place of Wood-Saxon distribution. The calculated eccentricity and eccentricity fluctuations are not highly sensitive to exact distribution. Figure 5.5 displays the n_{part} distributions for Au+Au and Cu+Cu collisions at 200 and 62.4 GeV calculated from Monte-Carlo Glauber Model for Nucleons as Participants. Figures 5.6 and 5.7 show the $\langle\varepsilon_{std}\rangle$, $\langle\sigma_\varepsilon\rangle$ and $\langle\varepsilon_{part}\rangle$ for Au+Au and Cu+Cu collisions at 200 and 62.4 GeV calculated from MCG-N model. Here, graphs are shown for different combinations of 'R' and 'a' to get systematic errors on the parameters. Au+Au and

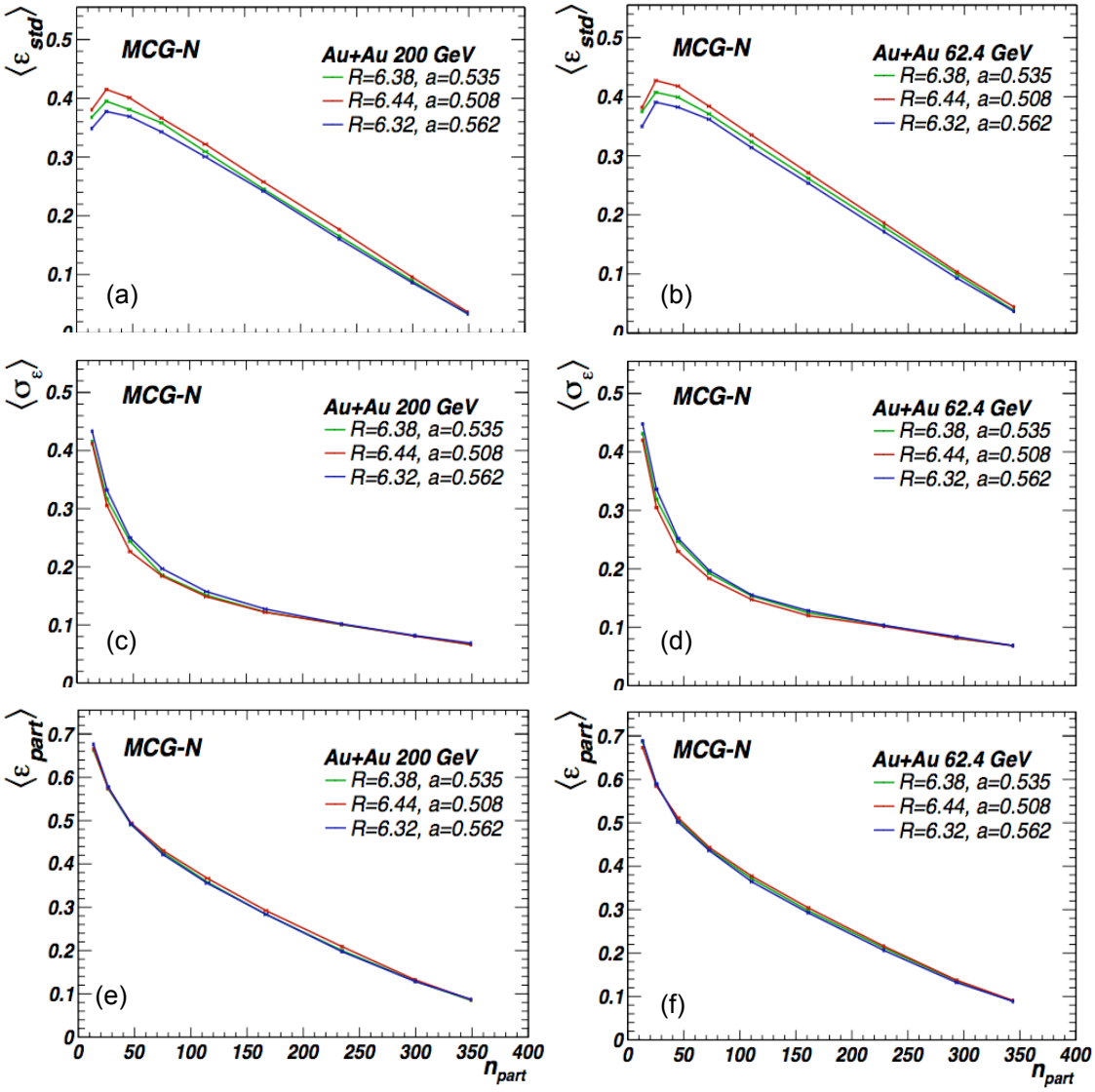

Figure 5.6: Results from Monte-Carlo Glauber Model for Nucleons as Participants (MCG-N): Eccentricity in reaction plane (ε_{std}) for (a) Au+Au 200 GeV and (b) Au+Au 62.4 GeV. Eccentricity fluctuations (σ_{ε}) for (c) Au+Au 200 GeV and (d) Au+Au 62.4 GeV. Eccentricity in participant plane (ε_{part}) for (e) Au+Au 200 GeV and (f) Au+Au 62.4 GeV.

Cu+Cu collisions follow the same trend for both the energies with $\langle\varepsilon_{std}\rangle$, $\langle\sigma_{\varepsilon}\rangle$ and $\langle\varepsilon_{part}\rangle$ decreasing with increase in the number of participants (n_{part}). The values are listed in Tables 5.2 and 5.3.

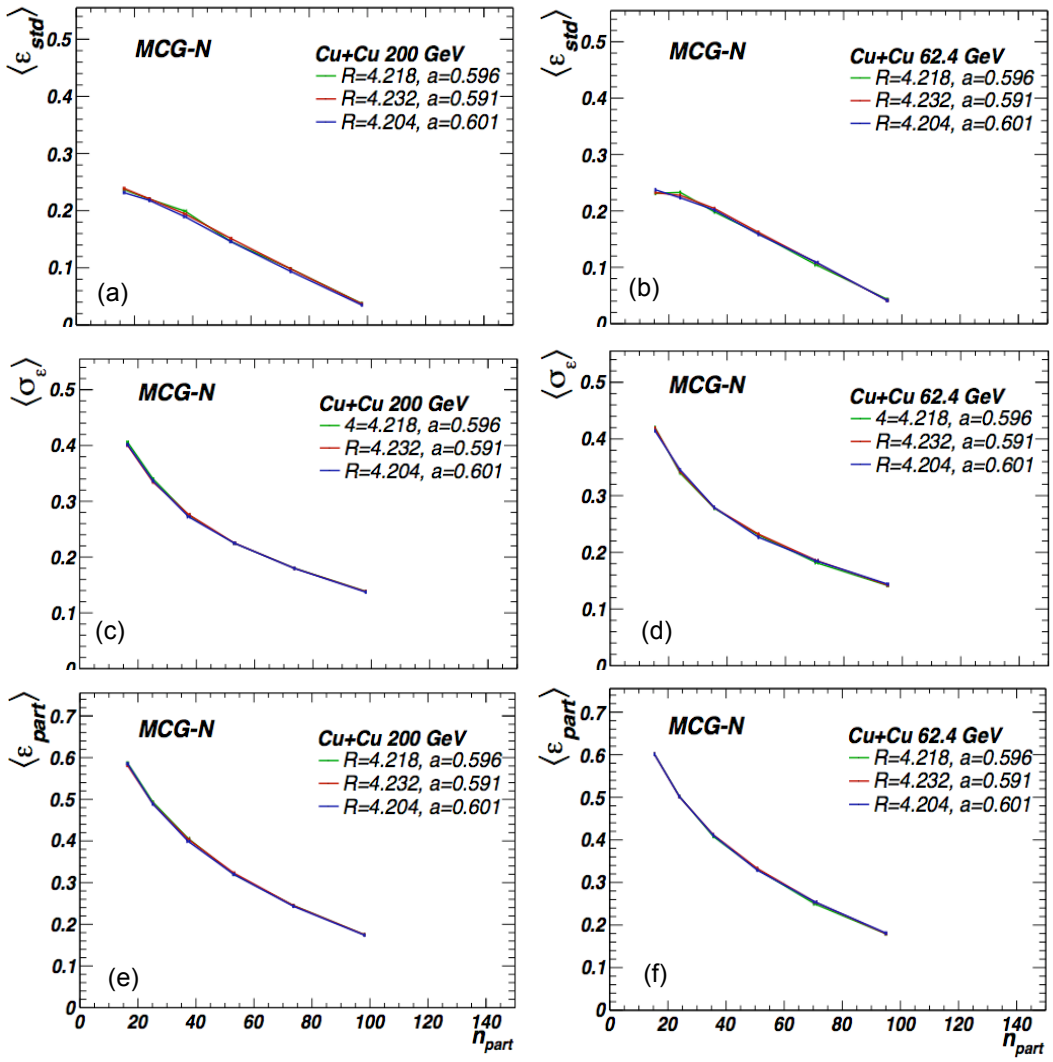

Figure 5.7: Results from Monte-Carlo Glauber Model for Nucleons as Participants (MCG-N): Eccentricity in reaction plane (ε_{std}) for (a) Cu+Cu 200 GeV and (b) Cu+Cu 62.4 GeV. Eccentricity fluctuations (σ_ε) for (c) Cu+Cu 200 GeV and (d) Cu+Cu 62.4 GeV. Eccentricity in participant plane (ε_{part}) for (e) Cu+Cu 200 GeV and (f) Cu+Cu 62.4 GeV.

Table 5.2: ε_{std}, ε_{part}, σ_{ε}, $\varepsilon\{2\}$ and $\varepsilon\{4\}$ with errors from Monte-Carlo Glauber Model for Nucleons as Participants (MCG-N) for Au+Au collisions.

Au + Au 200 GeV					
Cent. (%)	ε_{std}	σ_{ε}	ε_{part}	$\varepsilon\{2\}$	$\varepsilon\{4\}$
0-5	0.0346±0.0018	0.0674±0.0013	0.0860±0.0012	0.0983 ± 0.0014	
5-10	0.0910±0.0047	0.0812±0.0005	0.1304±0.0019	0.1459 ± 0.0018	0.0848±0.0235
10-20	0.1686±0.0081	0.1011±0.0007	0.2032±0.0058	0.2220± 0.0054	0.1682±0.0302
20-30	0.2498±0.0079	0.1245±0.0028	0.2878±0.0044	0.3082±0.0043	0.2611±0.0170
30-40	0.3112±0.0107	0.1529±0.0044	0.3609±0.0057	0.3842 ± 0.0048	0.3347±0.0164
40-50	0.3546±0.0117	0.1903±0.0064	0.4257±0.0047	0.4527±0.0036	0.3985±0.0113
50-60	0.3851±0.0160	0.2379±0.0119	0.4921±0.0020	0.5223±0.0013	0.4631±0.0040
60-70	0.3963±0.0188	0.3187±0.0133	0.5739±0.0008	0.6089 ±0.0028	0.5496±0.0095
70-80	0.3645±0.0159	0.4226±0.0106	0.6644±0.0016	0.7015±0.0064	0.6499±0.0185
Au + Au 62 GeV					
0-5	0.0405±0.0038	0.0684±0.0000	0.0898±0.0010	0.1028 ±0.0010	
5-10	0.0981±0.0053	0.0823±0.0013	0.1349±0.0027	0.1509±0.0026	0.0876±0.0313
10-20	0.1788±0.0074	0.1034±0.0001	0.2110±0.0048	0.2299±0.0044	0.1779±0.0223
20-30	0.2623±0.0088	0.1240±0.0042	0.2984±0.0058	0.3184±0.0047	0.2733±0.0164
30-40	0.3245±0.0107	0.1512±0.0039	0.3707±0.0065	0.3938±0.0053	0.3454±0.0174
40-50	0.3729±0.0111	0.1902±0.0068	0.4396±0.0037	0.4667±0.0027	0.4133±0.0081
50-60	0.4002±0.0178	0.2408±0.0111	0.5063±0.0050	0.5365±0.0038	0.4794±0.0113
60-70	0.4090±0.0184	0.3204±0.0157	0.5869±0.0027	0.6197±0.0034	0.5619±0.0116
70-80	0.3658±0.0161	0.4340±0.0138	0.6809±0.0078	0.7132±0.0079	0.6620±0.0228

Table 5.3: ε_{std}, ε_{part}, σ_{ε}, $\varepsilon\{2\}$ and $\varepsilon\{4\}$ with errors from Monte-Carlo Glauber Model for Nucleons as Participants (MCG-N) for Cu+Cu collisions.

Cu + Cu 200 GeV					
Cent. (%)	ε_{std}	σ_{ε}	ε_{part}	$\varepsilon\{2\}$	$\varepsilon\{4\}$
0-10	0.0361±0.0014	0.1379±0.0007	0.1744±0.0005	0.1980±0.0009	
10-20	0.0960±0.0022	0.1799±0.0003	0.2441±0.0010	0.2741±0.0011	0.1494±0.0203
20-30	0.1487±0.0027	0.2249±0.0002	0.3213±0.0016	0.3554±0.0014	0.2552±0.0095
30-40	0.1943±0.0049	0.2742±0.0021	0.4024±0.0034	0.4403±0.0034	0.3467±0.0169
40-50	0.2194±0.0014	0.3373±0.0028	0.4910±0.0024	0.5301±0.0019	0.4472±0.0072
50-60	0.2353±0.0036	0.4031±0.0029	0.5842±0.0030	0.6226±0.0034	0.5523±0.0117
Cu + Cu 62 GeV					
0-10	0.0421±0.0010	0.1427±0.0013	0.1803±0.0009	0.2052±0.0013	
10-20	0.1064±0.0023	0.1836±0.0019	0.2517±0.0023	0.2823±0.0029	0.1560±0.0496
20-30	0.1602±0.0018	0.2294±0.0027	0.3317±0.0011	0.3660±0.0023	0.2610±0.0170
30-40	0.2013±0.0030	0.2785±0.0008	0.4100±0.0019	0.4481±0.0015	0.3543±0.0069
40-50	0.2281±0.0048	0.3430±0.0028	0.5021±0.0006	0.5426±0.0012	0.4569±0.0048
50-60	0.2343±0.0032	0.4172±0.0030	0.6012±0.0002	0.6404±0.0003	0.5704±0.0017

5.2 Monte-Carlo Glauber Model for Constituent Quarks as Participants (MCG-Q)

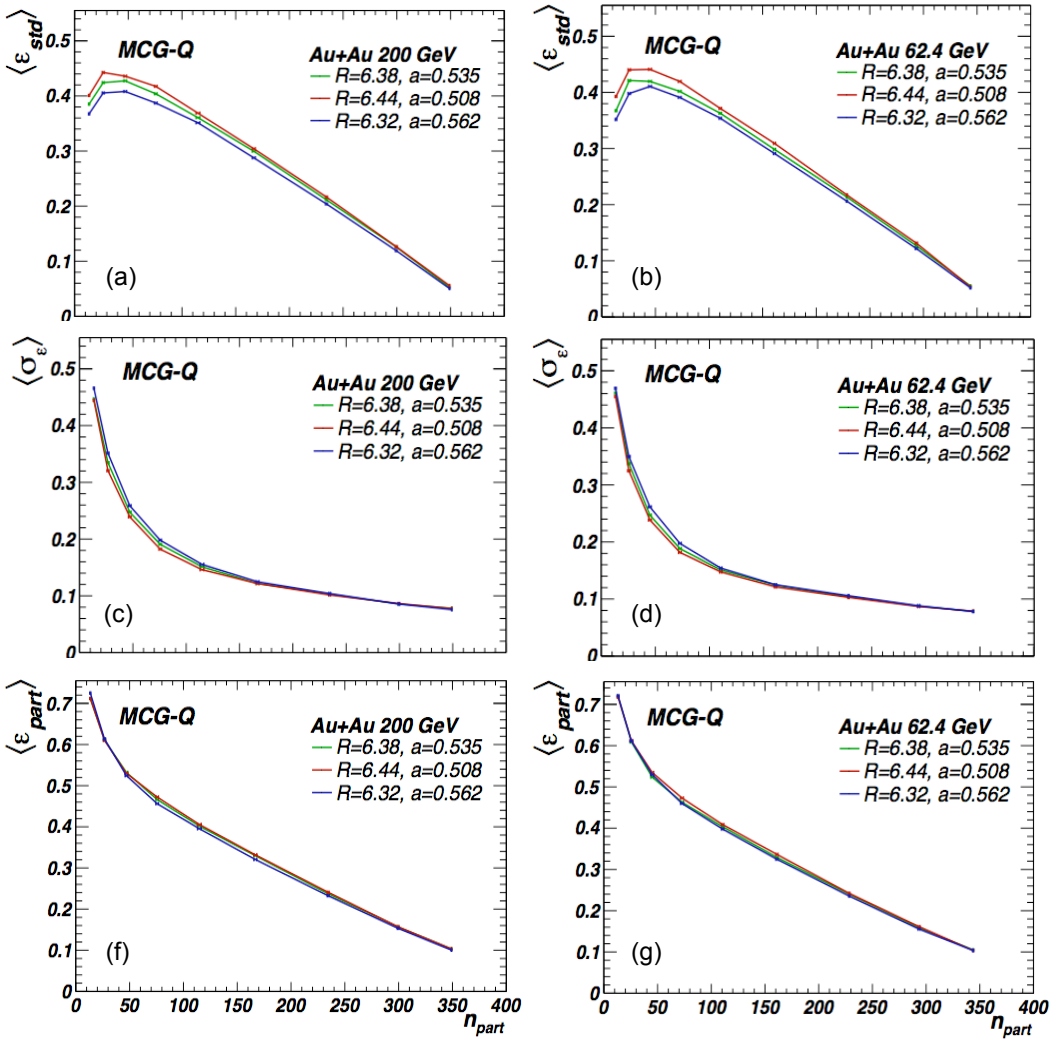

Figure 5.8: Results from Monte-Carlo Glauber Model for Constituent Quarks as Participants (MCG-Q): Eccentricity in reaction plane (ε_{std}) for (a) Au+Au 200 GeV and (b) Au+Au 62.4 GeV. Eccentricity fluctuations (σ_{ε}) for (c) Au+Au 200 GeV and (d) Au+Au 62.4 GeV. Eccentricity in participant plane (ε_{part}) for (e) Au+Au 200 GeV and (f) Au+Au 62.4 GeV.

The Monte-Carlo Glauber Model for Constituent Quarks as Participants is also based on the same assumptions as the Monte-Carlo Glauber Model with Nucleons as Participants (MCG-N) [11]. To calculate the collision parameters in MCG-Q model, firstly the nucleons are distributed inside the nucleus according to a Wood-Saxon density distribu-

tion and then quarks are distributed inside the nucleons according to another Wood-Saxon distribution which was used to calculate the collision parameters. The parameters used to distribute nucleons inside the nucleus are same as used in MCG-N model, but nucleon radius R= 0.865 fm and "skin depth" a=R/8 are used for the Wood-Saxon distribution to distribute quarks inside the nucleons. The number of participants in the MCG-Q model are approximately thrice in the MCG-N model. The inelastic cross-section for the quark is calculated from nucleon cross-section dividing by 7 instead of nine, considering approximately 20% shadowing corrections [16]. Also eccentricities are calculated using the Eqs. 5.5 and 5.6. The MCG-Q model also uses the negative binomial distribution to sample the multiplicity of each event. The parameters $\langle\varepsilon_{std}\rangle$, $\langle\sigma_{\varepsilon}\rangle$ and $\langle\varepsilon_{part}\rangle$ for Au+Au and Cu+Cu collisions at 200 and 62.4 GeV, calculated from MCG-Q model are shown in Figs. 5.8 and 5.9. These are listed in Tables 5.4 and 5.5. All the parameters follow the same trend for Au+Au and Cu+Cu collisions at 200 and 62.4 GeV as in the case of MCG-N model. Graphs are shown for different combinations of 'R' and 'a' to get systematic errors on the parameters.

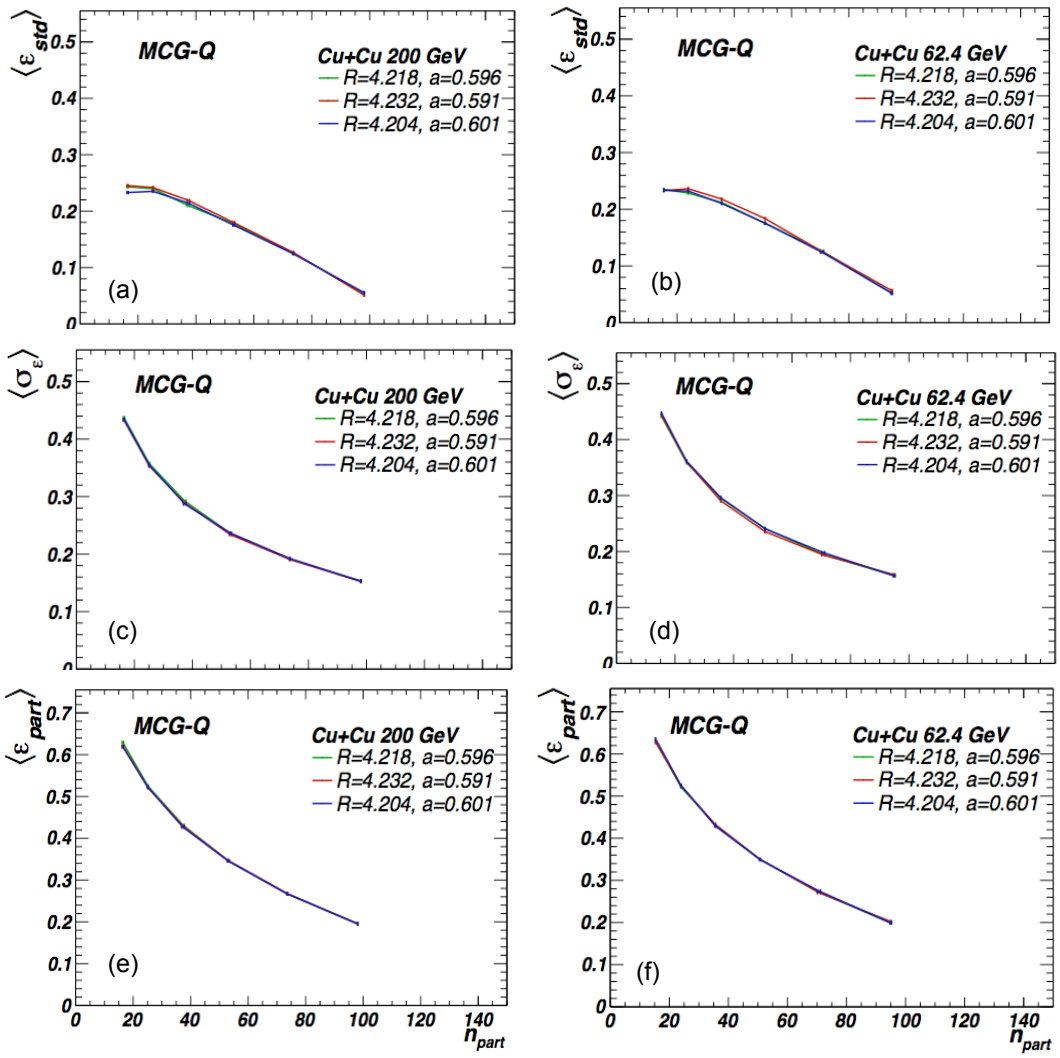

Figure 5.9: Results from Monte-Carlo Glauber Model for Constituent Quarks as Participants (MCG-Q): Eccentricity in reaction plane (ε_{std}) for (a) Cu+Cu 200 GeV and (b) Cu+Cu 62.4 GeV. Eccentricity fluctuations (σ_ε) for (c) Cu+Cu 200 GeV and (d) Cu+Cu 62.4 GeV. Eccentricity in participant plane (ε_{part}) for (e) Cu+Cu 200 GeV and (f) Cu+Cu 62.4 GeV.

Table 5.4: ε_{std}, ε_{part}, σ_{ε}, $\varepsilon\{2\}$ and $\varepsilon\{4\}$ with errors from Monte-Carlo Glauber Model for Constituent Quarks as Participants (MCG-Q) for Au+Au collisions.

Au + Au 200 GeV					
Cent. (%)	ε_{std}	σ_{ε}	ε_{part}	$\varepsilon\{2\}$	$\varepsilon\{4\}$
0-5	0.0530±0.0026	0.0769±0.0011	0.1017±0.0014	0.1159±0.0015	
5-10	0.1228±0.0036	0.0860±0.0005	0.1551±0.0019	0.1715±0.0023	0.1196±0.0182
10-20	0.2102±0.0063	0.1028±0.0012	0.2367±0.0042	0.2548±0.0038	0.2100±0.0159
20-30	0.2960±0.0083	0.1232±0.0015	0.3262±0.0057	0.3453±0.0053	0.3032±0.0179
30-40	0.3601±0.0087	0.1508±0.0046	0.4005±0.0051	0.4224±0.0043	0.3776±0.0134
40-50	0.4023±0.0152	0.1901±0.0079	0.4643±0.0081	0.4903±0.0066	0.4393±0.0200
50-60	0.4220±0.0139	0.2490±0.0098	0.5282±0.0040	0.5595±0.0030	0.5015±0.0091
60-70	0.4240±0.0186	0.3359±0.0154	0.6119±0.0017	0.6452±0.0022	0.5911±0.0057
70-80	0.3842±0.0167	0.4551±0.0108	0.7183±0.0068	0.7491±0.0063	0.7015±0.0176
Au + Au 62 GeV					
0-5	0.0535±0.0017	0.0783±0.0003	0.1043±0.0008	0.1183±0.0010	
5-10	0.1267±0.0049	0.0875±0.0006	0.1584±0.0029	0.1752±0.0025	0.1214±0.0166
10-20	0.2119±0.0056	0.1043±0.0015	0.2386±0.0033	0.2573±0.0030	0.2111±0.0126
20-30	0.3002±0.0091	0.1231±0.0019	0.3305±0.0059	0.3496±0.0054	0.3081±0.0180
30-40	0.3627±0.0088	0.1508±0.0034	0.4033±0.0055	0.4253±0.0048	0.3804±0.0147
40-50	0.4053±0.0142	0.1896±0.0079	0.4664±0.0066	0.4929±0.0056	0.4414±0.0171
50-60	0.4259±0.0152	0.2499±0.0115	0.5292±0.0057	0.5596±0.0049	0.5032±0.0152
60-70	0.4192±0.0211	0.3372±0.0125	0.6106±0.0016	0.6440±0.0012	0.5844±0.0039
70-80	0.3722±0.0205	0.4621±0.0071	0.7186±0.0003	0.7506±0.0015	0.7020±0.0042

Table 5.5: ε_{std}, ε_{part}, σ_{ε}, $\varepsilon\{2\}$ and $\varepsilon\{4\}$ with errors from Monte-Carlo Glauber Model for Constituent Quarks as Participants (MCG-Q) for Cu+Cu collisions.

Cu + Cu 200 GeV					
Cent. (%)	ε_{std}	σ_{ε}	ε_{part}	$\varepsilon\{2\}$	$\varepsilon\{4\}$
0-10	0.0533±0.0022	0.1526±0.0004	0.1953±0.0004	0.2206±0.0002	
10-20	0.1255±0.0012	0.1915±0.0007	0.2674±0.0004	0.2991±0.0004	0.1809±0.0043
20-30	0.1774±0.0023	0.2352±0.0014	0.3461±0.0005	0.3818±0.0002	0.2814±0.0030
30-40	0.2144±0.0047	0.2898±0.0025	0.4289±0.0025	0.4681±0.0026	0.3737±0.0128
40-50	0.2385±0.0034	0.3552±0.0021	0.5233±0.0018	0.5646±0.0022	0.4796±0.0094
50-60	0.2391±0.0061	0.4352±0.0022	0.6239±0.0054	0.6633±0.0051	0.5932±0.0163
Cu + Cu 62 GeV					
0-10	0.0542±0.0024	0.1575±0.0010	0.2006±0.0017	0.2267±0.0020	
10-20	0.1247±0.0006	0.1960±0.0021	0.2729±0.0019	0.3049±0.0019	0.1838±0.0214
20-30	0.1794±0.0041	0.2384±0.0029	0.3496±0.0004	0.3861±0.0002	0.2807±0.0013
30-40	0.2141±0.0038	0.2934±0.0029	0.4305±0.0019	0.4706±0.0015	0.3729±0.0065
40-50	0.2324±0.0038	0.3602±0.0014	0.5235±0.0021	0.5656±0.0020	0.4766±0.0082
50-60	0.2331±0.0004	0.4445±0.0029	0.6315±0.0038	0.6717±0.0033	0.6002±0.0102

5.3 Color Glass Condensate based Monte-Carlo Model (fKLN-CGC)

The Color Glass Condensate is a form of matter supposed to exist in relativistically colliding atomic nuclei. In the relativistically moving nuclei, the gluons appear as moving 'gluonic walls' due to the length contraction. At very high energy, the density of gluons in this wall increases greatly. Color Glass Condensate describes those walls and it is an intrinsic property of particles that can be observed under high-energy conditions. Color in the name color glass condensate refers to a type of charge that quarks and gluons carry as a result of the strong forces. The word glass is borrowed from the term for silica and other materials that are disordered and act like solids on short time scales but liquids on long time scales. In the gluon walls, the gluons themselves are disordered and do not change their positions rapidly because of time dilation. Condensate means the gluons have a very high density.

To study the fluctuations in initial conditions that may be due to eccentricity fluctuations from the CGC model, we use Monte-Carlo version of factorized Kharzeev-Levin-Nardi (fKLN) model [17,18] to generate the initial distribution of entropy density on an event-by-event basis. This model also implements the fluctuations of gluon distribution due to position of hard sources in the transverse plane [18] and improves the treatment of entropy production process and gives natural description near the edge regions compared to ordinary KLN approach [19,20]. The multiplicity distribution from fKLN-CGC model for Au+Au and Cu+Cu collisions are shown in Fig. 5.10. This method also uses the same Woods-Saxon parameters as used by previous models.

The transverse entropy density profile $s_0(x_\perp)$ is calculated first in each sample at an impact parameter for given centrality.

$$s_0(x_\perp) = s(\tau = \tau_0, x, y, \eta_s = 0) \tag{5.12}$$

where $\tau_0 = 0.6$ fm/c is the initial time for the hydrodynamical simulations. Variances are calculated using Eqs. 5.7 - 5.9. The entropy density profiles are used instead of the

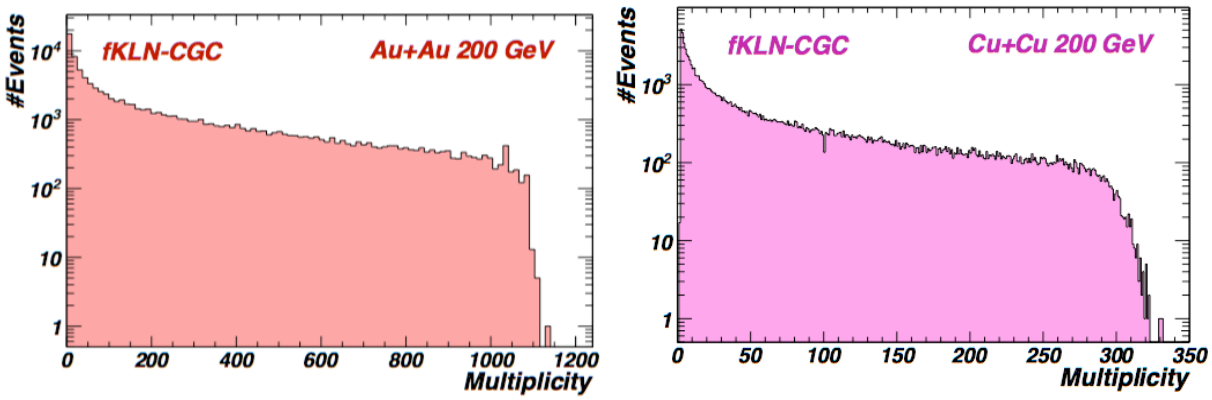

Figure 5.10: Multiplicity distributions from Monte-Carlo based Color Glass Condensate model (fKLN-CGC) for (Left) Au+Au 200 GeV (Right) Cu+Cu 200 GeV.

distribution of participants to calculate eccentricities and transverse area which makes eccentricity dependent on the transverse profile in hydrodynamic simulations. The eccentricity w.r.t. to reaction plane and participant plane are defined by Eqs. 5.5 and 5.6, respectively. The transverse area in reaction plane and participant plane is defined [21], respectively, as

$$S_{RP} = \pi\sqrt{\sigma_x^2\sigma_y^2} \tag{5.13}$$

$$S_{part} = \pi\sqrt{\sigma_x^2\sigma_y^2 - \sigma_{xy}^2} \tag{5.14}$$

The impact parameter vector and the true reaction plane are not known experimentally. So one can set an apparent frame of created matter shifted by $(x, y) = (\langle x\rangle, \langle y\rangle)$ and titled by Ψ from the true frame in the transverse plane,

$$tan\ 2\Psi = \frac{\sigma_y^2 - \sigma_x^2}{2\sigma_{xy}} \tag{5.15}$$

To correct the anisotropy of particle production, centre-of-mass system is shifted to the origin in the calculation frame and then profile is rotated in the azimuthal direction by Ψ to match the apparent reaction plane to true reaction plane. Then next sample of density profile is generated the same way and averaged over many samples. The procedure is

repeated for many samples to make the distribution smooth enough. The initial conditions obtained by doing this contains the effect of eccentricity fluctuations.

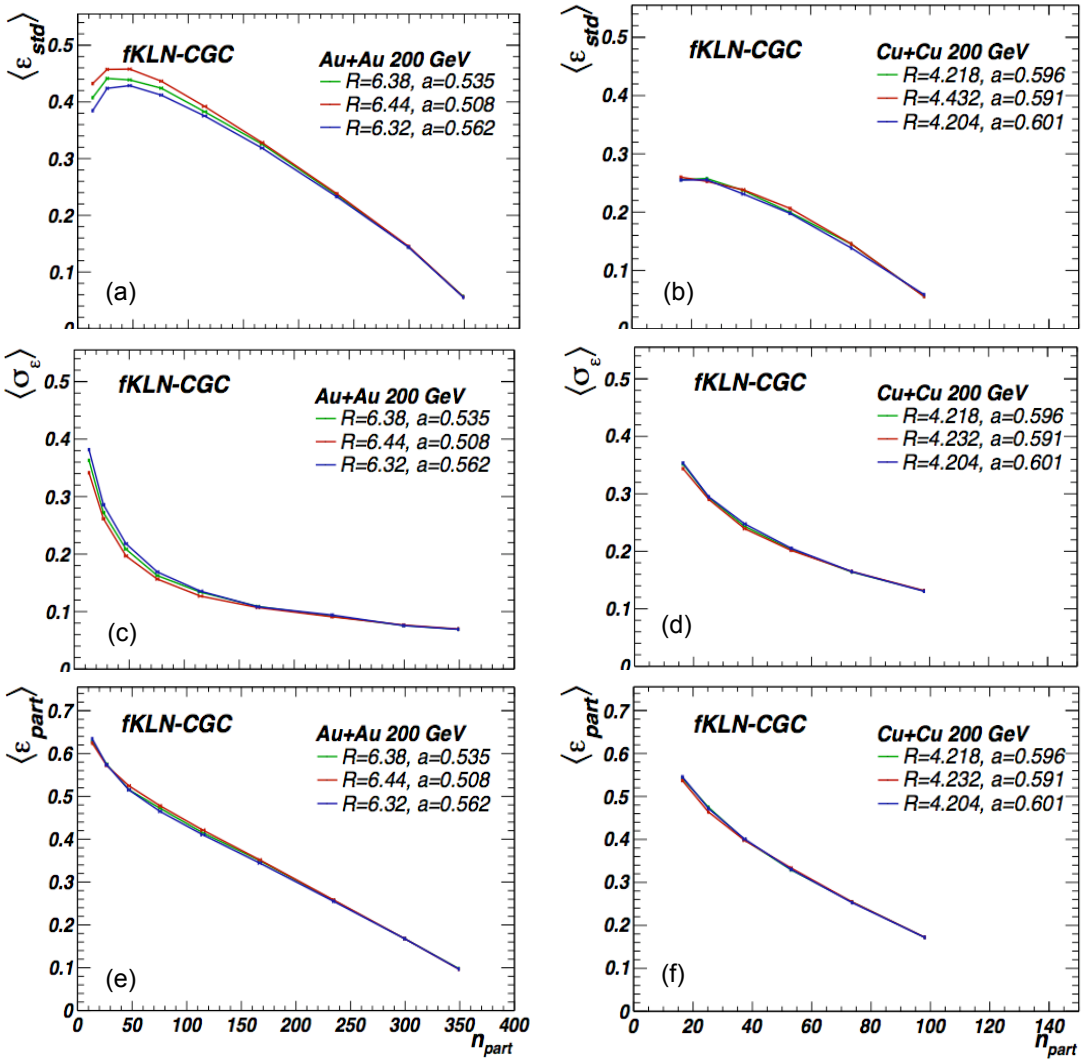

Figure 5.11: Results from Color Glass Condensate based Monte-Carlo Model (fKLN-CGC): Eccentricity in reaction plane (ε_{std}) for (a) Au+Au 200 GeV and (b) Cu+Cu 200 GeV. Eccentricity fluctuations (σ_ε) for (c) Au+Au 200 GeV and (d) Cu+Cu 200 GeV. Eccentricity in participant plane (ε_{part}) for (e) Au+Au 200 GeV and (f) Cu+Cu 200 GeV.

For the implementation of this method the saturation scale for a nucleus 'A' at a transverse coordinate $x_\perp$ in each sample is given by

$$Q^2_{s,A}(x;x_\perp) = Q^2_{s,0}\frac{T_A(x_\perp)}{T_{A,0}}\left(\frac{x_0}{x}\right)^\lambda \tag{5.16}$$

and similarly for other nucleus, where $Q^2_{s,0} = 2\ GeV^2,\ T_{A,0} = 1.53\ fm^{-2}, x_0 = 0.01$ and

$\lambda = 0.28$. The thickness function $T_A(x_\perp)$ at each transverse coordinate is determined by counting the number of wounded nucleons N within a tube of radius $r = \sqrt{\sigma_{NN}^{inel}/\pi}$ extending in the beam direction. Then for the given configuration of nucleons in colliding nuclei, the k_T-factorization formula [22] is applied for each transverse momentum coordinate to obtain distribution of gluons locally. We use the Monte-Carlo version of Kharzeev-Narid-Levin approach used by T. Hirano and Y. Nara [10]. In this approach, the distribution of gluons at each transverse momentum coordinate $x_\perp$ produced with rapidity y is given by the factorization formula [22]

$$\frac{dN_g}{d^2x_\perp dy} = \frac{2\pi^2}{C_F}\int \frac{d^2p_T}{p_T^2}\int^{p_T}\frac{d^2p_T}{4}\alpha_s(Q^2)\times\phi_A(x_1,(p_T+k_T)^2/2;x_\perp) \times\phi_A(x_1,(p_T-k_T)^2/2;x_\perp), \tag{5.17}$$

where $x_{1,2} = p_T\ exp(\pm y)/\sqrt{s}$ and p_T is the transverse momentum of the produced gluons. The upper limit for p_T integration used is 10 GeV/c. The unintegrated gluon distribution function is given by,

$$\phi_A(x,k_T^2;x_\perp) = \frac{kC_F}{2\pi^3}\frac{(1-x)^4}{\alpha_s(Q_s^2)}\frac{Q_s^2}{max(Q_s^2,k_T^2)} \tag{5.18}$$

where $C_F = (N_c^2-1)/(2N_c)$ and $k^2 = 1.75$ used for overall normalization of gluon multiplicity in order to fit data in collisions at RHIC [23].

The initial entropy density in the transverse plane is obtained by

$$s_0(x_\perp) = 3.6n_g = 3.6\frac{dN_g}{r_0 d^2x_\perp d\eta_s}\bigg|_{y=\eta_s=0} \tag{5.19}$$

Figure 5.11 shows $\langle\varepsilon_{std}\rangle$, $\langle\sigma_\varepsilon\rangle$ and $\langle\varepsilon_{part}\rangle$ for Au+Au and Cu+Cu collisions at 200 GeV. All parameters follow the same trend as shown in MCG-N and MCG-Q models. This model shows the same values for $\langle\varepsilon_{std}\rangle$, $\langle\sigma_\varepsilon\rangle$ and $\langle\varepsilon_{part}\rangle$ at 62.4 GeV for Au+Au and Cu+Cu collisions, indicating no dependence on energy of the collisions. Therefore only

the results for 200 GeV are shown.

The values of the parameters calculated from fKLN-CGC model for 200 and 62.4 GeV energies are tabulated in the Table 5.6.

Table 5.6: ε_{std}, ε_{part}, σ_{ε}, $\varepsilon\{2\}$ and $\varepsilon\{4\}$ with errors from Color Glass Condensate based Monte-Carlo Glauber (fKLN-CGC) for Au+Au and Cu+Cu collisions.

Au + Au					
Cent. (%)	ε_{std}	σ_{ε}	ε_{part}	$\varepsilon\{2\}$	$\varepsilon\{4\}$
0-5	0.0561±0.0008	0.0694±0.0003	0.0974±0.0006	0.1103±0.0007	
5-10	0.1446±0.0008	0.0761±0.0005	0.1679±0.0001	0.1815±0.0002	0.1475 ±0.0014
10-20	0.2356±0.0027	0.0924±0.0016	0.2566±0.0017	0.2712±0.0011	0.2385±0.0034
20-30	0.3235±0.0048	0.1079±0.0010	0.3480±0.0037	0.3630±0.0034	0.3325±0.0099
30-40	0.3837±0.0084	0.1312±0.0043	0.4157±0.0055	0.4333±0.0045	0.3990±0.0126
40-50	0.4243±0.0123	0.1627±0.0062	0.4714±0.0066	0.4929±0.0051	0.4530±0.0141
50-60	0.4433±0.0146	0.2074±0.0106	0.5198±0.0048	0.5461±0.0035	0.5012±0.0100
60-70	0.4406±0.0167	0.2737±0.0122	0.5736±0.0015	0.6026±0.0018	0.5530±0.0060
70-80	0.4084±0.0239	0.3615±0.0201	0.6294±0.0051	0.6609±0.0050	0.6096±0.0147
Cu + Cu					
0-10	0.0568±0.0017	0.1311±0.0006	0.1720±0.0002	0.1943±0.0002	0.0560±0.0148
10-20	0.1421±0.0036	0.1644±0.0005	0.2536±0.0008	0.2812±0.0012	0.1937±0.0093
20-30	0.2021±0.0043	0.2035±0.0018	0.3312±0.0022	0.3623±0.0023	0.2840±0.0116
30-40	0.2348±0.0036	0.2434±0.0042	0.3995±0.0016	0.4329±0.0017	0.3575±0.0076
40-50	0.2551±0.0024	0.2926±0.0022	0.4697±0.0056	0.5046±0.0050	0.4338±0.0173
50-60	0.2575±0.0024	0.3487±0.0049	0.5413±0.0043	0.5763±0.0041	0.5122±0.0128

5.4 Comparison of Different Models

Figures 5.12 (a&b) and 5.13 (a&b) show the variation of eccentricity in reaction plane (ε_{std}) with the collisions centrality for the Au+Au and Cu+Cu collisions at $\sqrt{s_{NN}}$=200 and 62.4 GeV. It is seen that fKLN-CGC model has the highest eccentricity wheres MCG-N has the lowest eccentricity for a given centrality. However, eccentricity fluctuations shown in Figs. 5.12 (c&d) and 5.13 (c&d) are minimum for fKLN-CGC whereas maximum for MCG-N model. The eccentricity in the participant is close for all the three models in Au+Au and Cu+Cu collisions at $\sqrt{s_{NN}}$=200 and 62.4 GeV(5.12 (e&f) and 5.13 (e&f)).

The higher values of eccentricities in fKLN-CGC model than the MCG-N and MCG-Q

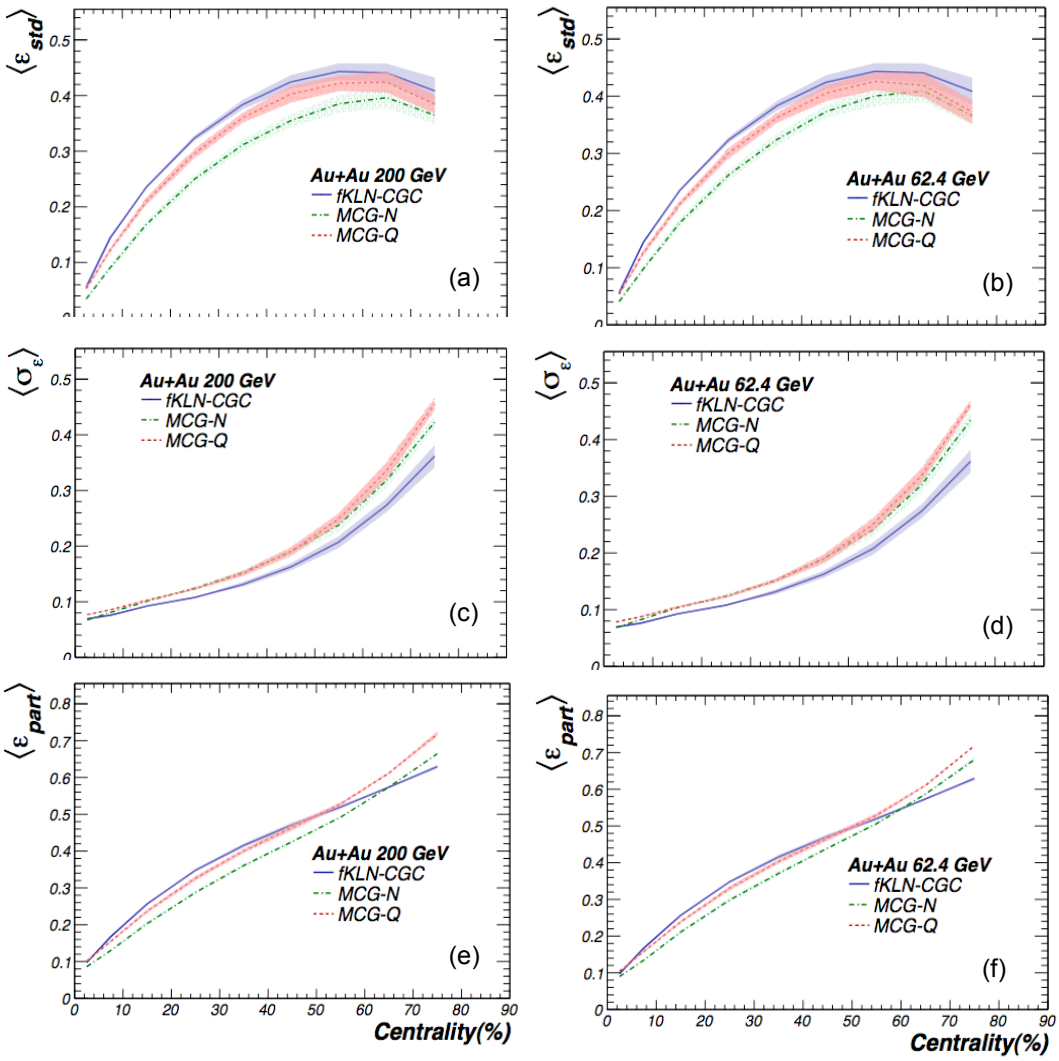

Figure 5.12: Comparison of three eccentricity models MCG-N, MCG-Q and fKLN-CGC: Eccentricity in reaction plane (ε_{std}) for (a) Au+Au 200 GeV and (b) Au+Au 62.4 GeV. Eccentricity fluctuations (σ_ε) for (c) Au+Au 200 GeV and (d) Au+Au 62.4 GeV. Eccentricity in participant plane (ε_{part}) for (e) Au+Au 200 GeV and (f) Au+Au 62.4 GeV, Shaded area in the figures represent the systematic errors from variation in 'R' and 'a'.

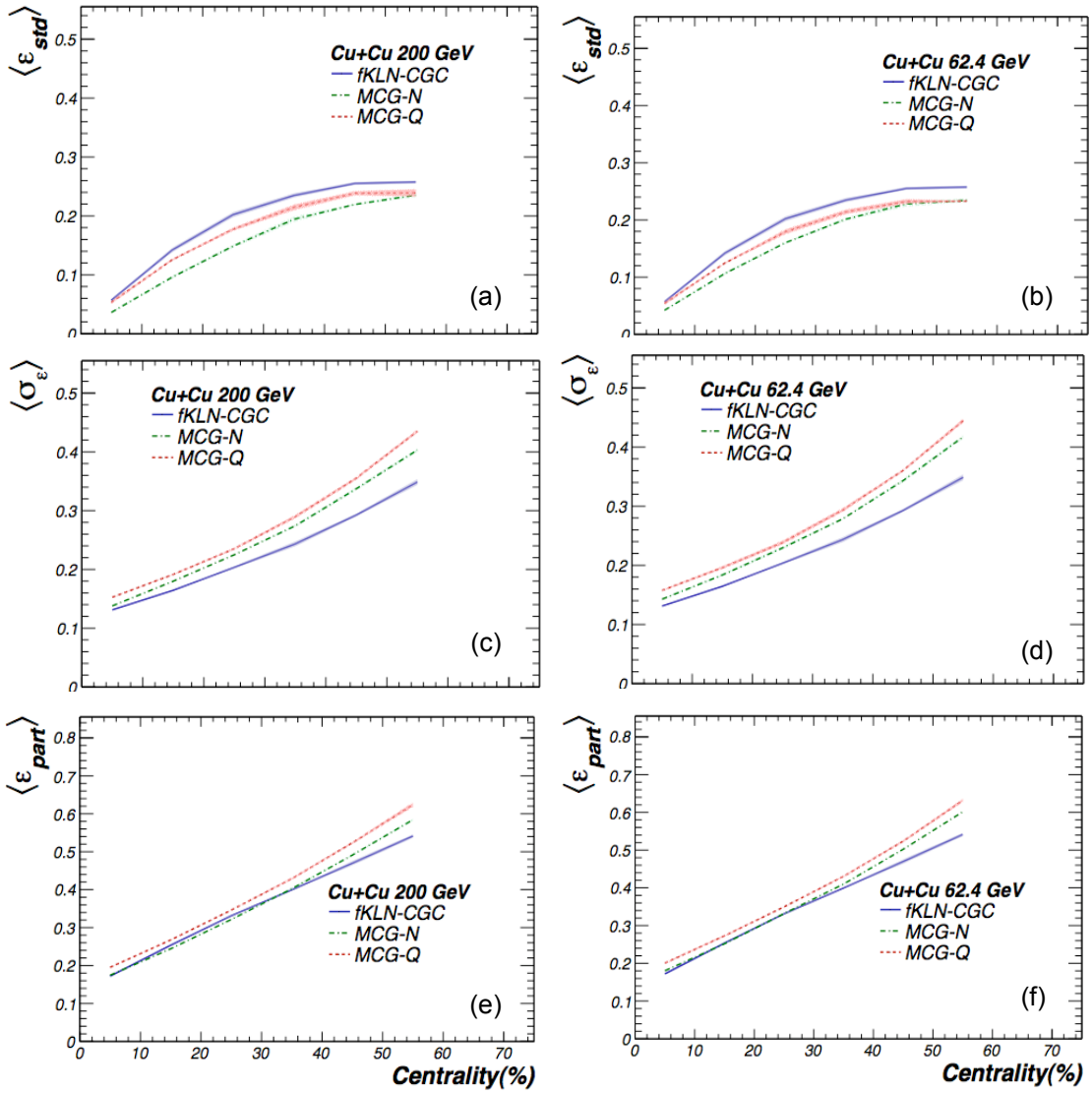

Figure 5.13: Comparison of three eccentricity models MCG-N, MCG-Q and fKLN-CGC: Comparison of (a) Eccentricity in reaction plane (ε_{std}) for Cu+Cu 200 GeV and (b) Cu+Cu 62.4 GeV. (c) Eccentricity fluctuations (σ_ε) for (c) Cu+Cu 200 GeV and (d) Cu+Cu 62.4 GeV. (e) Eccentricity in participant plane (ε_{part}) for Cu+Cu 200 GeV and (f) Cu+Cu 62.4 GeV, Shaded area in the figures represent the systematic error from variation in 'R' and 'a'.

models are inherent feature of k_T factorization approach used in which the number of produced gluons scales approximately with the smaller of the saturation scales of the two nuclei [19].

$$\frac{dN}{d^2x_\perp dy} \sim min\{Q^2_{s,A}(x_\perp), Q^2_{s,B}(x_\perp)\} \tag{5.20}$$

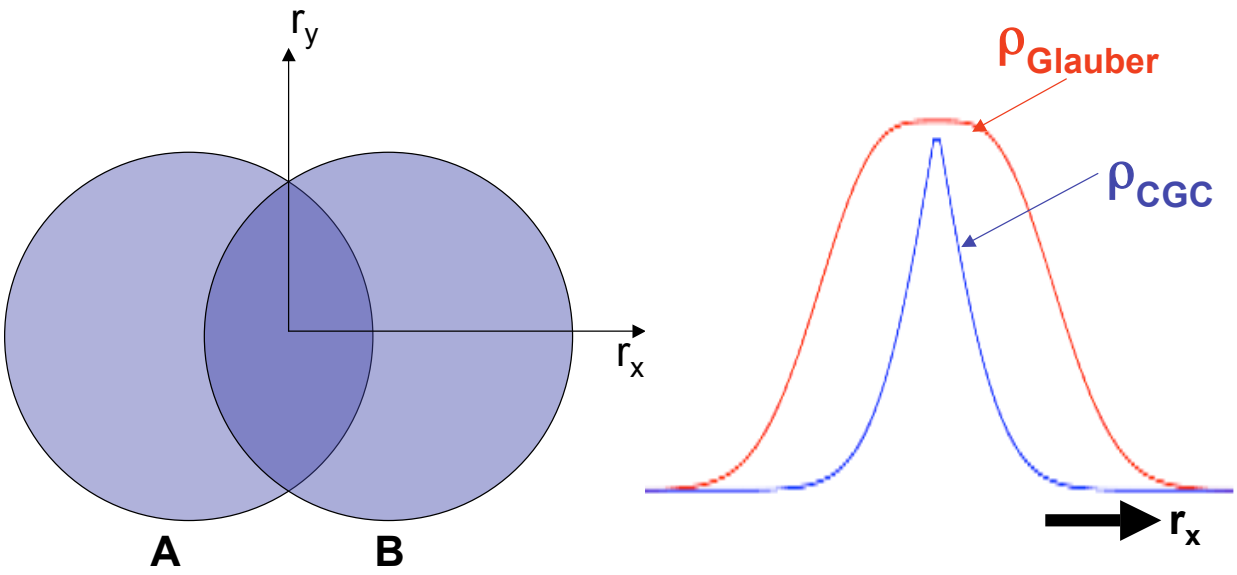

Figure 5.14: Along the r_x density of gluons models in CGC model falls off more rapidly than in glauber models while along r_y collision is symmetric and CGC gluon density behave similar to Glauber model.

Figure 5.14 shows two paths away from center of the overlap region. Along the positive r_x direction, number density scales as

$$\rho_{CGC}(r_x, 0) \sim Q^2_{s,A}(r_x, 0) \sim n_{part,A}(r_x, 0), \tag{5.21}$$

while along the negative r_x direction

$$\rho_{CGC}(r_x, 0) \sim Q^2_{s,B}(r_x, 0) \sim n_{part,B}(r_x, 0), \tag{5.22}$$

But in case of Glauber models, according to wounded nucleon model the density scales with the total number of participants from both the nuclei,

$$\rho_{Glauber}(r_x, 0) \sim n_{part,A}(r_x, 0) + n_{part,B}(r_x, 0), \tag{5.23}$$

which drops less rapidly with r_x since the drop of density towards the edge of more dilute nucleus is at least partly compensated by increasing number of participants from the other nucleus.

Along the r_y direction both the saturation scales are equal and hence

$$\rho_{CGC}(0, r_y) \sim (n_{part,A}(0, r_y) + n_{part,B}(0, r_y))/2 \sim \rho_{Glauber}(0, r_y), \tag{5.24}$$

Since density along the r_x direction drops more rapidly for CGC model than Glauber model and behaves same along the r_y direction, it results in higher eccentricities in CGC based model than Glauber models.

Bibliography

[1] S. A. Voloshin, A. M. Poskanzer and R. Snellings, arXiv:0809.2949 [nucl-ex].

[2] P. Sorensen, arXiv:0905.0174 [nucl-ex].

[3] K. H. Ackermann *et al.* [STAR Collaboration], Phys. Rev. Lett. **86**, 402 (2001); C. Adler *et al.* [STAR Collaboration], Phys. Rev. Lett. **87**, 182301 (2001); C. Adler *et al.* [STAR Collaboration], Phys. Rev. Lett. **89**, 132301 (2002); J. Adams *et al.* [STAR Collaboration], Phys. Rev. Lett. **92**, 052302 (2004); J. Adams *et al.* [STAR Collaboration], Phys. Rev. C **72**, 014904 (2005); J. Adams *et al.* [STAR Collaboration], Phys. Rev. Lett. **95**, 122301 (2005); K. Adcox *et al.* [PHENIX Collaboration], Nucl. Phys. A **757**, 184 (2005); J. Adams *et al.* [STAR Collaboration], Nucl. Phys. A **757**, 102 (2005); B. Alver *et al.* [PHOBOS Collaboration], Phys. Rev. Lett. **98**, 242302 (2007); B.B. Back *et al.* [PHOBOS Collaboration], Phys. Rev. C **72**, 051901(R) (2005); Phys. Rev. Lett. **94**, 122303 (2005).

[4] J. Adams *et al.* [STAR Collaboration], Phys. Rev. C **72**, 014904 (2005).

[5] H. Song and U. W. Heinz, arXiv:nucl-th/0812.4274.

[6] N. Borghini, P. M. Dinh and J. Y. Ollitrault, Phys. Rev. C **62**, 034902 (2000)

[7] M. Miller and R. Snellings, arXiv:nucl-ex/0312008.

[8] S. Manly *et al.* [PHOBOS Collaboration], Nucl. Phys. A **774**, 523 (2006)

[9] C. Alt *et al.* [NA49 Collaboration], Phys. Rev. C **68**, 034903 (2003); G. Aga- kichiev *et al.* [CERES/NA45 Collaboration], Phys. Rev. Lett. **92**, 032301 (2004).

[10] T. Hirano and M. Gyulassy, Nucl. Phys. A **769**, 71 (2006).

[11] Glauber R J 1959 Lectures in Theoretical Physics, edited by Brittin W E and Dunham L G (New York: Interscience) 315
Glauber R J 1967 High Energy Physics and Nuclear Structure, edited by Alexander G (Amsterdam: North-Holland) 311
Glauber R J 1970 High Energy Physics and Nuclear Structure, edited by Devons S (New York: Plenum) 207.

[12] M. L. Miller, K. Reygers, S. J. Sanders and P. Steinberg, Ann. Rev. Nucl. Part. Sci. **57**, 205 (2007).

[13] H. De Vries, C. W. De Jager and C. De Vries, Atom. Data Nucl. Data Table. **36**, 495 (1987).

[14] G. J. Alner *et al.* [UA5 Collaboration], Z. Phys. C **33**, 1 (1986).

[15] G. J. Alner *et al.* [UA5 Collaboration], Phys. Rep. **154**, 247 (1987).

[16] Anisovich and Shabelski, Quark Model and High Energy Physics, (2004).

[17] T. Hirano and Y. Nara, Phys. Rev. C 79, 064904 (2009).

[18] H. J. Drescher and Y. Nara, Phys. Rev. C **75**, 034905 (2007):arXiv:nucl-th/0611017v2 (2007).

[19] D. Kharzeev and M. Nardi, Phys. Lett. B **507**, 121 (2001); D. Kharzeev, E. Levin and M. Nardi, Nucl. Phys. A **730**, 448 (2004) [Erratum-ibid. A **743**, 329 (2004)]; Nucl. Phys. A **747**, 609 (2005).

[20] T. Hirano and Y. Nara, Nucl. Phys. A **743**, 305 (2004).

[21] B. Alver *et al.* [PHOBOS Collaboration], nucl-ex/0702036; Phys. Rev. C **77**, 014906 (2008).

[22] L. V. Gribov, E. M. Levin and M. G. Ryskin, Phys. Rept. **100**, 1 (1983).

[23] B. B. Back *et al.* [PHOBOS Collaboration], Phys. ReV. C **65**, 061901 (2002).

Chapter 6

Elliptic Flow of Charged Hadrons

In non-central heavy-ion collisions, the overlap area is almond shaped with a long and short axis. Significant re-scattering amongst the constituents of system can convert the initial coordinate-space anisotropy to a momentum-space anisotropy in the final state [1–3]. The spatial anisotropy decreases as the system expands so that any observed momentum anisotropy will be most sensitive to the early phase of the evolution before the spatial asymmetry is washed-out [4]. Ultra-relativistic nuclear collisions at Brookhaven National Laboratory's Relativistic Heavy Ion Collider (RHIC) [5] are studied in part to deduce whether quarks and gluons become deconfined during the high energy-density phase of these collisions. Since the azimuthal momentum-space anisotropy of particle production is sensitive to the early phase of the collision evolution, observables measuring this anisotropy are of special interest. The azimuthal angle (ϕ) dependence of particle momentum distribution can be expressed in the form of a Fourier series [6]:

$$\frac{dN}{d\phi} \propto 1 + \sum_n 2v_n \cos n\left(\phi - \Psi\right), \tag{6.1}$$

where Ψ is either the reaction-plane angle defined by the vector connecting the two colliding nuclei, or the participant plane angle defined by the deformation of the density distribution in the overlap zone [7]. The Fourier coefficients v_n can be measured and used to characterize the azimuthal anisotropy of particle production.

Elliptic flow (v_2) measurements [8] indicate that the matter created in collisions at

Relativistic Heavy Ion Collider (RHIC) behave as a prefect liquid with viscosity near a conjectured lower bound [9]. This conclusion is primarily based on hydrodynamic model predictions [8, 10]. Uncertainty about the conditions at the beginning of the hydrodynamic expansion, however, leads to large uncertainties in the model expectations [11, 12]. Since v_2 reflects the initial spatial eccentricity of the overlap region when two nuclei collide, fluctuations of v_2 should depend strongly on fluctuations in the initial eccentricity. Measurements of the system-size and energy dependence of v_2 and v_2 fluctuations are, therefore, useful for understanding the initial conditions of the expansion phase of heavy-ion collisions.

Methods used to study v_2 [13] are based on the correlations between the produced particles. Estimates of v_2 from produced particles can be biased by correlations which are not related to the reaction plane (non-flow $\delta_2 = \langle\cos(2\Delta\phi)\rangle - \langle v_2^2\rangle$) and by event-by-event fluctuations of v_2 (σ_{v_2}). Thus, an explicit measurement of v_2 would require measurements of non-flow and v_2 fluctuations. It has been shown that the various analyses of v_2 based on produced particles can be related to $v_2\{4\}^2 \approx \langle v_2\rangle^2 - \sigma_{v_2}^2$ and $v_2\{2\}^2 - v_2\{4\}^2 \approx \delta_2 + 2\sigma_{v_2}^2$ [14]. In case, the v_2 distribution is Gaussian in the reaction plane (not in the participant plane), the 6-particle cumulant $v_2\{6\}$ and higher orders will be equal to $v_2\{4\}$ and, therefore, will not add any new information. Within the accuracy of the data this has been found to be the case (*i.e.,* $v_2\{6\} \approx v_2\{4\}$) [15].

In this chapter, we present measurements of $v_2\{2\}$ and $v_2\{4\}$ in Au+Au and Cu+Cu collisions at $\sqrt{s_{NN}} = 200$ and 62.4 GeV. We present results on $v_2\{2\}^2 - v_2\{4\}^2 \approx \delta_2 + 2\sigma_{v_2}^2$ (referred to as σ_{tot}^2) and derive upper-limit on σ_{v_2}/v_2 based on several approximations. The upper-limit assumes δ_2=0. This is a robust upper limit since larger values of σ_{v_2}/v_2 would require negative values of non-flow contrary to expectations and to measurements of two-particle correlations [16]. We present model comparisons to the upper-limit of σ_{v_2}/v_2. Using same data and then alternatively assuming that eccentricity fluctuations lead to v_2 fluctuations ($\sigma_{v_2} = v_2\sigma_\varepsilon/\varepsilon$) we can compute the non-flow term required to satisfy the relationship $v_2\{2\}^2 - v_2\{4\}^2 \approx \delta_2 + 2\sigma_{v_2}^2$ for each model. Finally we present the ratio of v_2 to the initial eccentricity from these models.

The eccentricity calculated with respect to the participant axis is called ε_{part} and the eccentricity calculated with respect to the reaction plane is called ε_{std}. When v_2 fluctuations are dominated by eccentricity fluctuations, $v_2\{4\}$ is equal to the mean v_2 in the reaction plane and $\sqrt{v_2^2\{4\} + \sigma_{v_2}^2}$ is the mean v_2 in the participant plane in the Gaussian approximation for the flow fluctuations [17]. We note again that $\sigma_{v_2}^2$ is not experimentally accessible without the assumptions about delta.

6.1 Data Analyzed

Data analyzed consists of Au + Au and Cu + Cu collisions at $\sqrt{s_{NN}}$ = 62.4 and 200 GeV recorded with the STAR detector [18] at Relativistic Heavy Ion Collider (RHIC),

Table 6.1: Centrality bins used in Au+Au 200 and 62.4 GeV collisions for Run IV data.

Reference Multiplicity for Au+Au collisions			
Bin	**Centrality (%)**	**200 GeV**	**62.4 GeV**
1	0-5	520	373
2	5-10	441	313
3	10-20	319	222
4	20-30	222	154
5	30-40	150	102
6	40-50	96	165
7	50-60	57	38
8	60-70	31	20
9	70-80	14	9

Brookhaven National Laboratory, U.S.A. Charged particle tracking within pseudorapidity $|\eta| < 1$ and transverse momentum $p_T > 0.15$ GeV/c was preformed with the Time Projection Chamber (TPC) [19]. Beam-Beam Counters (BBC's) were used to trigger on events. We analyzed events from a centrality interval corresponding to 0%–80% and 0%–60% of the hadronic interaction cross-section, respectively, for Au+Au and Cu+Cu collisions. As in previous STAR analyses [20], we define the centrality of an event using reference multiplicity represented by the number of charged tracks with pseudorapidity $|\eta| < 0.5$, $p_T > 0.2$ GeV/c in the TPC having more than 10 measured space points and a distance of closest approach to the primary vertex (DCA) less than 2 cm [21]. Figure 6.1 displays

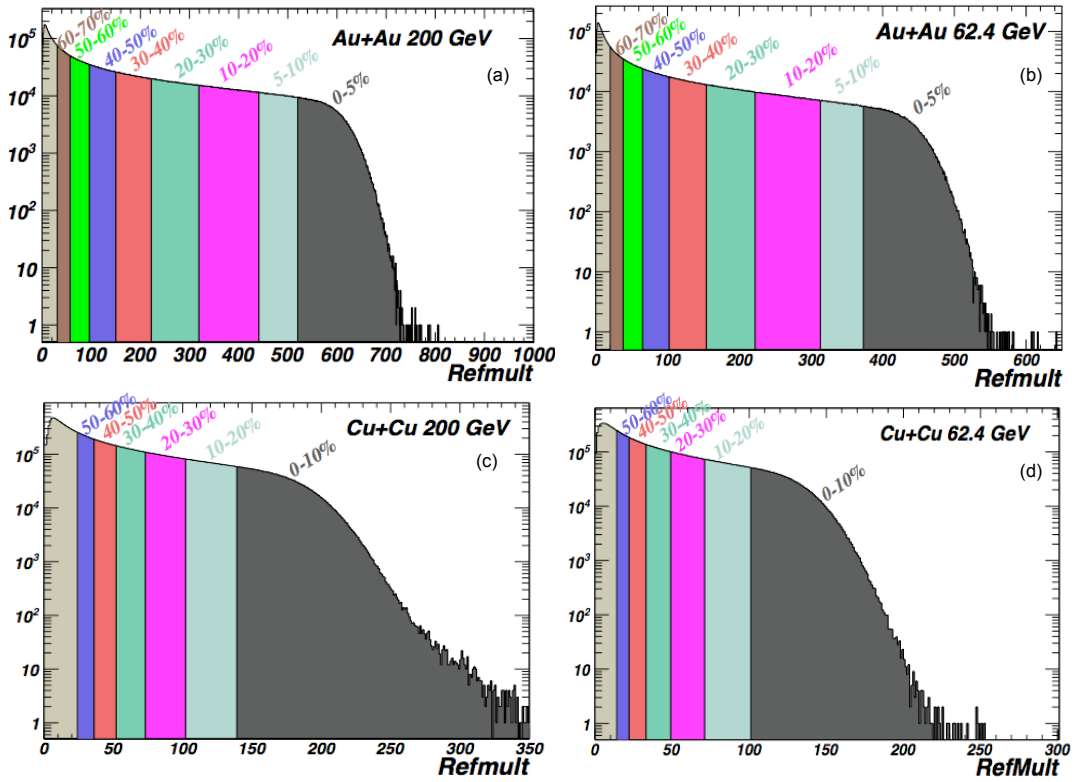

Figure 6.1: Reference multiplicity distributions for (a) Au+Au collisions at $\sqrt{s_{NN}}$=200 GeV (b) Au+Au collisions at $\sqrt{s_{NN}}$=62.4 GeV (c) Cu+Cu collisions at $\sqrt{s_{NN}}$=200 GeV (d) Cu+Cu collisions at $\sqrt{s_{NN}}$=62.4 GeV. The centrality cuts used are shown in these figures.

reference multiplicity distributions for Au+Au and Cu+Cu collisions at $\sqrt{s_{NN}}$=200 and 62.4 GeV indicating the different centrality cuts as listed in Tables 6.1 and 6.2. For this analysis we used charged tracks within $|\eta| < 1.0$ and $0.15 < p_T < 2.0$ GeV/c. Only events with primary vertices within 30 cm of the TPC center in the beam direction were analyzed. The data cuts used in the analysis are listed in Table 6.3. The number of events analyzed for each data set are listed in Table 6.4.

6.2 Elliptic Flow

We analyzed Cu + Cu and Au + Au collisions at center of mass energies $\sqrt{s_{NN}}$ = 62.4 and 200 GeV to study the energy and system-size dependence of elliptic flow, non-flow

Table 6.2: Centrality bins used in Cu+Cu 200 and 62.4 GeV collisions for Run V data.

Reference Multiplicity for Cu+Cu colliisions			
Bin	**Centrality (%)**	**200 GeV**	**62.4 GeV**
1	0-10	139	101
2	10-20	98	71
3	20-30	67	49
4	30-40	46	33
5	40-50	30	22
6	50-60	19	14

Table 6.3: Cuts used for the selection of data.

Cut	**Value**
p_T	0.15 to 2.0 GeV/c
η	-1.0 to 1.0
vertex z	-30.0 cm to 30.0 cm
vertex x,y	-1.0 cm to 1.0 cm
fit points	>15
fit points/max. pts.	>0.52
dca	< 3.0 cm
trigger	Minbias

and elliptic flow fluctuations. From previous studies we learnt that it is not possible to disentangle non-flow and v_2 fluctuations. We've used two methods to study $v_2\{2\}$ and $v_2\{4\}$; the q-distribution method and the Q-Cumulant method [22]. Both are based on multi-particle azimuthal correlations. The v_2 and σ^2_{dyn} determined using the reduced flow vector [23], discussed in Chapter 3, can be related as $v_2\{q,4\}^2 = v_2\{q\}^2$ where $v_2\{q,2\}$ and $v_2\{q,4\}$ are the two- and four-particle cumulants determined from the q-distribution which can be compared to other determinations of $v_2\{2\}$ and $v_2\{4\}$. We compared the results from q-distribution and Q-Cumulant. Based on simulations, we find that the q-distribution method used to study elliptic flow by fitting the distribution of magnitude of reduced $q = Q/\sqrt{M}$ vector deviates more for low multiplicity events. Therefore, the complete analysis has been done using the results from Q-Cumulant method.

Table 6.4: Number of events used for different data sets.

Data Set	Number of Events (Millions)
Au+Au 200 GeV	11.8 M
Au+Au 62.4 GeV	7.7 M
Cu+Cu 200 GeV	15 M
Cu+Cu 62.4 GeV	14.7 M

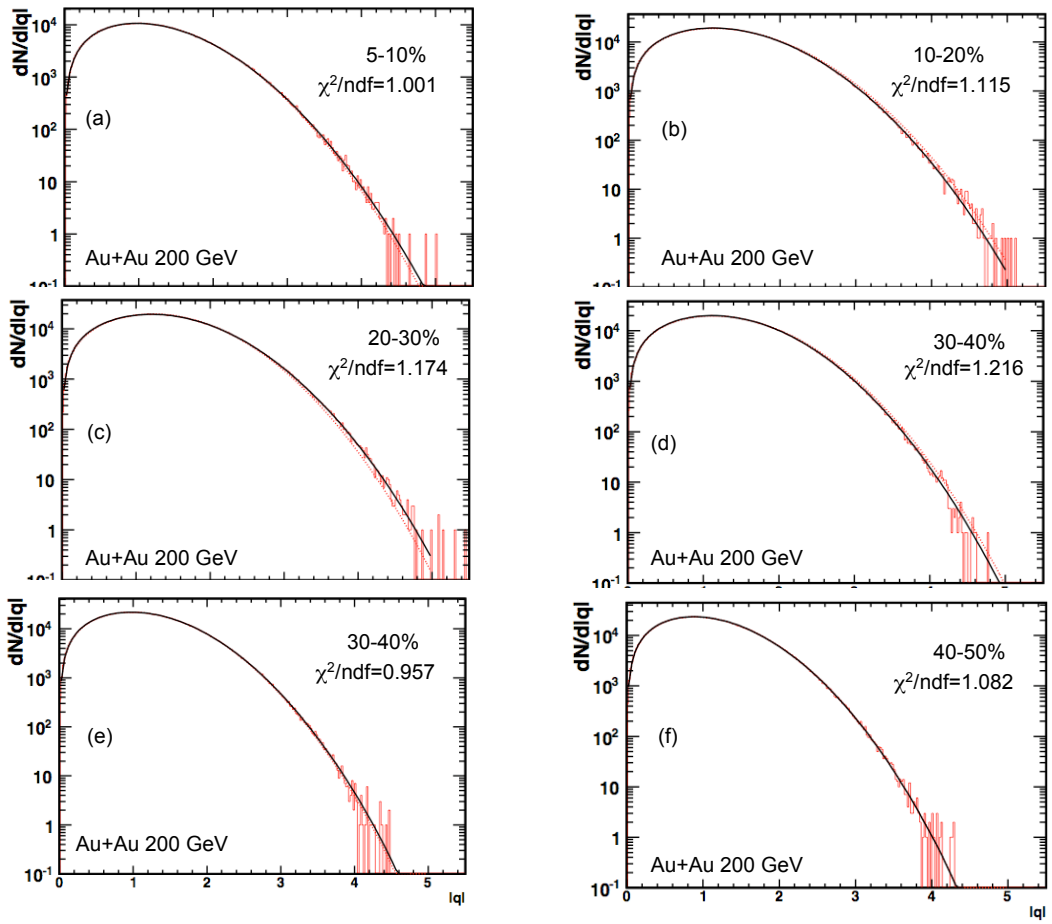

Figure 6.2: q-distribution fit for Au+Au collisions at 200 GeV for different centralities.

6.2.1 Elliptic Flow Using q-distribution

The q-distribution method is based on Gaussian distribution fitting of the magnitude of reduced flow vector q($= Q/\sqrt{M}$), *i.e.*,

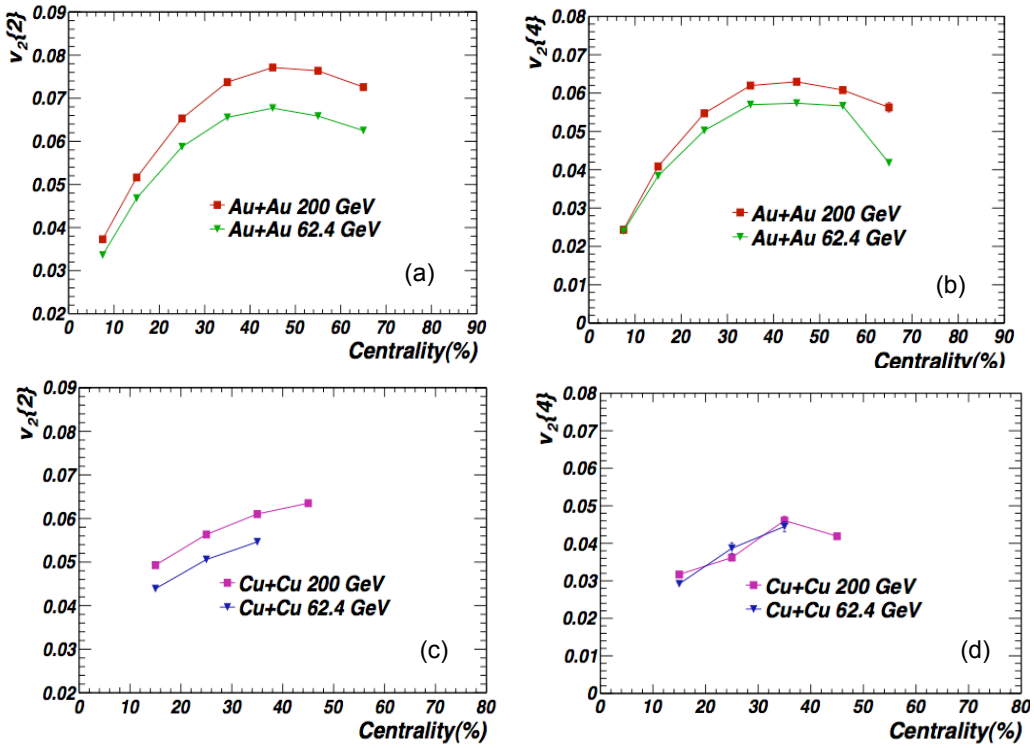

Figure 6.3: Centrality and energy dependence of (a) $v_2\{2\}$ for Au+Au collisions at $\sqrt{s_{NN}}$=200 and 62.4 GeV (b) $v_2\{4\}$ for Au+Au collisions at $\sqrt{s_{NN}}$=200 and 62.4 GeV (c) $v_2\{2\}$ for Cu+Cu collisions at $\sqrt{s_{NN}}$=200 and 62.4 GeV (b) $v_2\{4\}$ for Cu+Cu collisions at $\sqrt{s_{NN}}$=200 and 62.4 GeV, from q-distribution method.

$$\frac{dN}{q_n dq_n} = \frac{1}{\sqrt{\pi}\sigma_x\sigma_y} e^{-\frac{1}{2}\left(\frac{q_n^2+Mv_n^2}{\sigma_x^2}\right)} \times \sum_{k=0,2,4,\ldots}^{\infty} \left(1-\frac{\sigma_x^2}{\sigma_y^2}\right)^k \left(\frac{q_n}{v_n\sqrt{M}}\right)^k \frac{1}{k!}\Gamma\left(\frac{2k+1}{2}\right) I_k\left(\frac{q_n v_n\sqrt{M}}{\sigma_x^2}\right), \tag{6.2}$$

where Γ is the gamma function and I_k are modified Bessel's functions and

$$\begin{aligned} \sigma_{n,x}^2 &= \frac{1}{2}(1+v_{2n}-2v_n^2+(M-1)(\delta_n+2\sigma_{v_n}^2), \\ \sigma_{n,y}^2 &= \frac{1}{2}(1-v_{2n}+(M-1)(\delta_n+2\sigma_{v_n}^2))., \end{aligned} \tag{6.3}$$

where M is the number of tracks used in the calculation of q_n. Figure 6.2 shows the fit to q-distribution for Au+Au 200 GeV collisions for different centralities indicated in the figures.

The elliptic flow from two- and four-particles cumulants ($v_2\{2\}$, $v_2\{4\}$) calculated using q-distribution method and the difference $v_2\{2\}^2 - v_2\{4\}^2 (\approx \delta_2 + 2\sigma_{v_2}^2)$ for Au+Au and

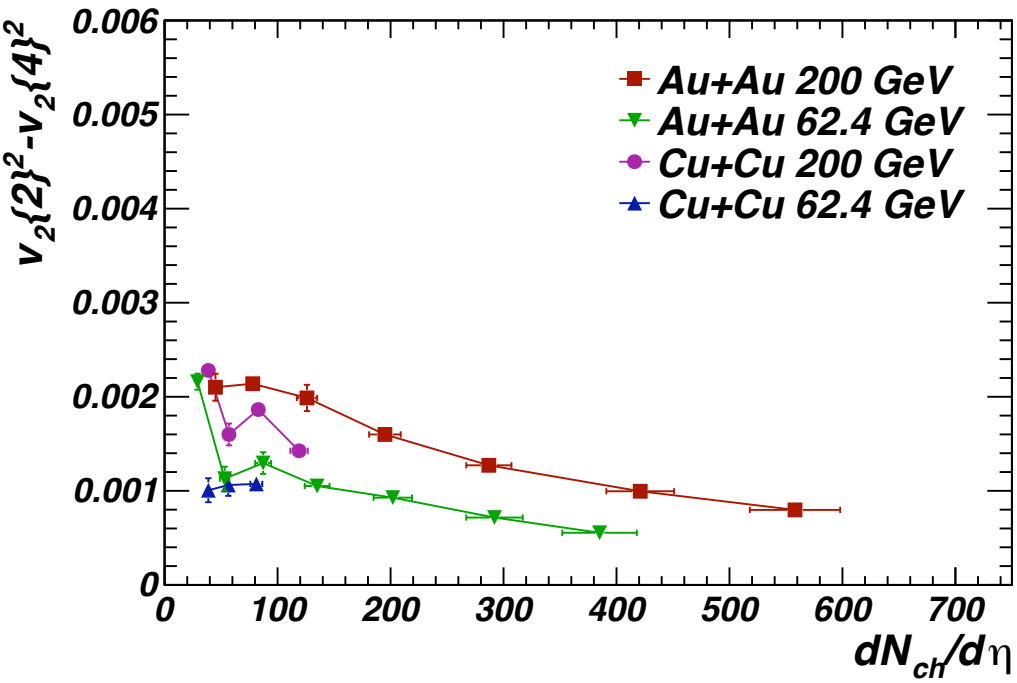

Figure 6.4: Dependence of $v_2\{2\}^2 - v_2\{4\}^2$ on charged particles multiplicity for Au+Au and Cu+Cu collisions at $\sqrt{s_{NN}}$=200 and 62.4 GeV collisions calculated from q-distribution method.

Cu+Cu collisions at centre of mass energies 200 and 62.4 GeV are shown in Fig. 6.3. The elliptic flow ($v_2\{2\}$, $v_2\{4\}$) values increase while going from central collisions to peripheral collisions and starts decreasing again for the most peripheral collisions in case of Au+Au and Cu+Cu collisions at centre of mass energies 200 and 62.4 GeV. But this method give non-determinable values of elliptic flow for Cu+Cu peripheral collisions due to small multiplicity values. The $v_2\{2\}$ increases with increase in energy of the collisions for the same system size Au+Au and Cu+Cu collisions. $v_2\{4\}$ remains same within errors for Cu+Cu collisions at 200 and 62.4 GeV whereas follows the same trend as $v_2\{2\}$ for Au+Au collisions.

The difference $v_2\{2\}^2 - v_2\{4\}^2$ shown in Fig. 6.4, related to non-flow and v_2 fluctuations decreases from peripheral to central collisions as expected due to the dilution of correlations as 1/M. Au+Au 200 GeV collisions show maximum in all the data sets for the same multiplicity of the charged particles, which is followed by Cu+Cu 200 GeV collisions. The Au+Au and Cu+Cu collisions at 62.4 GeV show close values for the difference $v_2\{2\}^2 - v_2\{4\}^2$ for the same charged particle multiplicity. Figure 6.5 shows the difference

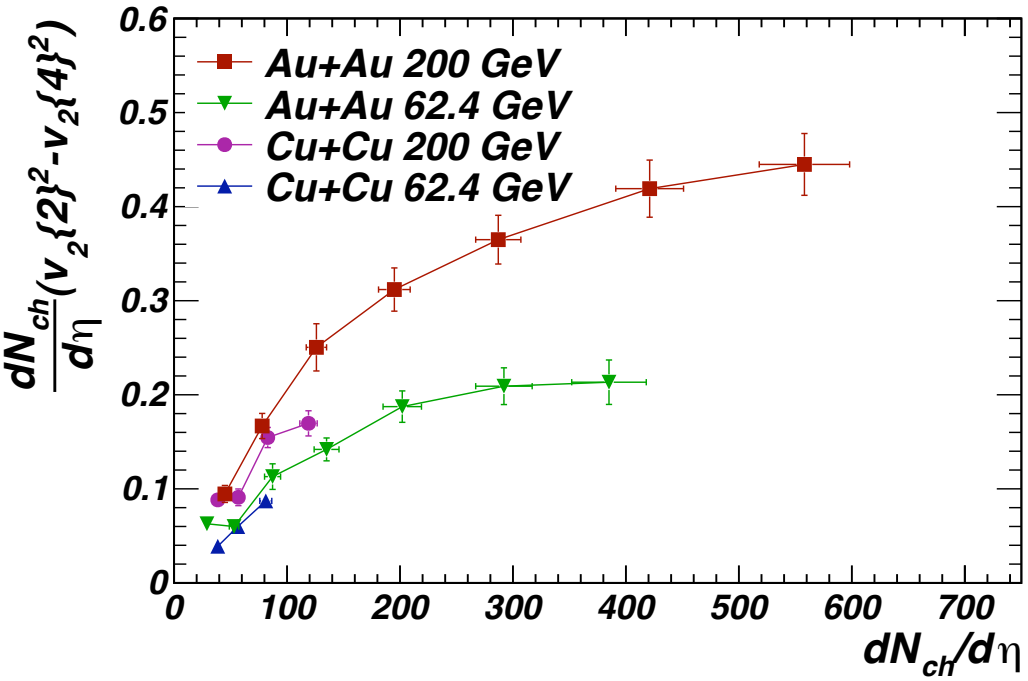

Figure 6.5: Dependence of multiplicity scaled $v_2\{2\}^2 - v_2\{4\}^2$ on charged particles multiplicity for Au+Au and Cu+Cu collisions at $\sqrt{s_{NN}}$=200 and 62.4 GeV collisions calculated from q-distribution method.

$v_2\{2\}^2 - v_2\{4\}^2$ scaled by charged particles multiplicity. It seems to follow the same trend for Au+Au and Cu+Cu collisions at 62.4 GeV and 200 GeV collisions.

6.2.2 Elliptic Flow Using Q-Cumulant

The elliptic flow results from two- and four-particle correlations ($v_2\{2\}$, $v_2\{4\}$) using Q-Cumulant method and $v_2\{2\}^2 - v_2\{4\}^2 (\approx \delta_2 + 2\sigma^2_{v_2})$ for Au+Au and Cu+Cu collisions at centre of mass energies 200 and 62.4 GeV are shown in Fig. 6.6. The elliptic flow calculated from Q-Cumulant method follow the same trend as calculated from q-distribution method. The difference $v_2\{2\}^2 - v_2\{4\}^2$ (Fig. 6.7) also follows the same trend but in case of Q-Cumulant method the difference $v_2\{2\}^2 - v_2\{4\}^2$ is independent of system-size within errors. The difference $v_2\{2\}^2 - v_2\{4\}^2$ scaled by charged particle multiplicity shown in Fig. 6.8 doesn't show system-size dependence within errors.

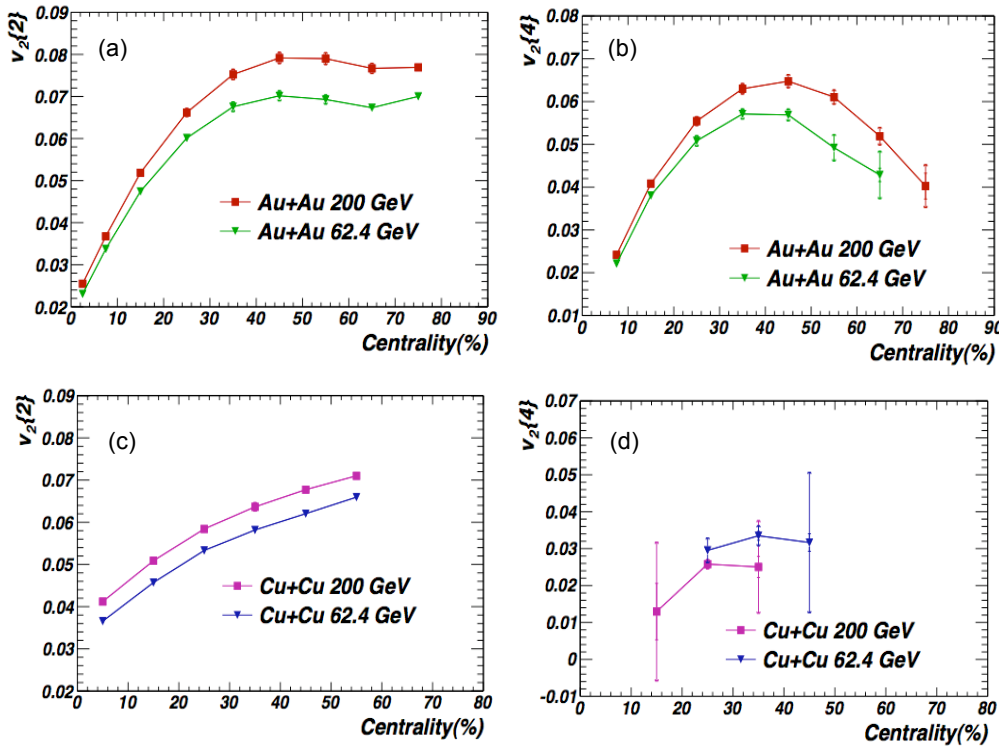

Figure 6.6: Centrality and energy dependence of (a) $v_2\{2\}$ for Au+Au collisions at $\sqrt{s_{NN}}$=200 and 62.4 GeV (b) $v_2\{4\}$ for Au+Au collisions at $\sqrt{s_{NN}}$=200 and 62.4 GeV (c) $v_2\{2\}$ for Cu+Cu collisions at $\sqrt{s_{NN}}$=200 and 62.4 GeV (b) $v_2\{4\}$ for Cu+Cu collisions at $\sqrt{s_{NN}}$=200 and 62.4 GeV, from Q-Cumulant method.

6.3 Comparison of Elliptic Flow Using q-distribution and Q-Cumulant

The results from the q-distribution method and Q-Cumulant method have been compared for the elliptic flow from two- and four-particle correlations. Figure 6.9 shows elliptic flow from two-particle correlations ($v_2\{2\}$) and four-particle correlations ($v_2\{4\}$) for the Au+Au and Cu+Cu collisions at $\sqrt{s_{NN}}$ = 200 and 62.4 GeV. The $v_2\{2\}$ calculated from the q-distribution method shows slightly low values (Figs. 6.9 (a) and (b)) than those calculated from the Q-Cumulant method for the peripheral collisions and the difference is more for the most peripheral collisions. Figures 6.9 (c) and (d) show $v_2\{4\}$ from the two methods, respectively, for Au+Au and Cu+Cu collisions at 200 and 62.4 GeV. $v_2\{4\}$ for the Au+Au collisions at both energies shows the same values within errors however $v_2\{4\}$ for the Cu+Cu collisions at these energies shows large difference between the two methods. The values calculated from the Q-Cumulant are significantly lower than those

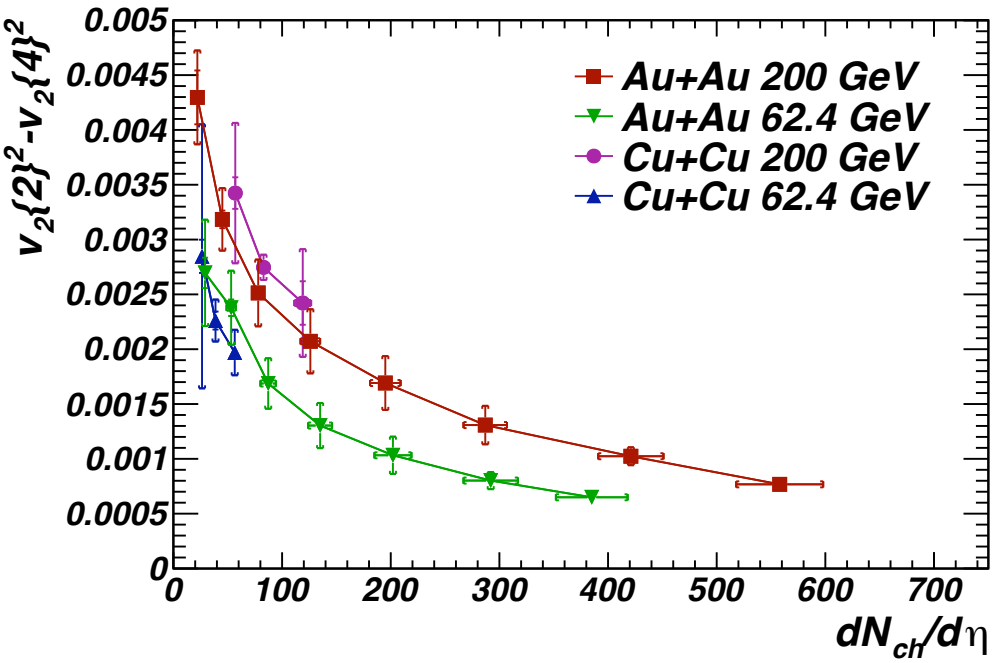

Figure 6.7: Dependence of $v_2\{2\}^2 - v_2\{4\}^2$ on charged particles multiplicity for Au+Au and Cu+Cu collisions at $\sqrt{s_{NN}}$=200 and 62.4 GeV collisions calculated from Q-Cumulant method.

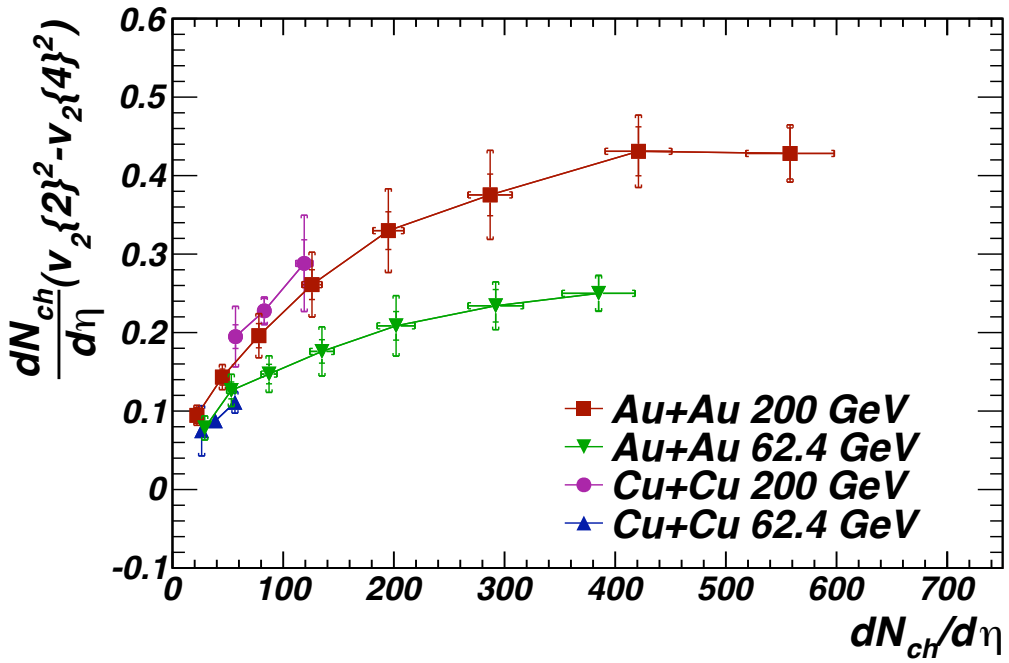

Figure 6.8: Dependence of multiplicity scaled $v_2\{2\}^2 - v_2\{4\}^2$ on charged particles multiplicity for Au+Au and Cu+Cu collisions at $\sqrt{s_{NN}}$=200 and 62.4 GeV collisions calculated from Q-Cumulant method.

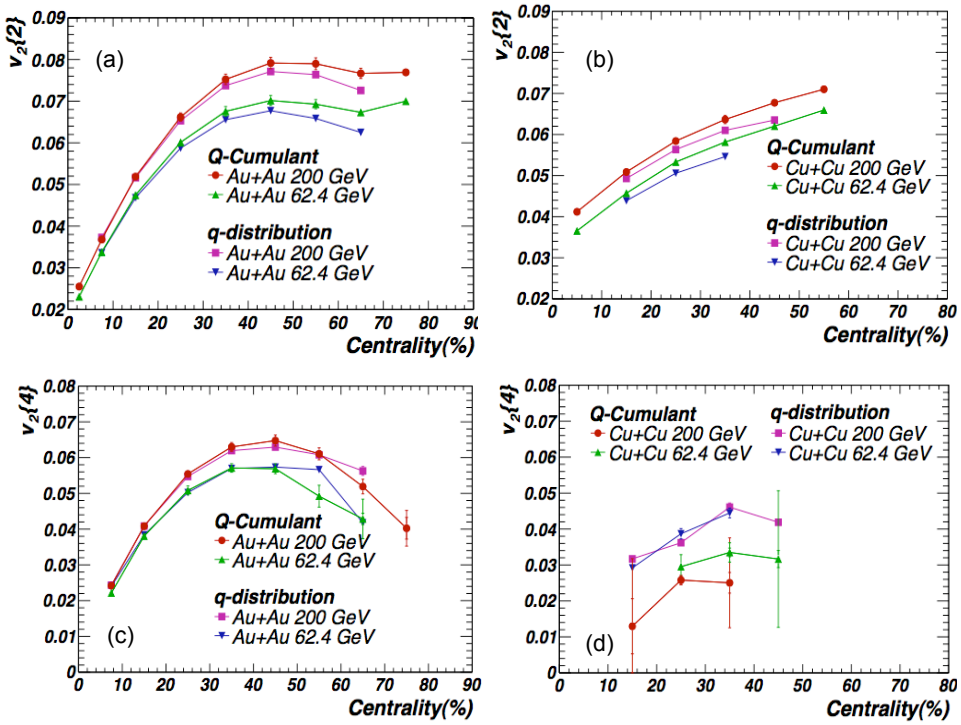

Figure 6.9: Comparison between the elliptic flow from q-distribution method and Q-Cumulant method for $\sqrt{s_{NN}}$=200 and 62.4 GeV (a) $v_2\{2\}$ for Au+Au collisions (b) $v_2\{4\}$ for Au+Au collisions (c) $v_2\{2\}$ for Cu+Cu collisions (d) $v_2\{4\}$ for Cu+Cu collisions.

calculated from the q-distribution method.

Figure 6.10 shows the comparison of the difference $v_2\{2\}^2 - v_2\{4\}^2$ between the two methods for Au+Au and Cu+Cu collisions at 200 and 62.4 GeV. The difference is same within errors for large multiplicities values in Au+Au collisions at 200 and 62.4 GeV but for low multiplicities the difference $v_2\{2\}^2 - v_2\{4\}^2$ from the q-distribution method is less than from Q-Cumulant method. The difference $v_2\{2\}^2 - v_2\{4\}^2$ for Cu+Cu collisions at 200 GeV lies close for both methods but for the 62.4 GeV collisions the two methods shows large difference with Q-Cumulant method giving significantly large values than the q-distribution method.

We carried out simulations to test q-distribution and Q-Cumulant methods because of the large difference observed in the elliptic flow for Cu+Cu collisions at $\sqrt{s_{NN}}$=62.4 GeV.

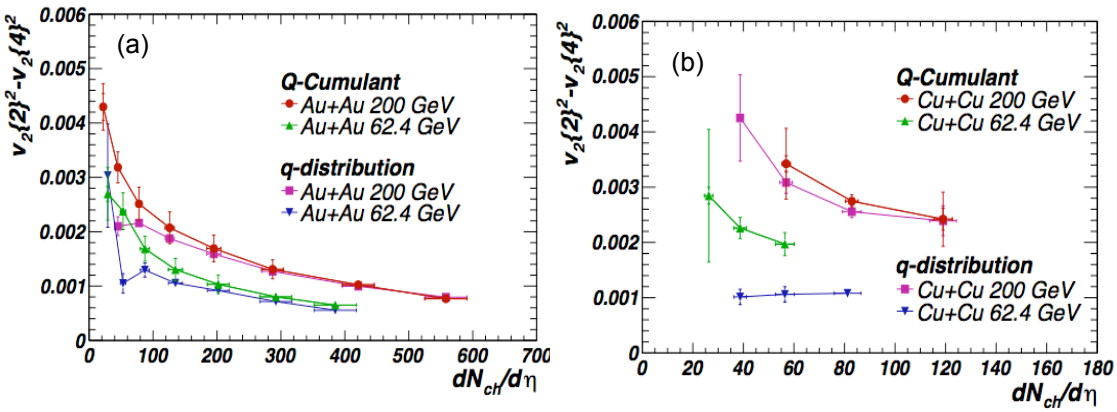

Figure 6.10: Comparison of $v_2\{2\}^2 - v_2\{4\}^2$ calculated from q-distribution method and Q-Cumulant method for Au+Au and Cu+Cu collisions at $\sqrt{s_{NN}}$=200 and 62.4 GeV.

6.4 Monte-Carlo Simulations of Elliptic Flow

The difference between the results from q-distribution method and Q-Cumulant method for the peripheral collisions motivated us to have closer look of the methods by doing simulation studies. We did the simulation for the elliptic flow by giving elliptic flow as input to the model and then tried to extract that elliptic flow from the simulated data by using q-distribution and Q-Cumulant method to check which method lies more closer to the input values. Glauber Monte Carlo model is used for the simulations and input for the v_2 to the model is assumed to be the function of n_{part} and ε_{part}. The number of events used for the simulations are 1.5 Millions. The multiplicity for the model is based on two component model and the non-flow is taken according to the parameterization :

$$N_{pairs} = M * (M-1)0.0145 * (2./n_{part}) * (0.22 * n_{bin}/n_{part} + 0.89) \tag{6.4}$$

where M, multiplicity of event, n_{part} and n_{bin} are calculated from Glauber Monte Carlo model. Figure. 6.11 shows the input to the models and results for the corresponding flow calculated using q-distribution and Q-Cumulant method. The solid black lines show the input to the model.

We found that both the methods deviate from the input for low multiplicities but q-distribution methods deviate more at low multiplicities and shows non-determinable

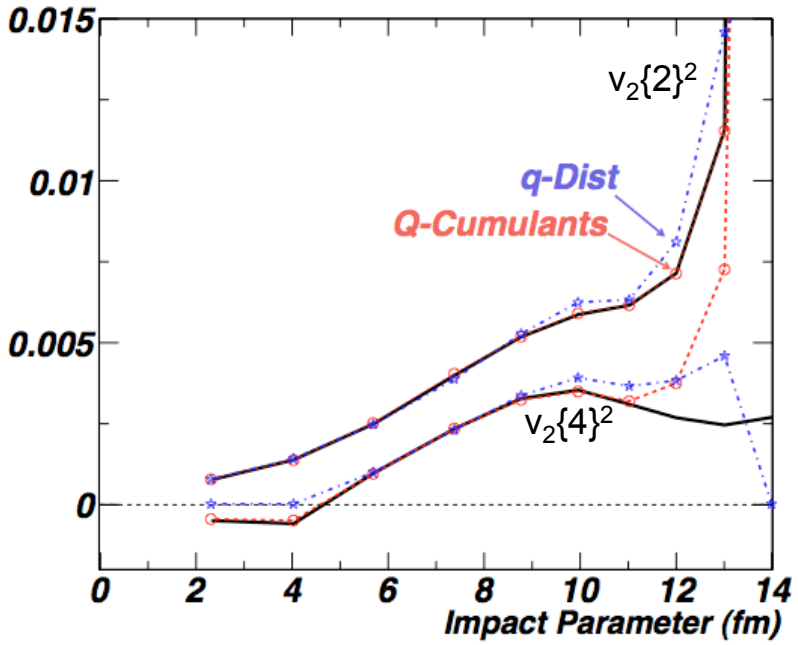

Figure 6.11: Comparison of q-distribution and Q-Cumulant methods for Au+Au collisions at $\sqrt{s_{NN}}$=200 GeV. The black solid lines show the input to the simulations for two- and four-partictles cumulants flow.

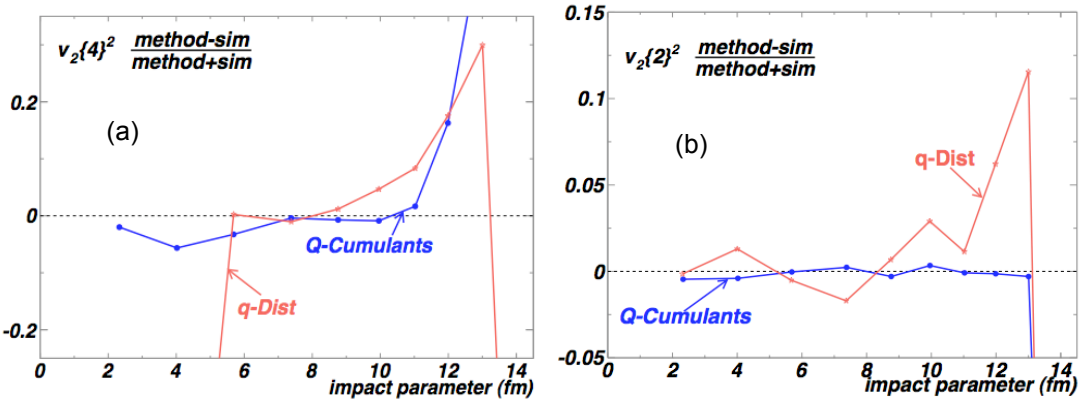

Figure 6.12: The ratio of methods to simulation input for Au+Au collisions at $\sqrt{s_{NN}}$=200 GeV (a) $v_2\{2\}^2$ (b) $v_2\{4\}^2$.

values for the elliptic flow. Figure 6.12 shows the ratio $v_2\{2\}^2$ and $v_2\{4\}^2$ taking the ratio of method to simulation. The ratio shows that q-distribution method shows large uncertainties. Based on the simulation study we decided to carry out the systematic study for the Q-Cumulant method only. Also, the non-flow and upper limit of v_2 fluctuations are calculated using the results from Q-Cumulant method.

6.5 Systematic Errors

The systematic studies has been carried out using the Q-Cumulant method by investigating the change in v_2 with the variation of following:

- Acceptance Corrections.
- Distance of Closest Approach (DCA).
- Transverse Momentum (p_T) Cut.

The results for Au+Au and Cu+Cu collisions with systematic and statistical errors are listed in the Tables 6.5 - 6.8.

Table 6.5: Results for Au+Au 200 GeV using Q-Cumulant Method

Au + Au 200 GeV				
S.No.	Centrality(%)	$v_2\{2\}$	Statistical Errors	Systematic Error
1.	0-5	2.549e-02	3.75e-05	2.88e-04
2.	5-10	3.677e-02	4.17e-05	3.20e-04
3.	10-20	5.187e-02	3.14e-05	6.31e-04
4.	20-30	6.619e-02	3.51e-05	9.90e-04
5.	30-40	7.523e-02	4.28e-05	1.26e-03
6.	40-50	7.916e-02	5.29e-05	1.35e-03
7.	50-60	7.899e-02	7.09e-05	1.42e-03
8.	60-70	7.667e-02	1.08e-04	1.23e-03
9.	70-80	7.692e-02	1.98e-04	9.62e-04
S.No.	Centrality(%)	$v_2\{4\}$	Statistical Errors	Systematic Error
1.	5-10	2.418e-02	3.91e-04	5.50e-04
2.	10-20	4.083e-02	1.53e-04	5.99e-04
3.	20-30	5.543e-02	1.34e-04	1.05e-03
4.	30-40	6.299e-02	1.56e-04	1.24e-03
5.	40-50	6.476e-02	2.04e-04	1.54e-03
6.	50-60	6.105e-02	3.24e-04	1.68e-03
7.	60-70	5.191e-02	7.56e-04	2.05e-03
8.	70-80	4.024e-02	3.03e-03	4.99e-03

6.5.1 Acceptance Corrections

The multi-particle correlations are strongly biased in case of the detector with non-uniform azimuthal acceptance. The cumulants have advantage of isolating the physical correlation between the particles which can be spoiled by the inefficiencies of the detector. Calculating

Table 6.6: Results for Au+Au 62.4 GeV using Q-Cumulant Method

Au + Au 62.4 GeV				
S.No.	Centrality(%)	$v_2\{2\}$	Statistical Errors	Systematic Error
1.	0-5	2.306e-02	5.70e-05	2.52e-04
2.	5-10	3.375e-02	6.40e-05	2.44e-04
3.	10-10	4.744e-02	5.37e-05	6.22e-04
4.	20-30	6.012e-02	5.41e-05	9.48e-04
5.	30-40	6.756e-02	5.41e-05	1.15e-03
6.	40-50	7.016e-02	9.91e-05	1.20e-03
7.	50-60	6.928e-02	1.02e-04	1.10e-03
8.	60-70	6.732e-02	2.37e-04	7.72e-04
9.	70-80	7.001e-02	3.41e-04	2.64e-04
S.No.	Centrality(%)	$v_2\{4\}$	Statistical Errors	Systematic Error
1.	5-10	2.213e-02	4.94e-04	2.03e-04
2.	10-20	3.807e-02	2.18e-04	6.80e-04
3.	20-30	5.082e-02	2.23e-04	1.24e-03
4.	30-40	5.710e-02	2.62e-04	1.19e-03
5.	40-50	5.688e-02	3.02e-04	1.37e-03
6.	50-60	4.921e-02	7.51e-04	3.06e-03
7.	60-70	4.285e-02	1.57e-03	5.53e-03

Table 6.7: Results for Cu+Cu 200 GeV using Q-Cumulant Method

Cu + Cu 200 GeV				
S.No.	Centrality(%)	$v_2\{2\}$	Statistical Errors	Systematic Error
1.	0-10	4.119e-02	3.96e-05	3.94e-04
2.	10-20	5.088e-02	4.54e-05	6.73e-04
3.	20-30	5.841e-02	5.17e-05	8.26e-04
4.	30-40	6.365e-02	8.64e-05	1.02e-03
5.	40-50	6.773e-02	1.08e-04	8.86e-04
6.	50-60	7.101e-02	1.23e-04	8.03e-04
S.No.	Centrality(%)	$v_2\{4\}$	Statistical Errors	Systematic Error
1.	10-20	1.295e-02	7.66e-03	1.88e-02
2.	20-30	2.580e-02	1.25e-03	1.23e-03
3.	30-40	2.504e-02	2.87e-03	1.25e-02

Table 6.8: Results for Cu+Cu 62.4 GeV using Q-Cumulant Method

Cu + Cu 62.4 GeV				
S.No.	Centrality(%)	$v_2\{2\}$	Statistical Errors	Systematic Error
1.	0-10	3.655e-02	6.55e-05	1.92e-04
2.	10-20	4.572e-02	6.86e-05	5.09e-04
3.	20-30	5.331e-02	7.10e-05	6.05e-04
4.	30-40	5.816e-02	9.37e-05	5.76e-04
5.	40-50	6.204e-02	1.32e-04	4.84e-04
6.	50-60	6.595e-02	2.23e-04	2.81e-04
S.No.	Centrality(%)	$v_2\{4\}$	Statistical Errors	Systematic Error
1.	20-30	2.953e-02	1.05e-03	3.34e-03
2.	30-40	2.349e-02	1.21e-03	2.68e-03
3.	40-50	3.165e-02	2.38e-03	1.90e-02

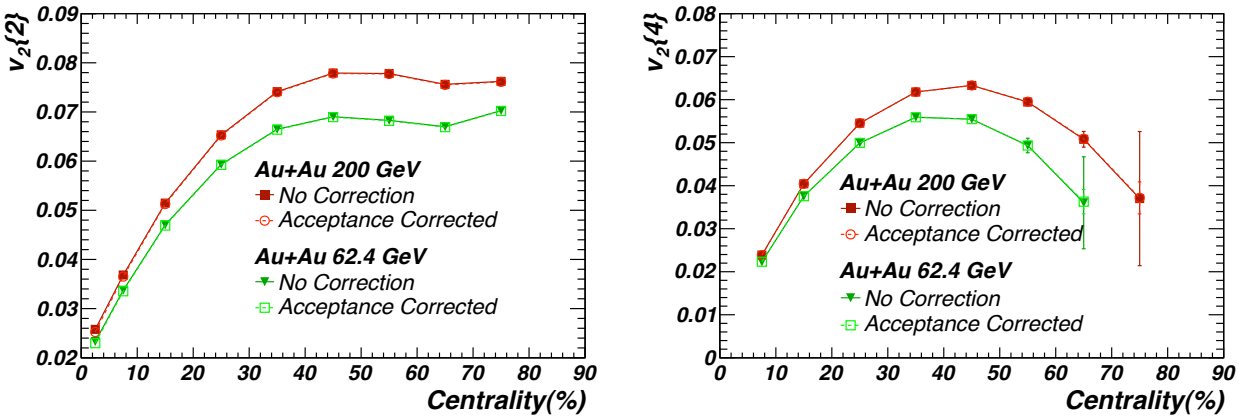

Figure 6.13: Effect of acceptance corrections for Au+Au collisions at $\sqrt{s_{NN}}$=200 and 62.4 GeV (Left) $v_2\{2\}$ (Right) $v_2\{4\}$.

the two- and four-particle cumulants we rejected the terms which vanish for the perfect detector. To include the effect of non-uniform azimuthal distribution we include those terms to calculate the two- and four-particle cumulants using the generalized Q-Cumulant [22] for 2^{nd} and 4^{th} order cumulants.

The second order generalized Q-Cumulant expressed as

$$QC\{2\} = \langle\langle cos\ n(\phi_1 - \phi_2)\rangle\rangle - \langle\langle cos\ n\phi_1\rangle\rangle^2 - \langle\langle sin\ n\phi_1\rangle\rangle^2, \tag{6.5}$$

the last two terms balance the effect of non-uniform acceptance on two-particle cumulants to make $QC\{2\}$ unbiased. These terms can be expressed in terms of real and imaginary

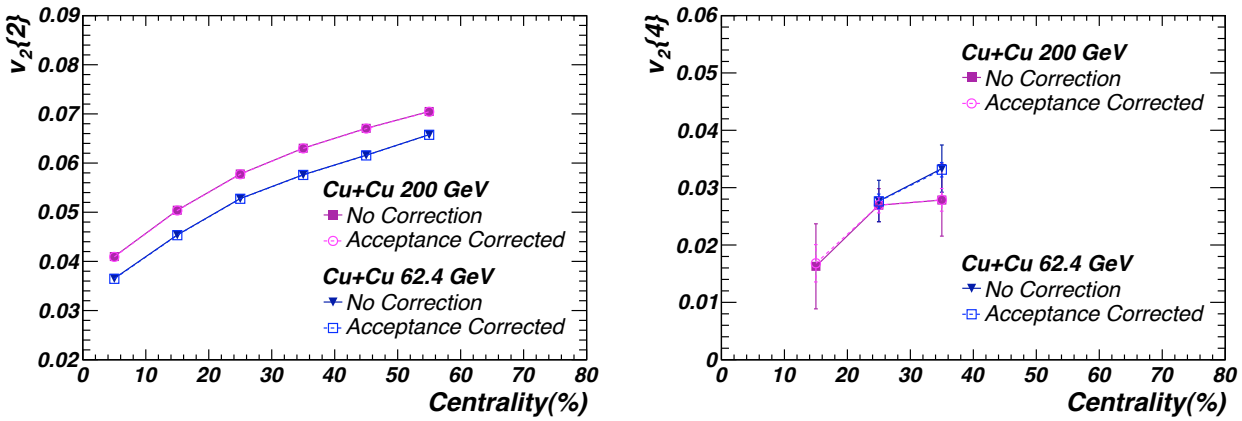

Figure 6.14: Effect of acceptance corrections for Cu+Cu collisions at $\sqrt{s_{NN}}$=200 and 62.4 GeV (Left) $v_2\{2\}$ (Right) $v_2\{4\}$.

parts of Q-vectors,

$$\langle\langle cos\ n\phi_1\rangle\rangle = \frac{\sum_{i=1}^{N}(Re[Q_n])_i}{\sum_{i=1}^{N} M_i}, \tag{6.6}$$

$$\langle\langle sin\ n\phi_1\rangle\rangle = \frac{\sum_{i=1}^{N}(Im[Q_n])_i}{\sum_{i=1}^{N} M_i}. \tag{6.7}$$

The last two terms in Eq. 6.5 explicitly quantify the bias of non-uniform acceptance to two-particle correlations.

The fourth order generalized Q-Cumulant expressed as:

$$\begin{aligned}
QC\{4\} &= \langle\langle cos\ n(\phi_1+\phi_2-\phi_3-\phi_4)\rangle\rangle - 2.\langle\langle cos\ n(\phi_1-\phi_2)\rangle\rangle^2 \\
&- 4.\langle\langle cos\ n\phi_1\rangle\rangle\langle\langle cos\ n(\phi_1-\phi_2-\phi_3)\rangle\rangle \\
&+ 4.\langle\langle sin\ n\phi_1\rangle\rangle\langle\langle sin\ n(\phi_1-\phi_2-\phi_3)\rangle\rangle \\
&- \langle\langle cos\ n(\phi_1+\phi_2)\rangle\rangle^2 - \langle\langle sin\ n(\phi_1+\phi_2)\rangle\rangle^2 \\
&+ 4.\langle\langle cos\ n(\phi_1+\phi_2)\rangle\rangle[\langle\langle cos\ n\phi_1\rangle\rangle^2 - \langle\langle sin\ n\phi_1\rangle\rangle^2] \\
&+ 8.\langle\langle cos\ n(\phi_1+\phi_2)\rangle\rangle\langle\langle cos\ n\phi_1\rangle\rangle\langle\langle sin\ n\phi_1\rangle\rangle \\
&+ 8.\langle\langle cos\ n(\phi_1-\phi_2)\rangle\rangle[\langle\langle cos\ n\phi_1\rangle\rangle^2 + \langle\langle sin\ n\phi_1\rangle\rangle^2] \\
&- 6.[\langle\langle cos\ n\phi_1\rangle\rangle^2 + \langle\langle sin\ n\phi_1\rangle\rangle^2]^2
\end{aligned} \tag{6.8}$$

The terms from third to tenth in the above equation balance the effect of non-uniform acceptance to "four-particle correlation minus two-particle correlation squared" making $QC\{4\}$ unbiased. These terms explicitly quantify the bias of non-uniform acceptance to"four-particle correlation minus two-particle correlations squared."

The new terms in the Eq. 6.8 can also be expressed in terms of Q-vectors

$$\langle\langle cos\ n(\phi_1+\phi_2)\rangle\rangle = \frac{\sum_{i=1}^{N}(Re[Q_nQ_n - Q_{2n}])_i}{\sum_{i=1}^{N} M_i(M_i-1)}, \tag{6.8}$$

$$\langle\langle sin\ n(\phi_1+\phi_2)\rangle\rangle = \frac{\sum_{i=1}^{N}(Im[Q_nQ_n - Q_{2n}])_i}{\sum_{i=1}^{N} M_i(M_i-1)}, \tag{6.9}$$

and

$$\langle\langle cos\ n(\phi_1-\phi_2-\phi_3)\rangle\rangle = \frac{\sum_{i=1}^{N}(Re[Q_nQ_n^*Q_n^* - Q_nQ_{2n}^* - 2(M_i-1)Q_n^*])_i}{\sum_{i=1}^{N} M_i(M_i-1)(M_i-2)}, \tag{6.10}$$

$$\langle\langle sin\ n(\phi_1-\phi_2-\phi_3)\rangle\rangle = \frac{\sum_{i=1}^{N}(Im[Q_nQ_n^*Q_n^* - Q_nQ_{2n}^* - 2(M_i-1)Q_n^*])_i}{\sum_{i=1}^{N} M_i(M_i-1)(M_i-2)}, \tag{6.11}$$

Figures 6.13 and 6.14 show the effect of acceptance correction on the $v_2\{2\}$ and $v_2\{4\}$ for Au+Au and Cu+Cu collisions at 200 and 62.4 GeV. The acceptance corrections has very small effect on the elliptic flow with $v_2\{2\}$ and $v_2\{4\}$ changes by less than 1% for all the centralities in Au+Au and Cu+Cu collisions.

6.5.2 Distance of Closest Approach (DCA)

The standard dca cut used in data analysis is $dca < 3\ cm$. To study the effect of change in dca, the dca cut has been varied to higher and lower values than the standard value. The dca cuts used for this purpose are $dca < 1\ cm$ and $dca < 4\ cm$. Figures 6.15 and 6.16 show the effect of decrease in dca cut on $v_2\{2\}$ and $v_2\{4\}$ for Au+Au and Cu+Cu collisions at 200 and 62.4 GeV. Thus, decreasing the dca increases $v_2\{2\}$ upto 2.5% and $v_2\{4\}$ upto

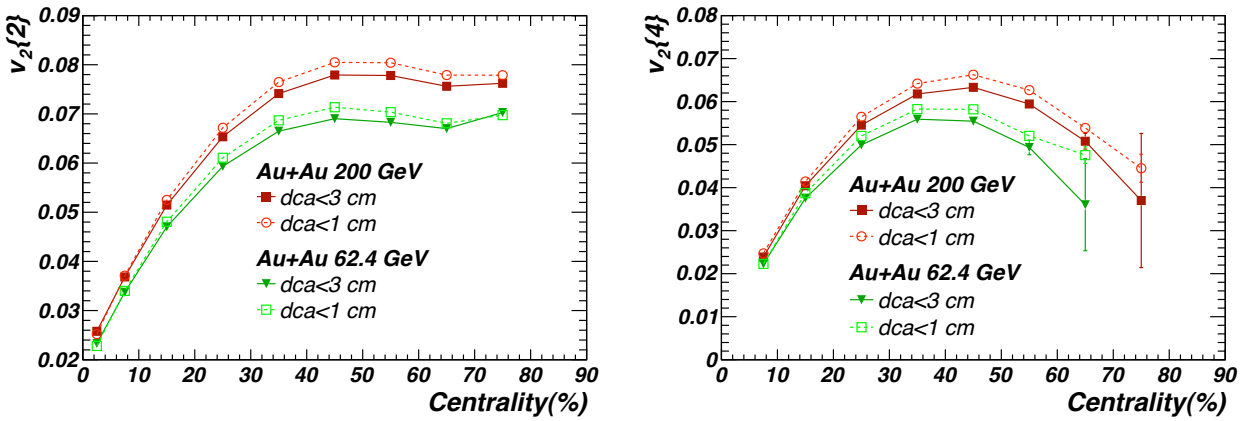

Figure 6.15: Effect of decreasing dca cut for Au+Au collisions at $\sqrt{s_{NN}}$=200 and 62.4 GeV (Left) $v_2\{2\}$ (Right) $v_2\{4\}$.

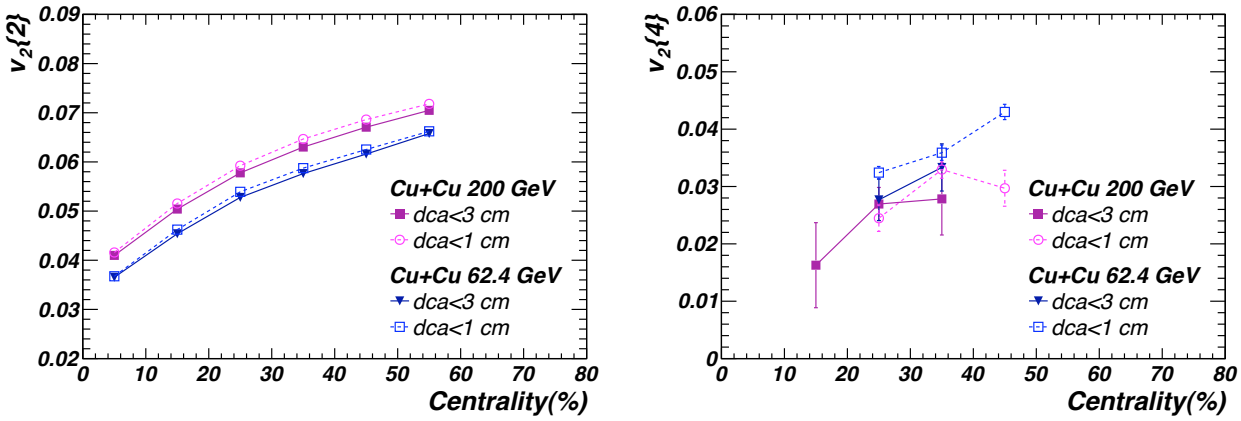

Figure 6.16: Effect of decreasing dca cut for Cu+Cu collisions at $\sqrt{s_{NN}}$=200 and 62.4 GeV (Left) $v_2\{2\}$ (Right) $v_2\{4\}$.

3% for the peripheral collisions in Au+Au collisions at 200 and 62.4 GeV and less than 2% for Cu+Cu collisions.

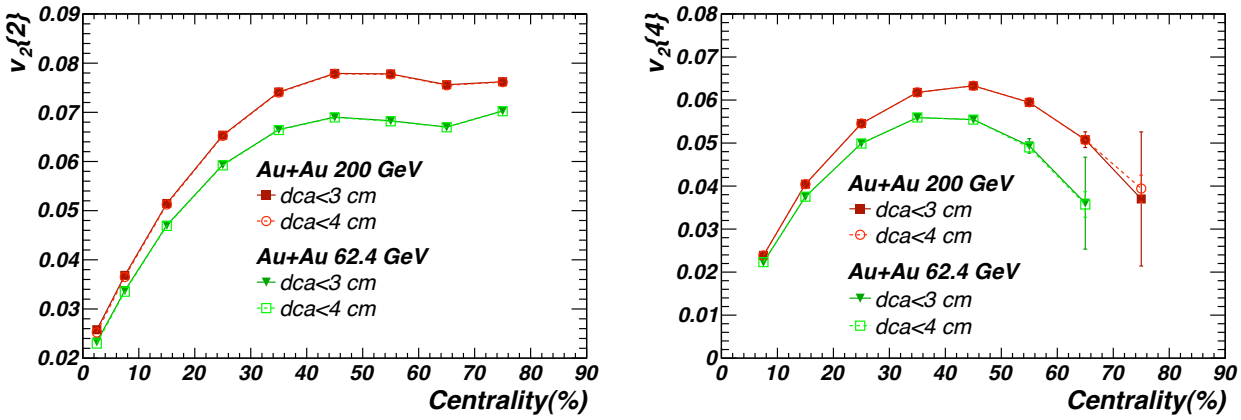

Figure 6.17: Effect of increasing dca cut for Au+Au collisions at $\sqrt{s_{NN}}$=200 and 62.4 GeV (Left) $v_2\{2\}$ (Right) $v_2\{4\}$.

Figures 6.17 and 6.18 show the effect of increasing the value of dca cut to $dca < 4\ cm$. It is seen that increasing dca cut changes the values of $v_2\{2\}$ and $v_2\{4\}$ by less than 1% .

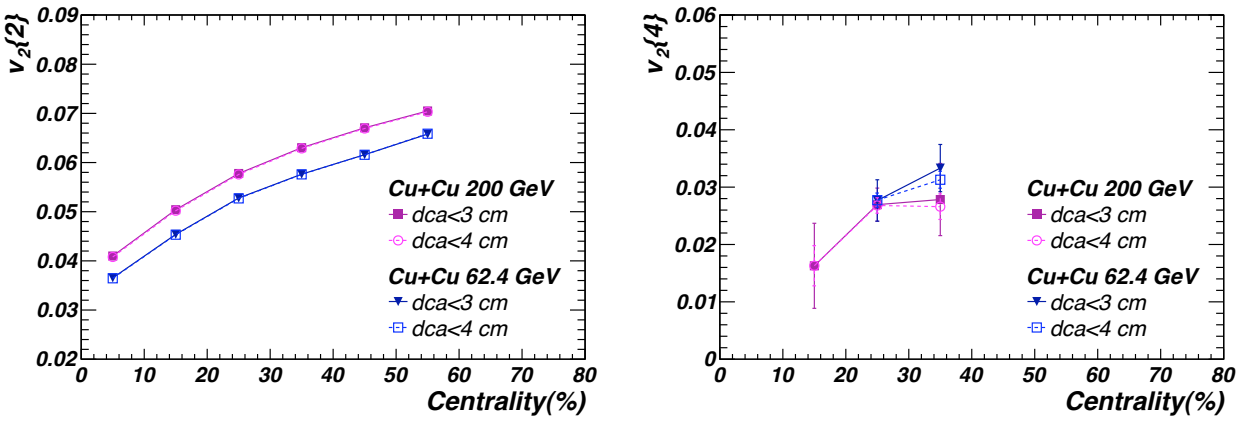

Figure 6.18: Effect of increasing dca cut for Cu+Cu collisions at $\sqrt{s_{NN}}$=200 and 62.4 GeV (Left) $v_2\{2\}$ (Right) $v_2\{4\}$.

6.5.3 Transverse Momentum (p_T) Cut

The p_T range of the tracks used in the analysis is $0.15 \leq p_T \leq 2.0$ GeV/c. The $v_2\{2\}$, $v_2\{4\}$, and the difference $v_2\{2\}^2 - v_2\{4\}^2$ has been calculated for Au+Au 200 GeV by varying the p_T cut to $0.15 \leq p_T \leq 1.5$, $0.15 \leq p_T \leq 3.0$ to check the effect on the results from the p_T range selected for the analysis. Figure 6.19 shows the $v_2\{2\}$, $v_2\{4\}$ and the difference $v_2\{2\}^2 - v_2\{4\}^2$ for the selected p_T ranges and their comparison with the standard p_T range used for the complete analysis. The increasing or decreasing the p_T range shows little effect on the $v_2\{2\}$ and $v_2\{4\}$ with values going slightly up and down, respectively, with p_T but the difference $v_2\{2\}^2 - v_2\{4\}^2$ shows very small effect with the variation in p_T range. We found that $v_2\{2\}$ and $v_2\{4\}$ increase roughly by 5% for $p_T < 1.5$ GeV compared to $p_T < 3.0$ but the difference between $v_2\{2\}^2$ and $v_2\{4\}^2$ changes by less than 1%.

6.6 Non Flow and v_2 Fluctuations

The azimuthal correlations which are not related to reaction plane are collectively known as non-flow (δ_2). However, multi-particle correlation methods used to study elliptic flow

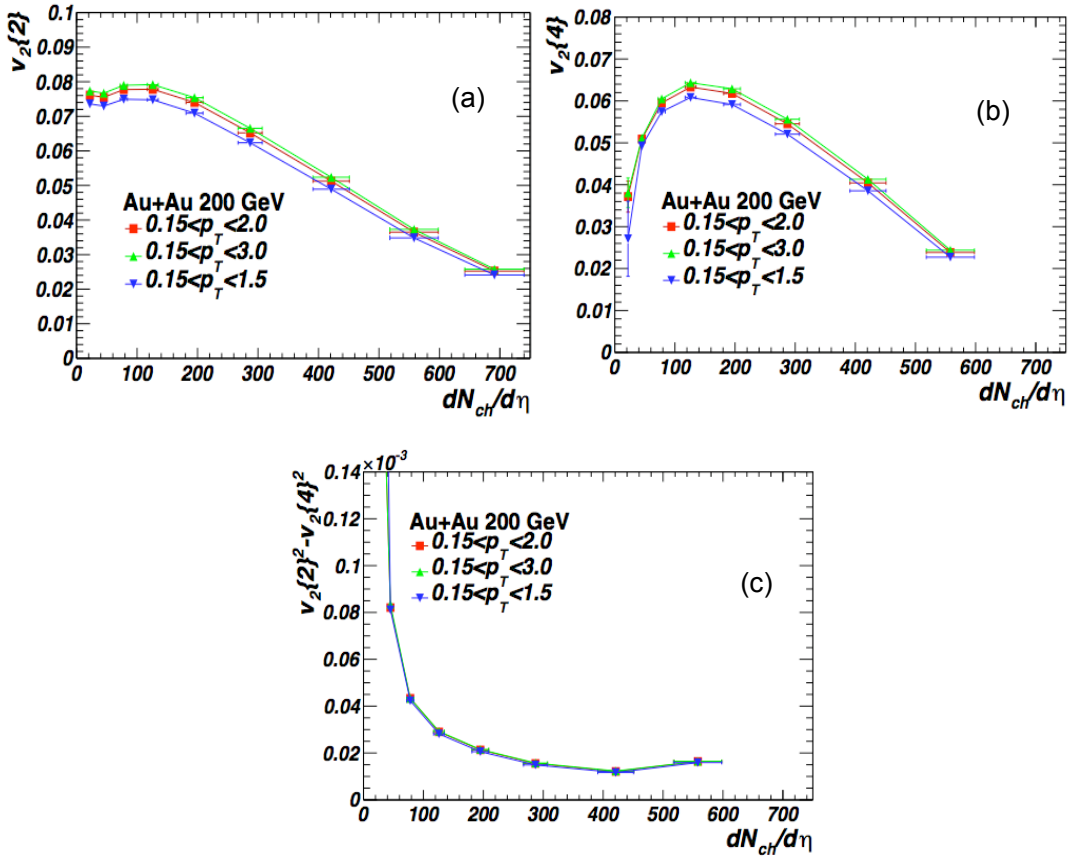

Figure 6.19: Comparison of results using different p_T ranges for Au+Au 200 GeV (a) $v_2\{2\}$ (b) $v_2\{4\}$ (c) $v_2\{2\}^2 - v_2\{4\}^2$.

have the capability to reduce the effect of non-flow correlations on the calculations of elliptic flow but they are not able to minimize the effect of all the non-flow correlations. Therefore, the measurements of non-flow is also an important issue for the explicit measurement of elliptic flow. Also event-by-event fluctuations in heavy ion collisions cause the fluctuations in elliptic flow [24]. Therefore, the comparison of experimental measurement of elliptic flow with the models which don't include event-by-event fluctuations is not a good idea for comparison of theory with the experiments. The fluctuations in elliptic flow may be due to the fluctuations in *spatial* anisotropy in the initial stage of collisions. The fluctuations in initial spatial anisotropy may be caused by the fluctuations in overlapped region of the overlapping nuclei. The effect of these fluctuations on elliptic flow is also important. Since initial anisotropy and elliptic flow are related as $v_2 \propto \varepsilon$, therefore, to study these fluctuations one needs to use models which give event-by-event measurement

of anisotropy parameter ε.

The event-by-event fluctuations in ε may cause fluctuations in elliptic flow. There may be other sources of elliptic flow fluctuations. To get an idea about the effect of eccentricity fluctuations on elliptic flow, different models for the eccentricity calculations have been used.

6.6.1 Like-Sign Study

The elliptic flow from two- and four-particle correlations has been also studied from like-sign tracks using Q-Cumulant method. The $v_2\{2\}$ from the like-sign tracks (Fig. 6.21 (a) and (b)) for Au+Au and Cu+Cu collisions at 200 and 62.4 GeV has been found to be slightly smaller than $v_2\{2\}$ from the charge independent studies which is expected due to small non-flow contribution in case of like-sign tracks correlations. The $v_2\{4\}$ (shown in

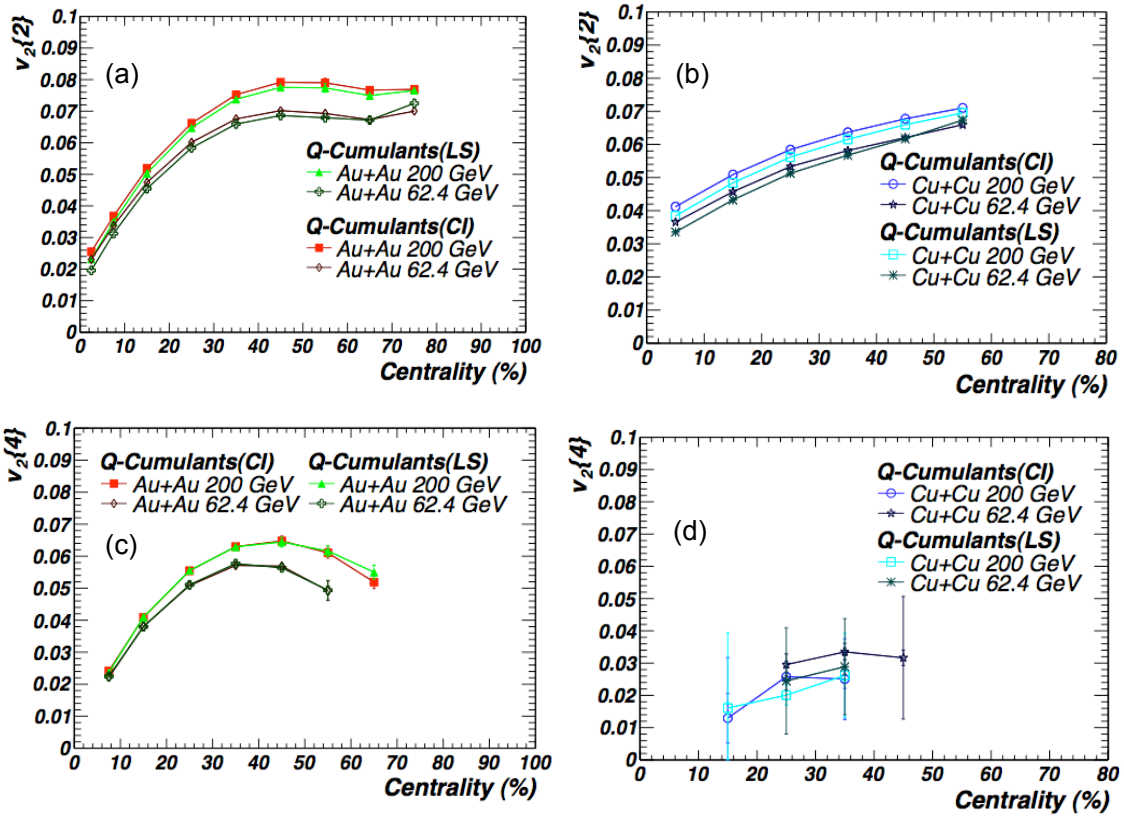

Figure 6.20: (Top Panel) Comparison of the $v_2\{2\}$ calculated from like-sign (LS) tracks and from charge independent (CI) studies for (a) Au+Au 200 and 62.4 GeV (b) Cu+Cu 200 and 62.4 GeV. (Bottom Panel) Similar comparison for $v_2\{4\}$ (c) Au+Au 200 and 62.4 GeV (d) Cu+Cu 200 and 62.4 GeV.

Figs. 6.21 (c) and (d)), however remains almost same within errors in case of like-sign and charge independent studies. Since the difference $v_2\{2\}^2 - v_2\{4\}^2$ is related to non-flow and v_2 fluctuations, so using the elliptic flow from like-sign studies may give better information for the non-flow calculated under the assumption that eccentricity fluctuations dominates v_2 fluctuations. All the results for non-flow and comparison of v_2 fluctuations in data with eccentricity fluctuations in the models have been made using elliptic flow measurement of like-sign charged particles and these may be better used to check the consistency of eccentricity models with the data.

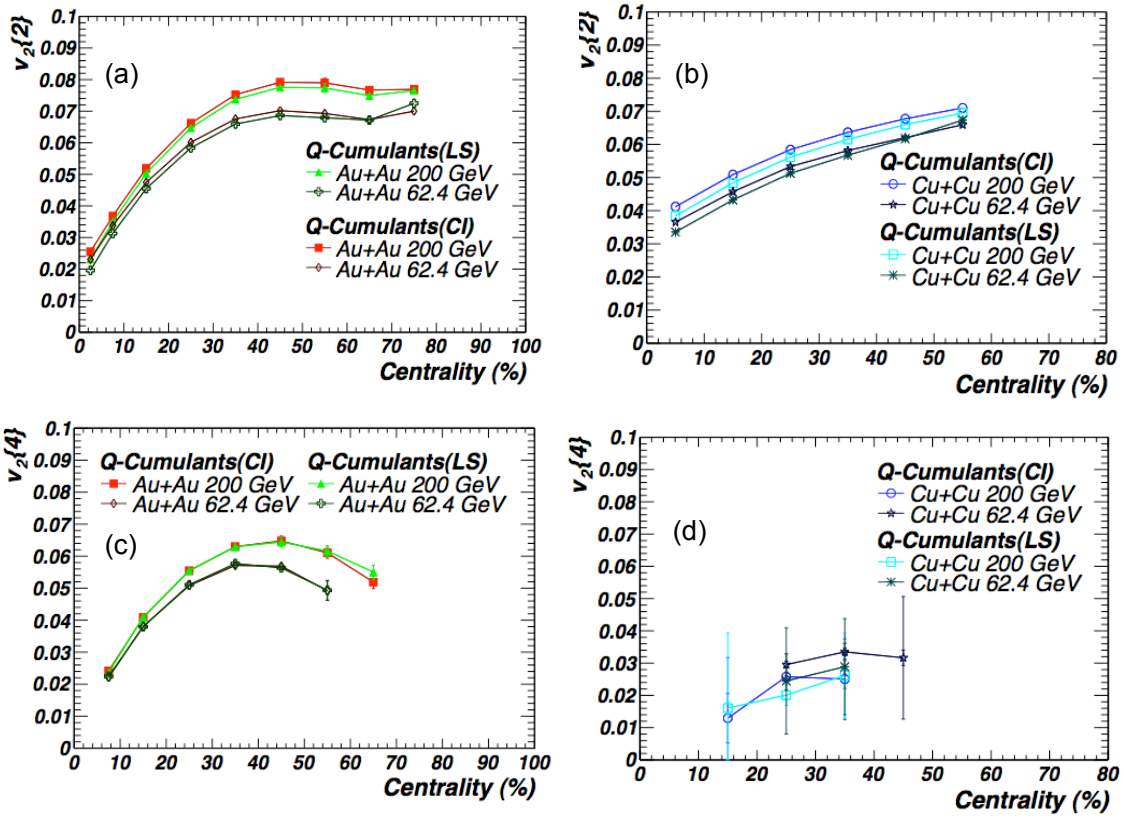

Figure 6.21: (Top Panel) Comparison of the $v_2\{2\}$ calculated from like-sign (LS) tracks and from charge independent (CI) studies for (a) Au+Au 200 and 62.4 GeV (b) Cu+Cu 200 and 62.4 GeV. (Bottom Panel) Similar comparison for $v_2\{4\}$ (c) Au+Au 200 and 62.4 GeV (d) Cu+Cu 200 and 62.4 GeV.

6.6.2 Comparison With Models

We compare our $v_2\{2\}$ and $v_2\{4\}$ results wih three different eccentricity models (viz., Monte-Carlo Glauber model with Nucleons as Participants (MCG-N), Monte-Carlo Glauber model with Quarks as Participants (MCG-Q) and Color Glass Condensate based Monte-Carlo model (fKLN-CGC)) for the initial eccentricity in heavy-ion collisions.

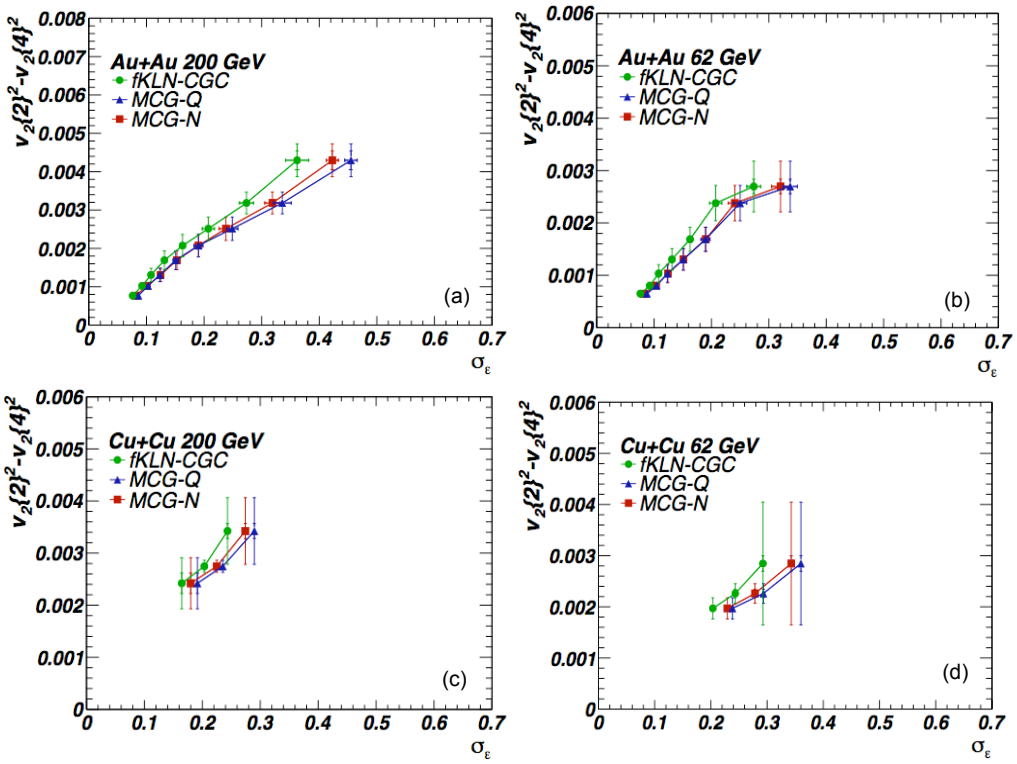

Figure 6.22: $v_2\{2\}^2 - v_2\{4\}^2$ *vs.* σ_ε, fluctuations in ε_{std} for MCG-N, MCG-Q and fKLN-CGC models for (a) Au+Au 200 GeV (b) Au+Au 62.4 GeV (c) Cu+Cu 200 GeV (d) Cu+Cu 62.4 GeV.

Firstly, we compare our elliptic flow results with the eccentricity models without invoking any assumption. Fig. 6.22 shows the variation of difference $v_2\{2\}^2 - v_2\{4\}^2$ with eccentricity fluctuations (σ_ε) in ε_{std} calculated for different models for Au+Au and Cu+Cu collisions at 200 and 62.4 GeV as indicated in figures. It is seen that $v_2\{2\}^2 - v_2\{4\}^2$ scales linearly with the eccentricity fluctuations indicating v_2 fluctuations may be due to the eccentricity fluctuations. Figure 6.23 shows the similar plots for three eccentricity models as indicated in the figures. We notice that the variation of $v_2\{2\}^2 - v_2\{4\}^2$ is independent of system-size within errors bars. Figure 6.24 shows the variation of $v_2\{2\}$ with ε_{part} from eccentricity models, $v_2\{2\}$ increases with ε_{part} for Au+Au and Cu+Cu collisions at 200

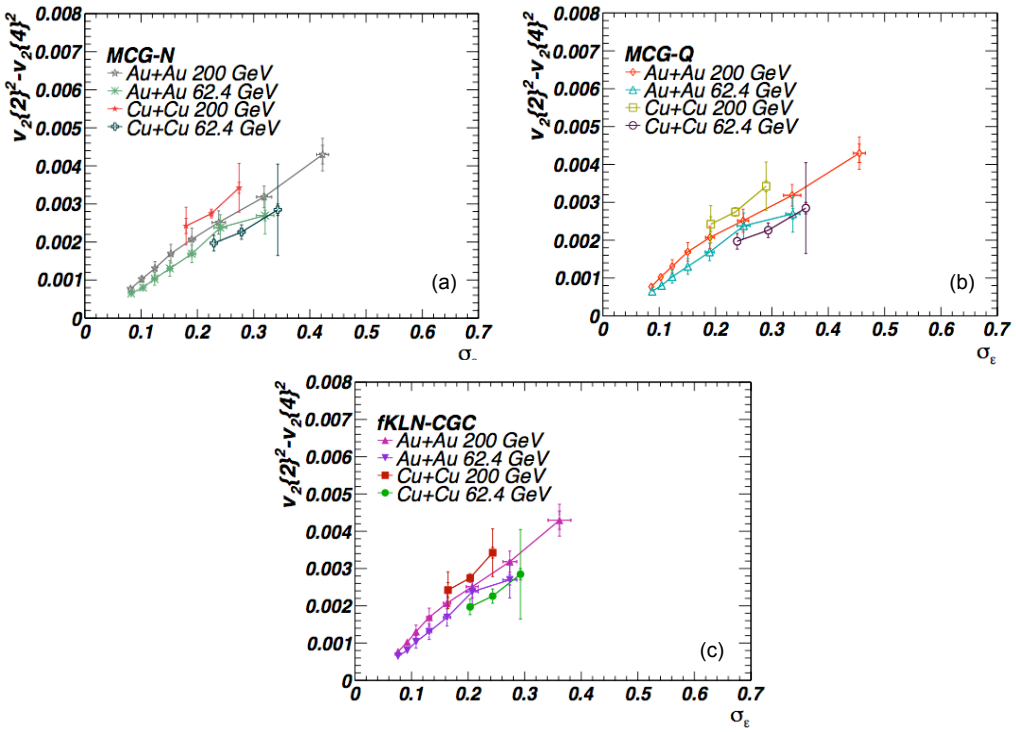

Figure 6.23: Comparison of $v_2\{2\}^2 - v_2\{4\}^2$ with σ_ε for Au+Au and Cu+Cu collisions at 200 and 62.4 GeV with σ_ε from the eccentricity models (a) MCG-N (b) MCG-Q (c) fKLN-CGC.

and 62.4 GeV. $v_2\{2\}$ nearly becomes independent of ε_{part} for the most peripheral collisions in Au+Au collisions at both the energies.

6.6.3 Upper Limit on v_2 Fluctuations

In order to compare our data with models for eccentricity fluctuations we compare σ_{v_2}/v_2 to $\sigma_\varepsilon/\varepsilon$. From the two- and four-particle cumulant data however, we can't uniquely determine the value of σ_{v_2} since $v_2\{2\}^2 - v_2\{4\}^2 \approx \delta_2 + 2\sigma_{v_2}$. However, we can derive an upper limit to the ratio σ_{v_2}/v_2 by setting $\delta_2 = 0$. This amounts to assuming that the difference between the second and fourth order cumulant is dominated by v_2 fluctuations. For the Gaussian form of the fluctuations the parameters $\langle v \rangle$, σ_{v_2} and δ_2 are correlated according to [25]:

$$v_2\{2\}^2 = \langle v \rangle^2 + \sigma_{v_2}^2 + \delta_2 \tag{6.12}$$

$$v_2\{4\}^2 = \sqrt{\langle v \rangle^4 - 2\langle v \rangle^2 \sigma_{v_2}^2 - \sigma_{v_2}^4} \approx \langle v \rangle^2 - \sigma_{v_2}^2 \tag{6.13}$$

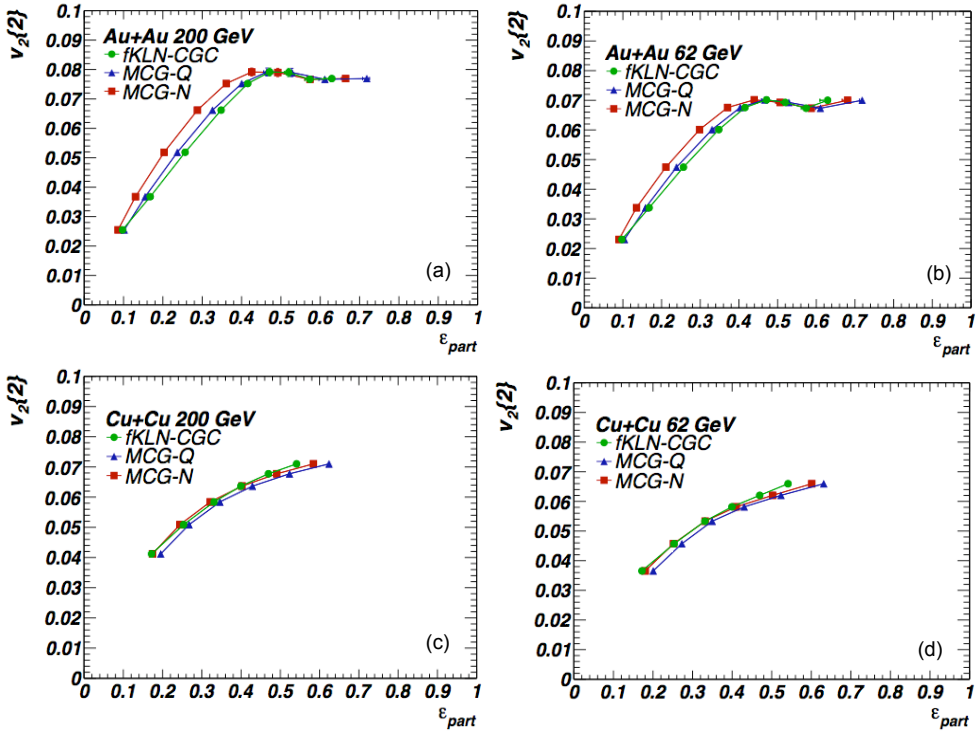

Figure 6.24: $v_2\{2\}^2 - v_2\{4\}^2$ *vs.* σ_ε for (a) Au+Au 200 GeV (b) Au+Au 62.4 GeV (c) Cu+Cu 200 GeV (d) Cu+Cu 62.4 GeV, σ_ε taken from MCG-N, MCG-Q and fKLN-CGC models.

For convenience, we define two parameters Σ and Δ using the Eq. (6.12) and Eq. (6.13)

$$\Sigma = \frac{v_2\{2\}^2 + v_2\{4\}^2}{2} = \frac{\delta_2}{2} + \langle v \rangle^2 \tag{6.14}$$

$$\Delta = \frac{v_2\{2\}^2 - v_2\{4\}^2}{2} = \frac{\delta_2}{2} + \sigma_{v_2}^2 \tag{6.15}$$

Taking $\delta_2 = 0$ in the above equations, the ratio

$$\sqrt{\frac{v_2\{2\}^2 - v_2\{4\}^2}{v_2\{2\}^2 + v_2\{4\}^2}}, \tag{6.16}$$

becomes an upper limit to the ratio $\sigma_{v_2}/\langle v_2 \rangle$ where, in the case that v_2 fluctuations are dominated by eccentricity fluctuations, $\langle v_2 \rangle$ is the average v_2 relative to the participant axis. The σ_v/v from the data has been compared with $\sigma_\varepsilon/\varepsilon$ from the models. Under the assumption $v_2 \propto \varepsilon$, the $\sigma_\varepsilon/\varepsilon$ derived from the models as:

$$\frac{\sigma_\varepsilon^2}{\varepsilon^2} = \frac{\varepsilon\{2\}^2 - \varepsilon\{4\}^2}{\varepsilon\{2\}^2 + \varepsilon\{4\}^2} \tag{6.17}$$

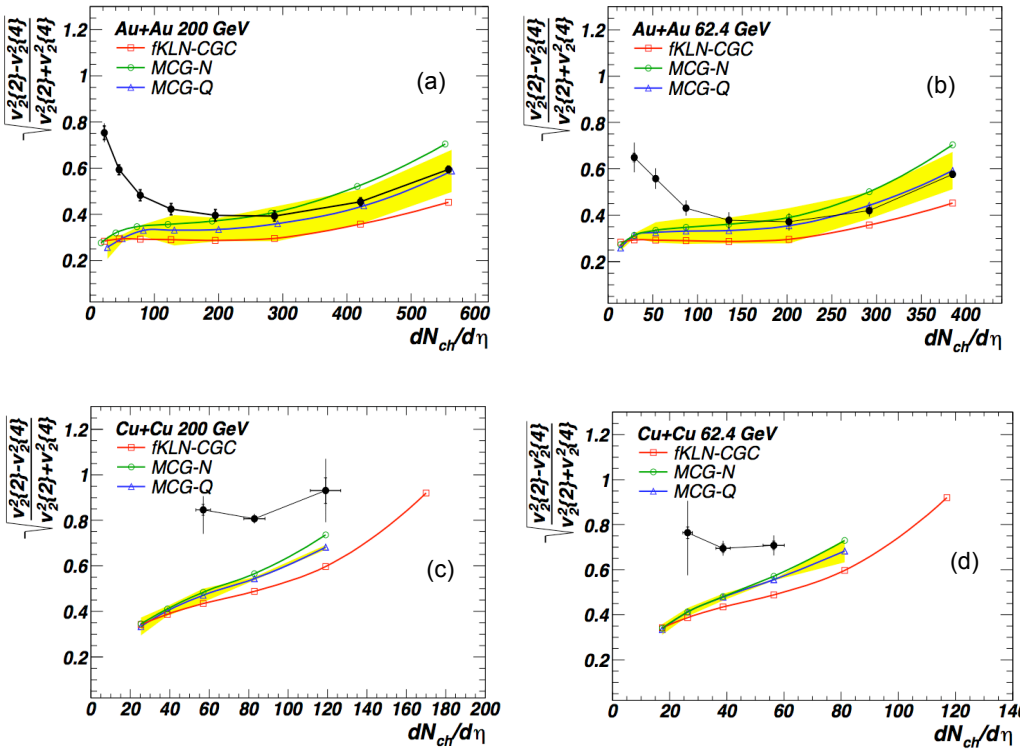

Figure 6.25: The upper limit on σ_v/v found using the LS results for $v_2\{2\}$ compared to $\sigma_{\varepsilon/\varepsilon}$ from three different eccentricity models for (a) Au+Au 200 GeV (b) Au+Au 62.4 GeV (c) Cu+Cu 200 GeV (d) Cu+Cu 62.4 GeV.

where $\varepsilon\{2\}^2 = \langle\varepsilon^2_{part}\rangle$ and $\varepsilon\{4\}^4 = -\langle\varepsilon^4_{part}\rangle + 2\langle\varepsilon^2_{part}\rangle^2$, ε_{part} is the eccentricity calculated in the participant plane.

Figure 6.25 shows variation of $\sqrt{\frac{v_2\{2\}^2 - v_2\{4\}^2}{v_2\{2\}^2 + v_2\{4\}^2}}$ with charged hadron multiplicity for Au+Au and Cu+Cu collisions at 200 and 62.4 GeV centre of mass energies. The data is compared to $\sigma_\varepsilon/\varepsilon$ for the three different eccentricity models. The centrality in the models is defined using multiplicity so that the model calculations include bin width effects and impact parameter fluctuations. The ratio for the MCG-N model rises quickly with centrality for Au+Au 200 and 62.4 GeV collisions and then overshoots the upper-limit in the most central collisions. The MCG-Q model approaches the upper limit in central collisions but never exceeds it. The fKLN-CGC model has smallest values and is well below the

upper limit for the entire centrality range. The fact that the MCG-N and MCG-Q models reach upper limit and in some cases exceed the upper limit means that for those models to be correct, non-flow should be small and in some cases negative. The upper limit on v_2 fluctuations for Cu+Cu collisions is larger than for Au+Au and lie near unity. All the models fall below the upper limit and differences between the models are small.

6.6.4 Non-Flow (δ_2) Using Eccentricity Models

It has been learnt from the previous analyses that the non-flow and v_2 fluctuations are not separable and cannot be measured independently. Therefore, the non-flow has been calculated by alternate approach using the eccentricity from three eccentricity models, viz., MCG-N, MCG-Q and fKLN-CGC. The $v_2\{2\}^2$ and $v_2\{4\}^2$ are related to non-flow (δ_2) and v_2 fluctuations (σ_{v2}) through the relation

$$v_2\{2\}^2 - v_2\{4\}^2 \approx \delta_2 + 2\sigma_{v_2}^2. \tag{6.18}$$

The non-flow from the above equation has been calculated under the assumption that eccentricity fluctuations lead to the v_2 fluctuations, *i.e.,*

$$\sigma_{v_2} \approx v_2 \frac{\sigma_\varepsilon}{\varepsilon}. \tag{6.19}$$

where σ_v and σ_ε are fluctuations in elliptic flow and initial state eccentricity, respectively.

Using the assumption in Eq. (6.19) and solving Eqs. 6.14 and 6.15 non-flow can be derived as below.

$$\Sigma = \frac{\delta_2}{2} + \langle v \rangle^2 \tag{6.20}$$

$$\Delta = \frac{\delta_2}{2} + \sigma_{v_2}^2 \tag{6.21}$$

$$\frac{\sigma_{v_2}^2}{\langle v \rangle^2} = \frac{\sigma_\varepsilon^2}{\varepsilon^2} = \frac{\Delta - \delta_2/2}{\Sigma - \delta_2/2} \tag{6.22}$$

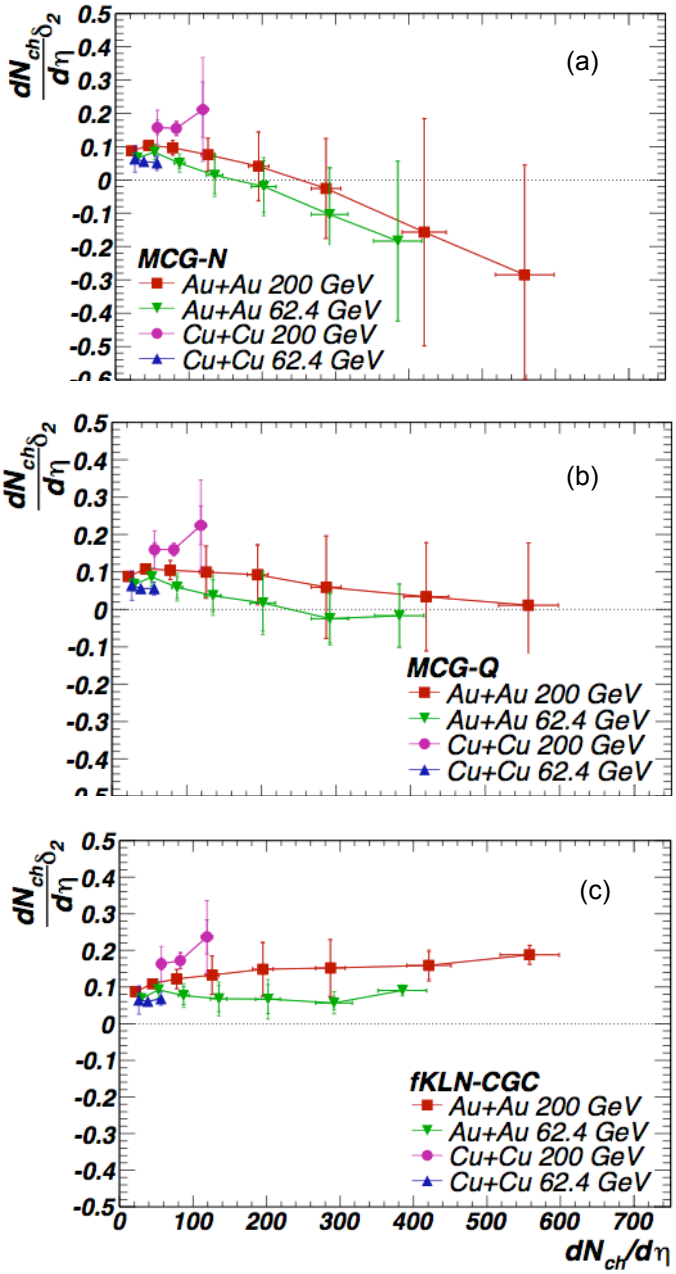

Figure 6.26: Multiplicity scaled non-flow for Au+Au and Cu+Cu collisions at 200 and 62.4 GeV by taking the eccentricity fluctuations from (a) MCG-N model (b) MCG-Q model (c) fKLN-CGC model.

$$\frac{\delta_2}{2} = \frac{\Delta - \frac{\sigma_\varepsilon^2}{\varepsilon^2}\Sigma}{1 - \frac{\sigma_\varepsilon^2}{\varepsilon^2}} \tag{6.23}$$

The Eq. (6.23) is used to calculate non-flow for Glauber models and CGC model.

In the absence of new physics, the term δ_2 will vary with event multiplicity as $1/M$. To cancel out the combinatorial $1/M$ dependence we scale δ_2 by the number of charged hadrons within $|\eta| < 0.5$ $dN_{ch}/d\eta$.

Figure 6.26 shows the like-sign $\frac{dN_{ch}}{d\eta}\delta_2$ that is required if Monte-Carlo Glauber model with Nucleons as Participants (MCG-N), Monte-Carlo Glauber model with Quarks as Participants (MCG-Q) and fKLN-CGC model give the correct description of the eccentricity fluctuations and if eccentricity fluctuations dominate v_2 fluctuations. Within errors, $\frac{dN_{ch}}{d\eta}\delta_2$ is the same in Cu+Cu collisions and Au+Au collisions at the same energies and event multiplicities. The value of $\frac{dN_{ch}}{d\eta}\delta_2$ (Fig. 6.26 (a)) required by MCG-N model falls with centrality and becomes negative for the most central Au+Au collisions. For this model of eccentricity fluctuations to be valid, the non-flow in central Au+Au collisions should be slightly negative. In case other sources besides eccentricity fluctuations contribute to v_2 fluctuations, the inferred non-flow should become even smaller. The smaller relative fluctuations for the Constituent Quark Participant model means this model would be consistent with larger non-flow (Fig. 6.26 (b)) values than the Nucleon Participant model. The required non-flow values are positive at all measured multiplicities. Figure 6.26 (c) shows $\frac{dN_{ch}}{d\eta}\delta_2$ from the fKLN-CGC model. This model has a larger average eccentricity and smaller eccentricity fluctuations than the other models leading to the smallest relative fluctuations of the three models. The multiplicity scaled non-flow is larger for 200 GeV collisions than 62.4 GeV collisions and Cu+Cu collisions seem to have the same non-flow values as Au+Au when they are compared at the same multiplicity. The multiplicity scaled non-flow implied by the fKLN-CGC eccentricity model increases with centrality. The rate of increase seems to be largest in the peripheral region and then levels off somewhat.

6.6.5 Eccentricity Scaled v_2

In this section, we show the ratio $\langle v_2\rangle/\langle\varepsilon\rangle$ for the three models of eccentricity. Taking $v_2 \propto \varepsilon$, implies $\langle v_2\rangle/\langle\varepsilon\rangle \approx v_2\{4\}/\varepsilon\{4\}$. In Fig. 6.27 shows the variation of $v_2\{4\}/\varepsilon\{4\}$ with charged particle multiplicity for Au+Au and Cu+Cu collisions at 200 and 62.4 GeV. The ratio seems to depend primarily on multiplicity for different systems and energies. Only the fKLN-CGC model displays a saturation of v_2/ε for $\frac{dN_{Ch}}{d\eta} > 300$. The Monte Carlo Glauber model with Nucleon Participants shows steepest increase in v_2/ε while the Constituent Quark model is intermediate between the sharp rise of the Nucleon Partici-

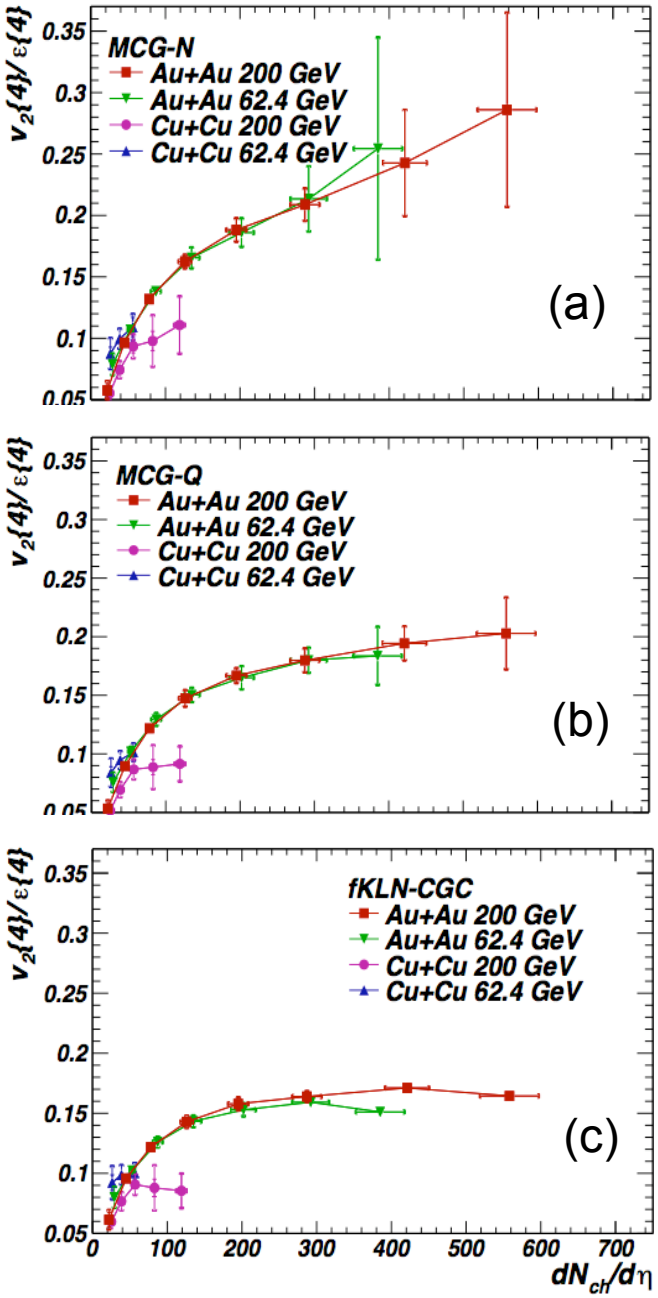

Figure 6.27: The eccentricity scaled v_2 for 200 and 62.4 GeV, Au+Au and Cu+Cu collisions with eccentricity taken from (a) MCG-N model (b) MCG-Q model (c) fKLN-CGC model.

pant model and the fKLN-CGC model. The hydrodynamical approximation $v_2 \propto \varepsilon$ [26] have been observed experimentally (Figs. 6.22 - 6.24) and saturation of v_2/ε for mid central collisions is strongly violated for the Nucleon Participant model implying that if the Nucleon Participant model is the correct eccentricity model, then the collisions at RHIC

are far from the ideal hydrodynamic limit. The fKLN-CGC model and Constituent Quark model imply that v_2 saturates or nearly saturates in central Au+Au collisions.

6.7 Conclusions

We presented STAR measurements of two- and four-particle v_2 cumulants ($v_2\{2\}$ and $v_2\{4\}$) for Au+Au and Cu+Cu collisions at $\sqrt{s_{_{NN}}}$=200 and 62.4 GeV alongwith the difference $v_2\{2\}^2 - v_2\{4\}^2 \approx \delta_2 + 2\sigma_{v_2} \equiv \sigma^2_{tot}$ for charge-independent and like-sign combinations of particles. The difference $v_2\{2\}^2 - v_2\{4\}^2$ increases with beam energy for both Cu+Cu and Au+Au collisions. For a given $\sqrt{s_{NN}}$ and particle multiplicity, $v_2\{2\}^2 - v_2\{4\}^2$ values are the same in Cu+Cu and Au+Au collisions within errors. Although the value of v_2 fluctuations could not be uniquely determined, $v_2\{2\}$ and $v_2\{4\}$ were used to obtain an upper-limit on the ratio σ_{v_2}/v_2. The eccentricity fluctuations from the MCG-N model are larger than the upper-limit from data for central Au+Au collisions but the MCG-Q and fKLN-CGC eccentricity models fall within the presented limit. To further investigate the models we calculated the value of the non-flow δ_2 implied by the models for eccentricity fluctuations under the assumption that $\sigma_{v_2}/v_2 = \sigma_\varepsilon/\varepsilon$. The non-flow values implied by the fKLN-CGC model are larger than those from either of the Monte Carlo Glauber models. The non-flow implied by the fluctuations in the MCG models becomes negative for central Au+Au collisions. This analysis challenges the models to describe all features of the data including both v_2 fluctuations and various correlations data. We presented v_2/ε for the three different eccentricity models and found that the fKLN-CGC model for eccentricity leads to a saturation of v_2/ε for Au+Au collisions with $\frac{dN_{\mathrm{Ch}}}{d\eta} > 300$ while v_2/ε is rising steeply at all centralities when the MCG-N model is used for ε. The saturation of v_2/ε for the fKLN-CGC eccentricity model is consistent with a nearly perfect hydrodynamic behavior for heavy-ion collisions at RHIC.

Bibliography

[1] J.-Y. Ollitrault, Phys. Rev. D **46**, 229(1992); H. Sorge, Phys. Rev. Lett. **82**, 2048 (1999).

[2] K. H. Ackermann *et al.* [STAR Collaboration], Phys. Rev. Lett. **86**, 402 (2001).

[3] B. B. Back *et al.* [PHOBOS Collaboration], Phys. Rev. Lett. **89**, 222301 (2002); K. Adcox *et al.* [PHENIX Collaboration], Phys. Rev. Lett. **89**, 212301 (2002).

[4] P. F. Kolb, J. Sollfrank and U. W. Heinz, Phys. Rev. C **62**, 054909 (2000).

[5] M. Harrison, T. Ludlam and S. Ozaki, Nucl. Instrum. Meth. A **499**, 235 (2003).

[6] S. Voloshin and Y. Zhang, Z. Phys. C **70**, 665 (1996).

[7] B. Alver *et al.*, Phys. Rev. C **77**, 014906 (2008) [arXiv:0711.3724 [nucl-ex]].

[8] K. H. Ackermann *et al.* [STAR Collaboration], Phys. Rev. Lett. **86**, 402 (2001); C. Adler *et al.* [STAR Collaboration], Phys. Rev. Lett. **87**, 182301 (2001); C. Adler *et al.* [STAR Collaboration], Phys. Rev. Lett. **89**, 132301 (2002); J. Adams *et al.* [STAR Collaboration], Phys. Rev. Lett. **92**, 052302 (2004); J. Adams *et al.* [STAR Collaboration], Phys. Rev. C **72**, 014904 (2005); J. Adams *et al.* [STAR Collaboration],

Phys. Rev. Lett. **95**, 122301 (2005); K. Adcox *et al.* [PHENIX Collaboration], Nucl. Phys. A **757**, 184 (2005); J. Adams *et al.* [STAR Collaboration], Nucl. Phys. A **757**, 102 (2005); B. Alver *et al.* [PHOBOS Collaboration], Phys. Rev. Lett. **98**, 242302 (2007); B.B. Back *et al.* [PHOBOS Collaboration], Phys. Rev. C **72**, 051901(R) (2005); Phys. Rev. Lett. **94**, 122303 (2005).

[9] P. Kovtun, D. T. Son and A. O. Starinets, Phys. Rev. Lett. **94**, 111601 (2005).

[10] P. Huovinen, P. F. Kolb, U. W. Heinz, P. V. Ruuskanen and S. A. Voloshin, Phys. Lett. B **503**, 58 (2001); D. Teaney, Phys. Rev. C **68**, 034913 (2003); K. Dusling and D. Teaney, Phys. Rev. C **77**, 034905 (2008) [arXiv:0710.5932 [nucl-th]].

[11] T. Hirano, U. W. Heinz, D. Kharzeev, R. Lacey and Y. Nara, Phys. Lett. B **636**, 299 (2006); T. Lappi and R. Venugopalan, Phys. Rev. C **74**, 054905 (2006).

[12] H. J. Drescher, A. Dumitru, A. Hayashigaki and Y. Nara, Phys. Rev. C **74**, 044905 (2006) [arXiv:nucl-th/0605012]; H. J. Drescher and Y. Nara, Phys. Rev. C **76**, 041903 (2007) [arXiv:0707.0249 [nucl-th]].

[13] A. M. Poskanzer and S. A. Voloshin, Phys. Rev. C **58**, 1671 (1998).

[14] Jean-Yves Ollitraut, A. M. Poskanzer and S. A. Voloshin, Nucl. Phys. A **830**, 279c-282c (2009).

[15] arXiv:nucl-ex/0308020v1 (2003).

[16] Although negative non-flow values can easily be generated from resonance decays in specific kinematic regions, we consider the case that the total non-flow should become negative highly unlikely and contradictory to studies of non-flow effect.

[17] Sergei A. Voloshin, Arthur M. Poskanzer, Aihong Tang and Gang Wang, Phys. Lett. B **659**, 537-541, (2008).

[18] K. H. Ackermann *et al.* [STAR Collaboration], Nucl. Instrum. Meth. A **499**, 624 (2003).

[19] K. H. Ackermann *et al.* [STAR Collaboration], Nucl. Phys. A **661**, 681 (1999).

[20] J. Adams *et al.* [STAR Collaboration], Phys. Rev. Lett. **92**, 052302 (2004).

[21] J. Adams *et al.* [STAR Collaboration], Phys. Rev. C **73**, 034906 (2006).

[22] A. Bilandzic, R. Snellings and S. Voloshin, [arXiv:1010.0233 [nucl-ex]].

[23] P. Sorensen [STAR Collaboration], J. Phys. G **35**, 104102 (2008) [arXiv:0808.0356 [nucl-ex]].

[24] M. Miller and R. Snellings, arXiv:nucl-ex/0312008.

[25] S. Voloshin and Arthur M. Poskanzer, Aihong Tang and Gang Wang , Phys.Lett. **B 659** 537-541,2008.

[26] R. S. Bhalerao *et. al.,* Phys. Lett. B **627**, 49 (2005).